



MINISTÉRIO DA
CIÊNCIA, TECNOLOGIA,
INOVAÇÕES E COMUNICAÇÕES



sid.inpe.br/mtc-m21c/2020/03.05.13.27-TDI

QUANTIFYING AND MONITORING TROPICAL FOREST MORTALITY WITH PASSIVE AND ACTIVE OPTICAL REMOTE SENSING

Ricardo Dal'Agnol da Silva

Doctorate Thesis of the Graduate
Course in Remote Sensing, guided
by Drs. Luiz Eduardo Oliveira e
Cruz de Aragão, and Lênio Soares
Galvão, approved in March 18,
2020.

URL of the original document:

<<http://urlib.net/8JMKD3MGP3W34R/424G29B>>

INPE
São José dos Campos
2020

PUBLISHED BY:

Instituto Nacional de Pesquisas Espaciais - INPE
Gabinete do Diretor (GBDIR)
Serviço de Informação e Documentação (SESID)
CEP 12.227-010
São José dos Campos - SP - Brasil
Tel.:(012) 3208-6923/7348
E-mail: pubtc@inpe.br

**BOARD OF PUBLISHING AND PRESERVATION OF INPE
INTELLECTUAL PRODUCTION - CEPPII (PORTARIA Nº
176/2018/SEI-INPE):****Chairperson:**

Dra. Marley Cavalcante de Lima Moscati - Centro de Previsão de Tempo e Estudos
Climáticos (CGCPT)

Members:

Dra. Carina Barros Mello - Coordenação de Laboratórios Associados (COCTE)
Dr. Alisson Dal Lago - Coordenação-Geral de Ciências Espaciais e Atmosféricas
(CGCEA)
Dr. Evandro Albiach Branco - Centro de Ciência do Sistema Terrestre (COCST)
Dr. Evandro Marconi Rocco - Coordenação-Geral de Engenharia e Tecnologia
Espacial (CGETE)
Dr. Hermann Johann Heinrich Kux - Coordenação-Geral de Observação da Terra
(CGOBT)
Dra. Ieda Del Arco Sanches - Conselho de Pós-Graduação - (CPG)
Sílvia Castro Marcelino - Serviço de Informação e Documentação (SESID)

DIGITAL LIBRARY:

Dr. Gerald Jean Francis Banon
Clayton Martins Pereira - Serviço de Informação e Documentação (SESID)

DOCUMENT REVIEW:

Simone Angélica Del Ducca Barbedo - Serviço de Informação e Documentação
(SESID)
André Luis Dias Fernandes - Serviço de Informação e Documentação (SESID)

ELECTRONIC EDITING:

Ivone Martins - Serviço de Informação e Documentação (SESID)
Cauê Silva Fróes - Serviço de Informação e Documentação (SESID)



MINISTÉRIO DA
CIÊNCIA, TECNOLOGIA,
INOVAÇÕES E COMUNICAÇÕES



sid.inpe.br/mtc-m21c/2020/03.05.13.27-TDI

QUANTIFYING AND MONITORING TROPICAL FOREST MORTALITY WITH PASSIVE AND ACTIVE OPTICAL REMOTE SENSING

Ricardo Dal'Agnol da Silva

Doctorate Thesis of the Graduate
Course in Remote Sensing, guided
by Drs. Luiz Eduardo Oliveira e
Cruz de Aragão, and Lênio Soares
Galvão, approved in March 18,
2020.

URL of the original document:

<<http://urlib.net/8JMKD3MGP3W34R/424G29B>>

INPE
São José dos Campos
2020

Cataloging in Publication Data

Silva, Ricardo Dal'Agnol.
Si38q Quantifying and monitoring tropical forest mortality with
passive and active optical remote sensing / Ricardo Dal'Agnol
da Silva. – São José dos Campos : INPE, 2020.
xxxii + 174 p. ; (sid.inpe.br/mtc-m21c/2020/03.05.13.27-TDI)

Thesis (Doctorate in Remote Sensing) – Instituto Nacional de
Pesquisas Espaciais, São José dos Campos, 2020.

Guiding : Drs. Luiz Eduardo Oliveira e Cruz de Aragão, and
Lênio Soares Galvão.

1. Forest mortality. 2. Amazon. 3. MODIS. 4. Very High
Resolution. 5. LiDAR. I.Title.

CDU 630*1:528.8(811)



Esta obra foi licenciada sob uma Licença [Creative Commons Atribuição-NãoComercial 3.0 Não Adaptada](https://creativecommons.org/licenses/by-nc/3.0/).

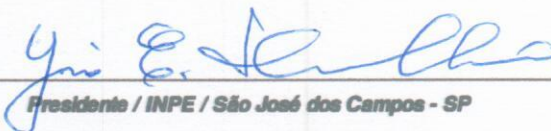
This work is licensed under a [Creative Commons Attribution-NonCommercial 3.0 Unported License](https://creativecommons.org/licenses/by-nc/3.0/).

Aluno (a): **Ricardo Dal' Agnol da Silva**

Título: "QUANTIFYING AND MONITORING TROPICAL FOREST MORTALITY WITH PASSIVE AND ACTIVE OPTICAL REMOTE SENSING"

Aprovado (a) pela Banca Examinadora em cumprimento ao requisito exigido para obtenção do Título de **Doutor(a)** em **Sensoriamento Remoto**

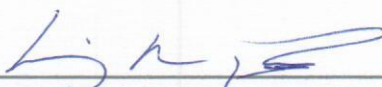
Dr. Yosio Edemir Shimabukuro


Presidente / INPE / São José dos Campos - SP

Participação por Vídeo - Conferência

Aprovado Reprovado

Dr. Luiz Eduardo Oliveira e Cruz de Aragão


Orientador(a) / INPE / São José dos Campos - SP

Participação por Vídeo - Conferência

Aprovado Reprovado

Dr. Lenio Soares Galvão


Orientador(a) / INPE / SJCampos - SP

Participação por Vídeo - Conferência

Aprovado Reprovado

Dr. Veraldo Liesenberg


Convidado(a) / UDESC / Lages - SC

Participação por Vídeo - Conferência

Aprovado Reprovado

Dr. Bruce Walker Nelson


Convidado(a) / INPA/Manaus / Manaus - AM

Participação por Vídeo - Conferência

Aprovado Reprovado

Este trabalho foi aprovado por:

maioria simples

unanimidade

São José dos Campos, 18 de março de 2020

*“A melhor maneira que a gente tem de fazer possível amanhã
alguma coisa que não é possível de ser feita hoje
é fazendo hoje aquilo que hoje pode ser feito.*

*Mas se eu não fizer hoje aquilo que hoje pode ser feito
e tentar fazer hoje aquilo que hoje não pode ser feito,
dificilmente eu faço amanhã aquilo que hoje não pude fazer”.*

Paulo Freire

To my parents Clora and Narciso.

To my wife Paloma.

ACKNOWLEDGMENTS

I thank the Postgraduate program in Remote Sensing (PGSER) from the National Institute for Space Research (INPE); teachers from the PGSER for the opportunity and knowledge; and colleagues and friends for all the fun times.

I am grateful to São Paulo Research Foundation (FAPESP) for my PhD fellowship in Brazil (grant 2015/22987-7) and abroad (grant 2017/15257-8); Conselho Nacional de Desenvolvimento Científico e Tecnológico (CNPq) for one month of fellowship; and to Coordenação de Aperfeiçoamento de Pessoal de Nível Superior (CAPES) for supporting the PGSER.

Thanks are also due to DigitalGlobe Foundation for the very high-resolution imagery grant; Sustainable Landscape project and EBA (INPE) project for the airborne LiDAR data; and NASA for the MODIS data.

I sincerely thank my advisors from INPE, Luiz Aragão and Lênio Galvão, for the trust, guidance, patience, long talks, and also for moments of laughter, during my journey of learning how to become a scientist. I have learned so much from you! Specifically, I thank Aragão for motivating me about thinking bigger and broader and on being a 'casca-grossa' scientist; and thank Lênio for always helping me to think about problems methodically, and contributing to shape my writing and analytical skills immensely! Besides my advisors, I would like to thank my colleague and friend Fabien, who was also like a mentor to me during the PhD, for all the time spent discussing research ideas and results. I have learned a lot with you, especially about being more precise on writing.

I am grateful to all the colleagues and friends that I have made while at INPE, who contributed to my personal and professional growth. Specifically, Yhasmin and Camila; long-distances did not even stop us from getting in touch, drinking a beer and having a good laugh; and Annia, I am not sure if we produce enough, but we for sure talk a lot, don't we?

From the University of Leeds/U.K., I thank my supervisor, Oliver Phillips, and Emanuel Gloor, who gladly participated in all our meetings and discussions, for

welcoming me to Leeds and mentoring me through a superb year of research and learning. I would like to thank also all the lovely people that I have met at the University; some of them became good friends. I hope to see you around more often, in special Adriane and Matt, Bruno and Karina, Julia and Chico, Marta and Alfredo, and Michelle. Special thanks here to Adriane and Matt for welcoming and hosting my wife Paloma and I in your home at Leeds for a while. Thanks!

I thank my brothers of life, Hyck and Humberto, for moments of joy while gaming or just talking about life stuff. These moments really helped me to unwind.

I thank my parents Clora and Narciso, who have always supported me to study. You inspired me to strive and do my very best in whatever I would like to do. If I am here now finishing this PhD, it is partly because of you.

Finally, I thank my wife Paloma, whose patience is borderline infinite: how does a person do not get tired of been taught every day lessons about satellite images, forests, bamboo, algorithms, LiDAR, gaps, etc.? Yeah, I know I overshare, I am sorry. Anyway, thanks for all the love, for being understanding when I am lacking, for being such an awesome partner and bringing me joy every day, for trying to cheer me up at those times when hope is lost, when no analyses work, and my work and goal to 'save the Amazon forests' looks like a failure. Thank you for sharing dreams with me! I would also like to thank my 'second family', Eliete, Carlos, Sofia, Jean and Rérica, for all the nice moments together.

ABSTRACT

Tree mortality is a key process in the global carbon cycle generally linked to climatic feedbacks and accelerated by human-induced disturbances in the Amazon. Remote sensing can complement ground observations of tree mortality to support Amazon-wide detection. However, different from temperate forests, tree mortality detection over tropical forests is challenging because of the high heterogeneity in forest structure and biodiversity. It requires the development of new methods with multiple data sources to address challenges such as the detection of vegetation-specific mortality at the landscape scale; the quantification of individual tree mortality related to logging at the local scale; and the characterization of gap dynamics as a proxy for tree mortality, potentially related to natural and anthropogenic activities, and up-scaling estimates from local to regional scales. Here, the objective was to develop and validate novel approaches for the detection and monitoring of tropical forest mortality, using Moderate Resolution Imaging Spectroradiometer (MODIS), Very High Resolution (VHR) and airborne Light Detection And Ranging (LiDAR) data acquired over the Amazon region. For the vegetation-specific approach at the landscape scale, MODIS data processed by the Multi-Angle Implementation of Atmospheric Correction (MAIAC) algorithm was used to map the bamboo die-off in the southwest Amazon and to test whether it enhanced fire occurrence. At the individual tree level, multi-temporal VHR data from the WorldView-2 and GeoEye-1 satellites were used to evaluate the detection of canopy tree loss from selective logging at the Jamari National Forest. Finally, to explore the use of gaps as a proxy for tree mortality, five multi-temporal LiDAR datasets, and 610 single-date flight lines were considered to provide a systematic assessment of gaps and tree mortality, and explore their relationships with environmental and climate drivers. Results at the landscape scale, using MODIS (MAIAC) data, showed automatic detection of historical bamboo die-off (accuracy of 79%) and mapping of 15.5 million ha of bamboo-dominated forests. The 'bamboo-fire hypothesis' was not supported, because the bamboo die-off areas did not show higher fire probability than the other areas. However, the fire occurrence was mostly associated with ignition sources from land use, suggesting a bamboo-human-fire association. At the local scale, individual tree losses from logging were successfully detected using VHR satellite imagery and a random forest (RF) model with 64% accuracy. In addition, large-gap openings associated with the tallest trees were more successfully detected by VHR data. At the local scale, LiDAR-gaps delineated using the relative height method, represented at least 50% of the tree mortality. The mortality of shorter trees at the canopy level (<25 m) was more successfully detected than the mortality of taller emergent trees (>25 m). Higher gap fractions (proxy for mortality) were associated with increased water deficit, soil fertility, and the occurrence of degraded and flooded forests. The Amazon-wide tree mortality map showed higher tree mortality rates in the west and southeast regions than in the central-east and north regions. This pattern was consistent with field-based observations. Overall, the findings highlighted the feasibility and importance of using passive and active optical remote sensing for detecting different processes of tropical forest mortality over a broad scale in the Amazon region.

Keywords: Forest mortality. Amazon. MODIS. Very High Resolution. LiDAR.

QUANTIFICANDO E MONITORANDO A MORTALIDADE DE FLORESTAS TROPICAIS COM SENSORIAMENTO REMOTO ÓPTICO PASSIVO E ATIVO

RESUMO

A mortalidade das árvores é um processo essencial no ciclo global do carbono, geralmente relacionado com *feedbacks* climáticos e acelerado por distúrbios antrópicos na Amazônia. O sensoriamento remoto pode complementar as observações de campo, a fim de apoiar a detecção de mortalidade na Amazônia. No entanto, diferentemente de florestas temperadas, a detecção da mortalidade de árvores em florestas tropicais é um desafio devido à alta heterogeneidade da estrutura florestal e biodiversidade. Isso requer o desenvolvimento de novos métodos com diferentes fontes de dados remotos para enfrentar desafios como a detecção de mortalidade de vegetações específicas na escala da paisagem; a quantificação de mortalidade de árvores individuais em escala local; e a caracterização da dinâmica das clareiras como um indicador da mortalidade de árvores, causada por atividades naturais e antropogênicas, calculada a partir do reescalonamento de dados locais para regionais. O objetivo da tese foi desenvolver novas abordagens para a detecção e monitoramento da mortalidade das florestas tropicais usando dados MODIS (MAIAC), de alta resolução espacial (VHR) e de LiDAR aerotransportado, adquiridos na Amazônia. Para a abordagem de vegetação específica em escala de paisagem, os dados MODIS (MAIAC) foram usados para detectar a morte de bambus no sudoeste da Amazônia e testar se ela aumenta a ocorrência de incêndios. No nível de árvores individuais, dados VHR multi-temporais dos satélites WorldView-2 e GeoEye-1 foram usados na detecção da perda de árvores no dossel proveniente de corte seletivo na Floresta Nacional do Jamari. Finalmente, para explorar o uso de clareiras como um indicador de mortalidade, cinco conjuntos de dados LiDAR multi-temporais e 610 linhas de voo mono-temporais foram utilizados para avaliar sistematicamente as clareiras e mortalidade de árvores e suas relações com fatores ambientais e climáticos. Na abordagem de vegetação específica, os resultados mostraram a detecção automática de mortalidade de bambus (precisão de 79%) e o mapeamento de 15,5 milhões de ha de florestas dominadas por bambu. A hipótese do fogo não foi corroborada, pois as áreas de bambu morto não apresentaram maior probabilidade de incêndio do que as outras áreas. No entanto, a ocorrência de incêndio foi associada a fontes de ignição de uso da terra, sugerindo uma associação bambu-homem-fogo. No nível de árvores individuais, os resultados mostraram que as perdas de árvores foram detectadas com sucesso usando imagens VHR e um modelo Random Forest (RF) com 64% de precisão. Além disso, grandes clareiras associadas às árvores mais altas foram detectadas com maior sucesso pelos dados VHR. Finalmente, no estudo das relações entre clareiras e mortalidade em toda a Amazônia, os resultados indicaram que as clareiras detectadas pelo LiDAR, usando o método da altura relativa, representaram pelo menos 50% da mortalidade das árvores. A mortalidade de árvores mais baixas no nível do dossel (<25 m) foi detectada com maior sucesso do que a mortalidade de árvores emergentes mais altas (> 25 m). A ocorrência de maiores frações de clareira

(indicador de mortalidade) foi associada ao aumento do déficit hídrico, a fertilidade do solo e a presença de florestas degradadas e inundadas. O mapa de mortalidade para Amazônia mostrou maiores taxas de mortalidade nas regiões oeste e sudeste do que nas regiões centro-leste e norte. Esse padrão foi consistente com as observações de campo. No geral, os resultados destacaram a viabilidade e importância do uso de sensoriamento remoto óptico passivo e ativo para detectar diferentes processos de mortalidade das florestas tropicais em ampla escala na Amazônia.

Palavras-chave: Mortalidade florestal. Amazônia. MODIS. VHR. LiDAR.

LIST OF FIGURES

	<u>Page</u>
Figure 2.1 - Tree mortality based on RAINFOR inventory data: (A) kriging-interpolation map of annual tree mortality (% yr ⁻¹); and (B) tree mortality rates by region.	10
Figure 2.2 - (A) Proportion of modes of death (standing dead, uprooted and broken) in northwestern and northeastern Amazon; (B) Wood density in Amazon regions.	11
Figure 2.3 - (A) The western Amazon region is more affected by blowdowns than the eastern region. The circles denote blowdown groupings. (B) Forests dominated by bamboo (hatched areas) in the southwestern Amazon.....	12
Figure 2.4 - Correlation of anomaly of vegetation indices with field-based forest mortality. (A) Enhanced Vegetation Index (EVI). (B) Normalized Difference Water Index (NDWI).....	18
Figure 2.5 - Tree mortality detection of individual trees based on Very High Resolution (VHR) optical imagery, between (A) 2000 (Ikonos) and (B) 2002 (QuickBird).	20
Figure 2.6 - Mortality detection by the difference between multi-temporal LiDAR Canopy Height Models (CHM) from (A) 1997, and (B) 2006. The image in (C) represents the difference between (A) and (B). Pr means the probability of death of the plant.....	21
Figure 2.7 - (A) Gap size-frequency distributions (SFD) of two vegetation types: Erosional <i>Terra Firme</i> (ETF) and Depositional Floodplain (DFP), and considering 1-m and 20-m height thresholds; (B) Vertical distribution of power-law exponents λ for each forest type.....	23
Figure 2.8 - Forest Canopy Height Models (CHM) of a Peruvian Amazon forest landscape, specifically at a (A) Depositional Floodplain (DFT), and an (B) Erosional <i>Terra Firme</i> (ETF). Each panel represents 50 ha.....	23
Figure 3.1 – Study area and examples of the developed mortality detection approaches. (A) The Amazon biome in South America divided into regions following Feldpausch et al. (2011); (B) MODIS (MAIAC) false-color composite of	

red (R), NIR (G) and SWIR (B) bands in Aug 2015. Living bamboo at the canopy is shown in light green color, while recently dead bamboo is shown in dark blue/gray color (Chapter 4); (C) VHR imagery and LiDAR CHM showing individual tree loss (Chapter 5); and (D, E, F) mortality and gap delineation over LiDAR CHM at TAP site (2012 and 2017) (Chapter 6). 27

Figure 3.2 – Vegetation types in the Amazon region. 28

Figure 3.3 – Environmental and climate variables for the Amazon forests. Average monthly (A) rainfall (mm) and (B) water deficit (mm) from the TerraClimate product (ABATZOGLOU et al., 2018); (C) Soil Cation Concentration (SCC) (ZUQUIM et al., 2019), a proxy for soil fertility; (D) Non-forest distance (km) derived from Global Forest Cover product (HANSEN et al., 2013), a proxy for forest degradation. 29

Figure 3.4 – Overview of the main methodological steps used in the data analysis. Details are provided in each corresponding chapter..... 30

Figure 4.1 – Methodology used in the data analysis..... 40

Figure 4.2 - Bamboo-dominated forests in southwestern Amazon. The image at background is a false-color composite from MODIS (MAIAC) images of bands 1 (Red), 2 (NIR) and 6 (shortwave infrared), in RGB, respectively, in August 2015. The black lines indicate the perimeter of the bamboo-dominated areas delineated in a previous study (CARVALHO et al., 2013)..... 41

Figure 4.3 - Spatial distribution of stable tree cover percentage percentiles (filtered for tree cover gain and loss, and for water bodies), indicating pixels below, above and within the 1st to 99th percentile range of tree cover found in bamboo-dominated forest (hatched), as delineated by Carvalho et al. (2013). 51

Figure 4.4 - Relative frequency of MODIS NIR-1 reflectance (band 2) from pixels with tree cover percentage (A) below, (B) above and (C) within the 1st to 99th percentile range of tree cover found in bamboo-dominated forest (hatched in Figure 4.3), as delineated by Carvalho et al. (2013)..... 52

Figure 4.5 - MODIS bamboo die-off detection map from 2001 to 2017 using the bilinear model of expected near-infrared (NIR) reflectance variations as a function of bamboo cohort age, for (A) NIR-1 and (B) NIR-2. Validation between detected die-off and visual interpreted die-off on MODIS false-color composites (2000-

2017) for (C) NIR-1 and (D) NIR-2. The dashed line represents the 1:1 line. Size of circles is related to the number of pixels that hit the same observed/estimate die-off year. 54

Figure 4.6 - Bamboo-dominated forest map and MODIS active fire detections during 2002-2017 (yellow crosses). Blue pixels are bamboo die-off patches detected during 2001-2017 using the bilinear model. Light green pixels are bamboo that did not die-off, but showed increasing NIR signal during 2001-2017, and presented greater NIR mean than forest. Dark green pixels are bamboo-free forests. White pixels are other land cover classes. The hatched polygon is the bamboo-dominated forests delineated by Carvalho et al. (2013). 55

Figure 4.7 - Empirical bamboo-age reflectance profiles at ages 0-28 years from MODIS bands 1 to 8 (A)-(H). Black lines represent the median, while the shaded gray areas represent the 1st and 99th percentile. 56

Figure 4.8 - Pearson's correlation coefficients between the median reflectance of bamboo-free forest with the pixel spectral response of bamboo-dominated forests. The results are plotted as function of the bamboo cohort age for MODIS NIR-1 (in black) and NIR-2 (in orange). 57

Figure 4.9 - MODIS bamboo die-off prediction map from 2000 to 2028 using the empirical reflectance profiles of the near-infrared 1 (NIR-1) reflectance as a function of bamboo cohort age (A). Validation between predicted die-off (2017-2028) and visual interpreted die-off from previous life cycle in Landsat false-color composites (1985-2000) (C) and residuals distribution (B). The dashed line represents the 1:1 line in (C) and age residual = 0 in (B). Size of circles is related to the number of pixels that hit the same observed/estimate die-off year. 58

Figure 4.10 - Distribution of predicted bamboo die-off area per year between 2000 and 2028 from MODIS NIR-1. 59

Figure 4.11 - Area-normalized MODIS fire frequency during 2002-2017. Gray boxes represent fire in dead bamboo (28, 0 and 1 years) and white boxes represent fire in live bamboo (2 to 27 years). 61

Figure 5.1 - Study area at the Jamari National Forest, Rondônia state, Brazil. The background of the left image is a true color composite from the GeoEye-1 satellite acquired on 02 July 2017 (UTM, datum WGS-84). The red and blue

rectangles represent the areas A and B covered by the LiDAR datasets, which were analyzed in sections 5.3.1 and 5.3.3, respectively. The black lines represent the boundaries of the UPAs. The satellite image is courtesy of the DigitalGlobe Foundation. 77

Figure 5.2 - Main steps of the data processing and analyses..... 79

Figure 5.3 - Tree loss detection using LiDAR Δ CHM in the Jamari National Forest over the UPA-06. Relative frequency of the most negative Δ CHM within a 30 m radius of (A) logged trees and (B) non-logged areas. (C) LiDAR-based tree loss map considering Δ CHM ≤ -10 m (UTM, datum WGS-84)..... 90

Figure 5.4 - Tree loss detection using VHR satellite data and RF model in the Jamari National Forest over the UPA-06. (A) Detection accuracy as a function of the tree loss probability cut-off. (B) Satellite-based tree loss map considering a tree loss probability ≥ 0.85 (UTM, datum WGS-84). (C) Nearest neighbor distances between satellite and LiDAR tree loss detections, as a function of distance (m). The gray area represents a CSR envelope with a 1% significance level ($n = 199$). 91

Figure 5.5 - Relative frequency of correct satellite tree loss detections for intervals of (A) LiDAR CHM height differences (Δ CHM), (B) LiDAR CHM pre-logging, and (C) LiDAR CHM post-logging. Mean and error bars (95% confidence interval) were calculated considering the 30 model runs. Numbers inside bars represent the average number of crowns among the 30 model runs. 93

Figure 5.6 - Variables' importance derived from the RF model using VHR satellite data to map tree loss events in Jamari National Forest ranked by their MDA. SD corresponds to the standard deviation. 94

Figure 5.7 - Filling of forest canopy gaps over time (2011 to 2017) in Jamari National Forest (UPA-01), as a function of the initial gap size class (m^2)..... 95

Figure 5.8 - Satellite-based tree loss map during 2014–2017 for a section of 76.6 km^2 inside the Jamari National Forest (UTM, datum WGS-84). The background corresponds to the isotropic kernel-smooth density of satellite-based tree losses per hectare. Black lines are the boundaries of the UPAs. 96

Figure 5.9 - Relationship between satellite-based tree loss and field logged trees per hectare in the UPAs labeled by the time difference (years) between the

logging and last image acquisition (2017). Each point represents a pixel of 100 × 100 m (1 ha) from which the estimates are extracted. Lines represent linear regression models between the two variables. Significance levels for regression slopes (β) are represented by asterisks: * \leq .05, ** \leq .01, and *** \leq .001. 98

Figure 6.1 - Overview of the main methodological steps used to answer the research questions (Q1 to Q5). CHM_{date1} and CHM_{date2} correspond to canopy height models derived from LiDAR data acquired on two different dates with a time interval of ~5 years. 110

Figure 6.2 – The Amazon biome in South America with colored regions indicating faster (west and southeast) and slower dynamics (central-east and north). The regions were adapted from Feldpausch et al. (2011). Small black lines represent single-date airborne LiDAR data acquisitions from the EBA project ($n = 610$ flight lines). Red triangles illustrate multi-temporal LiDAR data acquisition over five sites (BON, DUC, FN1, TAL and TAP). Circles indicate the location of field inventory plots. 111

Figure 6.3 - LiDAR-based canopy tree mortality variability with plot area for five Amazonian sites with multi-temporal data. The mortality coefficient of variation (CV) and the CV change rate are shown for DUC (A) and (B); TAP (C) and (D); FN1 (E) and (F); BON (G) and (H); and TAL (I) and (J). 121

Figure 6.4 - Example of detected canopy tree mortality (red) and gap delineation (yellow) based on relative height ($W=5$, $RH=50$) at the TAP site. The background is a Canopy Height Model (CHM) for 2012 in (A), and 2017 in (B) and (C). ... 124

Figure 6.5 - Percentage of correctly detected mortality by delineated gaps (Relative height method, $W=5$, $RH=50$) as a function of tree height classes for the sites: (A) DUC, (B) TAP, (C) FN1, (D) BON, (E) TAL, and (F) sites-average. The numbers close to the bars represent the absolute number of detections for that tree height class. The 95% CI (based on t-value score) is also indicated for the sites-average. 125

Figure 6.6 - Relationship between gap fraction (%) and annual tree mortality (% yr^{-1}) for 5-ha plot areas over the five studied sites (DUC, TAP, FN1, BON, and TAL). 126

Figure 6.7 - Canopy gaps based on the relative height ($W=5$, $RH=50$) across the Brazilian Amazon ($n = 610$ flight lines): (A) gap fraction (%); (B) gap size-frequency distribution (λ); (C) mean gap size (m^2); and (D) mean gap shape complexity index (GSCI)..... 127

Figure 6.8 - Relationships between gap fraction (log-scale) and predictors used in the final model: (A) soil cation concentration (SCC); (B) Non-forest distance (km) (log-scale); (C) Floodplains cover fraction; and (D) *Mean_def* / Mean monthly water deficit (mm). The dashed line represents a linear model. Red triangles on panel (D) represent samples with floodplains cover ≥ 0.5 132

Figure 6.9 - Amazon-wide tree mortality prediction and validation. (A) Map of tree mortality ($\%.yr^{-1}$) prediction at 5-km spatial resolution based on gap-mortality relationship (Figure 6.6) and gap/environmental-climate model (Table 6.3); (B) validation of modeled tree mortality using long-term inventory plot data from Brienen et al. (2015). Point colors represent the Amazon regions of Figure 6.2; and (C) modelled mortality ($\%.yr^{-1}$) per Amazonian region. Each boxplot represents $n > 40,000$ 5-km pixels. Mean modelled mortality was statistically different between regions ($p < 0.01$)..... 133

Figure A.1 - Spatial distribution of validation samples obtained from MODIS (2001–2017) imagery in red and Landsat (1985–2000) imagery in blue. The image at background is a false-color composite from MODIS (MAIAC) images of bands 1 (Red), 2 (NIR) and 6 (shortwave infrared), in RGB, respectively, in August 2015. 164

Figure A.2 - Temporal distribution of validation samples for bamboo die-off detection (2001–2017) from MODIS imagery; and for bamboo die-off prediction (2018–2028) from Landsat imagery. 165

Figure A.3 - Bamboo die-off during 2001–2017 from the combined detections using MODIS (MAIAC) NIR-1 and NIR-2 and the bilinear model. The black lines indicate the perimeter of the bamboo-dominated areas delineated in a previous study (CARVALHO et al., 2013). 166

Figure A.4 - MODIS bamboo die-off prediction map from 2000 to 2028 using the empirical reflectance profiles of the near infrared 2 (NIR-2) reflectance as a function of bamboo cohort age (a). Validation between predicted die-off (2017–

2028) and visual interpreted die-off from previous life cycle in Landsat false-color composites (1985–2000) (c) and residuals distribution (b). The dashed line represents the 1:1 line in (c) and age residual = 0 in (b). Size of circles is related to the number of pixels that hit the same observed/estimate die-off year..... 167

Figure C.1 - Spatial variability of canopy height model (CHM) across the Brazilian Amazon ($n = 610$ flight lines): (A) CHM average (CHM_{AVG}), (B) CHM standard deviation (CHM_{SD}), (C) 5th percentile (CHM_{P05}), and (D) 95th percentile (CHM_{P95}). Units represent meters. 173

Figure C.2 - Amazon-wide gap fraction prediction based on environmental and climate drivers. (A) Estimate gap fraction (%), and (B) standard deviation (SD) of gap fraction estimate (%). Areas in white correspond to either missing data or rivers. 174

LIST OF TABLES

	<u>Page</u>
Table 4.1 - Bamboo patch sizes obtained from die-off prediction using MODIS NIR-1 filtered by a minimum patch area of 10 km ² , and comparison of results with those from Carvalho et al. (2013).....	60
Table 5.1 - Acquisition details of Airborne LiDAR and VHR satellite data used for tree loss analyses. PAN = Panchromatic; B = blue; G = green; Y = yellow; R = red; NIR = Near infrared.	80
Table 5.2 - Acquisition details of Airborne LiDAR data used for gap recovery analysis.	87
Table 5.3 - Frequency of satellite-based tree loss events and field logged trees per hectare for the UPAs and undisturbed forests.....	97
Table 6.1 - Performance of different gap definitions to represent tree mortality for each site and an average between sites (sites-average). Methods and parameters are ranked by the Sites-Average F metric. Method's parameters include: W = window size (meters); RH = percentile of relative height cutoff; A = maximum gap area (ha); and H = fixed height cutoff. Performance metrics include: <i>p</i> = precision; <i>r</i> = recall; and <i>F</i> = F1-score. Values of <i>p</i> , <i>r</i> , and <i>F</i> range from 0 to 1, with larger values indicating better performance.	123
Table 6.2 - Pearson's correlation (<i>r</i>) between gap fraction and predictors. All correlations were significant at 1% statistical level, except for cells left blank.	129
Table 6.3 - Estimated regression parameters (B), standard errors (SE B), t values (t) and p-values for the Generalized Linear Model (GLM) to estimate gap fraction. Also, Standardized beta coefficients (β), ΔR^2 (change in R ² by adding the variable last on the model) and variance-inflation factors (VIC) for each predictor.	130
Table A.1 - Dates of TM/Landsat-5 images used for validation of bamboo die-off predictions. The date of each image (YYYY-MM-DD) is presented for each path-row (World Reference System 2) in the columns.	163
Table B.1 - ITC delineation assessment per plot for VHR satellite data.	171
Table B.2 - ITC delineation assessment per plot for airborne LiDAR data.....	171
Table C.1 - Multi-temporal airborne LiDAR data acquisition information.....	173

LIST OF ABBREVIATIONS

AGB	Aboveground Biomass
BDFFP	Dynamics of Forest Fragments Project
BIC	Bayesian Information Criterion
BON	Bonal site
BRDF	Bidirectional Reflectance Distribution Function
CHM	Canopy Height Models
CI	Confidence Interval
CSR	Complete Spatial Randomness
CV	Coefficient of Variation
CWD	Coarse Wood Debris
DBH	Diameter at Breast Height
DFP	Depositional Floodplain
DSL	Dry Season Length
DUC	Adolpho Ducke site
ETF	Erosional Terra Firme
EVI	Enhanced Vegetation Index
FN1	Feliz Natal site
GEDI	Global Ecosystem Dynamics Investigation
GLM	Generalized Linear Models
GPS	Global Positioning System
GSCI	Gap Shape Complexity Index
IBAMA	Brazilian Institute of Environment and Renewable Mineral Resources
INPE	National Institute of Space Research
ITC	Individual Tree Crown
LAI	Leaf Area Index
LiDAR	Light Detection And Ranging
MAIAC	Multi-Angle Implementation of Atmospheric Correction
MCWS	Marker-Controlled Watershed Segmentation
MDA	Mean Decrease Accuracy
MODIS	Moderate Resolution Imaging Spectroradiometer
NCCS	NASA Center for Climate Simulation

NDVI	Normalized Difference Vegetation Index
NDWI	Normalized Difference Water Index
NIR	Near Infrared
NPV	Non-Photosynthetically active Vegetation
OTB	Orfeo Toolbox
P05	5th percentile
P95	95th percentile
RF	Random Forest
RMSE	Root Mean Square Error
RTLS	Ross-Thick Li-Sparse
SCC	Soil Cation Concentration
SD	Standard Deviation
SFD	Size-Frequency Distribution
STL	Seasonal and Trend decomposition using Loess
SWIR	Shortwave infrared
TAL	Talismã site
TAP	Tapajós National Forest site
TM	Thematic Mapper
TRMM	Tropical Rainfall Measuring Mission
U.S.	United States
UPA	Annual Production Units
VHR	Very High Resolution
VIC	Variance-Inflation Factors

LIST OF SYMBOLS

B	Regression coefficients
$BRDF_n$	Bidirectional Reflectance Factor
F	F1-score
F_{geo}	geometric RTLS parameters
FN	False Negatives
FP	False Positives
F_{vol}	volumetric RTLS parameters
H	Height cutoff
IoU	Intersection-Over-Union
K_{geo}	geometric-optical BRDF kernel weights
K_{iso}	isotropic BRDF kernel weights
K_{vol}	volumetric BRDF kernel weights
m	Tree mortality
$Mean_def$	Mean water deficit
$Mean_pr$	Mean precipitation
$Mean_vs$	Mean wind speed
N_0	Initial number of trees
N_t	Final number of trees
P	Precision
R	Recall
RH	Relative height cutoff
SD_def	Standard deviation of water deficit
SD_pr	Standard deviation of precipitation
SD_vs	Standard deviation of wind speed
t	Census interval
TP	True Positives
W	Window size
β	Standardized beta coefficients
λ	Zeta distribution parameter

CONTENTS

	<u>Page</u>
1 INTRODUCTION	1
1.1 Overview	1
1.2 Objectives	3
1.3 Outline	4
2 LITERATURE REVIEW	7
2.1 Tree mortality: concepts and measurements	7
2.2 Mortality agents, mechanisms and spatio-temporal patterns.....	9
2.2.1 Patterns of tree mortality based on field inventory data	9
2.2.2 Main mechanisms of tree mortality	11
2.2.3 Canopy gaps and mortality.....	14
2.3 Remote sensing studies for mortality detection and monitoring	16
2.3.1 Canopy observed at the landscape scale	16
2.3.2 Individual trees observed at the local scale	19
2.3.3 Canopy gaps observed at the local scale.....	21
2.4 Perspectives for tree mortality studies using remote sensing over Amazonian tropical forests.....	24
3 GENERAL METHODOLOGY	27
3.1 Study area	27
3.2 Data and methods.....	30
4 LIFE CYCLE OF BAMBOO IN THE SOUTHWESTERN AMAZON AND ITS RELATION TO FIRE EVENTS	35
4.1 Introduction	36
4.2 Material and Methods	39
4.2.1 Study area.....	40
4.2.2 Satellite data and products	42
4.2.3 Bamboo life cycle spectral characteristics	45
4.2.4 Relationship between bamboo die-off events and MODIS active fire detections.....	49
4.3 Results.....	50

4.3.1	Tree cover analysis	50
4.3.2	Bamboo life cycle spectral characteristics	52
4.3.3	Relationship between bamboo die-off events and MODIS active fire detections.....	60
4.4	Discussion	62
4.4.1	Tree cover of bamboo-dominated and nearby forests.....	62
4.4.2	Automatic detection of bamboo die-off	63
4.4.3	Spatial distribution of bamboo-dominated forests.....	64
4.4.4	Bamboo cohort age and reflectance variability	65
4.4.5	Bamboo die-off prediction	67
4.4.6	Fire occurrence and bamboo	68
4.5	Conclusions	70
5	QUANTIFYING CANOPY TREE LOSS AND GAP RECOVERY IN TROPICAL FORESTS UNDER LOW-INTENSITY LOGGING USING VHR SATELLITE IMAGERY AND AIRBORNE LIDAR	73
5.1	Introduction	74
5.2	Study Area.....	76
5.3	Material and Methods	78
5.3.1	Tree Loss Detection using LiDAR Data.....	79
5.3.2	Tree Loss Detection using VHR Satellite Data and RF Model.....	82
5.3.3	Assessment of Tree-Fall Gaps Recovery Using LiDAR Data.....	86
5.3.4	Landscape Analysis of Satellite-Based Tree Loss Map	88
5.4	Results.....	89
5.4.1	Detecting Tree Loss Events Using LiDAR Data.....	89
5.4.2	Detecting Tree Loss Events Using VHR Satellite Data and RF Model.....	91
5.4.3	Tree-Fall Gap Recovery Assessment Using LiDAR Data.....	94
5.4.4	Landscape Analysis of Satellite-Based Tree Loss Map	96
5.5	Discussion	98
5.6	Conclusions	103
6	MODELLING AMAZON TREE MORTALITY FROM LIDAR-BASED GAP DYNAMICS AND ENVIRONMENTAL-CLIMATE DRIVERS	105

6.1	Introduction	106
6.2	Data and Methods	109
6.2.1	Study Area	110
6.2.2	Data Acquisition and Pre-Processing.....	112
6.2.3	Data Analysis.....	115
6.3	Results.....	120
6.3.1	Multi-Temporal Analysis of Gap-Mortality Relationship.....	120
6.3.2	Canopy-Gap Spatial Variability and Landscape and Regional- Drivers Across the Brazilian Amazon	126
6.3.3	Amazon-Wide Tree Mortality Prediction and Validation	132
6.4	Discussion	134
6.4.1	What is the minimum plot area necessary to obtain stable landscape-scale estimates of canopy tree mortality (Q1)?	134
6.4.2	How do canopy gaps relate to mortality rates of tropical forests and which gap definition best represents this relationship (Q2)?	135
6.4.3	How does canopy gap dynamics derived from airborne LiDAR data vary across the Brazilian Amazon forests (Q3)?.....	136
6.4.4	What landscape- and/or regional-scale factors drive gap variability in the Brazilian Amazon (Q4)?	138
6.4.5	Does tree mortality modelled from gaps and environmental-climate proxies reproduce spatial patterns from plot-based estimates across the Amazon (Q5)?	140
6.5	Conclusions	141
7	GENERAL DISCUSSION	143
8	CONCLUDING REMARKS	147
	REFERENCES.....	149
	APPENDICES A - SUPPLEMENTARY MATERIALS FROM CHAPTER 4	163
	APPENDICES B - SUPPLEMENTARY MATERIALS FROM CHAPTER 5	169
	APPENDICES C - SUPPLEMENTARY MATERIALS FROM CHAPTER 6	173

1 INTRODUCTION

1.1 Overview

Tree mortality is a key process of forest dynamics. Studies suggest that mortality is a predictor of aboveground biomass (AGB) (JOHNSON et al., 2016) and diversity (PHILLIPS et al., 2004). This process is also linked to biosphere-atmosphere feedbacks (FEARNSIDE, 1995; ANDEREGG et al., 2016). Although it is a natural process, it can be accelerated by human activities such as deforestation and forest degradation, and resultant habitat fragmentation (LAURANCE et al., 1998; LAURANCE et al., 2001; LAURANCE; WILLIAMSON, 2001). Changes in the pattern and scale of forest disturbance, either associated with the increasing occurrence of extreme drought events or water deficit (COX et al., 2008), in conjunction with a higher atmospheric CO₂ concentration, can be accelerating both mortality and recruiting (PHILLIPS et al., 2004; LAURANCE et al., 2009; BRIENEN et al., 2015). Such changes can modify the canopy structure and floristic composition, favoring the dominance of lianas in certain types of forests (FOSTER et al., 2008).

Although several studies have been conducted to understand the mechanisms of tree mortality, this knowledge is still insufficient, constraining our ability to accurately quantify global carbon budget and related environmental and climate change effects (ALLEN et al., 2010). This fact was highlighted in a recent study by Bugmann et al. (2019), who simulated forest dynamics from stand- to global-level using 15 ecosystem models with different formulations of tree mortality. These models showed markedly different results under the current climate scenario (10-40% deviations) and, especially, under simulated scenarios of climate change (20-170% deviations). Therefore, to properly assess environmental and climate change effects, we must reduce these uncertainties on tree mortality estimates.

Measurements of tree mortality from field inventory plots constitute the best available data source to understand and quantify the process. An excellent example is the RAINFOR network (MALHI et al., 2002). Using ground data, some studies indicated that tree mortality has been enhanced by water stress and drought in the Amazon forests (PHILLIPS et al., 2009). Patterns of higher

mortality have been observed at the western and southeastern Amazon when compared to the central-east and northern Amazonian regions. These patterns can be partially associated with soil properties (QUESADA et al., 2010). For instance, in the west Amazon, the soils are relatively new and shallower, having higher fertility than the soils from the central-east and north regions. These differences contribute to the faster forest dynamics, increased recruitment and mortality rates, and lesser specific wood density observed in the west Amazon (BAKER et al., 2004; JOHNSON et al., 2016). In addition, at the west, the trees tend to die and to be more frequently uprooted than at the east (CHAO et al., 2009). Higher wood density may be linked to greater uprooting resistance to wind or other disturbances.

Field data can be complemented by remote sensing imagery to improve the spatial characterization of the tree mortality patterns in the Amazon, allowing the extrapolation, or up-scaling, from the local field-plot information into the regional-scale maps (HUANG et al., 2019). The technique has been successfully applied for detecting tree mortality at temperate forests, where the droughts, diseases and insects' outbreaks cause widespread mortality (LIU et al., 2007; HICKE; LOGAN, 2009; DENNISON et al., 2010; MEDDENS et al., 2013). Over these forests, the detection is relatively simple due to the strong changes observed in the landscape (i.e., leaf/canopy color changes from green to red). The landscape changes occur massively because the temperate forests are very often composed of only a few canopy-dominant tree species. In contrast, tropical forests show larger species diversity than temperate forests, which creates difficulties for mortality detection. Thus, the remote sensing approaches used in temperate forests are not directly transferable to tropical forests.

For observing tropical forest mortality at the landscape level, medium-to-coarse spatial resolution satellite data have been used. The detected mortality events are generally associated with large-scale wind disturbances (RIFAI et al., 2016; NEGRÓN-JUÁREZ et al., 2018); wildfire (ANDERSON et al., 2015; SHIMABUKURO et al., 2019); flood (RESENDE et al., 2019); liana-infestation (FOSTER et al., 2008; MARVIN et al., 2016; TYMEN et al., 2016); and bamboo die-off (CARVALHO et al., 2013). For observing individual trees at the local scale, a few papers have investigated the detection of mortality from treefalls associated

with natural processes or logging (CLARK et al., 2004a; THOMAS et al., 2013; BOEHM et al., 2013; KELLNER; HUBBELL et al., 2017; LEITOLD et al., 2018). Some authors have also proposed the use of canopy gap information as a proxy for mortality (HUNTER et al., 2015).

At the landscape level of observation, data from the Thematic Mapper (TM)/Landsat-5 (30-m pixel size), Moderate Resolution Imaging Spectroradiometer (MODIS) onboard Terra and Aqua platforms (250-to-1000-m pixel size) and Advanced Land Observing Satellite (ALOS)/Phased Array type L-band Synthetic Aperture Radar (PALSAR) (7-to-44-m pixel size) have been considered in the data analysis. For the local-scale individual tree and canopy gap approaches, the remote sensing data used in these studies consisted of small-footprint airborne Light Detection And Ranging (LiDAR) with 1-m or even sub-meter spatial resolution Canopy Height Models (CHM), and Very High Resolution (VHR; 0.5-m spatial resolution) optical passive imagery, e.g. WorldView-2.

Independent of the data source selected for analysis, novel remote sensing approaches are necessary to detect and monitor tropical forest mortality over the Amazon forests. This knowledge is important to better understand the spatial distribution of tree mortality and to make inferences of the underlying causing factors. While the development of Amazon-wide applicable approaches is generally expected, strategies that consider specific vegetation types, such as the bamboo forests from southwestern Amazon, are also desirable. Inserted in this context, the present study has the objectives defined below.

1.2 Objectives

This study aimed to develop and validate novel approaches for detecting and monitoring the mortality of tropical forests using passive and active optical remote sensing. Given the great complexity of tropical forests in terms of structure and diversity, a unique approach to detect and monitor tropical forest mortality should not be feasible. Therefore, specific approaches focused on mortality processes at different levels of observations should be developed. They ranged from the

landscape scale of canopy observations to the local scale of individual trees and canopy gaps, exploring different passive and active optical remote sensors.

The scientific questions that motivated this study were:

- (i) Can bamboo die-off be automatically detected, and does it enhance fire occurrence at the southwest Amazon? (Chapter 4);
- (ii) Does multi-temporal VHR satellite imagery allow for generic semi-automatic detection of individual tree losses? (Chapter 5);
- (iii) How canopy gaps derived from airborne LiDAR data relate to tree mortality and how gap dynamics are controlled by environment-climate? (Chapter 6);
- (iv) Can the information of canopy gap dynamics be used to derive spatialized tree mortality estimates over the Amazon? (Chapter 6).

Given these questions, the specific objectives were:

- Develop a method based on a time series of MODIS satellite data, processed by the Multi-Angle Implementation of Atmospheric Correction (MAIAC) algorithm, to detect bamboo die-off; compare the die-off with active fire events; and determine whether die-off enhances fire occurrence at the southwest Amazon (Chapter 4);
- Develop a generic semi-automatic method to detect canopy individual tree losses based on multi-temporal VHR imagery (Chapter 5);
- Assess how gaps derived from airborne LiDAR data relate to tree mortality and environmental-climate factors, using these relationships to predict tree mortality over the entire Amazon region (Chapter 6).

1.3 Outline

This paper-format doctoral dissertation is organized as follows:

Chapter 1 introduces the importance of tropical forest mortality on the global and regional carbon cycle and biodiversity, briefly describing how it has been measured in the field or by remote sensing instruments.

Chapter 2 provides a literature review of tropical forest mortality concepts, agents, mechanisms and spatial patterns, describing the few remote sensing studies that addressed the detection of tropical forest mortality.

Chapter 3 describes the general methodology used in data analyses.

Chapter 4 assesses the detection of large-scale bamboo die-off in bamboo-dominated forests and its relationship with fire occurrence at the southwest Amazon. The detection was based on time series analysis of MODIS (MAIAC) surface reflectance data, from which the monitoring of temporal changes in the bamboo phenology was a key aspect of the investigation. The bamboo causes damage to other trees, constrains the forest biomass, enhances the overall forest tree mortality, and potentially favors fire occurrence. Therefore, its mapping can contribute to a better understanding of tree mortality associated with bamboo and fire dynamics within the southwest Amazon region. ^{*1}

Chapter 5 assesses the potential of multi-temporal VHR passive optical imagery (WorldView-2 and GeoEye-1) to detect individual tree loss at the Jamari National Forest, Rondônia state, Brazil. The idea was to develop a generic semi-automatic method to detect canopy tree mortality that could work with any tree that went through treefall. The experiment was based on selective logging rather than natural tree mortality due to the unique availability of tree-by-tree data at managed natural forests. Multi-temporal high spatial resolution data from airborne LiDAR served as a reference for comparison with the tree loss detected by the VHR passive optical imagery. ^{*2}

^{*1} This chapter is an adapted version of the paper: DALAGNOL, R. *et al.* Life cycle of bamboo in the southwestern Amazon and its relation to fire events. **Biogeosciences**, v. 15, n. 20, p. 6087–6104, 18 out. 2018.

^{*2} This chapter is an adapted version of the paper: DALAGNOL, R. *et al.* Quantifying Canopy Tree Loss and Gap Recovery in Tropical Forests under Low-Intensity Logging Using VHR Satellite Imagery and Airborne LiDAR. **Remote Sensing**, v. 11, n. 7, p. 817, 4 abr. 2019.

Chapter 6 investigates the use of canopy gap measurements derived from airborne LiDAR data to represent tree mortality. The goal here was to determine to what extent gaps could be used to infer about tree mortality and, by considering environmental-climate drivers' relationship with gaps, to predict tree mortality for the Amazon forests. The first part of this study was conducted over five sites across the Brazilian Amazon with available multi-temporal airborne LiDAR datasets, which were analyzed to measure how much of canopy tree mortality can be detected by gaps. The second part consisted of a systematic assessment of gap dynamics across the Brazilian Amazon using 610 non-overlapping LiDAR flight lines, investigating its relationship with environmental-climate drivers. The third part developed a modelling approach, combining the gap-mortality and environmental-climate/gap relationships to predict tree mortality across the Amazon biome. The estimates were compared with field observations. LiDAR-derived regional spatial patterns of tree mortality were established. ^{*3}

Chapter 7 presents a general discussion from the combined analyses of the chapters, exploring the perspectives for the next remote sensing studies of tropical forest mortality.

Chapter 8 summarizes the overall findings of the study.

In practice, the passage from Chapters 4 to 5 represents the transition from a vegetation-specific mortality approach (bamboo die-off) using coarse spatial resolution data into a more generic approach to detect individual tree loss using VHR data. On the other hand, the passage from Chapters 5 to 6 represents the transition in data source from passive to active optical remote sensing with the LiDAR being used to produce an Amazon-wide tree mortality map.

^{*3} This chapter correspond to the paper in preparation: DALAGNOL, R. *et al.* Modelling amazon tree mortality from LiDAR-based gap dynamics and environmental-climate drivers. To be submitted.

2 LITERATURE REVIEW

2.1 Tree mortality: concepts and measurements

Tree mortality is a key component of the carbon cycle and a predictor of vegetation biomass and biodiversity (JOHNSON et al., 2016; PHILLIPS et al., 2004). In the past decades, mortality rates have been increasing worldwide over distinct woodlands and forest regions, in association with severe droughts (HUANG et al., 2019). Thus, these mortality events have occurred at deep- or shallow-rooted vegetation and different climate envelopes. Increased tree mortality with drought has been reported also for the Amazon forests, which is likely linked to increasing climatic variability and feedbacks with growth (BRIENEN et al., 2015). Improving the knowledge of forest dynamics, especially tree mortality, is therefore important for the parametrization of climate and carbon models, which currently cannot replicate adequately the patterns observed in the field (BIRCHER et al., 2015). An accurate understanding of tree mortality patterns, including detection and causality, would help to parameterize and test forest carbon cycle models (KELLNER et al., 2009).

The mortality is a natural component of the forest dynamics caused by plant physiology, age/senescence, environmental factors, stress, and even random factors (KEANE et al., 2001). Amongst the potential causes of mortality, recent studies found that mortality has been enhanced by water stress in the Amazon forests (PHILLIPS et al., 2009). Two main hypotheses explain how a plant dies with water stress: hydraulic failure and carbon starvation (MCDOWELL et al., 2008). In addition to water stress, the effect of biotic attack (i.e. insects) should also contribute to exacerbating mortality (MCDOWELL et al., 2008). Other processes in the Amazon, either causing direct mortality or enhancing mortality rates after drought events, consist of wildfire (BARLOW et al., 2012; BRANDO et al., 2014; SILVA et al., 2018); fragmentation (LAURANCE et al., 1998; LAURANCE et al., 2001; LAURANCE; WILLIAMSON, 2001); wind disturbances (RIFAI et al., 2016; NEGRÓN-JUÁREZ et al., 2018); logging (ASNER et al., 2004; FELDPAUSCH et al., 2005); plant infestation/dominance; and competition such as that from liana (FOSTER et al., 2008; MARVIN et al., 2016; TYMEN et al., 2016) or bamboo (CARVALHO et al., 2013).

Measurements of tree mortality are primarily performed by repeated censuses of inventory plots, which are combined into networks for large-scale analysis of forest dynamics. For instance, the RAINFOR network, described by Malhi et al. (2002), is an excellent source of tree mortality information to date for the Amazon forests. However, although plot data allow a precise retrieval of tree mortality rates locally, they do not provide tools for monitoring tree mortality at larger scales. In this case, remote sensing data and related methods, in combination with field data, should be the optimal choice for global-scale forest stress and mortality detection and attribution (ALLEN et al., 2010).

One major challenge for the remote detection of Amazonian tree mortality is the great heterogeneity of tropical forests. In temperate forests, an insect or disease may attack massively all individuals from one species at a landscape causing widespread mortality. For instance, this is the case of the *Phytophthora ramorum* pathogen, which affects forests from California and Oregon in the United States (U.S.) (LIU et al., 2007). Another example is the mountain bark beetles that attack pines in the U.S. (HICKE; LOGAN, 2009; DENNISON et al., 2010; MEDDENS et al., 2013). The attack generally causes great leaf phenology changes, e.g. modifications in leaf color from green to red, which can be tracked by the spectral signal measured by the satellites. Different from temperate forests, which do not show a large diversity of canopy-dominant species on each landscape, tropical forests usually have hundreds of species per hectare (PHILLIPS et al., 2004). Therefore, remote sensing detection of mortality caused, for example, by biotic agents or droughts, is not as efficient as in temperate forests, because of the heterogeneity in species composition and their responses to factors causing mortality.

Remote sensing can detect other large-scale disturbances that cause mortality in tropical forests using passive multispectral optical sensors or active instruments such as LiDAR. One example of passive detection is the wind disturbance captured by Landsat data (RIFAI et al., 2016; NEGRÓN-JUÁREZ et al., 2018). Satellite instruments, such as the TM/Landsat-5 and the MODIS/Terra, have been used also to detect tree mortality associated to plant species infestation or dominance by liana (FOSTER et al., 2008; MARVIN et al., 2016; TYMEN et al., 2016) and bamboo (CARVALHO et al., 2013). There are also small-scale

disturbances generating individual tree mortality that can be visually detected using multi-temporal VHR imagery (CLARK et al. 2004b). For passive optical multispectral data, more elaborated procedures than visual image inspection include the use of statistical Bayesian frameworks applied over a time series of VHR imagery (KELLNER; HUBBELL, 2017). Tree mortality detection from active LiDAR has included the use of multi-temporal data (LEITOLD et al., 2018) and/or the analysis of canopy gaps derived from single-date airborne acquisition (HUNTER et al., 2015).

2.2 Mortality agents, mechanisms and spatio-temporal patterns

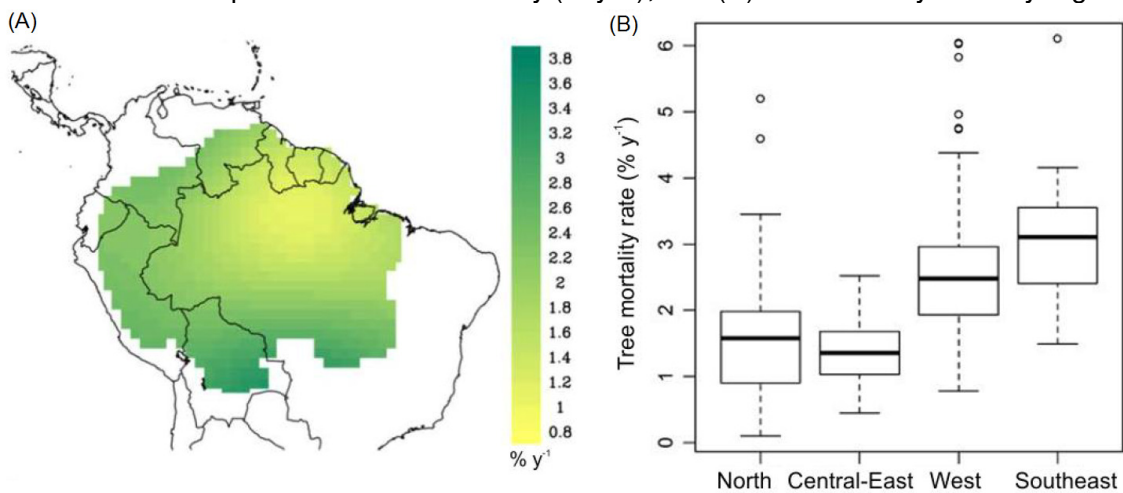
2.2.1 Patterns of tree mortality based on field inventory data

Tree mortality in Amazon forests has been associated with different factors related to the stand properties, species traits and environment (BAKER et al., 2004; CHAO et al., 2009; ANDEREGG et al., 2016; RIBEIRO, al., 2016; JOHNSON et al., 2016); tree size (RIBEIRO et al., 2016; THOMAS et al., 2013); hydraulic features (ANDEREGG et al., 2016); and topography/soil (DE TOLEDO et al., 2011; MARRA et al., 2014). The increased density of individuals may also be related to higher mortality because of the greater competition for resources (VAN GUNST et al., 2016).

In regular (non-drought) years, tree mortality in Amazon forests is around 2%yr⁻¹ and represents committed emissions of 1.3 ± 0.07 Pg C yr⁻¹ (JOHNSON et al., 2016). There is a spatial pattern of a higher rate of mortality in western and southeastern Amazon (2.62 and 3.19% yr⁻¹, respectively) than in central-eastern and northern Amazon (1.38 and 1.66% yr⁻¹, respectively) (Figure 2.1) (JOHNSON et al., 2016). However, in severe drought years, several studies reported higher tree mortality or carbon emissions in Amazon associated with El-Niño and heating of the northern Atlantic Ocean. Examples are the tree mortality increases from 2 to 3% yr⁻¹ in 1982/1983 over the tropical forests of Panama (CONDIT et al., 1995), and 1.1 to 1.9% yr⁻¹ in 1997/1998 over tropical forests of Central Amazon (WILLIAMSON et al., 2000). Furthermore, committed emissions of -1.60 Pg C yr⁻¹ (-2.63; -0.83), in areas affected by the 2005 drought (PHILLIPS et al., 2009), and -2.2 Pg C yr⁻¹ (-3.4; -1.2), in areas affected by the 2010 drought (LEWIS et

al., 2011), have been reported. El-Niño also affected the Amazon region in 2015/2016 with potential increases in mortality (JIMÉNEZ-MUÑOZ et al., 2016). Meanwhile, the differences in forest dynamics between the Amazon regions may be owed to soil properties. In the west Amazon, the soils are relatively new and shallower, having high fertility compared to the soils from the central-east and northern Amazon (QUESADA et al., 2011). These differences contribute to the faster forest dynamics, increased recruitment and mortality, and lesser specific wood density in the west Amazon, when compared to the opposite pattern observed in the central-east and north regions (BAKER et al., 2004; JOHNSON et al., 2016).

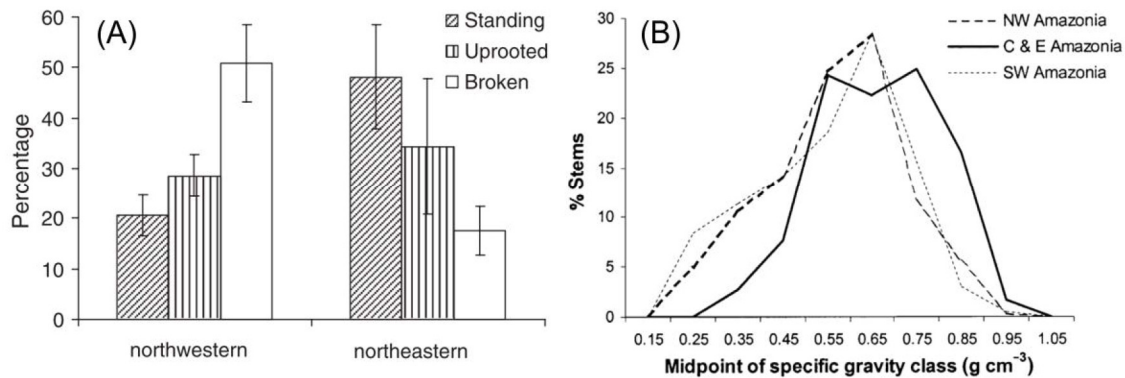
Figure 2.1 - Tree mortality based on RAINFOR inventory data: (A) kriging-interpolation map of annual tree mortality (% yr⁻¹); and (B) tree mortality rates by region.



Source: Adapted from Johnson et al. (2016).

Field observations showed that the west Amazon had an overall lower (0.57 g cm⁻³) specific wood density than the central-east region (0.66 g cm⁻³) (Figure 2.2B) (BAKER et al., 2004). Associated with the wood density, there was also a difference in the mode of death between the regions (Figure 2.2A). Western Amazon showed more broken dead trees, while central-east showed more standing dead trees (CHAO et al., 2009). The study of Ribeiro et al. (2016) found out that factors such as soil depth and uprooting resistance could also influence the mode of death. For example, large trees had higher resistance to uprooting and mechanical breakage than small trees.

Figure 2.2 - (A) Proportion of modes of death (standing dead, uprooted and broken) in northwestern and northeastern Amazon; (B) Wood density in Amazon regions.



Source: (A) Chao et al. (2009); (B) Baker et al. (2004).

2.2.2 Main mechanisms of tree mortality

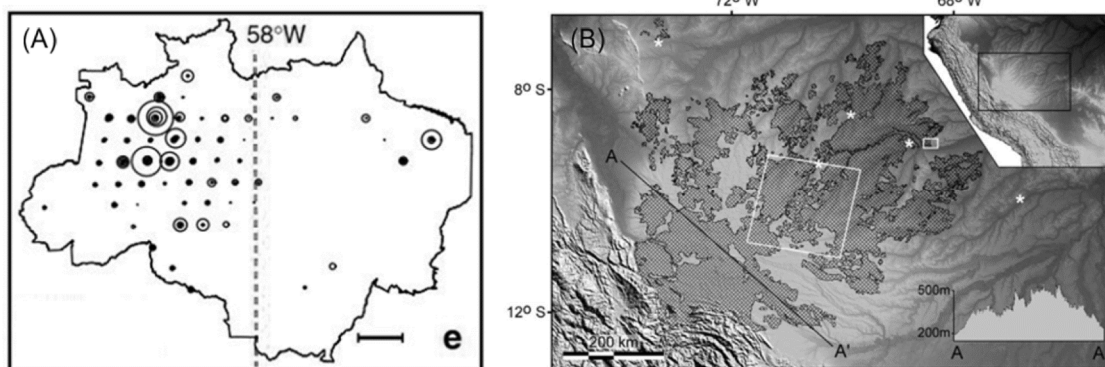
Water stress, and specifically water deficit, has been pointed out as a key driver of mortality in Amazon forests (PHILLIPS et al., 2009). According to McDowell et al. (2008), the two most accepted hypotheses for drought-related mortality are the carbon starvation and hydraulic failure. The hypothesis of carbon starvation predicts mortality when the duration of the drought is greater than the duration of the plant's carbohydrate reserves. Meanwhile, hydraulic failure occurs when the intensity of the drought exceeds the plant threshold for desiccation before the occurrence of carbon starvation. This process occurs when the plant tries to supply the high evaporative demand of the atmosphere. However, when the soil has limited access to water, air bubbles enter the xylem vessels causing cavitation and preventing the conductivity of the water inside the plant. In addition, both hypotheses can be amplified by biotic agents such as insects or diseases. For example, during water stress, the plant may stop producing resins that protect it from insects, or emit volatile gases such as ethanol, which attracts insects. An insect can also inoculate fungi in the plants' veins, preventing the passage of water.

Alternatively, flooding has also been reported as causing increased tree mortality over the Amazon forests (NELSON, 1994). It increases up to five-fold the regular mortality rates over non-flooded areas (MOSER et al., 2019). This is especially important considering the construction of mega-dams on the upper rivers of the

Amazon basin. They artificially alter the hydrological and discharge regimes (MOSER et al., 2019). Even though species at floodplains are usually adapted to the stress from floods, increases in average flood duration or water level have the potential for catastrophic mortality (GLOOR et al., 2015).

Blowdowns are one of the most common types of wind disturbances in the Amazon (ESPÍRITO-SANTO et al., 2010). The phenomenon is generated by strong winds that descend with high speeds toward the forest. They physically uproot and kill the trees, creating large clearings. The cleared areas or gaps generally cover more than 25 ha (RIFAI et al., 2016) and the most frequent scale of disturbance is around 100 ha. The largest documented blowdown to date has reached 3,370 ha of disturbance in Central Amazon forests (NELSON et al., 1994). However, the studies point out that events of this magnitude are very rare and, thus, the estimated biomass losses by the blowdowns ($0.01 \text{ Pg C year}^{-1}$) are very low compared to the small-scale disturbances (ESPÍRITO-SANTO et al., 2010; ESPÍRITO-SANTO et al., 2014). Overall, these wind disturbances in the Amazon occur more in the west than in the eastern regions, with a threshold of approximately 58° west longitude (Figure 2.3A) (NELSON et al., 1994; ESPÍRITO-SANTO et al., 2014). Coincidentally, the western Amazon region shows trees with predominantly low wood density (BAKER et al., 2004). This fact leads to a higher frequency of broken or uprooted dead trees, compared to the most common mode of death in the eastern region, which includes standing dead trees (CHAO et al., 2009).

Figure 2.3 - (A) The western Amazon region is more affected by blowdowns than the eastern region. The circles denote blowdown groupings. (B) Forests dominated by bamboo (hatched areas) in the southwestern Amazon.



Source: Adapted from (A) Espírito-Santo et al. (2014), and (B) Carvalho et al. (2013).

Plant infestation or dominance by liana and bamboo can greatly improve tree mortality rates and constraint carbon sequestration (FOSTER et al., 2008; CASTRO et al., 2013). Liana plants can enhance tree mortality up to double the landscape mortality rate for trees with >75% liana canopy cover (INGWELL et al., 2010). There are no reliable large-scale assessments of liana cover for the Amazon forests, but rough estimates are in the order of 100,000 km² (NELSON et al., 1994).

The bamboo-dominated forests occupy an area of 161,500 km² in the southwestern Amazon (about 3% of the entire Amazon) (Figure 2.3B) (CARVALHO et al., 2013). These forests have a high density of bamboo of the genus *Guadua* ($2,309 \pm 1,149$ ind ha⁻¹) with an average diameter of 4.4 ± 0.6 cm (CASTRO et al., 2013). The bamboo competes for resources with the rest of the species, while causes physical damage and tree strangulation (GRISCOM, 2003). Studies report that annual mortality in these areas is $3.6 \pm 2.5\%$ yr⁻¹ (CASTRO et al., 2013; Medeiros et al., 2013). This rate is much higher than the Amazon average rate, which is 1.96% yr⁻¹, or the average in the western region, which is 2.62% yr⁻¹ (JOHNSON et al., 2016). These individuals have a monocarp characteristic with a life cycle measured by remote sensing of approximately 27-28 years (CARVALHO et al., 2013). When they reach the end of their lives, they flourish and die synchronously in large areas. With the death of these bamboos, there is an accumulation of dry biomass in the forest, which can increase the probability of fire occurrence. This led researchers to the 'bamboo-fire hypothesis', pointing out that fire may explain the bamboo dominance in this region (KEELEY; BOND, 1999). In addition, as there is a mosaic of different ages of bamboo throughout the region, it is expected that the forest dynamics in this region will be highly variable (MEDEIROS et al., 2013).

Landscape changes resulting from anthropic action, such as fragmentation, also have an impact on the dynamics of the remaining forests and cause increases in tree mortality rates (LAURANCE et al., 1998; LAURANCE et al., 2001; LAURANCE; WILLIAMSON, 2001). Data collected in permanent inventory plots of the Dynamics of Forest Fragments Project (BDFFP) indicated that, on average, an annual mortality of 3-4% occurs in the first 60 m of the fragment's edge, about 2% of 60-100 m and 1-1.5% in the interior (LAURANCE et al., 1998). Therefore,

mortality rates about three times higher occurred at the edges than inside the fragment. Mechanisms behind the increased mortality with fragmentation include factors such as microclimate changes, wind turbulence (LAURANCE et al., 1998), number of edges (LAURANCE et al., 2011), and the type of land cover neighbor to the fragment (MESQUITA, et al., 1999). The more edges a fragment has, the higher its mortality rate, density of individuals and species richness (LAURANCE et al., 2011). Since 90% of the fragments of the Amazon are smaller than 4 km² (BROADBENT et al., 2008), greater impacts are expected due to the number of edges. Regarding the neighboring land cover, if it is a pasture, the fragment is more exposed to higher temperatures and humidity deficit. Consequently, there is a higher probability of burning, as fire is a traditional method of management in the Amazon (MESQUITA et al., 1999).

Wildfires are also an important driver of mortality in the Amazon forests. Even though their natural occurrence is relatively rare, e.g. fires ignited by lightning from thunderstorms, these disturbances associated with anthropogenic activities affect huge areas in the Amazon similarly to fragmentation (COCHRANE, 2003). Moreover, the likelihood of a forest getting on fire is increased by degradation processes such as logging or fragmentation (ARAGÃO et al., 2014), or by severe droughts such as the 2010 and 2015/2016 El Niño events (SILVA JÚNIOR et al., 2019). Mortality rates in fire-affected forests rise up to 36% after 3 years of fire occurrence (an average of 12% yr⁻¹) (BARLOW et al., 2012). Even after three decades following fire occurrence, the burned forests still exhibit 25% less biomass than the unburned forests (SILVA et al., 2018).

2.2.3 Canopy gaps and mortality

By classical definition, the gap is a 'hole' in the forest canopy that extends down to ≤ 2 m above ground (BROKAW, 1982). Other thresholds of height have been experimented in the literature, for example, 20 m. They can be used to characterize treefalls and possible trees with branch-fall or crown failure (ASNER et al., 2013). Treefall gaps are generated by disturbance events that may end in the death and fall of single or multiple trees. Therefore, strong relationships between gap areas and coarse wood debris (CWD) ($R^2 = 0.53$), and gap areas and the number of dead trees ($R^2 = 0.56$), were observed in tropical forests in

eastern Amazon by ground sampling (ESPÍRITO-SANTO et al., 2013). However, since CWD is also produced by branch-fall, and this is not precisely represented by gap sizes, the gap distribution alone cannot explain all the production of necromass in Amazon (ESPÍRITO-SANTO et al., 2013). Nevertheless, gap analysis is an alternative approach to measure tree mortality, that is, instead of tracking each tree's fate over time, gaps can be measured to report on the aggregated effect of mortality.

Treefall gaps are important sources of heterogeneity in the composition and dynamics of tropical forests (BROKAW, 1985). After the aperture of a gap in the canopy, there is an increase in light transmittance and small changes in nutrient concentrations that can promote alteration in canopy biophysical properties, e.g. leaf area index – LAI, canopy functions, e.g. photosynthesis, shifts in species composition, acceleration of biomass decomposition, etc. (CHAMBERS et al., 2013). However, this will depend on the gap sizes, where large gaps ($> 150 \text{ m}^2$) have more light infiltration than small gaps ($< 150 \text{ m}^2$) (BROKAW, 1985). In smaller gaps, shade-tolerant species might be able to grow due to the lack of competition by light-demanding species. Meanwhile, larger gaps promote the development of existing or new individuals of shrubs, lianas and large herbs (DENSLOW et al., 1998).

Gap size distribution is generally characterized by the prevalence of more frequent small than large-sized gaps, presenting a negative exponential or lognormal shape of the distribution (YAMAMOTO, 2000). The gap sizes vary among developmental stages of a forest, where the mean gap size is smaller in early development stages than in old-growth forests (YAMAMOTO, 2000). In the study of wind disturbance in Central Amazon, the gaps observed in the field had 6 to 8 dead trees and areas from 250 to 900 m^2 , while the mean gap size was 360 m^2 (NEGRÓN-JUÁREZ et al., 2011).

Measurement of gaps is a challenge for both field and remote sensing observations. While ground gap measurements are obtained directly by tape or indirectly estimated by canopy openness from hemispherical photography (DANSON et al., 2007), the CHM extracted from the LiDAR point cloud allows for the precise detection of gaps considering a height cutoff parameter (LOBO; DALLING, 2014). A study by Gaulton and Malthus (2010) attempted to validate

gap measurements from airborne LiDAR data with gaps measured on the ground. They concluded that it was very difficult to achieve a reliable relationship. This is likely because the high-precision of LiDAR-gap delineation potentially surpasses that of ground measurements, which tend to under-sample gaps. Nevertheless, airborne LiDAR data constitute the best tool available to map gap distribution at large scales.

The most common gap measurements include gap fraction (area occupied by gaps), gap size, and gap size-frequency distribution (SFD). To assess the gap SFD, the gap size distribution is assessed by fitting a discrete power-law probability (Zeta distribution) and obtaining the λ -scale parameter that characterizes the distribution (ESPÍRITO-SANTO et al., 2014). The meaning of λ refers to the gap dynamics. Larger λ (>2.0) represents a forest dominated by smaller gaps, while smaller λ (< 2.0) indicates forests dominated by larger gaps associated with the mortality of emergent trees (ASNER et al., 2013). However, since each study from the literature employs a different method to delineate gaps, it is not possible to compare the λ between the sites.

2.3 Remote sensing studies for mortality detection and monitoring

The remote sensing studies were divided into three categories that represent different scales of observation of mortality and best-suited data for analyses: (1) canopy observed at the landscape scale, (2) individual trees observed at the local scale, and (3) canopy gaps observed at the local scale.

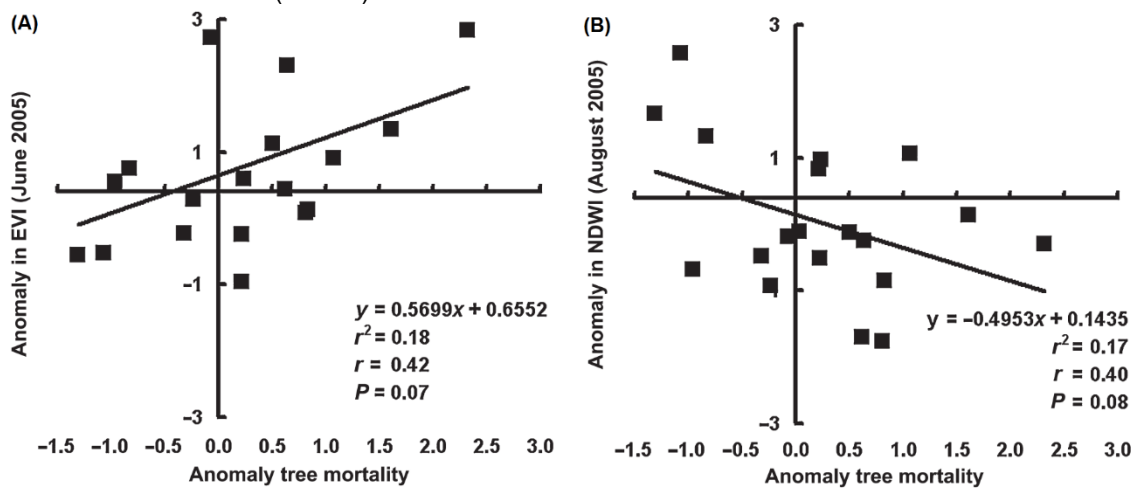
2.3.1 Canopy observed at the landscape scale

Amongst all mortality agents studied with remote sensing in the Amazon, blowdowns were the most reported (NELSON et al., 1994; CHAMBERS et al., 2009; ESPÍRITO-SANTO et al., 2010; CHAMBERS et al., 2013; MARRA et al., 2014; RIFAI et al., 2016). The studies have used optical passive data from Landsat satellites and spectral mixture modelling to map the area affected by the blowdowns, either based on a single-date analysis (NELSON et al., 1994; CHAMBERS et al., 2009; ESPÍRITO-SANTO et al., 2010), or a time series inspection (CHAMBERS et al., 2013; MARRA et al., 2014; RIFAI et al., 2016). In

both types of analyses, the studies extracted the non-photosynthetically active vegetation (NPV) fraction to infer about mortality fraction across the landscape. When the wind uproots trees, trunks and branches are usually exposed, an increase in the NPV fraction is generally observed. For the time-series analyses, the NPV variability over time (ΔNPV) was calculated and a threshold ($\Delta\text{NPV} \geq 0.16$) was determined to discriminate areas with disturbance from non-disturbance (MARRA et al., 2014; CHAMBERS et al., 2013). For instance, high values of ΔNPV meant more mortality. The studies also fitted models between ΔNPV and field-measured mortality (fraction) with very strong goodness of fit ($R^2 > 0.8$).

Drought-related mortality was also investigated in tropical forests by using the MODIS sensor and RAINFOR field data (ANDERSON et al., 2010). The relationship between the MODIS Enhanced Vegetation Index (EVI) and the Normalized Difference Water Index (NDWI) was assessed in comparison to field anomalies of tree mortality observed in the 2005 drought year (Figure 2.4). The EVI anomalies presented a positive association with the mortality anomalies (Figure 2.4A; $R^2 = 0.18$, $p = 0.07$), while the NDWI presented a negative relationship with it (Figure 2.4B; $R^2 = 0.17$, $p = 0.08$). Although relatively weak, the relationships were statistically significant. The EVI increase and the NDWI decrease with increasing mortality were associated with canopy structural changes that reduced the amount of shadows for the sensor. Therefore, with fewer shadows, the NIR signal was higher, and therefore the EVI was also higher. This is because EVI and NIR reflectance are highly correlated to each other (GALVÃO et al., 2011).

Figure 2.4 - Correlation of anomaly of vegetation indices with field-based forest mortality. (A) Enhanced Vegetation Index (EVI). (B) Normalized Difference Water Index (NDWI).



Source: Adapted from Anderson et al. (2010).

Mass mortality due to flooding has been mapped using ALOS/PALSAR data with high accuracy (87%) at the Central Amazon basin (RESENDE et al., 2019). The construction of a large dam close to the Uatumã River in 1987 led to abrupt changes in the hydrological cycle of this river, causing long-term changes to the forest dynamics. The authors used radar imagery to map the widespread standing dead trees and living trees. The SAR signal from living trees goes through lots of volumetric scattering in the canopy, which attenuate the returned signal. In contrast, the dead leafless trees and free water underneath the trunks produced a strong signal derived from the lack of a double-bouncing effect.

The large-scale bamboo die-off at the southwest Amazon region (Figure 2.3B) can be detected by optical sensors such as TM/Landsat-5 and MODIS/Terra time series (NELSON, 1994; CARVALHO et al., 2013). Carvalho et al. (2013) showed that forests having adult bamboos at the canopy had higher reflectance in the near infrared (NIR) wavelength than bamboo-free areas or areas with recently dead bamboo. Therefore, by visual analysis of annual composites of MODIS data, using the NIR as part of a false-color composite, they manually delineated patches of bamboo that synchronously died. One limitation of this approach is the identification of large areas based on the analyst's visual acuity. Further studies are therefore necessary to understand the bamboo life cycle and its spectral characteristics, as well as to establish automatic approaches for detecting die-off events in bamboo-dominated areas. These approaches can enable analyses of

ecological processes associated with these events, such as the interactions between bamboo and fire (KEELEY; BOND, 1999) and bamboo flowering wave patterns (FRANKLIN et al., 2010).

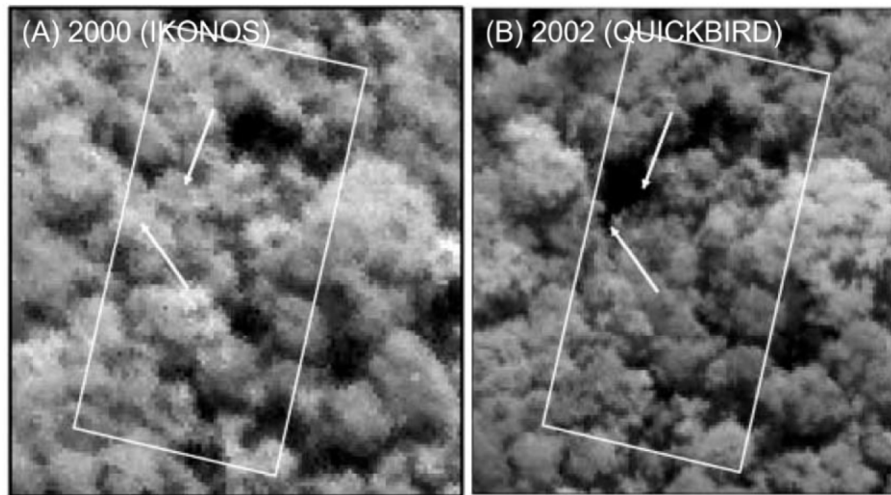
Liana infestation on the forest canopy has also been studied using remote sensing in a few tropical forest sites (FOSTER et al., 2008; MARVIN et al., 2016; TYMEN et al., 2016). Some of these approaches were based on Landsat multispectral data (FOSTER et al., 2008; TYMEN et al., 2016); Hyperion or airborne hyperspectral data (MARVIN et al., 2016); and airborne LiDAR data (TYMEN et al., 2016). The infestation may be characterized by low height and uniform canopies having a brighter green color than the surrounding forest canopies (FOSTER et al., 2008). Therefore, in general, the detection of liana-infested forests was attributed to a higher reflectance in the visible wavelength than the signal observed over non-infested forests (MARVIN et al., 2016). Although these liana-dominated forests showed distinct spectral characteristics and height than the surrounding non-infested forests, the studies so far did not point out a unique feature of the liana-forests that would allow for large-scale detection, similarly as the bamboo die-off.

2.3.2 Individual trees observed at the local scale

VHR satellite images allow for the identification of individual tree losses. By using multi-date imagery, a pioneer study assessed tree mortality in the tropical forest at La Selva station in Costa Rica (CLARK et al., 2004b). The study employed an Ikonos image (1 m spatial resolution) from 2000 and a QuickBird image (0.7 m spatial resolution) from 2002. The detection was performed by visually observing the omission of crowns from the first to the second date (Figure 2.5). When accounting for the number of dead trees, the satellite data produced a tree mortality rate of 2.8% yr⁻¹, which was comparable with the mortality measured in the field (3% yr⁻¹). The main challenges of applying this method to extensive analysis are the low availability of images due to the cloud cover and the impact of extremely different viewing-illumination geometry in both images that affect the amount of shadows viewed by the sensors (WULDER et al., 2008; ESPÍRITO-SANTO et al., 2013). Robust co-registering methods and spatial-spectral analysis are options to work with different geometries. The tree mortality analysis using

VHR data may be biased, to some extent, by better observations of crown suppressions of the tallest trees across dates.

Figure 2.5 - Tree mortality detection of individual trees based on Very High Resolution (VHR) optical imagery, between (A) 2000 (Ikonos) and (B) 2002 (QuickBird).



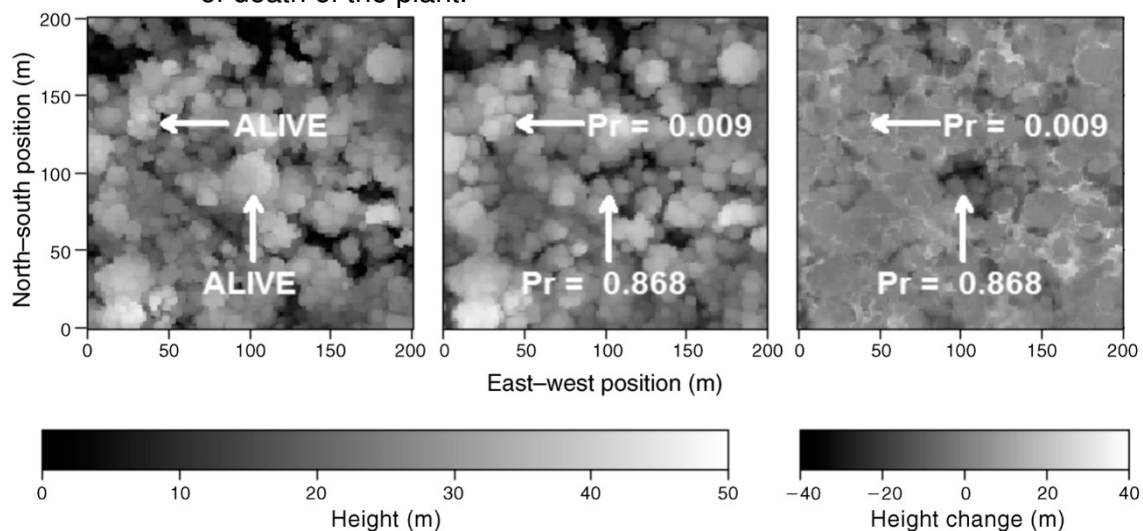
Source: Adapted from Clark et al. (2004b).

Using VHR imagery, Kellner and Hubbell (2017) applied a Bayesian model to detect the mortality of canopy tree species *Handroanthus guayacan* in tropical forests of the Barro Colorado Island (Panama) based on synchronous flowering patterns. Overall, each tree was observed on each image of the VHR time series. The method proposed by the authors assessed the probability of death based on the presence or absence of flowering. For instance, if the tree flowers, it is alive. If the tree does not flower on several subsequent images, the probability of death increases. They have estimated a lower rate of tree mortality for this species than the rate measured in the field campaigns, but the estimates were not statistically different from each other. As a constraint of this approach, it will work only for tree species with synchronous annual flowering, requiring also a dense time series of VHR imagery to track overtime this phenological event.

Airborne LiDAR also detects the mortality of individual trees (THOMAS et al., 2013). At the La Selva reserve in Costa Rica, Thomas et al. (2013) assessed the annual mortality rate of large trees (height ≥ 40 m) to test whether these individuals were experiencing higher or lower mortality than the other canopy individuals. The detection was performed by multi-temporal airborne LiDAR data with 0.33 m of spatial resolution for the years 1997 and 2006. A total of 121 large

trees were identified in the field. However, by applying a 40-m height threshold over the LiDAR CHM data, they detected 735 large trees in the study area. Considering the height difference between the 2006 and 1997 models, a logistic relationship was applied to determine the probability of the individual's mortality (Figure 2.6). Results from that study showed a lower mortality rate for large trees ($1.2\% \text{ year}^{-1}$) than for the rest of the canopy trees ($2.7\% \text{ year}^{-1}$). Remote sensing was essential in testing this hypothesis, since the number of large trees sampled in the field was much smaller than that covered by the LiDAR data, reducing the uncertainties in the predictions of the mortality rate.

Figure 2.6 - Mortality detection by the difference between multi-temporal LiDAR Canopy Height Models (CHM) from (A) 1997, and (B) 2006. The image in (C) represents the difference between (A) and (B). Pr means the probability of death of the plant.



Source: Adapted from Thomas et al. (2013).

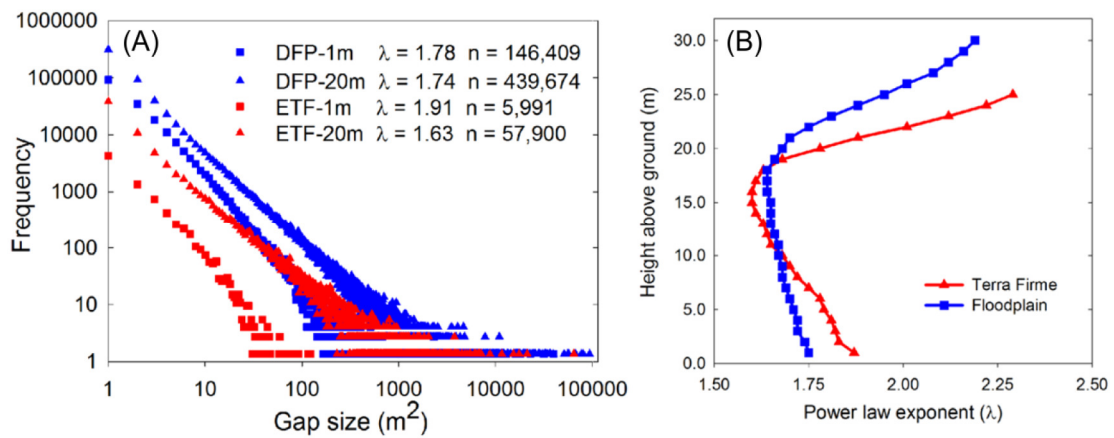
2.3.3 Canopy gaps observed at the local scale

Airborne LiDAR data have been used in Neotropical forests to quantify the spatial distribution, frequency and size of gaps (ASNER et al., 2013; LOBO; DALLING, 2014; ESPÍRITO-SANTO et al., 2014; GOULAMOUSSENE et al., 2016). The relationship of gaps with environmental, edaphic, and topographic variables has been also evaluated (GOULAMOUSSENE et al., 2016). Despite the use of LiDAR to assess the gap-phase dynamics in some tropical forest sites, an extensive analysis of the spatio-temporal distribution of gaps over the Amazon has not been developed yet.

The gaps retrieved from single-date images are sometimes called 'static' gaps because they represent the integration of past disturbance and forest regrowth. Their delineation is strongly dependent on the height cutoff definition, which can generate different amounts of gaps for analysis (ASNER et al., 2013; LOBO; DALLING, 2014; HUNTER et al., 2015). Height cutoffs from these studies ranged from 1 to 20 m, but 10 m was the most widely accepted value. Rather than using a single gap definition, Goulamoussène et al. (2017) proposed a method to calibrate the height cutoff to a forest site based on the statistical analysis of its height distribution and mixed models. Some caveats of this approach include not accounting for factors such as the presence of large open areas that were not necessarily treefall gaps; low height vegetation; and degraded or deforested areas. Another proposed approach was based on a dynamic definition using a relative height cutoff and a local moving window (GAULTON; MALTHUS, 2010). Still, this approach has not yet been tested over tropical forests.

From the SFD analyses of static gaps, Asner et al. (2013) showed that λ described differences in forest dynamics between the Erosional *Terra Firme* (ETF) and Depositional Floodplain (DFP) landscapes, with different vegetation types, geology and elevation (Figure 2.7A). When considering lower height thresholds to delineate a gap (nearest to the ground), the ETF showed a pattern of smaller gap sizes than the DFP, denoted by the superior λ exponents (Figure 2.7B). However, when increasing the height threshold at some point between 15 and 20 m, the ETF showed bigger gaps than the DFP, as expressed by the inferior λ exponents. Therefore, the λ considering different height thresholds inform about the variability of canopy structure on a vertical profile.

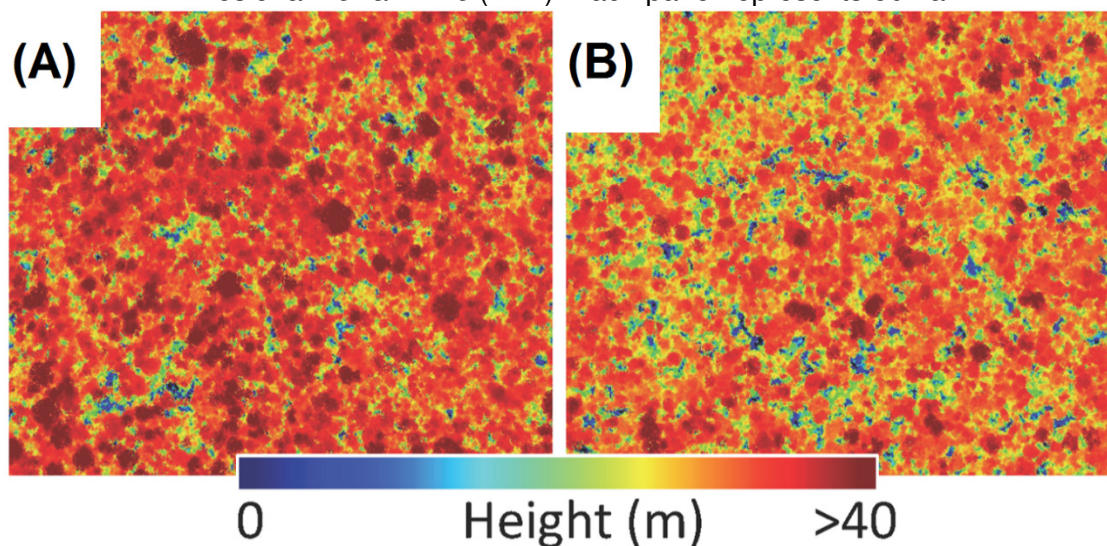
Figure 2.7 - (A) Gap size-frequency distributions (SFD) of two vegetation types: Erosional *Terra Firme* (ETF) and Depositional Floodplain (DFP), and considering 1-m and 20-m height thresholds; (B) Vertical distribution of power-law exponents λ for each forest type.



Source: Adapted from Asner et al. (2013).

A visual example of the gaps is shown in Figure 2.8 for Peruvian tropical forests based on the study by Asner et al. (2013). The forest at the left panel (Figure 2.8A) shows a more closed canopy than the one at the right panel (Figure 2.8B). Although the gaps are not strictly delineated in the figures, they are mostly represented by the blue areas having low height values. The exact delineation of gaps will depend on the selected height cutoff.

Figure 2.8 - Forest Canopy Height Models (CHM) of a Peruvian Amazon forest landscape, specifically at a (A) Depositional Floodplain (DFT), and an (B) Erosional *Terra Firme* (ETF). Each panel represents 50 ha.



Source: Adapted from Asner et al. (2013).

Gap distribution can also be analyzed over time. The ‘dynamic’ gaps are the new gaps observed between a given interval of time, using multi-temporal data (MARVIN et al., 2014; HUNTER et al., 2015). There are not many studies on dynamic gaps because of the requirement of multi-temporal data. However, they should be more related to the carbon fluxes within the given period, expressing the dynamics of regeneration. In a study at a lowland tropical forest in southwestern Colombia, Marvin et al. (2014) showed that there were three times more static (1.6 gaps ha⁻¹) than dynamic gaps (0.5 gaps ha⁻¹), and that 60% of the dynamic gaps happened close to pre-existing gaps. Other studies also present evidence that new gaps are prone to occur closer to pre-existing gaps, following the hypothesis of ‘gap contagiousness’ (MARVIN et al., 2014; HUNTER et al., 2015).

2.4 Perspectives for tree mortality studies using remote sensing over Amazonian tropical forests

Based on the literature review, the main drivers of mortality for Amazonian tropical forests are associated with factors that affect forest dynamics such as water stress, wind (blowdown), species dominance (liana and bamboo), and human-related disturbance (fragmentation and logging). Remote sensing has been used only locally to detect tree mortality related to some of these processes. However, the number of studies on the topic is relatively small considering the importance of the Amazon. As far as we know, there are no proposed remote sensing approaches for large-scale monitoring of tree mortality in the Amazon aiming at providing spatialized inter-annual mortality estimates. Moreover, there is probably no ‘one’ approach that can solve this problem alone. Thus, region- or vegetation- specific approaches may be necessary.

Estimates of tree mortality should play a key role in calibrating and validating ecosystem models for a better representation of the carbon cycle in the Amazon. From the previous literature review, the remote sensing perspectives for a better understanding of tropical forest mortality in the Amazon region depend on several factors. For instance, they include the need to: (1) develop quantitative approaches from passive optical multispectral imagery or preferentially active LiDAR data for detecting tree mortality over the entire ecosystem; (2) assess how

much do canopy gaps represent tree mortality; (3) adapt strategies of tree mortality detection for specific vegetation types such as bamboo-dominated forests, using high-temporal resolution data from MODIS or satellite constellations for tracking their phenological response or life cycle, and liana-infested forests; (4) combine remote sensing, climatic and environmental data for a better comprehension of the factors causing tree mortality; and (5) integrate the resultant tree mortality map into the ecosystem models.

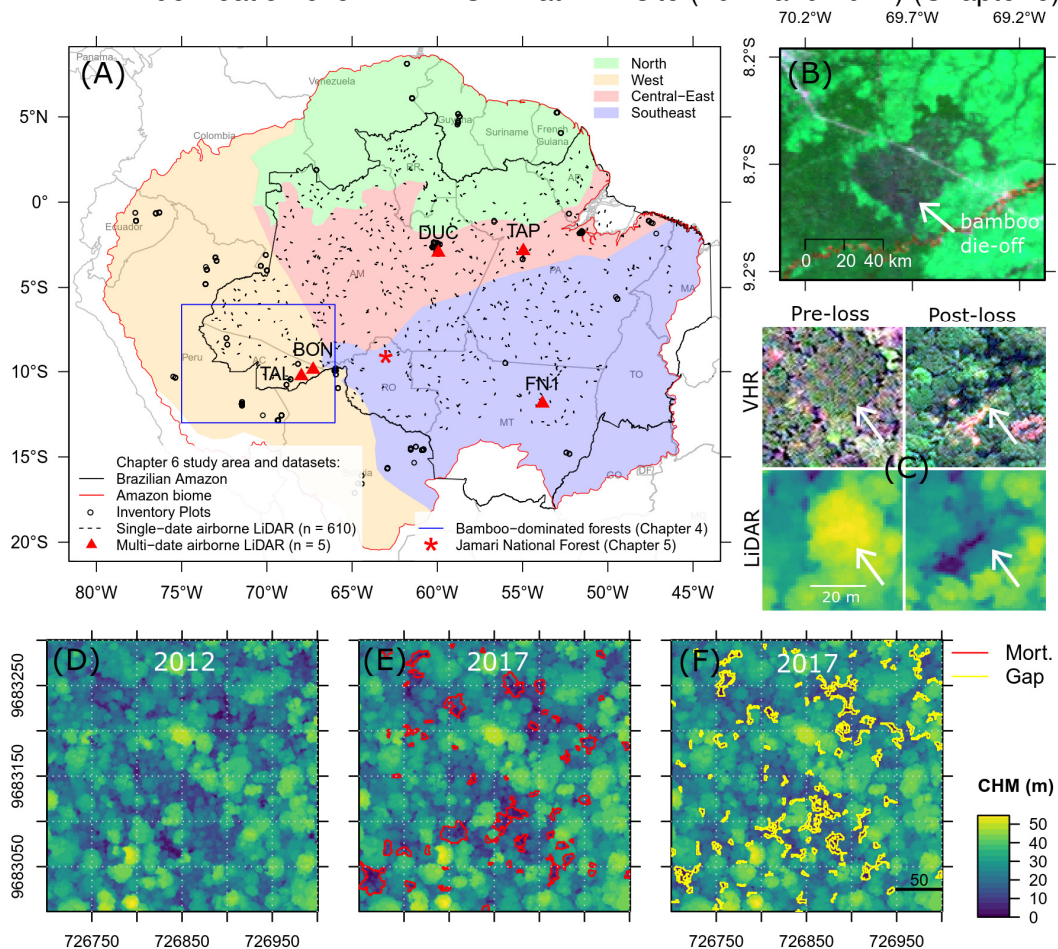
The present doctoral dissertation is inserted in this context. It addresses some of the above-mentioned requirements to improve knowledge on tree mortality of Amazonian tropical forests, while it provides the necessary information for the development of the other topics.

3 GENERAL METHODOLOGY

3.1 Study area

The study area is the Amazon biome (Figure 3.1) (EVA; HUBER, 2005). To facilitate the representation of results, we divided the Amazon into four regions with distinct geography and substrate origin. Following Feldpausch et al. (2011), they are: (1) west region, covering Colombia, Ecuador, Peru and Bolivia, with fertile soils originated from recently weathered Andean deposits; (2) southeast region, including Brazil and Bolivia; (3) central-east region, covering Brazil and mostly comprised of old soils derived from sedimentary rocks; and (4) north region, encompassing Guyana, French Guiana and Venezuela.

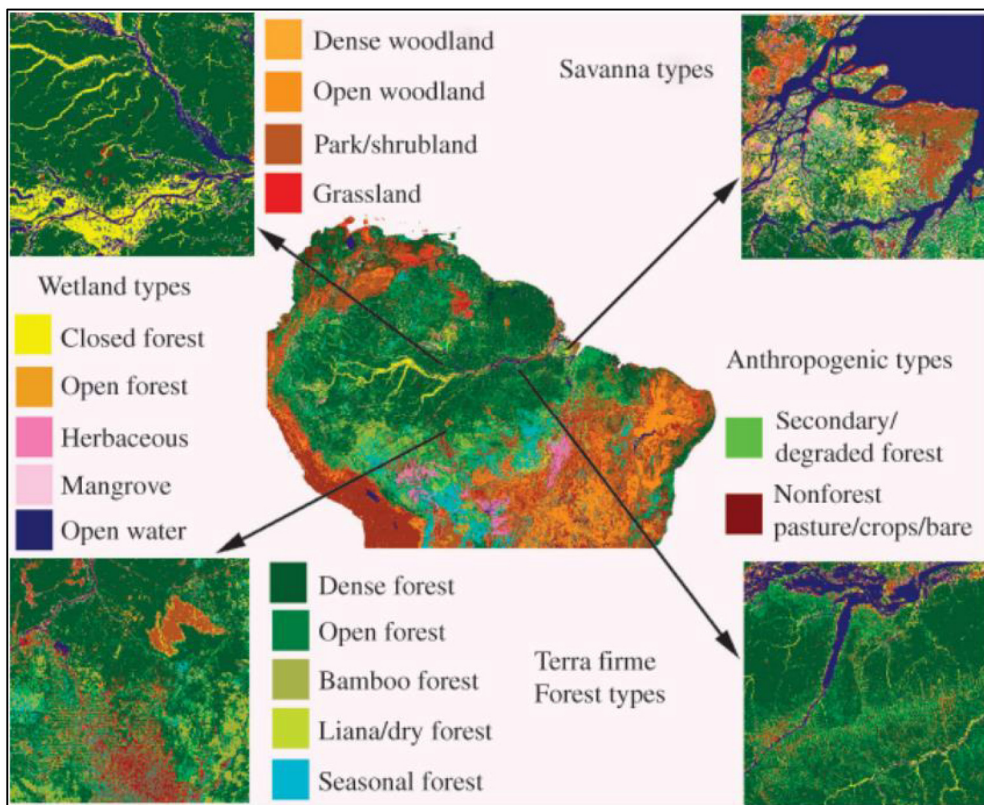
Figure 3.1 – Study area and examples of the developed mortality detection approaches. (A) The Amazon biome in South America divided into regions following Feldpausch et al. (2011); (B) MODIS (MAIAC) false-color composite of red (R), NIR (G) and SWIR (B) bands in Aug 2015. Living bamboo at the canopy is shown in light green color, while recently dead bamboo is shown in dark blue/gray color (Chapter 4); (C) VHR imagery and LiDAR CHM showing individual tree loss (Chapter 5); and (D, E, F) mortality and gap delineation over LiDAR CHM at TAP site (2012 and 2017) (Chapter 6).



Source: Produced by the author.

Amazon is very diverse in vegetation types (Figure 3.2). The broadest division of vegetation types is the *terra firme*, wetlands, savanna, and anthropogenic types, which are then divided into several sub-types (SAATCHI et al., 2007). The predominant natural vegetation is Dense Ombrophylous Forest with 5.3 million km², which corresponds to 70% of the Amazon and 40% of all tropical forests in the world (ARAGÃO et al., 2014). Although there is no forest degradation product available for the Amazon biome, the non-forest distance (km) (Figure 3.3D) derived from the Global Forest Cover product v1.4 (HANSEN et al., 2013) shows forests nominally undisturbed up to 30 km farther from any deforestation, vegetation regrowth or water channel, i.e. potential pathways of human-influence. The mean distance is 2.5 km, ranging from 0.1 to 10 km (5 and 95th percentiles).

Figure 3.2 – Vegetation types in the Amazon region.

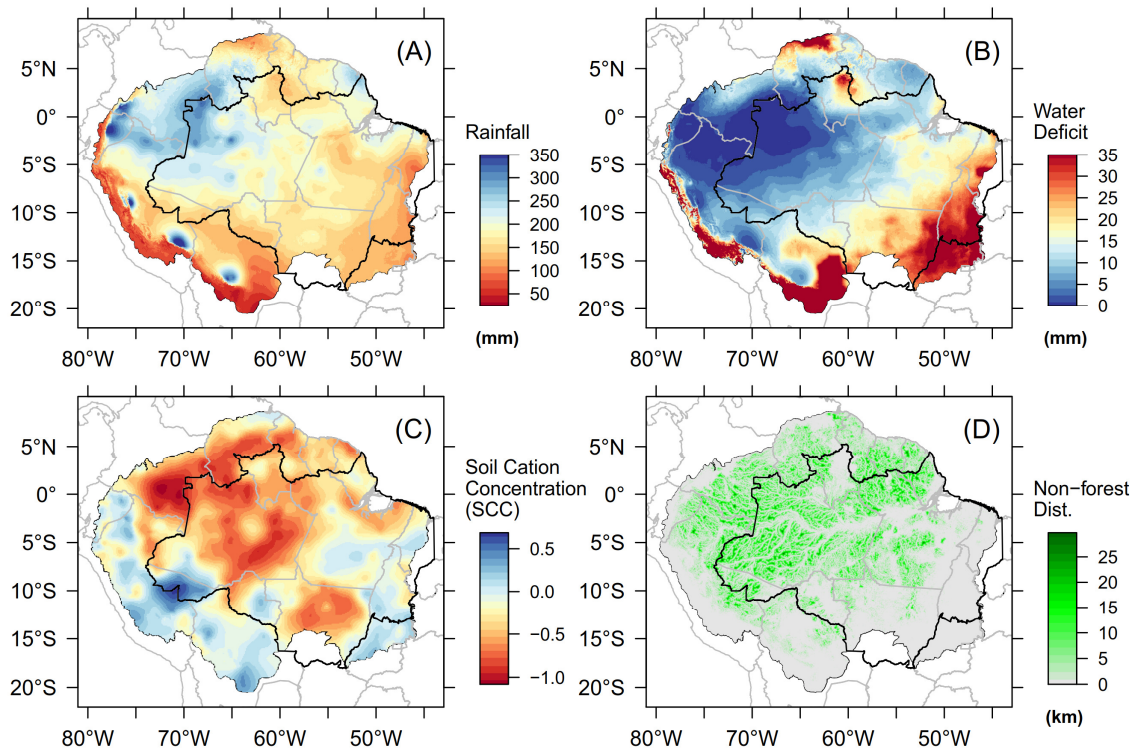


Source: Saatchi et al. (2007).

In the majority of the region, the Köppen climate is Am and Af, presenting high precipitation rates in all months (avg. 100 to 300 mm month⁻¹) (Figure 3.3A). High temperatures and varying start and length of the dry season are observed, which lasts from 1 month in the northwest to 4 months in the southeast (MOURA et al., 2015). Average monthly water deficits, derived from the TerraClimate product

(ABATZOGLOU et al., 2018), range from 0 to 35 mm. They increase from the northwest to the southeast Amazon (Figure 3.3B). Although Amazonian soils are very diverse, the predominant types are Ferralsols and Acrisols in the southeast and north Amazon region; Ferralsols and Plinthosols in the central-east Amazon region; and Acrisols and Cambisols in the west Amazon region (QUESADA et al., 2011). The western region from Figure 3.1 shows newer geological materials, in contrast to older materials in the other regions (QUESADA et al., 2011). Soil fertility, proxied by the Soil Cation Concentration (SCC) (ZUQUIM et al., 2019), shows higher values at the west and east than southeast, central and north regions (Figure 3.3C). Terrain elevation is generally lower than 200 m. The Amazon presents the most extensive floodplains on the planet (800,000 km²) (MELACK et al., 2010). Human occupation in Amazon represented around 23.6 million people in 2007, accounting for only the Brazilian Amazon (IBGE, 2010), where 70% of the population lived in cities (PADOCH et al., 2008).

Figure 3.3 – Environmental and climate variables for the Amazon forests. Average monthly (A) rainfall (mm) and (B) water deficit (mm) from the TerraClimate product (ABATZOGLOU et al., 2018); (C) Soil Cation Concentration (SCC) (ZUQUIM et al., 2019), a proxy for soil fertility; (D) Non-forest distance (km) derived from Global Forest Cover product (HANSEN et al., 2013), a proxy for forest degradation.

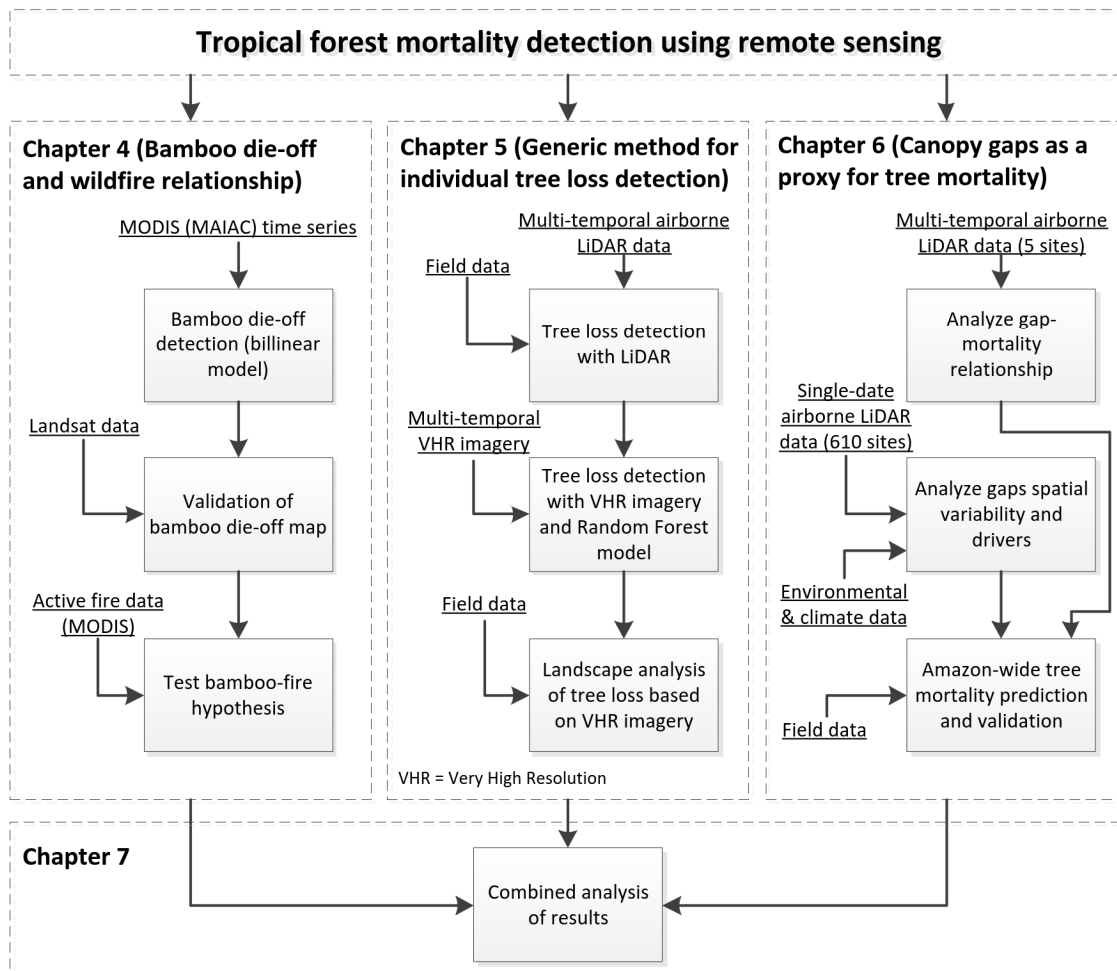


Source: Produced by the author.

3.2 Data and methods

Three remote sensing strategies to detect tropical forest mortality at different observation levels (canopy at the landscape scale, individual trees and canopy gaps at the local scale) were developed and validated in this study (Figure 3.4). The main methodological steps for these analyses are described in the paragraphs below. More detailed methodological information can be found in each chapter.

Figure 3.4 – Overview of the main methodological steps used in the data analysis. Details are provided in each corresponding chapter.



Source: Produced by the author.

In Chapter 4, an approach was presented to automatically detect the bamboo die-off at landscape scale, based on time series of MODIS (MAIAC) data and characteristics of bamboo life cycle and phenology. This part of the study was conducted at the southwest Amazon (blue rectangle in Figure 3.1A), covering around 16 million ha, mostly over Brazil (Acre state) and Peru. The bamboo life

cycle length spans approximately 28 years. When it ends, the bamboo massively and synchronously reproduces and die, falling off the canopy and leaving huge amounts of dry biomass over the understory. The assumption behind the detection was that when bamboo dies, the canopy near infrared (NIR) spectral response abruptly drops because of the reduction of leaves. The dataset used for the bamboo mapping was a time series of the surface reflectance from MODIS (MAIAC) product (DALAGNOL et al., 2018b) corrected for viewing-illumination geometry by the Bidirectional Reflectance Distribution Function (BRDF) at 1-km scale, ranging from 2001 to 2017, considering the composite from August of each year. To detect the abrupt NIR changes, a simulated bilinear model was developed consisting of a NIR signal increase from 1 to 28 years of bamboo life and an abrupt decrease in year 29 (death). Then, the observed signal from each pixel was compared to the bilinear model, assessing the point of maximum correlation between the two. The year with the maximum significant correlation would consist of the die-off year. For validation, a time series of TM/Landsat-5 imagery (30 m) was used for visual analysis of the bamboo die-off at high-resolution. Considering a false-color composite of bands 1 (red), 2 (NIR) and 6 (SWIR), in RGB channels, respectively, the recent die-off was characterized by a change from light green to dark blue/gray colors (Figure 3.1B). Therefore, samples of die-off from each year (2001-2017) were collected and compared to the die-off map. After detection and validation, active fire data from MODIS were acquired and used to test whether fire occurred more frequently after bamboo die-off ('bamboo-fire hypothesis').

In Chapter 5, a semi-automatic generic method was developed for individual tree loss detection. The method was based on multi-temporal VHR ($\leq 1 \times 1$ m) passive optical imagery and RF model. The study area consisted of 76.6 km² of forests inside the Jamari National Forest in the Brazilian Amazon (red asterisk in Figure 3.1B), where part of this forest has been managed by selective logging. This experiment was based on detecting tree loss from selective logging rather than natural tree mortality due to the unique availability of a tree-by-tree geolocation dataset of logged trees. The dataset used in this part of the study consisted of WorldView-2 and GeoEye-1 imagery acquired pre- (2014) and post-logging (2017); airborne LiDAR data acquired pre- (2015) and post-logging (2017); and

tree-by-tree field data with the geolocation of each logged tree ($n = 172$ trees). To detect tree loss, I first assessed the LiDAR height change for geolocations of logged and non-logged trees (example in Figure 3.1B) and produced a tree loss map based on LiDAR. This map was used to sample locations of tree loss and non-tree loss, extracting spectral data from the VHR dataset. The spectral data were used to train the Random Forest model. The model was then applied to map the landscape tree loss, beyond the LiDAR coverage. The results were assessed face to the expected loss inside and outside the management units considering the year of management.

In Chapter 6, I explored the use of canopy gaps as a proxy for tree mortality at the local scale. I assessed gap dynamics relationship with environmental and climate variables and modelled/spatialized tree mortality for the entire Amazon biome. For this purpose, airborne multi-temporal LiDAR datasets acquired over five sites located in an AGB gradient (red triangles at Figure 3.1A), and mono-temporal LiDAR data acquired at 610 sites distributed across the Brazilian Amazon (black dashed lines in Figure 3.1A) were considered in the analysis. First, the gap-mortality relationship was investigated over the five sites using multi-temporal data. An example of mortality and gap delineation is shown in Figure 3.1D-F. Mortality was extracted considering the height difference between two acquisitions, while gaps were delineated considering only the most recent LiDAR acquisition. Gap delineation by the relative height and fixed height cutoff methods were compared. Second, a systematic assessment of gap dynamics was conducted across the Brazilian Amazon considering the 610 flight lines. The data were used to calculate the gap fraction on each site ($n = 610$) and to analyze the spatial patterns from its relationship with environmental and climate drivers. Finally, the tree mortality was predicted for the whole Amazon biome by combining the models for the environmental-climate/gap relationship and gap-mortality model. The map was validated against field-based tree mortality data ($n = 88$ locations) from the RAINFOR network (MALHI et al. 2002). The spatial patterns of tree mortality were compared with previous results from the literature and Amazonian regions.

In Chapter 7, the main findings of chapters 4, 5, and 6 were discussed in terms of an integrated view of mortality detection given different spatial scales, mortality

processes, and applied data. We discussed also the potential for new developments on the detection of tropical forest mortality using remote sensing data.

4 LIFE CYCLE OF BAMBOO IN THE SOUTHWESTERN AMAZON AND ITS RELATION TO FIRE EVENTS ⁴

Abstract: Bamboo-dominated forests comprise 1 % of the world's forests and 3 % of the Amazon forests. The *Guadua spp.* bamboos that dominate the southwest Amazon are semelparous, thus flowering and fruiting occur once in a lifetime before death. These events occur in massive spatially organized patches every 28 years and produce huge quantities of necromass. The bamboo-fire hypothesis argues that increased dry fuel after die-off enhances fire probability, creating opportunities that favor bamboo growth. In this study, our aim is to map the bamboo-dominated forests and test the bamboo-fire hypothesis using satellite imagery. Specifically, we developed and validated a method to map the bamboo die-off and its spatial distribution using satellite-derived reflectance time series from the Moderate Resolution Imaging Spectroradiometer (MODIS) and explored the bamboo-fire hypothesis by evaluating the relationship between bamboo die-off and fires detected by the MODIS thermal anomalies product in the southwest Amazon. Our findings show that the near-infrared (NIR) is the most sensitive spectral interval to characterize bamboo growth and cohort age. Automatic detection of historical bamboo die-off achieved an accuracy above 79 %. We mapped and estimated 15.5 million ha of bamboo-dominated forests in the region. The bamboo-fire hypothesis was not supported, because only a small fraction of bamboo areas burned during the analyzed timescale, and, in general, bamboo did not show higher fire probability after the die-off. Nonetheless, fire occurrence was 45 % higher in dead than live bamboo in drought years, associated with ignition sources from land use, suggesting a bamboo-human-fire association. Although our findings show that the observed fire was not sufficient to drive bamboo dominance, the increased fire occurrence in dead bamboo in drought years may contribute to the maintenance of bamboo and potential expansion into adjacent bamboo-free forests. Fire can even bring deadly consequences to these adjacent forests under climate change effects.

⁴ DALAGNOL, R. *et al.* Life cycle of bamboo in the southwestern Amazon and its relation to fire events. **Biogeosciences**, v. 15, n. 20, p. 6087–6104, 18 out. 2018.

4.1 Introduction

Bamboo-dominated forests represent 1 % of global forests. They occur in tropical, subtropical and mild temperate zones and are found mainly in Asia (24 million ha), South America (10 million ha) and Africa (2.8 million ha) (LOBOVIKOV et al., 2007). Their spatial distribution is likely underestimated in South America as a recent study showed that these forests cover at least 16.15 million ha of Amazonian forests over Brazil, Peru and Bolivia (CARVALHO et al., 2013).

Bamboo is a major forest product that plays an important economic and cultural role in the Amazon. It has been used for over a millennium by indigenous people for shelter, food, fuel, hunting, fishing, and musical instruments (LOBOVIKOV et al., 2007; ROCKWELL et al., 2014). The first studies on the distribution of these forests in the Amazon region postulated that they occurred as a consequence of human disturbance or were deliberately planted (SOMBROEK, 1966; BALÉE, 1989). However, recent phytolith analysis revealed that bamboo dominated these forests before human occupation in South America (OLIVIER et al., 2009; WATLING et al., 2017).

In the southwest Amazon, the predominant forest type is non-flooded open-canopy rain forest on *terra firme*, often dominated by *Guadua* bamboos and mostly (93 %) preserved (IBGE, 2006; TRANCOSO et al., 2010). In bamboo-dominated areas, two species of semi-scandent woody bamboos predominate: *Guadua weberbaueri* Pilger and *Guadua sarcocarpa* Londoño and Peterson. Like many other woody bamboo species, these *Guadua* bamboos are semelparous, producing flowers and fruits once in a lifetime before dying (JANZEN, 1976; GRISCOM; ASHTON, 2003). Flowering, fruiting and death can be massive and highly synchronized in space and time. Their diameter at breast height (DBH) ranges from 4 to 24 cm (CASTRO et al., 2013). Height can reach up to 30 m but usually varies from 10 to 20 m (LONDOÑO; PETERSON, 1991). The juvenile bamboos usually reach the sunlit portion of canopy by 10 years of age, when they accelerate in growth (SMITH; NELSON, 2011). They do not form continuous pure stands, being mixed among the trees, yet achieve remarkable high densities ($2,309 \pm 1,149$ ind ha⁻¹) and have significant ecological impacts (Castro et al., 2013). Thus, these forests support up to 40 % less tree species diversity than nearby bamboo-free forests and from 30 to 50 % less carbon stored as a

consequence of the lower woody tree density (SILVEIRA, 2001; ROCKWELL et al., 2014). Bamboo-dominated forests also have elevated tree mortality rates ($3.6 \pm 2.5 \% \text{ yr}^{-1}$) (CASTRO et al., 2013; MEDEIROS et al., 2013) when compared even to the typically fast-turnover forests in western Amazon ($2.62 \% \text{ yr}^{-1}$) (JOHNSON et al., 2016). A total of 74 different bamboo populations, that is, patches having individuals of the same internal age, have been so far identified in the southwest Amazon, with a mean patch area of 330 km^2 , and up to $2,570 \text{ km}^2$ for the largest patch (CARVALHO et al., 2013). The mean lifetime of these bamboos was estimated as 28 years (CARVALHO et al., 2013). However, it can vary from 28-32 years within patches, depending on species composition and/or local environmental factors.

The locally synchronized death of semi-scandent bamboos produces large amounts of necromass in large patches over a short time. Decomposition of dead leaves and branches is rapid, but a layer of culms can remain intact on the forest floor for up to three years (SILVEIRA, 2001). When neighboring populations (patches) of bamboo go through reproductive events one after another in successive years, this is known in the literature as a flowering wave. This process generates mosaics of patches with different ages within the landscape. The current hypotheses to explain this phenomenon include climatic variations; severe environmental pressures such as floods and fire (FRANKLIN et al., 2010; SMITH; NELSON, 2011); and incipient allochronic speciation - stochastically forming small and rare temporally offset daughter patches at the margin of an expanding parent population.

Two main hypotheses, which are not competing but complementary, have been proposed to explain the dominance of semi-scandent bamboos in Amazon forests. Firstly, they cause elevated physical damage to trees by loading and crushing, while also suppressing recruitment of late succession tree species (GRISCOM; ASHTON, 2003). Secondly, they increase fire probability via their mast seeding behavior followed by the synchronized death of the adult cohort, which produces large fuel loads. The fire would then eliminate canopy trees, form gaps and inhibit tree recruitment, while creating an optimal environment for the bamboo seedling cohort. This latter hypothesis is called the bamboo-fire hypothesis (KEELEY; BOND, 1999). This hypothesis is attractive as it explains

how bamboos can regain dominance of the forest after relinquishing space to trees when the adults die. Analysis of charcoal in soils of three Amazon bamboo-dominated forests sites showed a long history of fire occurrence (MCMICHAEL et al., 2013). Smith and Nelson (2011) showed that fire disturbance favored the expansion of bamboos in the Amazon. Another study indicated that pre-Columbian people used fire and bamboo die-off patches to facilitate forest clearing and construct geoglyphs, which, nowadays, can be found under the closed-canopy forest (MCMICHAEL et al., 2014). Although these studies do not support fire as the main driver of bamboo distribution (bamboo-fire hypothesis), they show associations between the bamboo die-off and increased fire occurrence, and potential human interactions on these processes.

Bamboo-dominated *terra firme* forests in the southwest Amazon can be detected by the optical bands of orbital sensors at the adult stage, while the borders of each internally synchronized population can be detected after die-off events (NELSON, 1994). Carvalho et al. (2013) showed that the NIR spectral band of the Thematic Mapper (TM)/Landsat-5 allowed the best discrimination between bamboo-free forest, forest with adult bamboo and forest with recently dead bamboo. Forests with adult bamboos showed higher reflectance in the NIR than bamboo-free or with recently dead bamboo. Forests in which the newly sprouted cohort of seedlings is confined to the understory were not visually distinguishable from bamboo-free forest. The juvenile bamboo stays hidden in the understory up to 10 years of age, which is the moment they start reaching the canopy (SMITH; NELSON, 2011; CARVALHO et al., 2013). When analyzing Enhanced Vegetation Index (EVI) data from the Moderate Resolution Imaging Spectroradiometer (MODIS), processed by the Multi-Angle Implementation of Atmospheric Correction (MAIAC) algorithm (LYAPUSTIN et al., 2012), Wagner et al. (2017) detected some patches of adult bamboo during a climate driver study of Amazon forest greening. The bamboo patches presented two peaks of MODIS EVI per year (dry and wet seasons) compared to one peak observed in the wet season over bamboo-free forest.

Because the previous investigations used visual interpretation of satellite data and performed manual delineation of the bamboo areas (CARVALHO et al., 2013), they were limited to the identification of large areas and constrained by

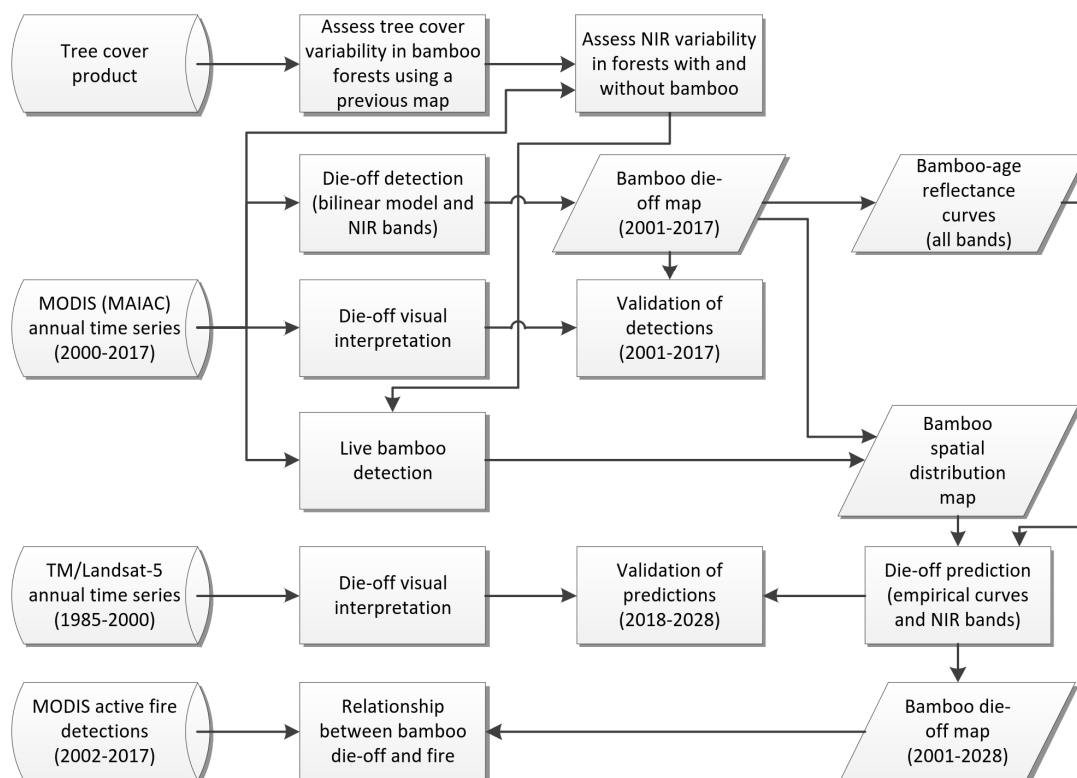
the analyst's visual acuity. Further studies are therefore necessary to understand the bamboo life cycle, its spectral characteristics, as well as, to establish automatic approaches for detecting die-off events in bamboo-dominated areas. These approaches can enable analyses of ecological processes associated with these events, such as the interactions between bamboo and fire (KEELEY; BOND, 1999), bamboo flowering wave patterns (FRANKLIN et al., 2010) and the distribution of 'bamboo-specialist' bird species (KRATTER, 1997).

In this study, our aim is to map the bamboo-dominated forests and test the bamboo-fire hypothesis. Specifically, we (i) described the tree cover and MODIS NIR reflectance variation in areas with and without bamboo; (ii) assessed a method to map the die-off, spatial distribution and age structure of bamboo-dominated areas; and (iii) investigated the relationship of bamboo with fire occurrence in the southwest Amazon. We also aimed to provide near-term, spatially resolved predictions of future bamboo behavior to allow our method to be further tested, validated, and improved over the coming years.

4.2 Material and Methods

An overview of the analyses conducted in the study was presented in Figure 4.1 and then described in detail in the subsequent sections.

Figure 4.1 – Methodology used in the data analysis.

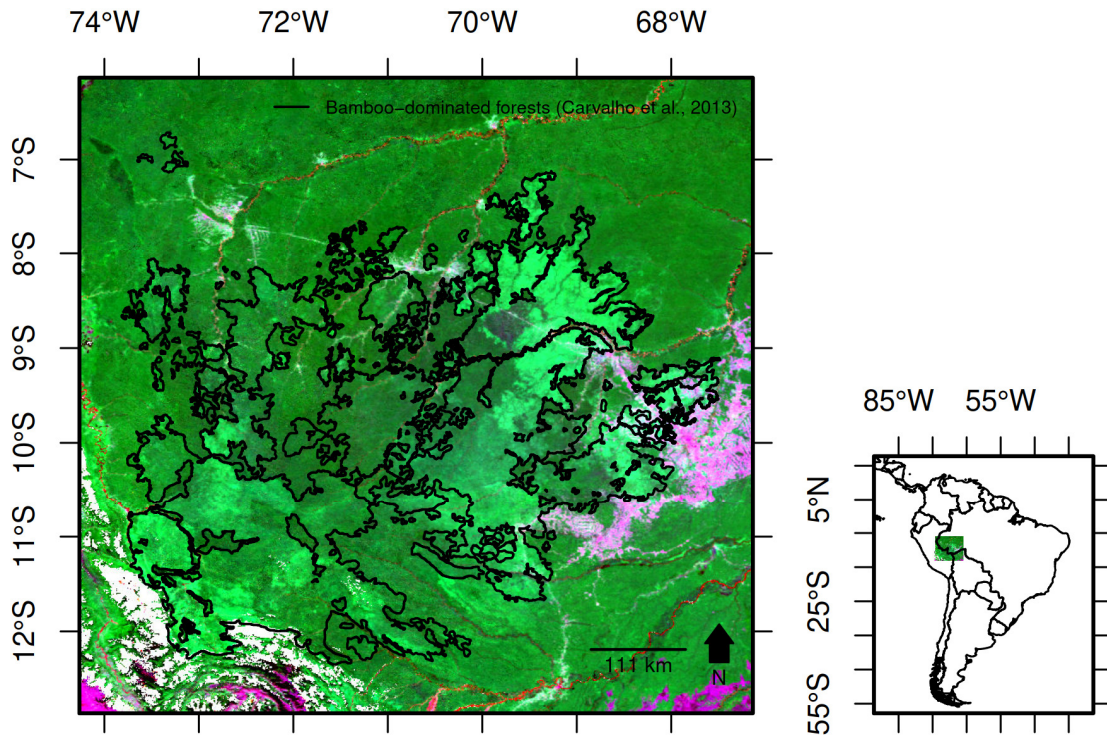


Source: Produced by the author.

4.2.1 Study area

The study area is located in the southwest Amazon between the longitudes 74° W and 67° W and latitudes 13° S and 6° S, covering parts of Brazil, Peru and Bolivia (Fig. 4.2). The predominant forest type is non-flooding open-canopy rain forest on *terra firme*, often dominated by bamboos of *Guadua* genera and mostly (93 %) preserved from human disturbances (IBGE, 2006; TRANCOSO et al., 2010).

Figure 4.2 - Bamboo-dominated forests in southwestern Amazon. The image at background is a false-color composite from MODIS (MAIAC) images of bands 1 (Red), 2 (NIR) and 6 (shortwave infrared), in RGB, respectively, in August 2015. The black lines indicate the perimeter of the bamboo-dominated areas delineated in a previous study (CARVALHO et al., 2013).



Source: Produced by the author.

The most important soil types are chromic alisol, red-yellow argisol, haplic cambisol, ferrocyclic podsol, haplic gleysol, red-yellow latosol, chromic luvisol, and haplic plinthosol (DOS SANTOS et al., 2011). In bamboo-dominated areas, the soils have a tendency to be more fertile, richer in exchangeable cations, more easily eroded, more poorly drained, and more clay-rich than the soils where bamboo is excluded (CARVALHO et al., 2013). Naturally high erosion leads to a gently rolling hilly landscape (MCMICHAEL et al., 2014) with muddy streams and rivers. Based on a 19-year time-series of the Tropical Rainfall Measuring Mission (TRMM) satellite, annual rainfall ranges from 1800 mm to 3400 mm, with zero to five dry months (i.e., less than 100 mm mo⁻¹). The average temperature is 27 °C. Minimum rainfall and temperature occur in July (DALAGNOL et al., 2017).

4.2.2 Satellite data and products

4.2.2.1 MODIS (MAIAC) surface reflectance data

A time series of MODIS (MAIAC) data was pre-processed in order to map the bamboo ages and die-off - further described in the die-off detection section. Daily surface reflectance data were obtained from the MODIS product MCD19A1-C6, acquired from Terra and Aqua satellites, from 2000 to 2017 (LYAPUSTIN; WANG, 2018), corrected for atmospheric effects by the MAIAC algorithm (LYAPUSTIN et al., 2012). The data were obtained from the NASA Center for Climate Simulation (NCCS) repository (available at: <ftp://dataportal.nccs.nasa.gov/DataRelease/>). We used MAIAC surface reflectance and BRDF products at spatial resolution of 1 km, daily temporal resolution, in eight spectral bands: Red, 620-670 nm (B1); NIR-1, 841-876 nm (B2); Blue-1, 459-479 nm (B3); Green, 545-565 nm (B4); NIR-2, 1230-1250 nm (B5); Shortwave infrared-1 (SWIR-1), 1628-1652 nm (B6); SWIR-2, 2105-2155 nm (B7); and Blue-2, 405-420 nm (B8).

In order to minimize the differences in sun-sensor geometry between the MODIS scenes, which could affect our time series analysis, the daily surface reflectance was normalized to a fixed nadir-view and a 45° solar zenith angle using a Bidirectional Reflectance Distribution Function (BRDF) and the Ross-Thick Li-Sparse (RTLS) model (LUCHT; LEWIS, 2000). Parameters of the RTLS model and BRDF kernel weights are part of the MAIAC product suite with temporal resolution of 8 days - a period when daily observations of different view angles were integrated and used for BRDF parameters retrieval. Hence, the normalized surface reflectance, called Bidirectional Reflectance Factor (BRF_n), was calculated using the Eq. 4.1 and RTLS volumetric (f_{vol}) and geometric (f_{geo}) parameters, and BRDF isotropic (k_{iso}), volumetric (k_{vol}) and geometric-optical (k_{geo}) kernel weights (LYAPUSTIN et al., 2012).

$$BRF_n = BRF * \frac{k_{iso} - 0.04578 * k_{vol} - 1.10003 * k_{geo}}{k_{iso} + f_{vol} * k_{vol} + f_{geo} * k_{geo}} \quad (4.1)$$

The BRF_n data were aggregated into 16-day composite intervals by calculating the median on a per-pixel basis. The composites were then merged and

converted to geographic projection (datum WGS-84). All these procedures were implemented in R language (R CORE TEAM, 2016).

Annual composites of MODIS NIR surface reflectance data were selected for the die-off detection. The images were selected between July and September to minimize cloud coverage. Furthermore, during these months, the bamboo patches at the adult stage present a well-defined phenological response (peak in MODIS EVI), which is not present in primary forests without bamboo dominance (WAGNER et al., 2017). When useful data were not available in the time series due to cloud cover or low-quality pixel retrievals, an imputation method was applied to fill the gaps using the whole time series. As the bamboo-dominated forests present a seasonal spectral response, the imputation was conducted by the Seasonal and Trend decomposition using Loess (STL) method (CLEVELAND et al., 1990). This method decomposes the signal into trend, seasonal and irregular components, interpolates the missing values, and then reverts the time series. It is effective when dealing with missing values in seasonal signals when compared to other imputation methods (STEFFEN, 2015).

4.2.2.2 TM/Landsat-5 surface reflectance product

A time series of Thematic Mapper (TM)/Landsat-5 data was obtained from 1985 to 2000 (one image per year), in order to visually detect bamboo die-off events and create a validation dataset for die-off predictions using MODIS (MAIAC) between 2018 to 2028 - further described in the die-off prediction section. We selected atmospherically corrected surface reflectance images (Landsat collection 1 Level-1) (available at: <https://earthexplorer.usgs.gov/>) from the quarter July-August-September to increase the chances of obtaining cloud-free data and reduce spectral variations associated with vegetation seasonality. The path-row (World Reference System 2) of the time series were: 006-065, 003-066, 002-067, 003-067, 005-067, and 003-068. The acquisition dates for each path-row are shown in the Table A.1.

4.2.2.3 Tree cover product

In order to mask areas that were not covered by intact forests (deforested, degraded, and secondary forests, pastures and swidden fields) and to analyze the tree cover variability of the bamboo-dominated forests, we used the global forest cover loss 2000-2016 dataset (Available at: https://earthenginepartners.appspot.com/science-2013-global-forest/download_v1.4.html). The dataset is based on Landsat time series data at 30 m spatial resolution (HANSEN et al., 2013), and consists of tree cover percentage, gain, and loss during 2000-2016, and a mask indicating permanent water bodies. It was re-sampled to 1 km spatial resolution using the average interpolation in order to match the resolution of the MODIS (MAIAC) data. A mask of intact forests was created using the tree cover data to select pixels: (i) without permanent water bodies, (ii) without gain or loss of tree cover during the 2000-2016 period; and (iii) above a threshold of 95 % tree cover to detect and filter out non-forested pixels. Furthermore, in order to filter the active fire data for the bamboo-fire analysis, yearly non-forest fraction masks were created considering the cumulative forest loss of each year from 2000-2016.

The tree cover product was analyzed considering the pre-existent bamboo-dominated forest map from Carvalho et al. (2013) in order to explore the variability of tree cover in forests with and without bamboo, which might help mapping the bamboo-dominated forests. We expect that bamboo-dominated forests present lower tree cover values than bamboo-free forests due to its fast dynamics and higher mortality (CASTRO et al., 2013; MEDEIROS et al., 2013). The map from Carvalho et al. (2013) was obtained by visual interpretation of live-adult bamboo using two Landsat mosaics 10 years apart from each other (1990 and 2000), supported by the known locations and dates of five bamboo dominated areas. Considering only the pixels inside the bamboo-dominated forests map, we calculated the 1st, 50th and 99th percentiles of the tree cover product and generated a map showing the areas below the 1st, between the 1st and 99th, and above the 99th percentiles of tree cover. The map was qualitatively analyzed exploring the areas covered by each of the percentile classes.

The tree-cover percentile map was also used to assess the variability of NIR reflectance in forests with and without bamboo in order to test if their NIR signals

were different and contributed to the bamboo-dominated forests mapping. We tested only the NIR because of the expected great separability between areas with and without bamboo resultant from the higher NIR signal in bamboo-dominated areas (CARVALHO et al., 2013). We analyzed the MODIS NIR-1 reflectance considering all pixels over time in each tree cover classes: below 1st, between 1st and 99th, and above the 99th percentile. The NIR value distributions were tested for normality using a two-sided Kolmogorov-Smirnov test at a 1 % significance level. For normal distribution, the average and standard deviation were computed. For skewed distribution, a more appropriate method was applied to estimate the average, standard deviation and skewness parameter (x_i) (FERNANDEZ; STEEL, 1998).

4.2.2.4 MODIS active fire detections product

To test the bamboo-fire hypothesis, a fire occurrence dataset was obtained from MODIS/Aqua satellite active fire data at 1 km spatial resolution from the Brazilian Institute of Space Research (INPE) Burn Database (Available at: <http://www.inpe.br/queimadas/bdqueimadas/>) for the period of 2002-2017 over the study area. This dataset corresponds to geolocations of active burning areas in the moment of satellite overpass.

4.2.3 Bamboo life cycle spectral characteristics

4.2.3.1 Die-off detection and validation

To automatically detect the bamboo die-off from 2001 to 2017, we compared each pixel's MODIS (MAIAC) NIR reflectance time series to a bilinear model using Pearson's correlation and an iterative shift approach. The model consisted in a linear increase in reflectance from 1 to 28 % between 1 and 28 years of bamboo age followed by an abrupt decrease to 0 % when the die-off occur. The model conception was based on Carvalho et al. (2013), who showed that forests with adult bamboo had higher NIR reflectance than forests with juvenile and recently dead bamboo, or without bamboo. They also showed that bamboo presented a life cycle of approximately 28 years. Thus, since not much was known about the spectral behavior of bamboo growth with age, we chose a bilinear model to

characterize the bamboo signal change over time because it was the simplest way to represent the change between life stages. We also assumed the signal coming from the trees as constant over time. Therefore, inter-annual reflectance variations were attributed to structural changes in the canopy related to bamboos. The Pearson's correlation coefficient (r) between the NIR reflectance time series and the bilinear model for a given pixel was iteratively tested by shifting the position of the NIR time series inside the bilinear model vector. The position showing the highest r corresponded to the estimated age of that pixel from which the die-off year was retrieved. Only pixels with very significant correlations ($p < 0.001$) were selected. The model was tested with both MODIS (MAIAC) NIR bands: NIR-1 band 2 (841-876 nm) and NIR-2 band 5 (1230-1250 nm). Both bands are sensitive to canopy structure scattering, but NIR-2 is also partially sensitive to leaf/canopy water scattering (GAO, 1996), so that could lead to a different detection between bands.

For validation purposes, we compared the detected die-off events with recently dead bamboo areas visually identified in MODIS false color composites (bands 1, 2 and 6 in RGB). In this color composite (Figure 4.2), adult bamboo patches show bright green color due to the comparatively higher NIR reflectance, while dead bamboo patches present dark blue/gray color. The visual inspection of bamboo die-off using MODIS and Landsat data was consistent with five bamboo mass flowering events observed in the field (CARVALHO et al., 2013). In each of the dead bamboo patches visually detected, the geographic location and die-off year were registered for a sample of 5 random pixels. A total of 78 dead bamboo patches were identified in the 2001-2017 period. Thus, the validation dataset was composed of 390 pixels with corresponding year of bamboo death - the spatial and temporal distribution of the samples were shown in Figure S4.1 and A.2. For these pixels, the die-off year detected by our model was retrieved and compared to the validation dataset. To assess the detection, we calculated the accuracy (%) on detecting the exact die-off year, Pearson's correlation and p -value, and the root mean square error (RMSE) between the automatically detected and visually interpreted die-off year.

4.2.3.2 Spatial distribution detection

To map the spatial distribution of bamboo-dominated forests for the whole area, we first mapped the live bamboo and then combined it with the die-off detection map (2001-2017). We used two assumptions to map the live bamboo. Over the 18 years' period, a live bamboo-dominated pixel should present: (i) mean NIR reflectance equal to or greater than the median signal of bamboo-free forests; and (ii) an increasing NIR reflectance over time. The median bamboo-free forest signal was derived using the tree cover mask and a threshold that excluded all the potential bamboo-dominated pixels. The threshold was defined as the tree cover percentage above the 99th percentile from bamboo-dominated forests as delineated by Carvalho et al. (2013). We tested whether the mean NIR reflectance of each pixel was statistically lower than the forest median signal using the Student's t-test, and excluded those pixels. Furthermore, we obtained a linear regression model between the reflectance of each pixel in the time series and a linear increasing vector to identify reflectance increase over time in the bamboo areas. We selected only pixels that showed a very significant ($p < 0.001$) and positive regression slope, indicating the reflectance increase in the NIR. To assess the overall consistency of the map, we compared it with the available bamboo-dominated forests distribution map from Carvalho et al. (2013).

4.2.3.3 Bamboo cohort age and spectral variability

We used the die-off map to retrieve spectral data corresponding to each bamboo age in order to assess the spectral variability during the bamboo life cycle, that is, when the signal changes and why, and to corroborate the assumptions made in the bilinear model. Data from all MODIS bands were extracted using the estimated die-off year with very significant correlation ($p < 0.001$) as a starting point. Bamboo cohort age was then calculated backwards and forwards in time during the 2000-2017 period. Reflectance percentiles (1st, 50th and 99th) per age were calculated to obtain the entitled empirical bamboo-age reflectance profiles.

The spectral variability with cohort age was also analyzed in relation to the bamboo-free signal in order to assess the separability of forests with and without

bamboo. Pearson's correlation between the median bamboo-free signal, as obtained in a previous section, and bamboo-dominated forest pixel's signal were calculated and assessed as a function of cohort age. The assessment was conducted using the NIR-1 and NIR-2 bands.

4.2.3.4 Die-off prediction

To assess the age structure of bamboo patches during the whole life cycle, we explored the prediction of die-off events for the bamboo that did not die-off during 2001-2017. This was conducted using the NIR-1 and NIR-2 empirical bamboo-age empirical reflectance profiles as a reference instead of the bilinear model. Since the NIR time series would not present the abrupt change associated with the die-off, the empirical reflectance profiles should reflect the spectral changes over time with bamboo growth. The prediction followed the same procedures of the detection on assessing the point of maximum correlation between the NIR reflectance time series, but, now, comparing to the empirical bamboo-age reflectance profiles and predicting the die-off for a whole life cycle during 2001-2028.

Since the validation for 2018-2028 predictions could not be conducted using MODIS (Terra and Aqua) data because its time series do not span that time period, we used yearly TM/Landsat-5 color composites (bands 2, 4 and 1 in RGB) during the 1985-2000 period to visually detect the bamboo die-off events that occurred in the last bamboo life cycle and validate the predictions. We assumed that the die-off events that happened in this period would happen again in the next life cycle of the bamboo, from 2018 to 2028. Therefore, we added 29 years to the visually detected die-off year in order to match the next life cycle. The sampling procedure for the validation dataset was similar to the detection, where 5 pixels were randomly collected for each recently dead bamboo patch visually identified in a given year. A total of 35 dead bamboo patches were identified and 175 pixels were collected with the corresponding years of death. The assessment was conducted by calculating the same metrics as in the die-off detection section. Additionally, in order to assess if the prediction error was randomly distributed, the residuals from predicted minus observed die-off year, where observed is the

die-off from the Landsat validation dataset, was tested for normality using a two-sided Kolmogorov-Smirnov test at a 1 % significance level.

Since not much was known about the size of bamboo patches, we analyzed the patch size distribution from the prediction map considering grouped pixels with the same die-off year as patches. These grouped pixels with same die-off year were segmented into patches and the patch size distribution was assessed by quantifying the number, minimum, maximum, mean and median size of bamboo patches. In order to filter out noise in the predictions (i.e. loose pixels), the minimum patch size was set to 10 km².

4.2.4 Relationship between bamboo die-off events and MODIS active fire detections

Active fire detections from MODIS/Aqua during 2002-2017 were filtered using yearly non-forest fraction masks. This ensured that active fires occurring over deforested and degraded forests, pastures or swidden areas were removed, and only pixels over forested areas remained in each year. To visualize where the fire occurred, the active fires were plotted over the bamboo spatial distribution map. The number of fires occurring over live bamboo and dead bamboo (died-off during 2001-2017) was calculated.

To test whether there was a higher fire occurrence over recently dead bamboo than live bamboo, the active fire detections were analyzed as a function of dead (28, 0 and 1 years) and live bamboo (2 to 27 years) classes. For this purpose, each active fire detection was labeled accordingly to the bamboo age of the pixel where it occurred from the prediction map and then merged into the two classes. We controlled for three factors that could affect fire probability: area of bamboo mortality, climate, and proximity to ignition sources. Since the total area of a specific age class could interfere with fire frequency, that is, more area would mean higher probability of fire occurrence, we normalized the fire frequency by the area (ha) of its respective age class within the buffer with most fire occurrences, in the year of fire occurrence. Severe droughts affected the Amazon in 2005, 2010 and 2015/2016, and especially the southwest in 2005 (ARAGÃO et al., 2007; PHILLIPS et al., 2009; LEWIS et al., 2011; ARAGÃO et al., 2018).

As drought years can enhance fire occurrence in the Amazon (BRANDO et al., 2014; ARAGÃO et al., 2018), we analyzed separately the fire frequency in regular and drought years. To assess the influence of ignition sources on the fire occurrence, we filtered active fire detections using buffers of 1, 2 and 3 km around the non-forested areas using the yearly non-forest fraction mask and assessed the number of active fire detections considering each buffer.

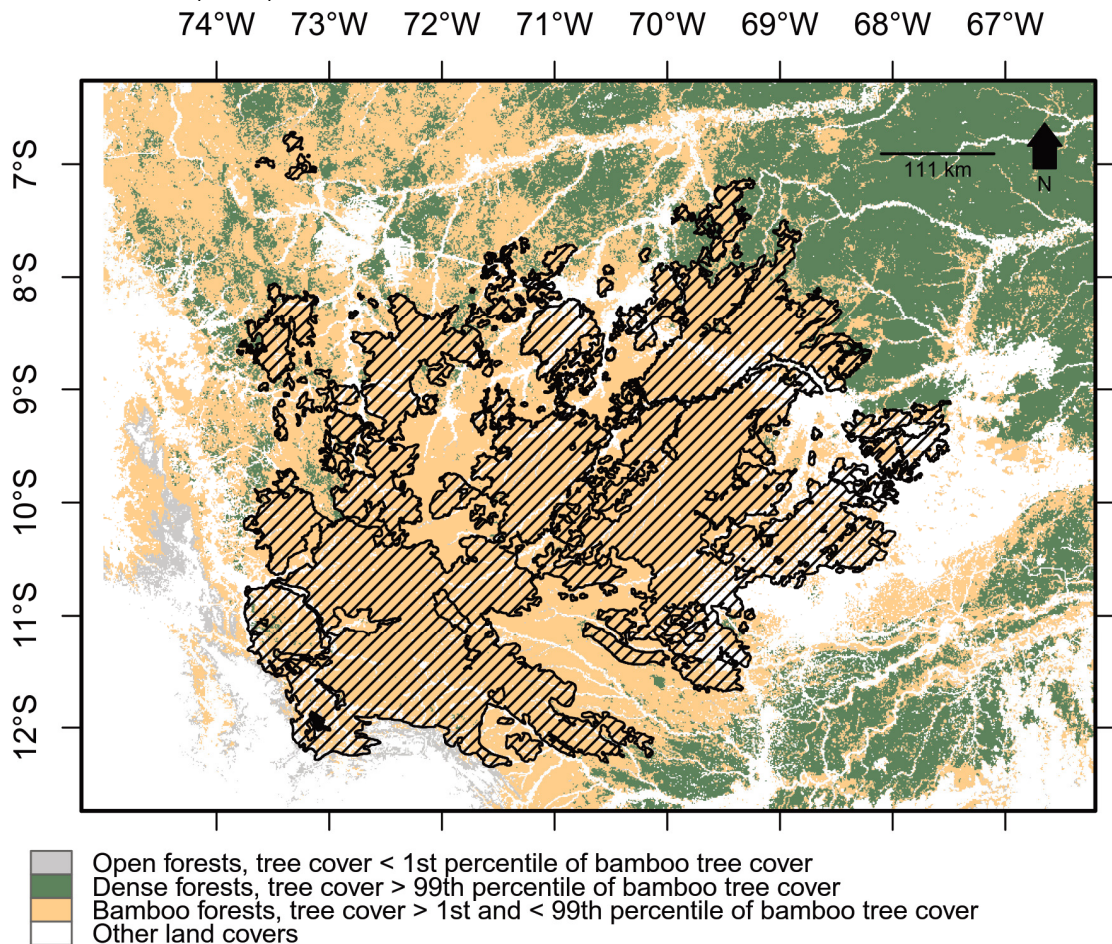
The area-normalized fire frequency over dead and live bamboo was compared using a two-way Analysis of Variance (ANOVA) to test whether there were more fire in dead than live bamboo. We tested the effects of bamboo life stage (live or dead), year of fire occurrence and their interactions over active fire detections.

4.3 Results

4.3.1 Tree cover analysis

Bamboo-dominated forest, as mapped by Carvalho et al. (2013), spanned a very narrow range of values in the Landsat-derived percent of tree cover product. The 1st and 99th percentiles of tree cover in the bamboo areas were 96.95 % and 99.88 %, respectively, while the median was 99.18 % (Figure 4.3). Forests identified as bamboo-free by Carvalho et al. (2013) had tree cover above the 99th percentile at the northeast of the study area, but below the 1st percentile at the southwest of the study area. At the northwest, bamboo-free forests presented tree cover similar to that of bamboo-dominated, i.e., between the 1st and 99th percentile.

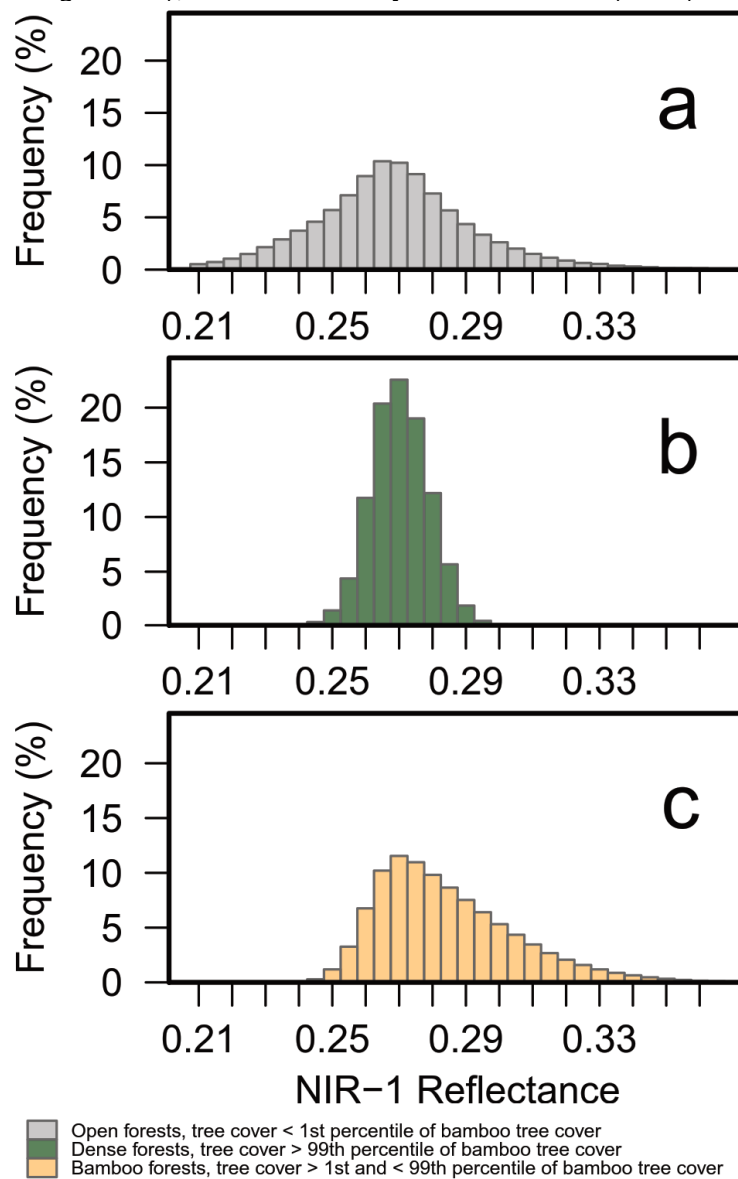
Figure 4.3 - Spatial distribution of stable tree cover percentage percentiles (filtered for tree cover gain and loss, and for water bodies), indicating pixels below, above and within the 1st to 99th percentile range of tree cover found in bamboo-dominated forest (hatched), as delineated by Carvalho et al. (2013).



Source: Produced by the author.

The MODIS NIR-1 reflectance values over the 2000-2017 period in bamboo-free forests that had tree cover above the 99th percentile of bamboo-dominated areas (Figure 4.4B) did not significantly differ from normal distribution ($p = 0.33$). The bamboo-free forests showed the lowest standard deviation (mean = 27.3 % reflectance; SD = 0.9 %) when compared to the bamboo-dominated forests (Figure 4.4C). Bamboo-free forests that had tree cover below the 1st percentile of bamboo-dominated areas (Figure 4.4A) presented a left-skewed distribution with similar reflectance to the 99th percentile but with higher SD (mean = 27.2 %, SD = 2.6 %, and $\xi = 1.2$). Bamboo-dominated forests (Figure 4.4C, pixels inside the hatched polygon in Figure 4.3) presented a right-skewed distribution with higher NIR-1 reflectance (mean = 28.7 %, SD = 2.1 % and $\xi = 1.9$) than the bamboo-free forests.

Figure 4.4 - Relative frequency of MODIS NIR-1 reflectance (band 2) from pixels with tree cover percentage (A) below, (B) above and (C) within the 1st to 99th percentile range of tree cover found in bamboo-dominated forest (hatched in Figure 4.3), as delineated by Carvalho et al. (2013).



Source: Produced by the author.

4.3.2 Bamboo life cycle spectral characteristics

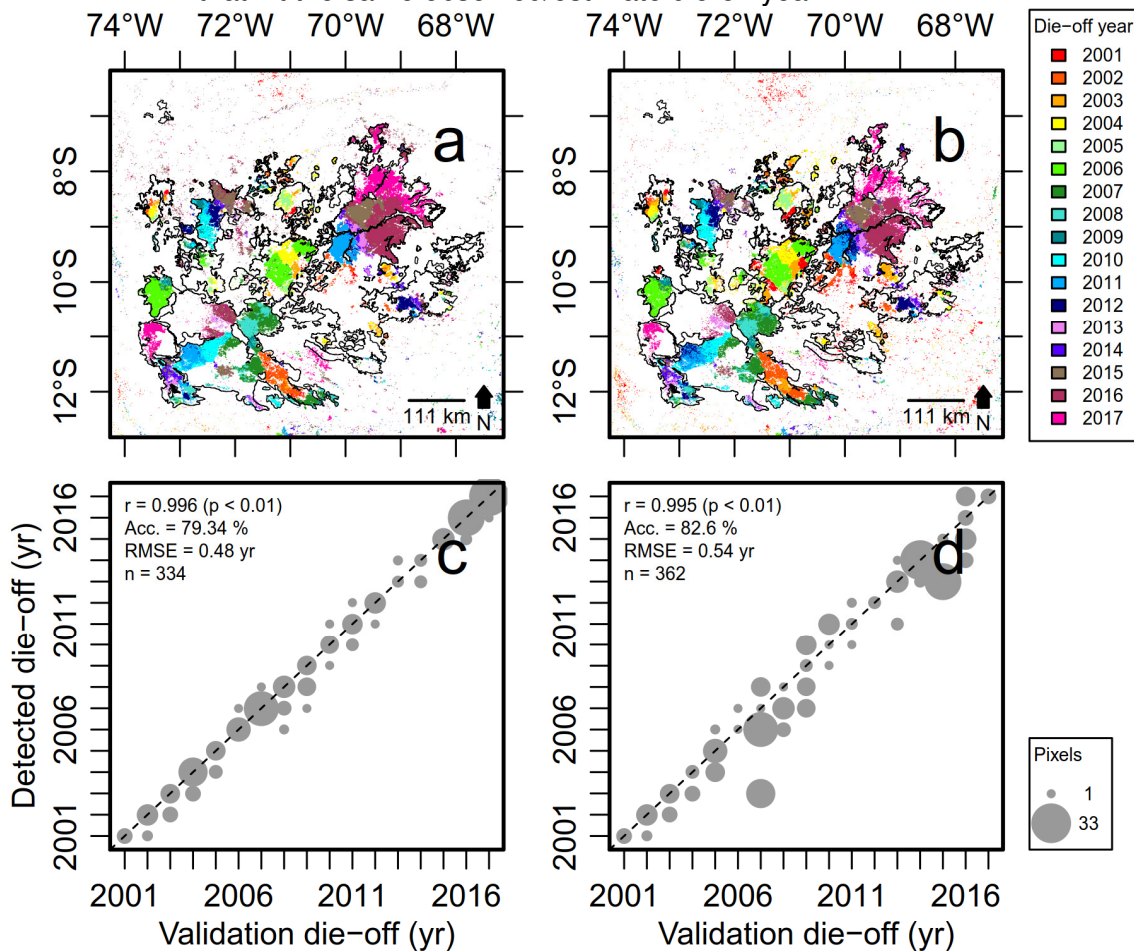
4.3.2.1 Die-off detection

When we applied our automatic die-off approach over the canopy-scattering (NIR-1; band 2) and canopy-water (NIR-2; band 5) sensitive MODIS NIR bands, differences in detected bamboo areas were observed (81480 km² for NIR-1 and 86628 km² for NIR-2). Despite these differences, the resultant die-off year maps

were consistent to each other (Figs. 4.5A and 4.5B) with 81 % of the detected die-off events located inside the bamboo-dominated area reported by Carvalho et al. (2013). The die-off patches that were detected over a 18-year period inside the previous bamboo-dominated forest map represented 40.7 % and 42.7 % of the total bamboo area using MODIS NIR-1 and NIR-2, respectively. In Figure 4.5A and 4.5B, 83.6 % of the dead bamboo pixels mapped using the two NIR bands showed the same year of death between the maps. When comparing the areas detected solely by one of the two bands, NIR-1 detected more pixels toward the end of the time period, i.e. die-off areas from 2017 in the north-east between 8-9° S and 69-70° W. NIR-2 detected additional pixels in the beginning of the time period, i.e. die-off areas from 2001 in the central region between 9-10° S and 70-71° W. Interestingly, some small patches between 8-9° S and 73-74° W presented a unidirectional wave of mortality from north to south with a delay of one year between adjacent patches.

The correlation coefficients found in all the mapped pixels with significant relationship with our bilinear model ($p < 0.001$) were strong ($r > 0.7$). More than 50 % presented even stronger correlations ($r > 0.8$), and 15 % of pixels presented very strong correlation ($r > 0.9$). When the automatic die-off estimates were validated with the visually inspected die-off from 2001-2017, the accuracy from NIR-2 was slightly higher (82.6 %) than that from NIR-1 (79.3 %) (Figs. 4.5C and 4.5D). Both bands showed similarly strong Pearson's correlation ($r > 0.99$, $p < 0.01$), whilst NIR-1 showed slightly lower RMSE (0.48 years) than that from NIR-2 (0.54 years). From the 390 pixels in the validation dataset, 334 and 362 pixels were detected as bamboo die-off by the bilinear model ($p < 0.001$) using the NIR-1 and NIR-2, respectively. The missing 56 (14.4 %) and 28 (7.2 %) pixels were considered as omission errors for NIR-1 and NIR-2. When we combined the two maps into a single die-off detection map (Figure A.3), a total of 374 pixels from the validation dataset were successfully detected, resulting in only 16 (4.1 %) missing pixels not detected as bamboo die-off, while accuracy and RMSE were 80 % and 0.51 yr, respectively.

Figure 4.5 - MODIS bamboo die-off detection map from 2001 to 2017 using the bilinear model of expected near-infrared (NIR) reflectance variations as a function of bamboo cohort age, for (A) NIR-1 and (B) NIR-2. Validation between detected die-off and visual interpreted die-off on MODIS false-color composites (2000-2017) for (C) NIR-1 and (D) NIR-2. The dashed line represents the 1:1 line. Size of circles is related to the number of pixels that hit the same observed/estimate die-off year.



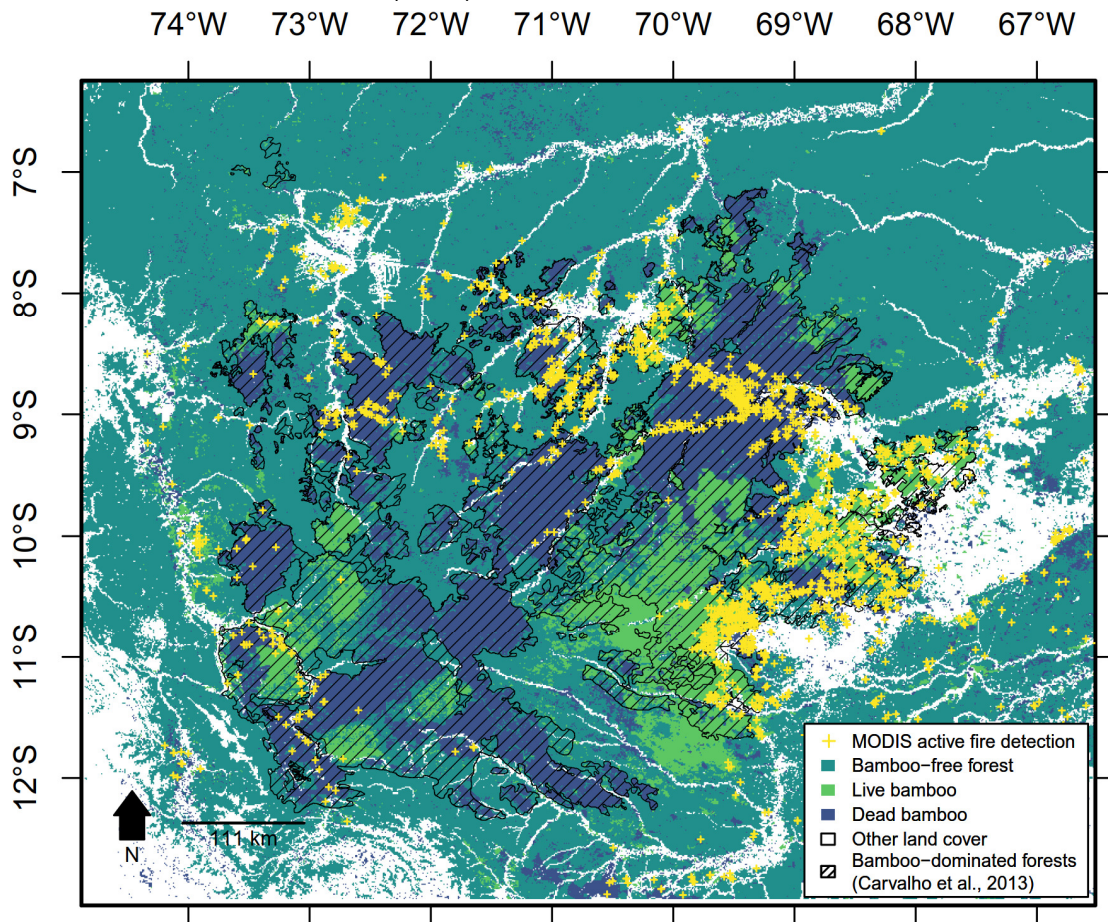
Source: Produced by the author.

4.3.2.2 Spatial distribution of bamboo-dominated forests

The bamboo-dominated forests were mapped by combining the die-off detection during 2001-2017 (Figure A.3) with the live bamboo detection (Figure 4.6). The die-off detection was based on both MODIS NIR-1 and NIR-2, which presented high accuracies, mapping slightly different bamboo patches in Figure 4.5. The live bamboo detection was based only on NIR-1, which did not saturate with bamboo growth over time in Figure 4.7. A total of 155,159 km² of bamboo-dominated forest was detected in the area. Of these, 112,570 km² or 72.5 % were located inside the bamboo forest mapped by Carvalho et al. (2013). A total of

68.8 % of the bamboo forest area from Carvalho et al. (2013) was covered by the detection. A few large patches were found outside of the previously mapped bamboo spatial distribution, such as in 11.5° S; 70° W, and 13° S; 71° W.

Figure 4.6 - Bamboo-dominated forest map and MODIS active fire detections during 2002-2017 (yellow crosses). Blue pixels are bamboo die-off patches detected during 2001-2017 using the bilinear model. Light green pixels are bamboo that did not die-off, but showed increasing NIR signal during 2001-2017, and presented greater NIR mean than forest. Dark green pixels are bamboo-free forests. White pixels are other land cover classes. The hatched polygon is the bamboo-dominated forests delineated by Carvalho et al. (2013).



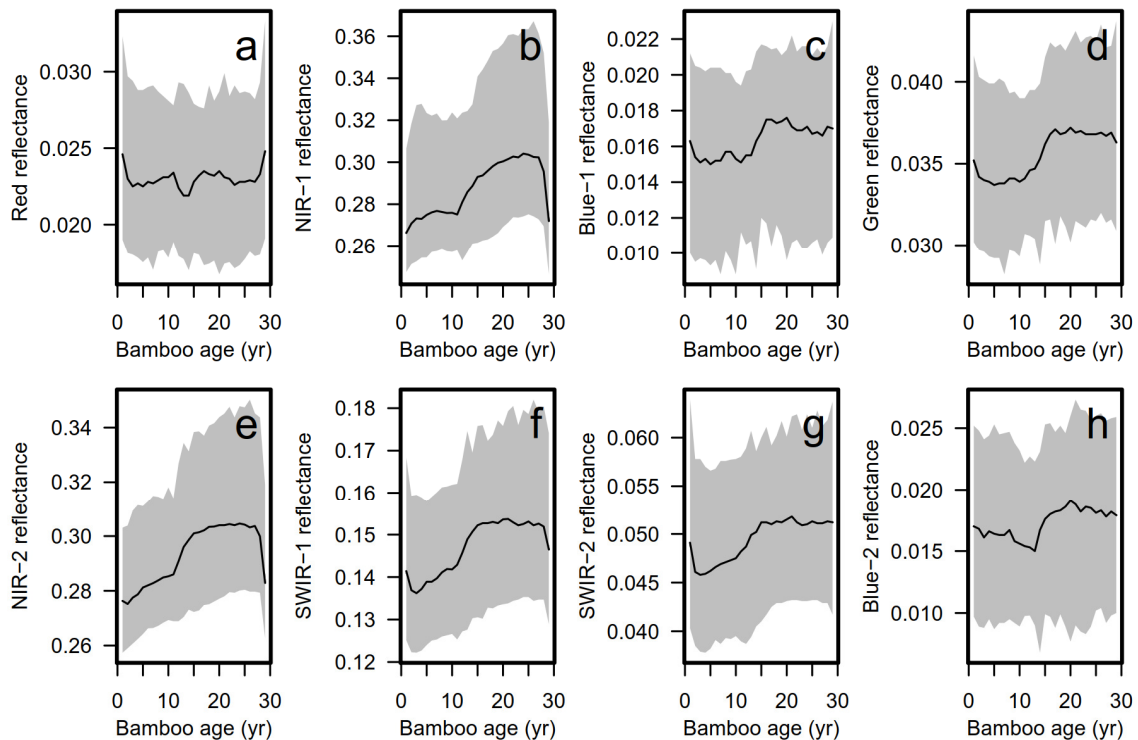
Source: Produced by the author.

4.3.2.3 Bamboo cohort age and spectral variability

The reflectance of the MODIS NIR-2 and the two SWIR bands slowly increased with bamboo development up to about 12 years of age, and then increased very steeply from 12-14 years (Figure 4.7). NIR-1 did not show the same reflectance increase up to 12 years as NIR-2, but also showed the steep increase in

reflectance between 12-14 years. A pronounced but temporary dip in Red and Blue-2 reflectance occurred concurrently with this brief and rapid NIR and SWIR increase. Green reflectance increased up to about 17 years then leveled off. The response of two SWIR bands and the NIR-2 band all leveled off after 15 years. The NIR-1, however, showed increasing reflectance over the cohort remaining life span, until the age of synchronous die-off. The bamboo die-off was marked by a sharp decrease in MODIS NIR-1 and NIR-2 reflectance between 28 and 29 years of age (Figure 4.7). A reflectance change with bamboo death was not well defined in the SWIR-1 and SWIR-2 bands. The reflectance of all bands presented high dispersion with coefficients of variation ranging from 5.9 to 20.3 %.

Figure 4.7 - Empirical bamboo-age reflectance profiles at ages 0-28 years from MODIS bands 1 to 8 (A)-(H). Black lines represent the median, while the shaded gray areas represent the 1st and 99th percentile.

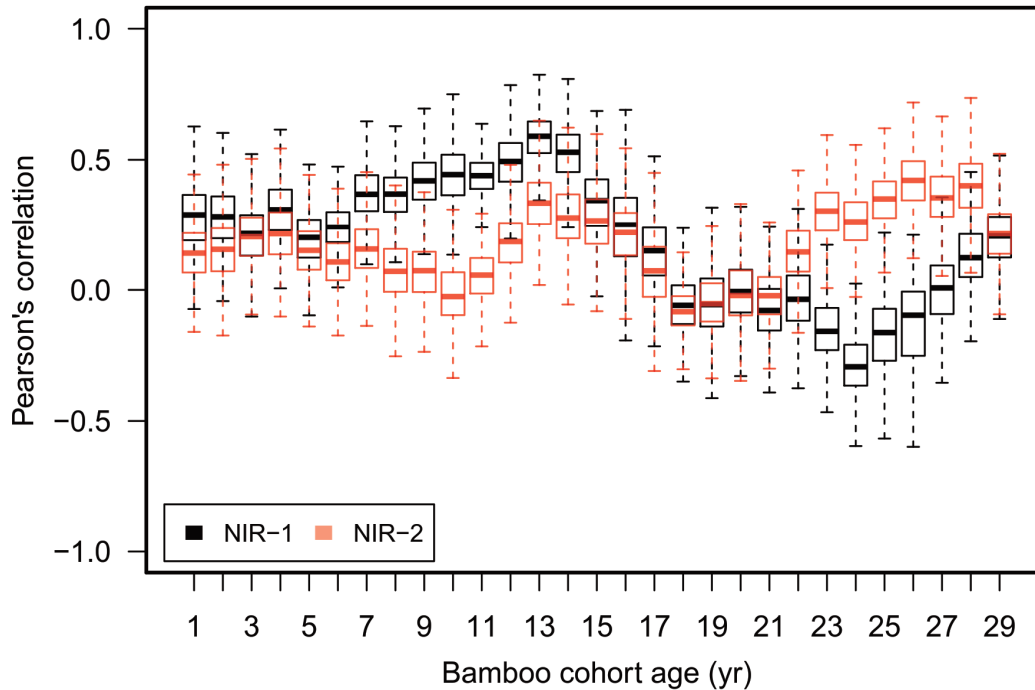


Source: Produced by the author.

The mean Pearson's correlation between the median bamboo-free forest and bamboo-dominated forests NIR-1 reflectance decreased from 0.41 to -0.02 in the transition from juvenile (1-14 years) to adult bamboo stage (15-28 years) (Figure 4.8, black boxes). The correlation in the partially water-sensitive NIR-2 did not follow the same pattern (Figure 4.8, orange boxes). In NIR-2, the correlation was

similar in juvenile ($r = 0.19$) and adult bamboo stages ($r = 0.2$). The correlation's standard deviation was 0.14 and 0.2 for juvenile and adult stages in both bands.

Figure 4.8 - Pearson's correlation coefficients between the median reflectance of bamboo-free forest with the pixel spectral response of bamboo-dominated forests. The results are plotted as function of the bamboo cohort age for MODIS NIR-1 (in black) and NIR-2 (in orange).



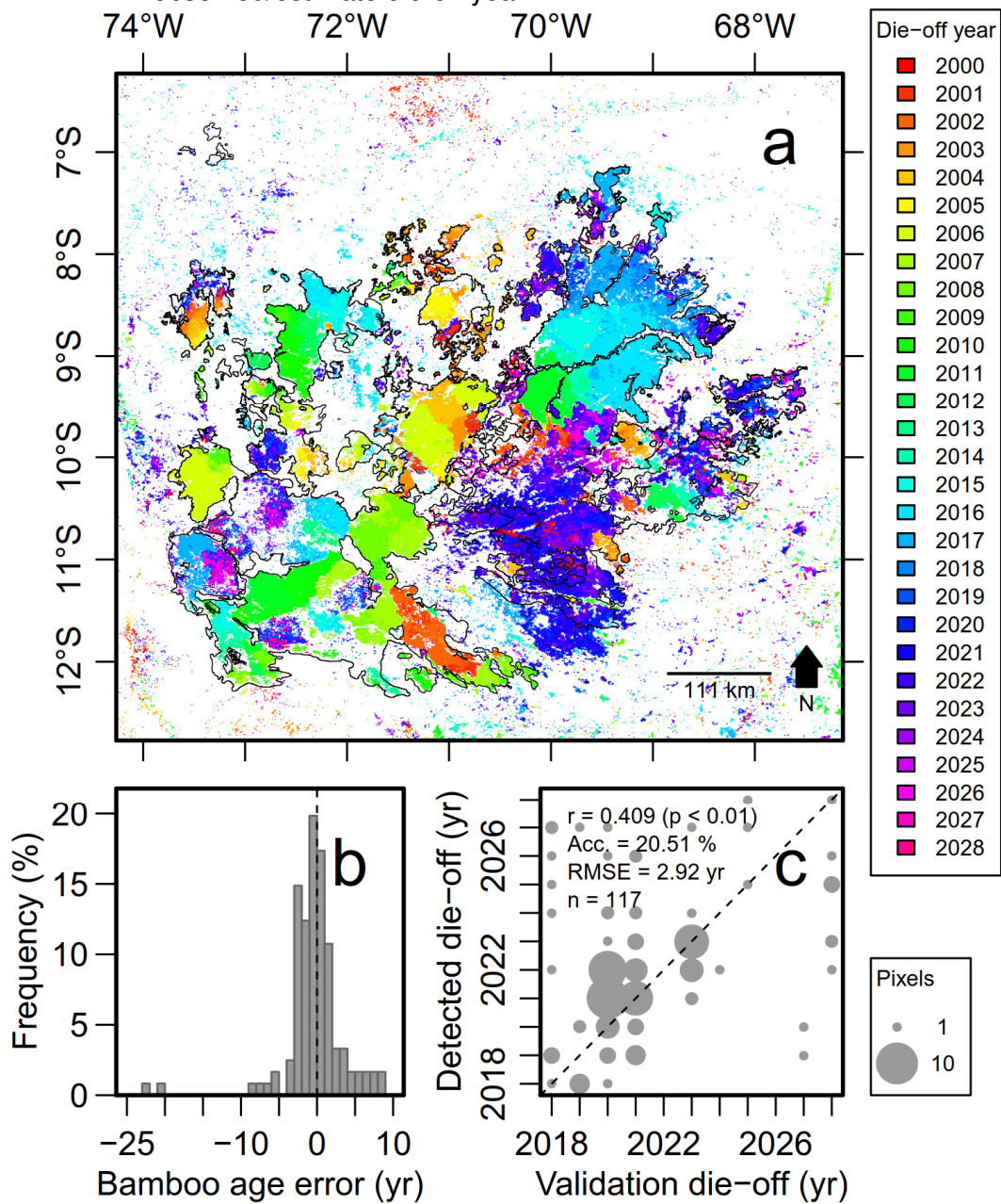
Source: Produced by the author.

4.3.2.4 Die-off prediction

Based on the NIR-1 and NIR-2 reflectance from 0-28 years of age, we predicted the die-off year from 2000 to 2028 for the whole bamboo spatial distribution (Figure 4.9A and Figure A.4A, respectively). The estimated die-off years using the empirical reflectance profiles during 2001-2017 were 85 % similar to the detection using the initial bilinear model (Figure 4.5). The empirical reflectance profiles achieved an accuracy of 75.45 % (RMSE = 1.11 years) and 69.23 % (RMSE = 1.08 years) for NIR-1 and NIR-2, respectively, on predicting the exact die-off year during 2001-2017, when compared to the visual inspection of MODIS color composites. Die-off prediction during 2018-2028 using the empirical reflectance profiles (Figure 4.7) with NIR-1 and NIR-2 were inspected for consistency using the visual interpretation of TM/Landsat-5 time series (Figure 4.9C and Figure A.4C, respectively). NIR-1 and NIR-2 presented low accuracy

(20.5 and 3 %, respectively) to predict the exact die-off year with high RMSE (2.92 and 4.25 years, respectively) and significant weak to moderate correlations ($r = 0.41$ and $p < 0.01$; 0.23 and $p < 0.02$, respectively).

Figure 4.9 - MODIS bamboo die-off prediction map from 2000 to 2028 using the empirical reflectance profiles of the near-infrared 1 (NIR-1) reflectance as a function of bamboo cohort age (A). Validation between predicted die-off (2017-2028) and visual interpreted die-off from previous life cycle in Landsat false-color composites (1985-2000) (C) and residuals distribution (B). The dashed line represents the 1:1 line in (C) and age residual = 0 in (B). Size of circles is related to the number of pixels that hit the same observed/estimate die-off year.

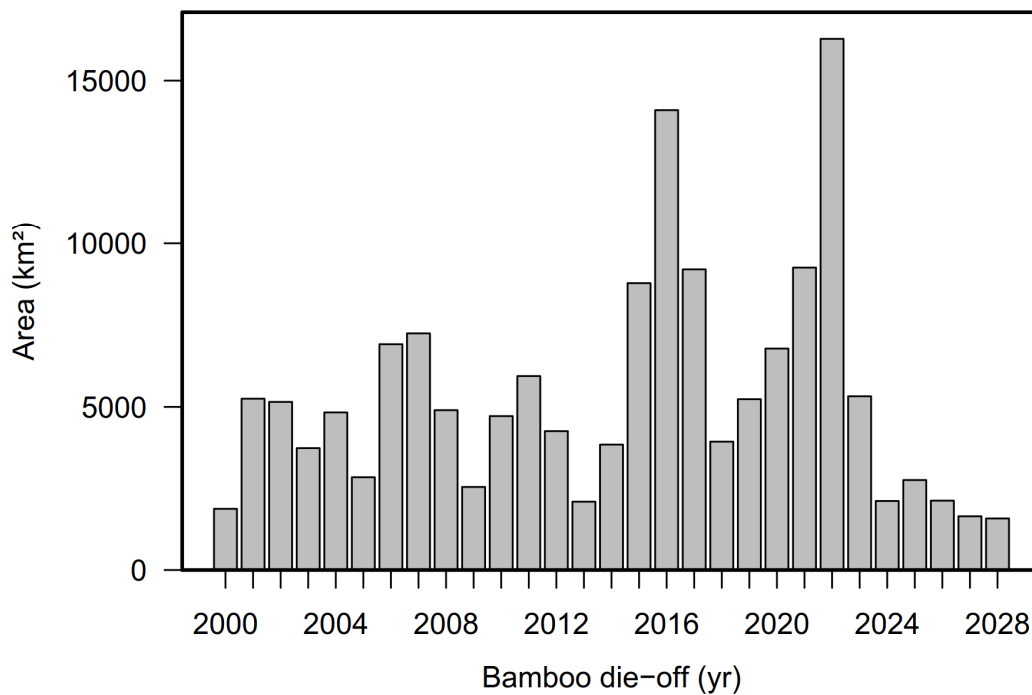


Source: Produced by the author.

The residuals distributions of both NIR-1 and NIR-2 prediction models (Figure 4.9B and Figure A.4B, respectively) were not significantly different from normal ($p > 0.1$). The NIR-1 model had a mean age error closer to zero (-0.7 years) than that observed from NIR-2 (-1 years). This indicates an average underestimate of the true die-off year when using MODIS NIR-1 and NIR-2, respectively. The standard deviation of the residuals was smaller for NIR-1 (5 years) than for NIR-2 (9 years).

Because the MODIS NIR-1 prediction model (Figure 4.9) showed higher precision and less bias than the model based on NIR-2 (Figure A.4), we extracted the predicted die-off years from the NIR-1 model to estimate the total area of bamboo die-off per year (Figure 4.10) and bamboo population (patch) size distribution (Table 4.1). Total die-off per year was different from a uniform temporal distribution ($p < 0.01$). For an uniform distribution, the yearly die-off areas would be close to the average of 5350 km². Within the period 2000-2017, the years 2006, 2007, 2011, 2015 and 2016 showed higher than average die-off area (Figure 4.10). The largest die-off area was observed in 2016 (14099 km²). For the 2018-2028 predicted period, the year of 2022 is expected to show the largest bamboo die-off area (16276 km²).

Figure 4.10 - Distribution of predicted bamboo die-off area per year between 2000 and 2028 from MODIS NIR-1.



Source: Produced by the author.

The detection for 2001-2008, a period that matches the time interval analyzed visually by Carvalho et al. (2013), showed 372 die-off patches with mean size of 80 km² and maximum size of 2234 km² (Table 4.1). Carvalho et al. (2013) found 74 patches with mean size of 330 km² and maximum size of 2570 km² during the same period. The detection for 2001-2017 showed 802 patches with mean size of 85 km² and maximum size of 6162 km² (Table 4.1). Some patch structures had long and linear perimeters, while others had rectangular shapes (for example near 69° 45' W, 8° 48' S, and 71° 13' W, 9° 47' S) or rounded borders (for example near 70° 45' W, 9° 39' S). We also detected a unidirectional flowering wave from north to south in the patch between 8-9° S and 73-74° W, which was also reported by Carvalho et al. (2013).

Table 4.1 - Bamboo patch sizes obtained from die-off prediction using MODIS NIR-1 filtered by a minimum patch area of 10 km², and comparison of results with those from Carvalho et al. (2013).

Study	Period	n	Mean (km ²)	SD (km ²)	Min (km ²)	Max (km ²)	Median (km ²)
Carvalho et al. (2013)	2001-2008	74	330	-	-	2570	-
This study	2001-2008	372	79.56	242.89	10	2234	21
This study	2001-2017	802	84.57	310.39	10	6162	20
This study	2018-2028	778	33.84	72.38	10	1154	17
This study	2000-2028	1603	59.05	226.66	10	6162	18

Source: Produced by the author.

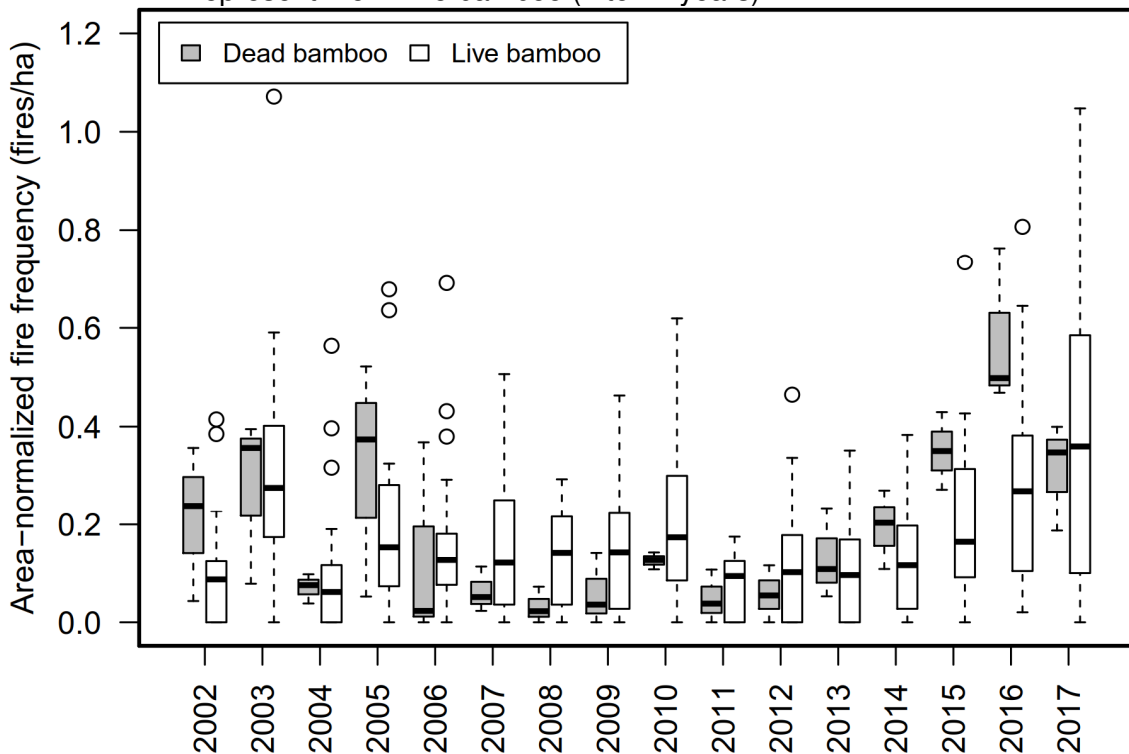
4.3.3 Relationship between bamboo die-off events and MODIS active fire detections

Active fire detections were not found in all bamboo patches that died (Figure 4.6). We found a total of 2371 MODIS active fire detections inside bamboo-dominated forests between 2002 and 2017, from which 1424 detections (60 %) occurred in bamboo patches that died-off and 947 detections (40 %) occurred in live bamboo patches. Active fires were detected mostly near non-forested areas (Figure 4.6 in gray). When we excluded the detections up to 1, 2 and 3 km around these areas,

the total detections decreased to 1330 (56 %), 18 (0.76 %) and 3 (0.12 %), respectively.

Overall, there was a similar number of active fire detections per hectare in dead and live bamboo (0.18 fires ha⁻¹) (Figure 4.11). The ANOVA did not show statistically significant differences in the area-normalized mean active fire detections for the interaction between bamboo stage (dead or live) and year of fire occurrence factors ($p = 0.67$). Individually, bamboo stage also did not show statistical significance on area-normalized mean active fire detections ($p = 0.986$). On the other hand, year of fire did show statistical significance on area-normalized mean active fire detections ($p < 0.01$). The years 2017 and 2016 presented significant higher area-normalized mean active fire detections (0.46 and 0.35 fires ha⁻¹, respectively) than the other years ($p < 0.01$).

Figure 4.11 - Area-normalized MODIS fire frequency during 2002-2017. Gray boxes represent fire in dead bamboo (28, 0 and 1 years) and white boxes represent fire in live bamboo (2 to 27 years).



Source: Produced by the author.

For severe drought years, the area-normalized active fire detections in 2005 (0.32 and 0.18 fires ha⁻¹), 2010 (0.22 and 0.12 fires ha⁻¹), 2015 (0.35 and 0.20 fires ha⁻¹) and 2016 (0.57 and 0.33 fires ha⁻¹) over dead and live bamboo, respectively, were not statistically different between the two bamboo life stages ($p = 0.127$).

Even though, drought years presented in average 45 % higher area-normalized mean active fire detections in dead (0.342 fires ha⁻¹) than live (0.236 fires ha⁻¹) bamboo.

4.4 Discussion

4.4.1 Tree cover of bamboo-dominated and nearby forests

We found that the bamboo-dominated forests had a narrow range of tree cover values (96.95 to 99.89 %) and was below the tree cover values of the closed forests nearby (above 99.89 %). This suggests that these forests have a largely closed canopy but are slightly more open than closed forests without bamboo. Evergreen trees are the dominant life form over most of the southwest Amazon forests, including the ones where bamboo is very abundant. The trees generally comprise 50 % or more of the canopy area in a Landsat or MODIS pixel, even when the bamboo cohorts are at adult stage and dense (CARVALHO et al., 2013). They also fully dominate the canopy during 30 % of the bamboo life cycle, while juvenile bamboo is confined to the forest understory (Smith and Nelson, 2011). Even though, the tree cover percent of bamboo-dominated forests was slightly smaller than the bamboo-free areas. We believe this might be related to (i) an increased gap opening associated with faster forest dynamics and tree mortality of these areas influenced by bamboo (CASTRO et al., 2013; MEDEIROS et al., 2013), or (ii) artifacts of the tree cover computation method that uses the pixels' reflectance from Hansen et al. (2013).

The MODIS NIR-1 reflectance was normally distributed over bamboo-free forests (Figure 4.4B), while it showed a right skewed distribution over the bamboo-dominated forests (Figure 4.4C). This result was expected considering that undisturbed old-growth bamboo-free forests are more or less stable over time while bamboo-dominated forests canopy undergo structural changes when the bamboo reach the height of tree crowns after 12 years of age (SMITH; NELSON, 2011). This is supported by our results that show a continuous increase of NIR reflectance with bamboo age and an abrupt increase of NIR around the age of 12 years.

4.4.2 Automatic detection of bamboo die-off

The automatic detection of bamboo die-off performed very well with an accuracy above 79 % when estimating the exact year of bamboo death and a mean error of 0.5 years. When comparing the NIR-1 and NIR-2 bands, the leaf/canopy water sensitivity from NIR-2 might have contributed for a slightly better performance on bamboo die-off detection and the detection of different areas between the bands, which contributed for a larger coverage of the bamboo-dominated forests (Figure A.3). This different sensitivity to vegetation structure is specially highlighted in Figure 4.7 where the NIR-2 remains at its lowest during 0-2 years, explaining why NIR-2 band maps different areas than NIR-1.

Our die-off map is an improvement of the current available maps from the literature, because the die-off detection conducted in previous works was solely based on the visual inspection of Landsat and MODIS color composites during 2000-2008, thus leading toward the identification of big clusters of pixels that went through die-off (Table 4.1) (NELSON, 1994; CARVALHO et al., 2013). Our method is automatic, easy to implement, and can detect relatively small patches because it runs on a per pixel basis. However, we do not advise to attempting detection of very small patches ($< 10 \text{ km}^2$) when using MODIS data due to limitations of the spatial resolution of the sensor (1 km). It is important to note that the detected bamboo die-off areas were not confounded with recently deforested areas, as the tree cover product did not point out forest losses in bamboo die-off areas. Since the method can detect bamboo die-off without a priori knowledge of the bamboo spatial distribution (Figure 4.6), it could be used to better describe and understand the spatial organization of the bamboo stands that show synchronized die-off in forests around the world.

Our validation dataset was composed of 390 pixels visually detected in 78 bamboo patches during 2001-2017 using MODIS imagery. Therefore, we are confident that the sampling was representative to our study area given that we found 802 patches in the same time period, that is, the sample consisted in around 10 % patches. It is noted, however, that our visual analysis mostly sampled big patches that died-off, because those were the ones that we could be sure that were bamboo die-off. The high detection accuracy of bamboo die-off events also highlights the quality of the MODIS (MAIAC) data, which are suitable

for bamboo-dominated forests mapping. The MAIAC algorithm improves the accuracy of cloud detection, aerosol retrieval and atmospheric correction compared to the standard MODIS product processing (HILKER et al., 2014). Combined with the appropriate normalization for sun-sensor-target geometry using BRDF modelling, the MAIAC contributed to minimize inter-annual artifacts in the time series for an accurate detection.

4.4.3 Spatial distribution of bamboo-dominated forests

A total of 155,159 km² (15.5 million ha) of bamboo-dominated forests were mapped in the southwestern Amazon by combining the automatic detection of die-off and live bamboo (Figure 4.6). Most of the detected areas (72.5 %) were located inside the 16.5 million ha of the bamboo-dominated forests mapped by Carvalho et al. (2013), although covering only 68.8 % of the previous detected areas. This difference was partially due to the increased land cover change in the region past-2010 - period when Carvalho et al. (2013) performed their analysis, and areas where our method did not detect bamboo-dominated forests. Despite the differences, we detected clusters of pixels that were very likely bamboo-dominated patches outside of the previously mapped areas (11.5° S, 70° W, and 13° S, 71° W). These areas should be further investigated in field to verify if they are indeed bamboo-dominated forests.

Compared to our results with 1 km spatial resolution, the map from Carvalho et al. (2013) (30 m spatial resolution) underestimated the bamboo-dominated forests in the order of 30 %. A possible explanation is that the authors considered live-adult bamboo and used only two Landsat mosaic images 10 years apart from each other (1990 and 2000) for mapping, thus not observing part of the bamboos that were at juvenile stage and hidden in the understory of the canopy strata at that time. Another possibility is the limitation of visual interpretation and manual delineation of small bamboo patches. Our map was obtained on a per-pixel basis by assessing each pixel's spectral trajectory (refer to Figure 4.7), thus reducing errors of omission by considering both live and dead bamboo for mapping, and by using a longer time series (18 years) for the detection.

The potential limitations of our map include the coarser spatial resolution (1 km) when compared to the previous map (30 m). In addition, we likely underestimated the true bamboo distribution because of the previously discussed uncertainties in detecting juvenile bamboos, given the current temporal coverage of the MODIS (MAIAC) time series. A more accurate mapping of bamboo spatial distribution would require that all bamboo died-off during the time series (i.e. requiring at least 28 years of data). Currently, the only dataset that has such temporal coverage comes from the Landsat satellites with 47 years of data of variable spatial resolution up to 80 m spatial resolution (1972-2018) or 34 years of data of 30 m (1985-2018). The challenge in applying such detection with Landsat imagery relies in the dataset acquisition of yearly time series of cloud- and aerosol-free images for the whole area, and signal normalization between images. The area coverage takes at least 16 different Landsat World Reference System path/row scenes.

4.4.4 Bamboo cohort age and reflectance variability

When reconstructing the spectral response of the bamboo-dominated forest as a function of cohort age (Figure 4.7), we found that two spectral bands, the NIR-1 and NIR-2, followed our initial assumption of overall reflectance increase with bamboo cohort age and of sharp decrease at the time of die-off.

Between 1 and 12 years of cohort age, the NIR-1 reflectance did not show a continuous increase (Figure 4.7), while it presented strong correlation ($r = 0.41$) with bamboo-free forest (Figure 4.8). The NIR-2 reflectance, however, showed a slight monotonical increase (Figure 4.7) with weak correlation ($r = 0.19$) to bamboo-free forest (Figure 4.9). Even though, the accuracy on detecting juvenile bamboos was poor (Figure 4.9). Thus, it is very difficult to identify the bamboo dominated patches in this hidden juvenile age without identifying the prior death event, as reported in a previous study (CARVALHO et al., 2013).

The NIR signal suddenly increased at 12-14 years of age, which we believe had two possible explanations. First, there was a change in the density of leafy bamboo branches in the upper forest canopy, where they are visible to the satellite. This is supported by the field observations of Smith and Nelson (2011),

in which juvenile bamboo cohorts reach the upper forest canopy by 10 years of age and accelerate in growth due to increased access to solar radiance. They observed that bamboo density doubled (from 1000 to 2000 culms ha⁻¹) and basal area almost tripled (from 2.1 to 5 m² ha⁻¹) between 10 and 12 years of age. The second explanation could be an artifact of our unbalanced sampling for this set of cohort ages. The reflectance values collected for 12-15 years of cohort age were only available from the extremes of our time series (2000 and 2017) due to the bamboo 28 years life cycle and the 18 years of MAIAC data availability.

From 14-27 years, a smooth steady increase occurs only in the NIR-1 signal until the synchronous cohort death, while the NIR-2 signal seems to have saturated at about age 15 years maintaining a constant signal of 0.3 reflectance until it drops steeply at cohort death. Thus, NIR-1 should present better results for predicting the bamboo age of adult-live stands. Finally, the sharp decrease of NIR-1 and NIR-2 at 28-29 years explain why our bilinear model performed well detecting the time of death. At the time of death, there is a high abundance of dead/dry bamboo branches in the canopy, which reflect less amounts of NIR energy than leafy and photosynthetically active bamboo.

The increases in red reflectance at the die-off, as well as at 1 year of age (Figure 4.7A), can also be related to the high abundance of dry bamboo with decreased leaf chlorophyll content and increased non-photosynthetic content. Dry, or dead, vegetation is non-photosynthetically active, and, thus, the incoming red energy near 672 nm is not absorbed by the plant's chlorophyll, that is, causing an increase in the red reflectance (DAUGHTRY, 2000). The dry culms can take up a few years to decompose (CARVALHO et al., 2013), which may explain the reason for still observing an increased red signal at 1 year of age.

The reflectance profiles also showed a large spectral variability in bamboo-dominated forests with age, which very likely occur due to different bamboo abundance and/or forest structure among the area, as well as the inter-annual variability in the signal. Even though, we were able to extract the annual changes in reflectance and predict bamboo ages with 2.92 and 4.25 years RMSE (Figure 4.9) using NIR-1 and NIR-2, respectively. The data of each age class was merged from different year composites of the whole time series, thus incorporating the noise in inter-annual variability. Three factors contributing to such noise could be

the: (i) temporary formation of green leafy secondary forest, spectrally similar to adult bamboo, in large forest gaps left by the dead bamboo; (ii) semideciduous nature of the trees that are mixed in with bamboo, in the seasonally drier parts of the bamboo range; and (iii) death of bamboo revealed suppressed trees below the bamboo canopy. Nevertheless, because our detection and prediction methods were not based on absolute reflectance values, but on the correlation between the time series and a reference, such as the bilinear model or the empirical reflectance profile, we do not believe that the large spectral variability should have a major impact on the detection/prediction.

4.4.5 Bamboo die-off prediction

By applying the empirical bamboo-age reflectance profiles, we estimated the bamboo die-off year for all bamboo patches of the region providing a detailed map of the age structure of bamboo-dominated forest (Figure 4.9) and bamboo patch sizes description (Table 4.1). The estimated die-off events between 2000 and 2017 were similar to the ones detected using the bilinear model because of the abrupt spectral changes with die-off. Regarding predictions between 2018 and 2028, the estimate of the exact die-off year was not so accurate (at best 20 % accuracy) because those bamboo patches were mainly at the juvenile stage during the MODIS (MAIAC) time series period and did not die. However, we believe that the predictions using the NIR-1 were at acceptable levels (RMSE = 2.92 years) when considering that: (i) the Landsat validation points based on visual interpretation can have a deviation of 1 year; and (ii) we assumed that every bamboo cohort had the same life cycle length of 28 years, while we know that it can vary between 27-32 years (CARVALHO et al., 2013). The validation dataset for the predictions (2017-2028) corresponded to 175 pixels in 35 bamboo patches and represented 4.5 % of the 778 bamboo patches predicted for the 2018-2028 time period.

We believe that knowing where and when the bamboo dies is an important information for future studies of the bamboo-dominated forests ecosystems, and the potential applications of the bamboo die-off year or age map are various. Since areas with dead bamboo are difficult to maintain trails and hinder the work of rubber trappers (CARVALHO et al., 2013), it can be used in forest

management planning in order to avoid areas where die-off year occurred in the last 3 years and dry culms are still not decomposed, or to avoid areas with likely future die-off. It can also be used for public policy planning regarding food and human health security, for example, in bamboo forests in southeast Asia, where the bamboo reproductive events cause huge rodent invasion and proliferation that then damage nearby crop plantations (FAVA; COLOMBO, 2017). It could also be used to explore broader scientific questions on the ecology of bamboo-dominated forests such as studies on maintenance/expanse of bamboo patches, flowering waves, cross-pollination between patches, fauna habitat dynamics, impacts on short and long-term carbon dynamics.

4.4.6 Fire occurrence and bamboo

We could not support the bamboo-fire hypothesis from Keeley and Bond (1999) because fire occurred only in a small fraction of bamboo-dominated areas during the 16 years of fire analysis (Figure 4.6), equivalent to 2371 km² of burnt area or 0.0955 % of the total bamboo area (155,159 km²) burning each year. In addition, the statistical tests comparing dead and live bamboo fire frequency showed that dead bamboo did not burn more than live bamboo (Figure 4.11). Hence, we believe in other explanations for bamboo maintenance in the forest, such as bamboo itself being responsible for its maintenance in the forest due to the damage it causes in the trees while increasing tree mortality (GRISCOM; ASHTON, 2003).

We also did not observe an overall increased fire probability over dead than live bamboo in non-drought years. However, our findings suggest that forests with recently dead bamboo exposed to severe drought are more susceptible to fire occurrence, as there were 45 % higher area-normalized mean active fire detections in dead than live bamboo during severe drought years, such as 2005, 2010, 2015 and 2016. When considering the total fire occurrence, we did not observe an overall significant increase in fire occurrence during the 2005 and 2010 major droughts when compared to the other regular years (BRANDO et al., 2014). We believe that this is because we filtered the active fire occurring inside the bamboo-dominated areas and pixels with, theoretically, zero non-forested areas using the tree cover products (HANSEN et al., 2013), thus excluding the

areas of increased fire occurrence in 2005 and 2010 that were reported in the literature (BRANDO et al., 2014).

The fire occurrence beyond 2 km inside the forest was probably underestimated because the forest canopy can obscure fires that occur only on the understory, and, thus, are not detected by the MODIS/Aqua satellite (ROY et al., 2008). In addition, the MODIS active fire detections should be treated as a lower bound of fire occurrence, as it underestimates fire occurrences in the order of 5 % for small fires with less than 0.09 km², or 10 % of MODIS spatial resolution, due to the coarse spatial resolution, high cloud cover, and when having high viewing angles (> 15 °) (MORISSETTE et al., 2005). Nevertheless, we do not believe this might have an impact on rejecting the bamboo-fire hypothesis due to the minimal fraction of fire occurrences occurring over the large bamboo-dominated forests.

Large areas of bamboo die-off that burned occurred close to agricultural lands near Sena Madureira city in the state of Acre, Brazil, during 2015, 2016 and 2017. The combination of increased dry fuel material from bamboos and nearby ignition sources from land use might have contributed to this increased fire occurrence. This result supports the notion that bamboo die-off enhances fire probability by increasing the dry fuel material in the forest. As we observed in the red wavelength, the reflectance increase was probably associated with greater amounts of dry biomass or non-photosynthetic vegetation in the die-off year and up to 1 year of age (Figure 4.7A).

The fire occurrences over bamboo-dominated forests were therefore associated with the proximity to ignition sources, as less than 1 % of forest fire events occurred more than 2 km apart of non-forested areas. This was expected because fire depends on both fuel and ignition to occur. Thus, areas closer to deforested areas, roads and rivers would have higher probability to burn, as probably occurred in 2015, 2016 and 2017. The study of Kumar et al. (2014) found that 50 % of MODIS active fire detections were found within 1 km of roads and rivers, and 95 % of the active fires were found within 10 km of roads and rivers in Brazilian Amazon. Fire is known to be associated to deforestation and land use practices in Amazon such as slash-and-burn and land preparation, where people remove trees of economic interest and then set the areas on fire in order to clear the land and implement crop plantations or pasture (ROY et al.,

2008). Thus, this reinforces a bamboo-human-fire association through the increased land use and cover change. This association is slightly different than it was in pre-Columbian times (MCMICHAEL et al., 2014), where geoglyph builders could have used the bamboo die-off patches and fire as an easier way to clear the forest cover to build their monuments, but it should also favor increases in fire occurrence on the vicinities of bamboo-dominated areas, thus leading to potential bamboo expansion.

The higher fire probability in dead bamboo patches during drought events, along with the increasing human influence, can favor increases in bamboo abundance and expansion over time by assisting them in their competition with trees. A previous study showed that fire favored the *Guadua* bamboo expansion in the region, because the bamboo individuals have faster responses to catastrophic disturbance such as fires than tree species (SMITH; NELSON, 2011). Thus, when a fire occurs inside or close to a bamboo forest patch, it may favor the growth of bamboo seedlings - derived from the massive amount of seeds that have been launched during the reproductive phase and prior to death - and the vegetative expansion of the adult bamboo.

Our findings regarding bamboo die-off year being associated to fire occurrence, mainly in drought years, might have implications to fire control policies, such as in the state of Acre in Brazil, where many bamboo-dominated areas occur near human settlements and that these extreme climate events are occurring within 5 years' interval in Amazon. By knowing where and when the die-offs are occurring, public policies can be made to avoid fire ignitions in such areas or prepare the fire brigades to attend to potential fires.

4.5 Conclusions

This study demonstrates that the NIR reflectance is more sensitive to the bamboo life cycle than the other spectral intervals and can be used to detect and map bamboo-dominated forests distribution, age structure, and death. The automatic bamboo die-off detection achieved an accuracy above 79 % by assessing the point of maximum correlation between the NIR time series and a bilinear model of linearly increasing NIR with a sharp decrease at the end. After merging the die-

off map with the live bamboo map, a total of 155,159 km² of bamboo-dominated forests was mapped in the region. It is noted, however, that this area was probably still underestimated due to the limited temporal coverage of the MODIS (MAIAC) time series restricted to the last two decades. The bamboo-fire hypothesis was not supported by our results, because only a small fraction of bamboo areas burned during the analysis timescale. In general, bamboo did not show higher fire probability after the reproductive event and die-off, meaning that fire should not be the driver for bamboo dominance. Nonetheless, under severe droughts effects, forests with recently dead bamboo are more susceptible to fire than forests with live bamboo, being affected by 45 % more fire occurrence. The fire in these areas is mostly associated with ignition sources from land use, suggesting a bamboo-human-fire association. The interaction of dead bamboos and ignitions cause increased fire occurrence that may contribute to the maintenance of bamboo, burn adjacent forested areas and promote tree mortality, and ultimately the expansion of bamboo into adjacent areas.

Further research related to bamboo dynamics can use the bamboo die-off map that we produced to pinpoint the location of reproductive and die-off events in space and time in order to support studies of bamboo maintenance and colonization, wildfire dynamics, carbon assimilation in trees and bamboos, tree mortality, fauna/flora demography and species distribution, etc. The mapping approach can be applied with other remote sensing data, such as Landsat data with better spatial resolution and longer time series, and tested with different spectral bands and attributes to further improve the detection. It can also be applied in other areas around the world that have bamboo-dominated forests. Using this approach, one can evaluate the temporal dynamics of the reproductive events, e.g. spreading of flowering waves, and map the bamboo-dominated areas.

5 QUANTIFYING CANOPY TREE LOSS AND GAP RECOVERY IN TROPICAL FORESTS UNDER LOW-INTENSITY LOGGING USING VHR SATELLITE IMAGERY AND AIRBORNE LIDAR ⁵

Abstract: Logging, including selective and illegal activities, is widespread, affecting the carbon cycle and the biodiversity of tropical forests. However, automated approaches using very high resolution (VHR) satellite data (≤ 1 m spatial resolution) to accurately track these small-scale human disturbances over large and remote areas are not readily available. The main constraint for performing this type of analysis is the lack of spatially accurate tree-scale validation data. In this study, we assessed the potential of VHR satellite imagery to detect canopy tree loss related to selective logging in closed-canopy tropical forests. To do this, we compared the tree loss detection capability of WorldView-2 and GeoEye-1 satellites with airborne LiDAR, which acquired pre- and post-logging data at the Jamari National Forest in the Brazilian Amazon. We found that logging drove changes in canopy height ranging from -5.6 to -42.2 m, with a mean reduction of -23.5 m. A simple LiDAR height difference threshold of -10 m was enough to map 97% of the logged trees. Compared to LiDAR, tree losses can be detected using VHR satellite imagery and a random forest (RF) model with an average precision of 64%, while mapping 60% of the total tree loss. Tree losses associated with large gap openings or tall trees were more successfully detected. In general, the most important remote sensing metrics for the RF model were standard deviation statistics, especially those extracted from the reflectance of the visible bands (R, G, B), and the shadow fraction. While most small canopy gaps closed within ~ 2 years, larger gaps could still be observed over a longer time. Nevertheless, the use of annual imagery is advised to reach acceptable detectability. Our study shows that VHR satellite imagery has the potential for monitoring the logging in tropical forests and detecting hotspots of natural disturbance with a low cost at the regional scale.

Keywords: remote sensing; forest management; disturbance monitoring; forest dynamics; multi-temporal analysis; WorldView-2; GeoEye-1; random forest; Amazon; Jamari National Forest

⁵ DALAGNOL, R. *et al.* Quantifying Canopy Tree Loss and Gap Recovery in Tropical Forests under Low-Intensity Logging Using VHR Satellite Imagery and Airborne LiDAR. **Remote Sensing**, v. 11, n. 7, p. 817, 4 abr. 2019.

5.1 Introduction

Logging, including illegal and selective activities, causes mostly small-scale but spatially widespread disturbances in tropical forests. Illegal logging accounts for ~40% of all logging in tropical forests and up to 72% of all logging in the Brazilian Amazon (CONTRERAS-HERMOSILLA et al., 2007; LAWSON; MACFAUL, 2010). Despite the large uncertainties, it has been estimated to affect ~12,000 km² year⁻¹ of forests in the Brazilian Amazon and is responsible for gross carbon losses of ~0.08 Pg C year⁻¹ or ~33% of the Amazon's annual carbon emissions between 1999 and 2002 (ASNER et al., 2005; ARAGÃO et al., 2014). Besides the direct implications on the carbon cycle, logging also causes ecological impacts, such as the increased mortality of remaining trees, increased fire risk, and losses of floral and faunal biodiversity (COCHRANE 2003; ASNER et al., 2005; LAMANNA; MARTIN, 2017). Furthermore, the long-term effects of logging on forest dynamics and turnover remain poorly understood, but likely persist for decades (OSAZUWA-PETERS et al., 2015).

Given the impacts of logging on a forest's carbon stocks and biodiversity, there is a growing interest in tracking these direct human-induced forest disturbances (BUCHANAN et al., 2018). This is critical for better understanding the contribution of logging to the carbon budget and ultimately supporting actions for climate change mitigation (ARAGÃO et al., 2014). However, unlike forest clear-cutting, logging is not easily detected by remote sensing. Compared to clear-cutting, logging causes subtler changes to the canopy, such as opening gaps over logging decks and roads, but most of the canopy damage is due to the direct impacts of tree-falls (ASNER et al., 2005). Furthermore, the detection challenge increases for low-impact logging (i.e. selective or reduced impact logging). These activities are carefully planned to minimize environmental impacts by only extracting targeted individual trees of non-endangered species with high market value. However, Johns et al. (1996) suggest that even reduced-impact felling and extraction may cause high damage and mortality to non-targeted trees, such as killing up to five other non-targeted trees. These events cause abrupt changes to the canopy structure, but still pose a challenge for remote sensing detection.

Satellite imagery from the Landsat series (30 m resolution) has been successfully used to map logging disturbances in Amazon forests using mono-temporal

(STONE; LEFEBVRE, 1998; ASNER et al., 2005) or multi-temporal (WANG et al., 2019) approaches. However, although Landsat satellites provide the longest historical time series (1984-today), the spatial resolution of their instruments is limited to capture all the small-scale disturbances associated with logging and especially low-impact logging. Alternatively, studies have shown that VHR satellite imagery (≤ 1 m spatial resolution) is a promising way to map small-scale disturbances from natural mortality and logging by the visual inspection of multi-date imagery (READ et al., 2003, CLARK et al., 2004a, 2004b). More recently, Kellner; Hubbell (2017) applied an automated method to detect the mortality of canopy tree species *Handroanthus guayacan* in tropical forests based on synchronous flowering. However, their method only works for tree species with synchronous annual flowering. At this time, we still lack information about the effects of tree size, tree-fall gap opening, and time after the event on the sensitivity of the disturbance detection from the VHR satellite data.

Automated disturbance detection using VHR satellite imagery still poses technical challenges, as differences in view-illumination geometries between the pairs of images may cause a mismatch of tree crown geo-location (GUO et al., 2007; WULDER et al., 2008). Thus, the appearance of artifacts due to canopy shadowing, and related changes in the crown relative position for the sensor, canopy shape and apparent area, can induce misclassification of disturbance (WULDER et al., 2008). Therefore, the high local canopy spectral variability hampers the success of pixel-based change detection approaches (GUO et al., 2007). To solve these problems, some studies suggest the application of object-based analyses (GUO et al., 2007; WULDER et al., 2008) focusing on physically meaningful features rather than pixels. This is often done by segmenting images into individual tree crown (ITC) polygons, which minimizes the high local spectral variability in the canopy, and reduces problems of tree crown geo-misallocation.

Airborne LiDAR data have also been used to investigate the impacts of selective logging (ASNER et al., 2010; D'OLIVEIRA et al., 2012; ANDERSEN et al., 2014) and natural tree mortality (LEITOLD et al., 2018) in the Amazon. These studies pointed out that the height difference between a pair of LiDAR data, acquired pre- and post-logging, was strongly related to the aboveground biomass (AGB) change. These approaches enabled the estimation of AGB loss due to logging

with fairly low (2–18%) uncertainty, and with precise observation of canopy gaps. Although they achieved a high precision for estimating small-scale disturbance impacts, airborne LiDAR data are not ideal for operational monitoring over large and remote areas because of the high costs associated with data acquisition. Nevertheless, studies suggest that the combination of airborne LiDAR and VHR satellite data could prove useful to quantitatively assess and validate how VHR satellite data can observe individual canopy tree loss (READ et al., 2003).

In this study, we explore the potential of VHR satellite imagery as a means to detect canopy tree loss associated with low-intensity logging in closed-canopy tropical forests. Specifically, we address the following questions: (1) How does logging drive changes in forest canopy height? (2) Can low-intensity logging events be detected by VHR satellite data? (3) Which remote sensing metrics are the most important for tree loss detection? (4) For how long after a disturbance can VHR satellite data still detect it? (5) Is the satellite-based tree loss map consistent across disturbed and undisturbed forests?

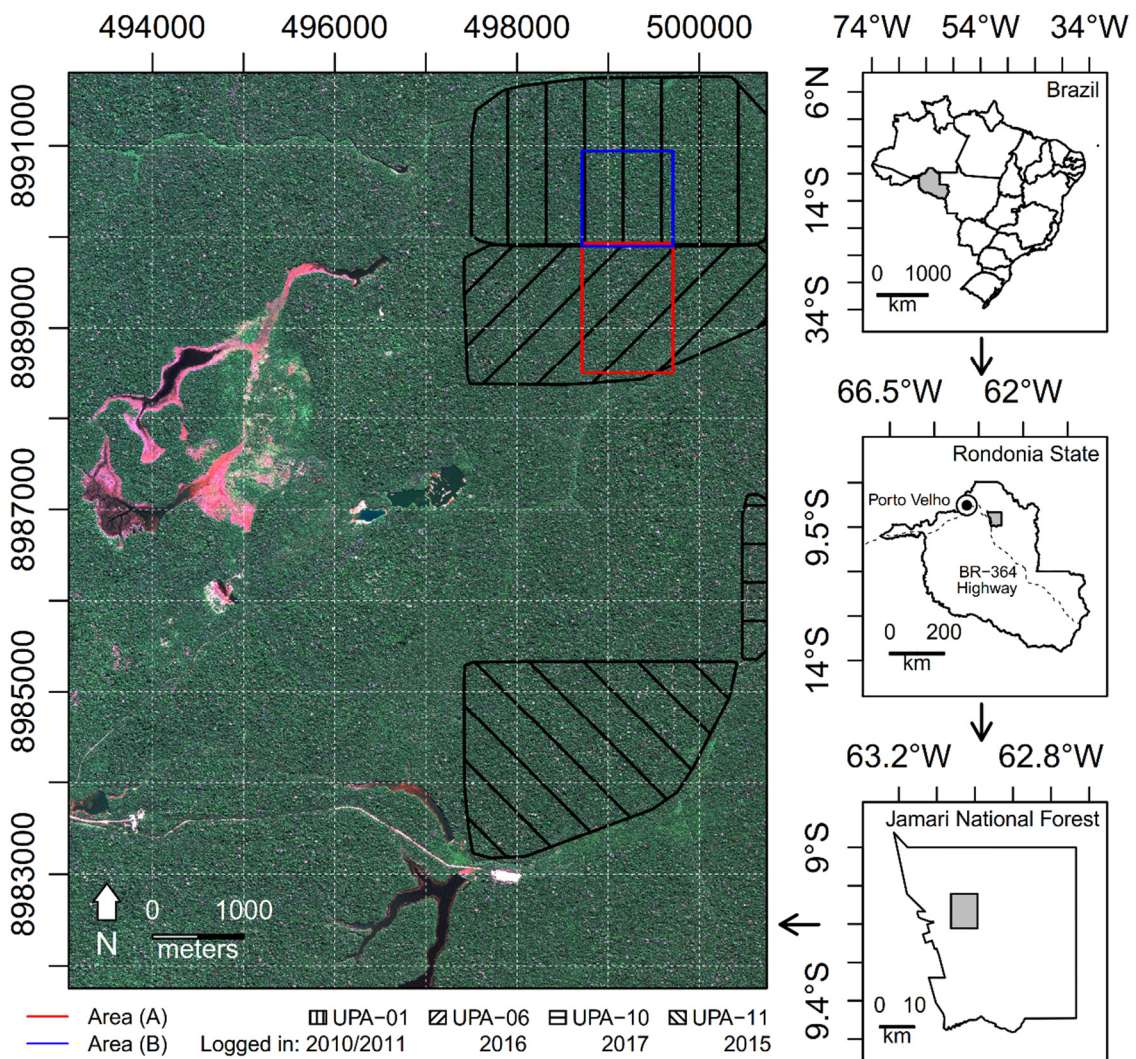
To answer these questions, we acquired a complete dataset of multi-date (pre- and post-logging) airborne LiDAR and VHR satellite data from WorldView-2 and GeoEye-1 satellites, and a comprehensive field dataset of tree-by-tree georeferenced logged trees at Jamari National Forest in the Brazilian Amazon. This enabled us to evaluate the potential of optical remote sensing to detect tree-by-tree disturbances against a carefully collected airborne LiDAR and ground record of logging. Although the tree-by-tree dataset covers only the logged trees, and not all the killed trees during the felling process, it guided the assessment of structural changes in the canopy as sensed by LiDAR data. This fact then allowed the assessment of mortality using VHR data.

5.2 Study Area

The study area is located at the Jamari National Forest (09°10'S, 63°01'W), next to the BR-364 highway, 90 km from Porto Velho city, capital of the Rondônia state, Brazil (Figure 5.1). The Jamari Forest covers 2,200 km² of *terra firme* lowland rain open forests (IBGE, 2006), with tree species of high commercial value. From the total area, 960 km² (44%) has been allocated for private selective

logging concessions since 2008. The forest concessions are administered and managed by the Brazilian Institute of Environment and Renewable Mineral Resources (IBAMA) and the Brazilian Forest Service, respectively. Wood extraction is limited to (i) non-endangered species allowed by IBAMA; (ii) trees with a diameter at breast height (DBH) greater than 50 cm; and (iii) an extraction density of up to 25.8 m³ ha⁻¹. The managed areas are left to recover naturally for 25 years after extraction.

Figure 5.1 - Study area at the Jamari National Forest, Rondônia state, Brazil. The background of the left image is a true color composite from the GeoEye-1 satellite acquired on 02 July 2017 (UTM, datum WGS-84). The red and blue rectangles represent the areas A and B covered by the LiDAR datasets, which were analyzed in sections 5.3.1 and 5.3.3, respectively. The black lines represent the boundaries of the UPAs. The satellite image is courtesy of the DigitalGlobe Foundation.



Source: Produced by the author. Image is a courtesy of Digital Globe Foundation.

This study focuses on an area of 76.6 km² inside the total managed area, with the availability of images from a pair of VHR satellites (WorldView-2 and GeoEye-1). The area covers four annual production units (UPA): UPA-01 (logged in 2010/2011), UPA-06 (logged in 2016), part of UPA-10 (logged in 2017), and UPA-11 (logged in 2015). Two smaller sections of the study area were analyzed using LiDAR datasets (Figure 5.1): (A) 1.4 km² over UPA-06 observed pre- and post-logging by the satellite and LiDAR instruments (analyses of sections 5.3.1 and 5.3.2), and (B) 1.04 km² over UPA-01 evaluated by a time series of LiDAR data from 2011 to 2017 (analysis of section 5.3.3). The imagery also covers an active legal mining site of Cassiterite ore, located in the western part of the study area. The forests outside of UPAs and away from the mining site are nominally undisturbed.

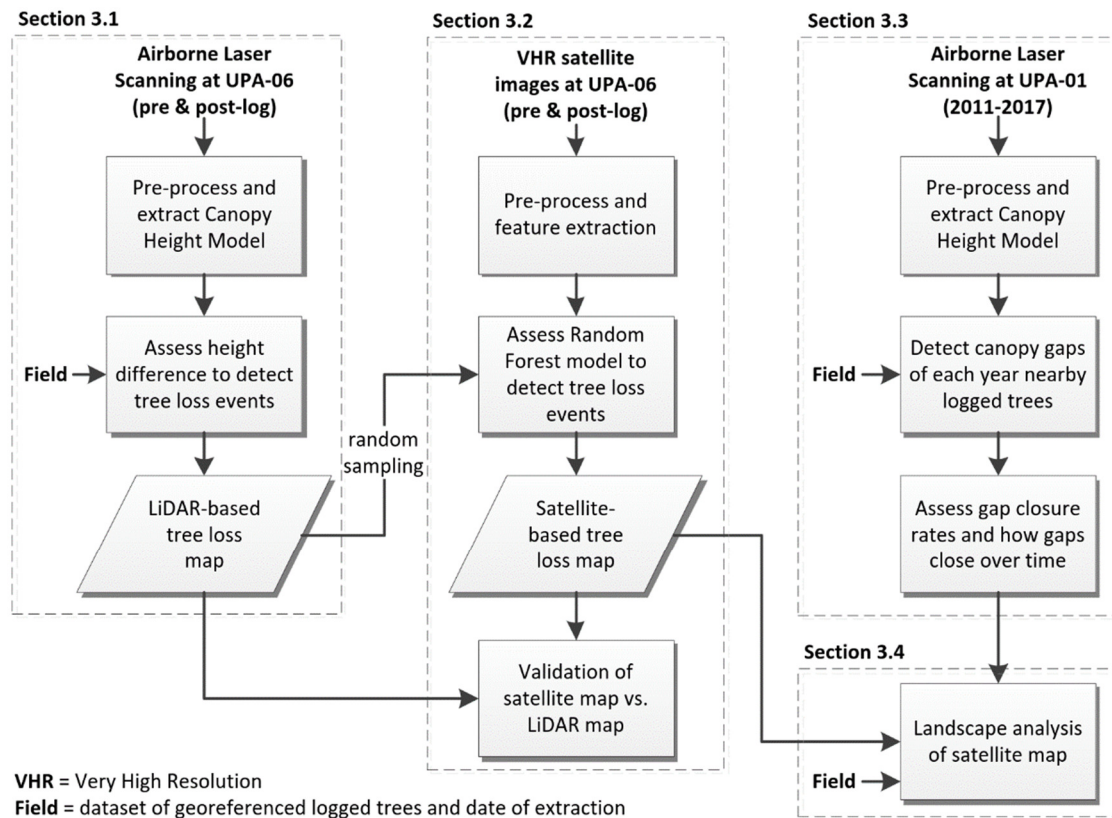
Based on a forest inventory of the UPA-06 conducted by the concessionaire in 2015 (prior to logging), the logged trees include at least 18 different species, with DBH ranging from 50 to 185 cm (mean = 92 cm) and height ranging from 11 to 28 m (mean = 20 m). The region has two well-defined seasons: a wet season from December to May, and a dry season from June to November, with annual precipitation of 2000 mm, varying from 14 mm in the driest month (July) to 318 mm in the wettest (January), as indicated by Tropical Rainfall Measuring Mission (TRMM) data (product TRMM 3B43 v7 at 0.25 deg). Monthly mean temperature ranges from 24 °C in June/July to 27 °C in October, according to the Climatic Research Unit (product v4.01) (HARRIS et al., 2014). The terrain is hilly, with heights ranging from 90 to 158 m above the sea level as measured by the Shuttle Radar Topography Mission v2.1 (USGS, 2006).

5.3 Material and Methods

The overview of this study is shown in Figure 5.2. In the first section, we used airborne LiDAR data and logged trees' geolocation to assess height differences related to logging and create a LiDAR-based tree loss map. In the second section, using the LiDAR map as a reference for tree loss samples, we trained an RF model with VHR satellite metrics to create a satellite-based tree loss map. The satellite map was validated using the whole LiDAR map. Then, we conducted a sensitivity analysis to explore the variability of results regarding the forest

structure and changes. In the third section, we analyzed a time series of airborne LiDAR data to detect tree-fall gaps and track vegetation recovery and gap closure over time. Finally, in the fourth and last section, we analyzed the whole satellite map over previously known selectively logged areas and undisturbed forests to detect hotspots of disturbances and discuss the detection capabilities using VHR satellite data.

Figure 5.2 - Main steps of the data processing and analyses.



Source: Produced by the author.

5.3.1 Tree Loss Detection using LiDAR Data

We used airborne LiDAR data and field logged tree coordinates to characterize canopy height changes associated with tree loss events derived from logging. Using this information, we created a tree loss map. We acquired airborne LiDAR data over 1.4 km² of forests at the UPA-06 during 2015 (pre-logging) and 2017 (post-logging) (Table 5.1 and area A in Figure 5.1). The LiDAR point cloud (x, y, z coordinates) was processed into a canopy height model (CHM) following four steps of pre-processing: point classification, generation of a Digital Terrain Model

(DTM), height normalization, and extraction of CHM. First, we classified the points into ground or vegetation classes using the *lasground*, *lasheight*, and *lasclassify* functions from LAStools 3.1.1 (ISENBURG, 2018). Second, to ensure that potential acquisition effects between the two datasets did not interfere with the analysis, we merged their points classified as ground and created a combined DTM with a 1 x 1 m pixel using the *TINSurfaceCreate* function from FUSION/LDV 3.6 (MCGAUGHEY, 2016). The combination of point clouds generates more precise DTM and CHM for both dates and allows a more precise determination of height difference. Third, we normalized the point's height to height above ground by subtracting the combined DTM height from their values. Finally, we extracted the CHMs considering the highest height of vegetation on each 1 x 1 m pixel using the *CanopyModel* function from FUSION/LDV. No adjustment for horizontal displacement between the datasets was necessary because tree crowns' positioning agreed nearly perfectly, as verified by visual inspection. Both LiDAR collections had very high point densities (≥ 12 points m^{-2} in overall, ≥ 4 points m^{-2} reaching the ground), which vary across studies, depending on the platform used for data collection.

Table 5.1 - Acquisition details of Airborne LiDAR and VHR satellite data used for tree loss analyses. PAN = Panchromatic; B = blue; G = green; Y = yellow; R = red; NIR = Near infrared.

Information	LiDAR Date 1	LiDAR Date 2	Satellite Date 1	Satellite Date 2
Sensor	Laser scan Optech 3100	Laser scan Optech ALTM Gemini	WorldView-2 satellite	GeoEye-1 satellite
Acquisition date	21 Sep 2015	20 Apr 2017	10 Oct 2014	02 Jul 2017
Acquisition altitude	750 m	700 m	770 km	770 km
Scan frequency	100 kHz	100 kHz	-	-
Off-nadir angle	15°	15°	26°	20°
View elevation	-	-	60°	68°
View azimuth	-	-	74°	64°
Sun elevation	-	-	69°	49°
Sun azimuth	-	-	85°	38°
Data type, bands, and spatial resolution	Point cloud (x,y,z) with 33.6 points m^{-2}	Point cloud (x,y,z) with 12 points m^{-2}	PAN - 0.5 m; Spectral - 2.4 m: coastal, B, G, Y, R, Red edge, NIR-1, NIR-2	PAN - 0.5 m; Spectral - 1.8 m: B, G, R, NIR

Source: Produced by the author.

As already mentioned, we adopted an object-based approach instead of a pixel-based analysis for both LiDAR and VHR analysis. To delineate the ITCs using the LiDAR data, we applied the voronoi-based method (*FindTreesCHM* and *ForestCAS* functions) from the *rLiDAR* R-package (SILVA et al., 2017). More details on ITC delineation are described in the Supplementary Material 1. The pre-logging LiDAR CHM was used as the input because the tree crowns from logged trees were still intact.

To characterize canopy height changes associated with tree loss events and to define a threshold to detect canopy tree loss from logging, we assessed the LiDAR CHM height difference between the acquisitions ($\Delta\text{CHM} = \text{CHM}_{\text{date2}} - \text{CHM}_{\text{date1}}$) considering 172 ground-mapped logged trees. Tree geolocation was acquired by the forest concessionaire in 2015, prior to the logging activities that occurred in August 2016, using a Garmin 64S handheld global positioning system (GPS) (~10 m precision). We assessed the distribution of most negative height differences in a 30 m radius around logged trees ($n = 172$) and around non-logged trees areas ($n = 146$). This radius was chosen to account for (1) tree coordinate displacement due to GPS location error and differences of geo-location between tree trunks and crowns, and (2) displacement between tree coordinates and the areas actually impacted by the tree losses. To ensure that the non-logged tree areas did not overlap with each other nor with areas included within logged trees' radii, we randomly distributed points across the area at least 60 m away from the logged tree coordinates and from each other. We defined the ΔCHM threshold that maximally separated the distributions of height difference from logged and non-logged areas by fitting a logistic regression model and inspecting the results.

Using the ΔCHM threshold, we detected tree losses associated with logging and generated the LiDAR-based tree loss map. To assess how far the detected tree loss events occurred from logged trees, we analyzed the nearest neighbor distances between the two datasets. We also calculated the rate of tree loss occurrence per area and the percentage of canopy change between 2015 and 2017.

5.3.2 Tree Loss Detection using VHR Satellite Data and RF Model

5.3.2.1 Satellite Data Acquisition and Preprocessing

We acquired VHR satellite data of the study area during 2014 (WorldView-2) and 2017 (GeoEye-1) (Table 5.1). The intersection of the two images covered an area of 76.6 km², of which 1.4 km² overlapped with the LiDAR data of UPA-06 forests (Figure 5.1). In order to convert the VHR data into surface reflectance, we applied the 6S radiative transfer model (VERMOTE et al., 1997). This was conducted using the *OpticalCalibration* function implemented in the Orfeo Toolbox (OTB) 6.4 (GRIZONNET et al., 2017). After the correction, we selected only the blue, green, red, and near infrared (NIR) bands, because these bands were available for both GeoEye-1 and WorldView-2 satellites. To resample the pixel size of the multispectral data at the resolution of the panchromatic imagery (0.5 m), we applied the Bayes data fusion method (FASBENDER et al., 2008) implemented in OTB 6.4. This fusion method is a probabilistic approach that combines the higher spatial resolution from the panchromatic band with the spectral bands. It is considered one of the best methods for preserving the spectral information from VHR satellite images when compared to other traditional fusion methods (FASBENDER et al., 2008).

In order to match the tree crowns between LiDAR and satellite datasets, we co-registered (i.e. aligned) the VHR satellite data with the LiDAR CHM. Only a translation of a few pixels was necessary to match the datasets. As the pair of images was acquired under different sun-sensor geometry angles and by different sensors (Table 5.1), to ensure that the signals of VHR satellite images were comparable, we normalized the post-logging image based on the pre-logging image. The normalization was done using the histogram matching method by the *histMatch* function from the *RStoolbox* R-package (LEUTNER et al., 2018). This method extracts the cumulative distribution functions from both images, adjusting the target histogram as a function of the source histogram.

5.3.2.2 Selection and Extraction of VHR Satellite Metrics

In addition to the reflectance of the spectral bands, we calculated two widely used vegetation indices to explore forest structural changes: the normalized difference

vegetation index (NDVI) (ROUSE et al., 1974) and the enhanced vegetation index (EVI) (HUETE et al., 2002). Since shade is known to be associated with tree mortality (ANDERSON et al., 2010), we also calculated a set of shadow metrics to be used in the modelling. To detect the shadow, we employed a simple thresholding method using the NIR band of the post-logging VHR image. We manually sampled shaded ($n = 100$) and non-shaded ($n = 100$) pixels to define a threshold separating the two classes. The threshold was determined considering the first percentile of NIR reflectance (NIR = 0.21) that covered the non-shaded pixels. Hence, all pixels with values below this threshold were classified as shadow. This shadow map was later used to calculate shadow metrics for RF modelling after performing the ITC delineation.

Using the NIR band from the pre-logging VHR data, we delineated ITCs with the marker-controlled watershed segmentation (MCWS) method. The *vwf* and *mcws* functions from the *ForestTools* R-package were used (PLOWRIGHT et al., 2018) (more details in Supplementary Material 1).

Based on the LiDAR-based tree loss map, we selected ITC samples representing tree loss and non-tree loss events ($n = 200$ each) to train the RF model. The tree loss samples were collected randomly from the LiDAR tree loss map. To collect non-tree loss samples, we selected samples at least 5 m away from the LiDAR tree loss detections to minimize potential mismatches of tree crown locations between LiDAR and VHR data. Then, we extracted the VHR satellite data (reflectance of the red, green, blue, and NIR bands; NDVI and EVI; and shadow) from date1 and date2 for each sample.

Using the extracted data, we created a total of 18 metrics for RF modelling. Since each ITC contains hundreds of pixels, we first summarized the values inside the ITCs of each of the four reflectance bands and two vegetation indices by calculating the mean and standard deviation (SD); then, we calculated the mean and SD differences (date2 – date1) metrics for each attribute. For the shadow attribute, considering only the values from date2, we calculated six metrics to describe the distribution of shadows inside the tree crowns. The first metric was the shadow fraction, which consisted of the ratio between the area occupied by shadow pixels and the total ITC area. The shadow pixels inside ITC were segmented and the segments were analyzed to create the remaining five metrics:

number of segments and maximum, mean, median, and SD of segments' size. To remove noise, we filtered out segments consisting of only one pixel.

5.3.2.3 RF Model

RF is a machine-learning algorithm, which consists of an ensemble of decision trees (BREIMAN, 2001). RF reduces the prediction variance by using a large number of decision trees. We trained RF models using 18 VHR satellite metrics as predictors to classify 400 samples as tree loss or non-tree loss events. This was performed using the *randomForest* R-package v4.6-12 (LIAW; WIENER, 2002). Thus, to create the model, we generated 1000 decision trees; each tree was created using a random subset consisting of 2/3 of the samples; and for each node of a tree, only three from the 18 predictors were randomly chosen for that node classification.

Since each decision tree has a classification response for a given sample, the ensemble of responses corresponds to a pseudo-probability for classifying that sample as tree loss or non-tree loss. In general, the majority of votes is chosen as the response. However, since our classification problem was binary (presence or absence of tree loss) and our interest was to optimize the precision (inverse of commission error) of the tree loss occurrence class, we used a weighted voting approach towards this class, minimizing commission errors, but increasing omission errors. Finally, we applied the model to predict the class of every ITC and create a satellite-based tree loss map.

5.3.2.4 Validation of the Satellite-Based Tree Loss Map

To validate the satellite map, we used the LiDAR map as a reference. We intersected both maps and obtained the number of true positives (*TP*), false positives (*FP*), and false negatives (*FN*). *TP* is defined as the number of ITCs correctly identified by the satellite map, judged by whether they intersected with the ITCs of the LiDAR map; *FN* is the number of ITCs not identified by the satellite map, but identified by the LiDAR map; and *FP* is the number of ITCs incorrectly identified by the satellite map, i.e., ITCs which do not occur in the LiDAR map. For the intersections, we used a small buffer of one meter around the tree loss

detections to minimize effects of artificial tree crown displacement between satellite and LiDAR datasets. To evaluate the accuracy of the model, we used TP , FP , and FN to calculate two accuracy metrics: precision (P) and recall (R) (Eq. 5.1 and 5.2). Precision is the inverse of the commission error and measures how much of the satellite detections coincided with the LiDAR detections. The recall is the inverse of omission error and measures how many ITCs of the LiDAR map were detected by the satellite map.

$$P = TP/(TP + FP) \quad (5.1)$$

$$R = TP/(TP + FN) \quad (5.2)$$

We performed additional analyses to explore the model sensitivity to random sampling and tree loss probability cutoff, the spatial dependence of detections between satellite and LiDAR maps, variable importance for modelling, and sensitivity of detections to vertical structure change and tree height. To explore the model sensitivity to sampling, we trained 30 RF models using different random sampling runs. The accuracy metrics (P and R) from the models were aggregated into mean and 95% confidence intervals. To explore the tree loss probability cutoff sensitivity and select a threshold to generate a map, while ensuring that the model predictions had a high precision, we assessed the model performance as a function of the RF tree loss probability ranging from 0.5 to 0.95.

As an independent measure of detection capability, we tested if there was significant spatial dependence between tree losses detected by VHR satellite imagery and LiDAR data. For this purpose, we extracted the nearest neighbor distances between the tree loss detections of the two maps, and compared the cumulative distribution of nearest neighbor distances with a completely random (Poisson) point process. We simulated 199 realizations of the random point process using a Monte Carlo approach and created an envelope of complete spatial randomness (CSR) with a 1% significance level. This was done using the *envelope* and *Gcross* functions from the *spatstat* R-package v1.47 (BADDELEY et al., 2015). If the observed distribution was located inside the CSR envelope, that would mean that VHR satellite detections occurred independently in space from the LiDAR detections and vice versa.

The sensitivity of detection success to vertical structure change and tree height was assessed by exploring the LiDAR CHM pre- and post-logging heights, and Δ CHM over correct VHR satellite detections.

Finally, to explore the importance of the different VHR satellite variables for the modelling, we ranked the variables according to the mean decrease accuracy (MDA) metric (BREIMAN, 2001). Once each node had been determined in a decision tree, this metric was computed by removing a single variable from the pool of variables and assessing the decrease in the model accuracy. The mean and 95% confidence interval of MDA for each variable were computed for the 30 models. The variables with the largest MDA were ranked highest in importance. To further test whether a variable was significantly important in the voting process of the RF, we compared the observed MDA versus a null distribution of MDA. We created this null distribution by running the model 30 times while shuffling the sample responses randomly. This was performed using the *rfPermute* v2.1.6 R-package (ARCHER, 2018). We reported which variables showed MDAs significantly different from the null distribution considering a 5% significance level.

5.3.3 Assessment of Tree-Fall Gaps Recovery Using LiDAR Data

Following the assumption that the VHR detection of tree loss events depends on the observation of forest canopy gaps created by the tree-falls, and given that gaps recover over time through new recruitment and recovery of existing trees, we expect a time dependence between the tree loss detection and the time since disturbance. Therefore, we investigated the rate and mechanisms of gap closure over time using a time series of airborne LiDAR observations of a 1.04 km² forest section collected in 2011, 2013, 2014, 2015, and 2017 over UPA-01 (Table 5.2 and area B in Figure 5.1), which was logged during 2010 and 2011. We processed the data to obtain the LiDAR CHM for each date following the same procedures described in section 5.3.1.

Table 5.2 - Acquisition details of Airborne LiDAR data used for gap recovery analysis.

Information	2011	2013	2014	2015	2017
Laser Scan Sensor	Optech 3100	Optech, Orion	Trimble, Harrier 68i	Optech 3100	Optech ALTM Gemini
Acquisition Date	17 Nov 2011	20 Sep 2013	09 Oct 2014	21 Sep 2015	20 Apr 2017
Acquisition Altitude (m)	850	853	500	750	700
Scan Frequency	59.8 kHz	67.5 kHz	400 kHz	100 kHz	100 kHz
Off-Nadir Angle	11.1 °	11.1 °	15 °	15 °	15 °
Point Cloud Density m⁻²	15.43	15.48	30.39	33.63	12

Source: Produced by the author.

We defined canopy gaps as holes in the forest canopy extending up to 10 m in height above the ground and with at least 5 m² of contiguous area. Although this height threshold is higher than the classic Brokaw's gap definition of 2 m height above ground (BROKAW, 1982), previous studies of gap dynamics with airborne LiDAR in tropical forests showed that gaps extending up to different heights above ground, e.g. 10 to 11 m, were consistent with gaps observed in the field, (GOULAMOUSSENE et al., 2017; LOBO; DALLING, 2014). Following previous studies (LOBO; DALLING, 2014), the minimum gap area was chosen as a small value (5 m²) in order to assess the gap filling variability from smaller to bigger gap sizes. Moreover, the optimal choice of height and minimum area varies across forest types. Hence, the gaps were delineated as follows: (1) all CHM pixels with a height below 10 m were classified as gaps; (2) the pixels defined as gaps were segmented into polygons; (3) polygons were filtered for a minimum area of 5 m². Since the logging activities in 2010 and 2011 occurred earlier than the first LiDAR acquisition in 2011, we were unable to exactly extract the areas affected exclusively by the selective logging. Thus, to prioritize the observation of logging disturbance rather than gaps caused by natural mortality, we only selected gaps occurring within a 30 m distance from the logged tree's locations in UPA-01 ($n = 215$).

To estimate the rate of gap closure over time, we calculated each gap's relative size with respect to its initial size in 2011. We extracted the average gap size change considering all gaps, but also by size classes of up to 25, 25–50, 50–100, 100–500, and larger than 500 m². We defined gap closure as decreases of gap

size over time. This means that the vegetation inside the gap is reaching an average height of 10 m. In addition, we estimated the gap fraction (percentage of area occupied by gaps) for each year and the percentage of gaps that have fully closed.

To improve our understanding of the mechanisms of gap filling, we also assessed the percentage of height gains and losses inside gaps and whether the gaps closed by horizontal and/or vertical vegetation regrowth. To separate vertical from horizontal growth, we followed the procedures described in Hunter et al. (2015). First, we estimated a maximum possible tree height growth rate per year, which we defined as the mean plus three standard deviations of the mean height change inside gaps. Then, we applied this threshold to classify pixels inside gaps as horizontal (height change above maximum growth) or vertical growth (height change below maximum growth). Horizontal growth means the ingrowth of trees to the sides instead of actual growth in height. For those pixels classified as vertical growth, we estimated an average growth rate. To estimate the maximum tree height growth and obtain a stable estimate, we only extracted the values from pixels near to the center of the gaps, that is, at least 5 m from the edges. Therefore, the smaller gaps were not included in this estimate.

5.3.4 Landscape Analysis of Satellite-Based Tree Loss Map

We applied the VHR satellite data and RF model to detect tree loss events for the whole study area. This area is much larger (area = 76.6 km²) than that analyzed in section 5.3.2 (1.4 km²). Thus, in order to be able to visualize the spatial distribution of tree loss events, we created a map using the isotropic kernel-smooth density estimator for aggregating the events into cells of 100 × 100 m (DIGGLE, 1985). We identified areas of greater tree loss occurrence (hotspots) according to the Z-score statistic, the absolute difference between each pixel's tree loss value, and tree loss mean normalized by the standard deviation and a 5% significance level. To compare our results with an independent source of disturbance mapping, we acquired the global forest cover loss 2000–2017 dataset (available at <https://earthenginepartners.appspot.com/science-2013-global-forest>). This product, created by Hansen et al. (2013) using Landsat data

(30 m spatial resolution), has been widely used for forest disturbance monitoring around the world.

We assessed and compared the number of tree loss events inside each UPA and the undisturbed forest areas. The undisturbed forests were those outside of UPAs, excluding water bodies and deforestation up to 2017, according to the INPE-PRODES deforestation product (INPE, 2018). We also excluded areas of cloud cover of the pre-logging image by manually delineating the clouds using a true-color composite. We estimated the canopy turnover time simply as the ratio of the average number of ITCs (canopy tree crowns) to the annualized number of tree losses per unit of area.

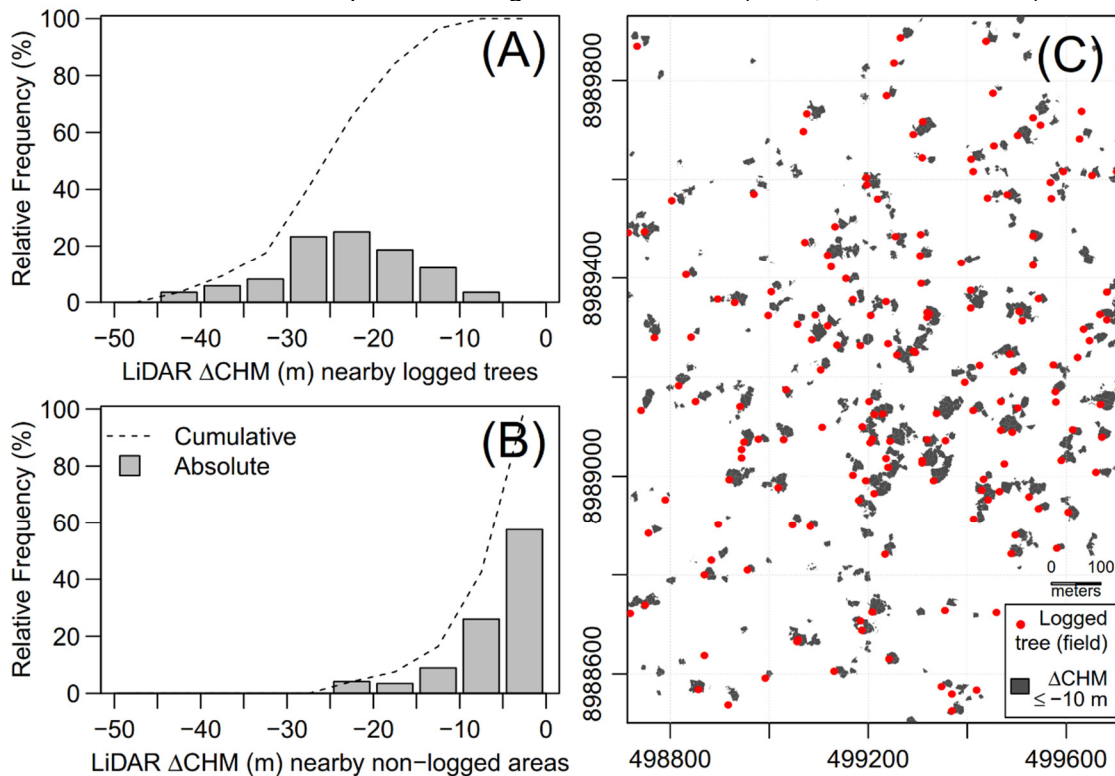
To explore how much of the variability of satellite tree loss detections is explained by the logged trees recorded in the field dataset, we used the same kernel approach to estimate the density of logged trees inside the managed areas (UPA-01, UPA-06, UPA-10, and UPA-11). We then overlaid the two maps and extracted the pixel-by-pixel density of tree loss events from satellite and field estimates. The relationship between the two variables using linear regression models was then assessed.

5.4 Results

5.4.1 Detecting Tree Loss Events Using LiDAR Data

We observed LiDAR Δ CHM ranging from -5.6 to -42.2 m, with a mean of -23.5 m, for the ITCs nearby (within 30 m of distance) the 172 logged trees in Jamari National Forest (Figure 5.3A). For the non-logged areas ($n = 146$), we noted a distribution of Δ CHM values ranging from -0.3 to -22 m, with a mean of -5.9 m (Figure 5.3B). This means that, between 2015 and 2017, the largest canopy changes occurred nearby logged trees' locations. The distributions in Figures 3a and 3b did not show positive values because we only assessed the most negative height difference in the area's neighborhood.

Figure 5.3 - Tree loss detection using LiDAR Δ CHM in the Jamari National Forest over the UPA-06. Relative frequency of the most negative Δ CHM within a 30 m radius of (A) logged trees and (B) non-logged areas. (C) LiDAR-based tree loss map considering Δ CHM ≤ -10 m (UTM, datum WGS-84).



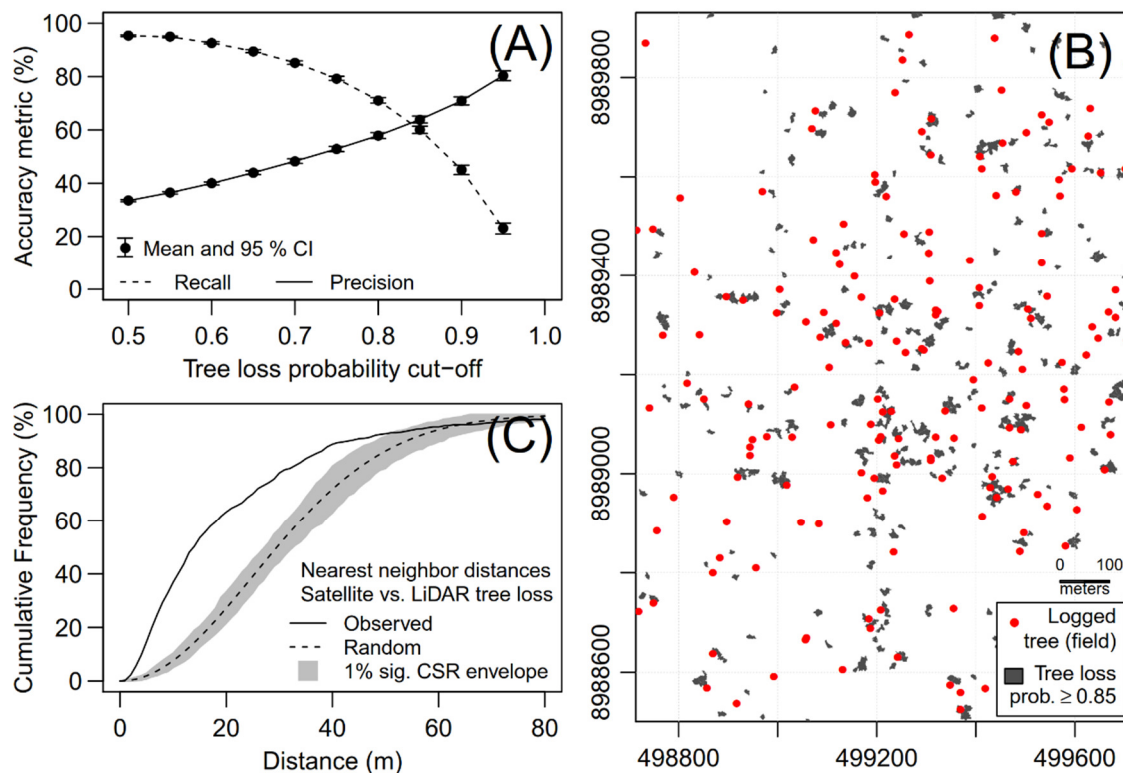
Source: Produced by the author.

We obtained a Δ CHM threshold of -10 m, where 96.5% of the logged trees ($n = 166/172$) were detected and only 16.4% of the non-logged random areas were misattributed ($n = 24/146$). Using this threshold, 888 tree loss events (634 trees km^{-2}) were detected between 2015 and 2017 (Figure 5.3C). This corresponded to a canopy change of 6.15% in terms of area. While this detection rate was larger than the number of logged trees of 172 trees (122 trees km^{-2}), it also included trees that were eventually killed during the logging activities and tree losses from natural mortality that occurred during the studied period. This rate was likely also influenced by the average overestimate of the number of trees of about 30% (Supplementary Material 1). Nevertheless, the detected tree loss events occurred predominantly nearby logged trees' location, with an average nearest neighbor distance of 25.86 m, while only 10% of the tree loss events were located farther than 50 m from the logged trees (see also Figure 5.3C).

5.4.2 Detecting Tree Loss Events Using VHR Satellite Data and RF Model

We trained RF models using VHR satellite data to detect tree loss or non-tree loss areas (Figure 5.4). Overall, we observed that an increase in the cut-off of tree loss occurrence probability (0.5 to 0.95) was associated with an increase in precision (33 to 80%) and a decrease in recall (95 to 23%) (Figure 5.4A). Given that a useful model requires high precision, we chose a tree loss probability cut-off of 0.85, which resulted in a moderate-to-high precision of 63.9% (95% CI: 62.6%, 65.2%), and a moderate recall of 60.1% (95% CI: 58.7%, 61.4%). Thus, taking the LiDAR map as a reference, on average, 64% of the satellite detections were correct, and more than half (60%) of the total tree losses were detected.

Figure 5.4 - Tree loss detection using VHR satellite data and RF model in the Jamari National Forest over the UPA-06. (A) Detection accuracy as a function of the tree loss probability cut-off. (B) Satellite-based tree loss map considering a tree loss probability ≥ 0.85 (UTM, datum WGS-84). (C) Nearest neighbor distances between satellite and LiDAR tree loss detections, as a function of distance (m). The gray area represents a CSR envelope with a 1% significance level ($n = 199$).



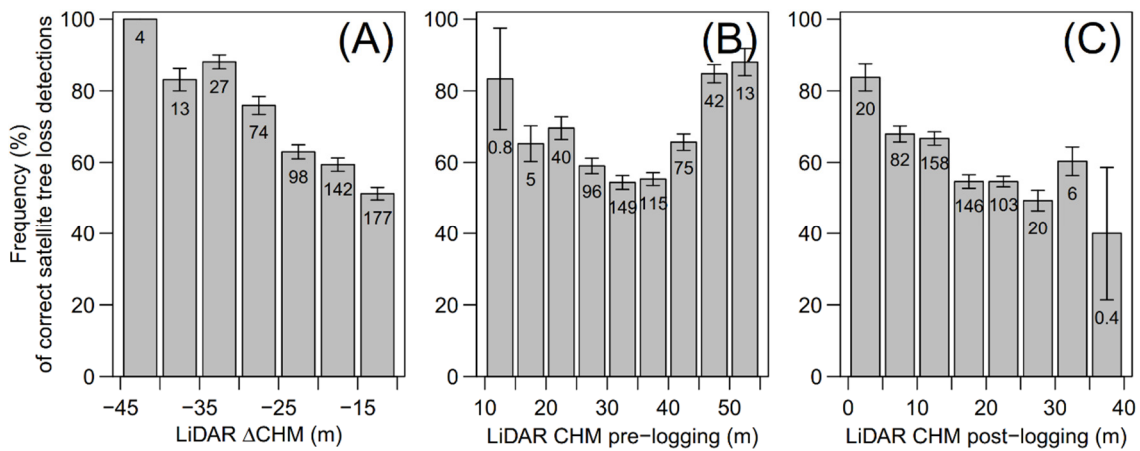
Source: Produced by the author.

We generated a map using the average of the 30 RF models and a tree loss probability cut-off of 0.85 (Figure 5.4B). This map detected 357 tree loss events (255 trees km⁻²), of which 74.5% intersected the tree losses detected in the LiDAR

map, and 25.5% did not intersect it (commission errors). Part of these errors should represent actual tree losses captured by the VHR satellite data due to its extended observation period in comparison to LiDAR data (Table 5.1). We detected 50.8% of the tree loss events from the LiDAR map (omission error of 49.2%). The detections corresponded to 2.55% of canopy area change between 2014 and 2017. Even though, in this map, we only detected 51% of the total tree loss events, the satellite detections were predominantly located nearby LiDAR detections, with a mean nearest neighbor distance of 21.2 m (95% CI: 19.8 m, 22.7 m) (Figure 5.4C). Moreover, the observed distribution of nearest neighbor distances between the two maps (solid line in Figure 5.4C) lied beyond the upper-part of the 1% significance CSR envelope ($p < .01$), which meant that the satellite detections were not simply randomly distributed, but were clustered with the LiDAR detections (Figure 5.4C).

The accuracy of satellite tree loss detections was sensitive to the magnitude of changes in the vertical structure of the canopy and size (height) of the trees (Figure 5.5). Tree losses with higher Δ CHMs (-45 to -25 m) were more easily detected ($> 75\%$ frequency) compared with tree losses with lower Δ CHMs (-25 to -10 m) (45 to 60%) (Figure 5.5A). Tree losses from the tallest trees (≥ 45 m) were more successfully detected ($> 80\%$) than for other height classes (Figure 5.5B). However, the high accuracy for the shortest trees (10–15 m) was probably associated with the low average number of samples ($n = 1$) and does not truly mean a higher accuracy for this height class. Finally, tree losses that created deep gap openings (0 to 5 m height above ground) were the most successfully detected ($> 80\%$) (Figure 5.5C).

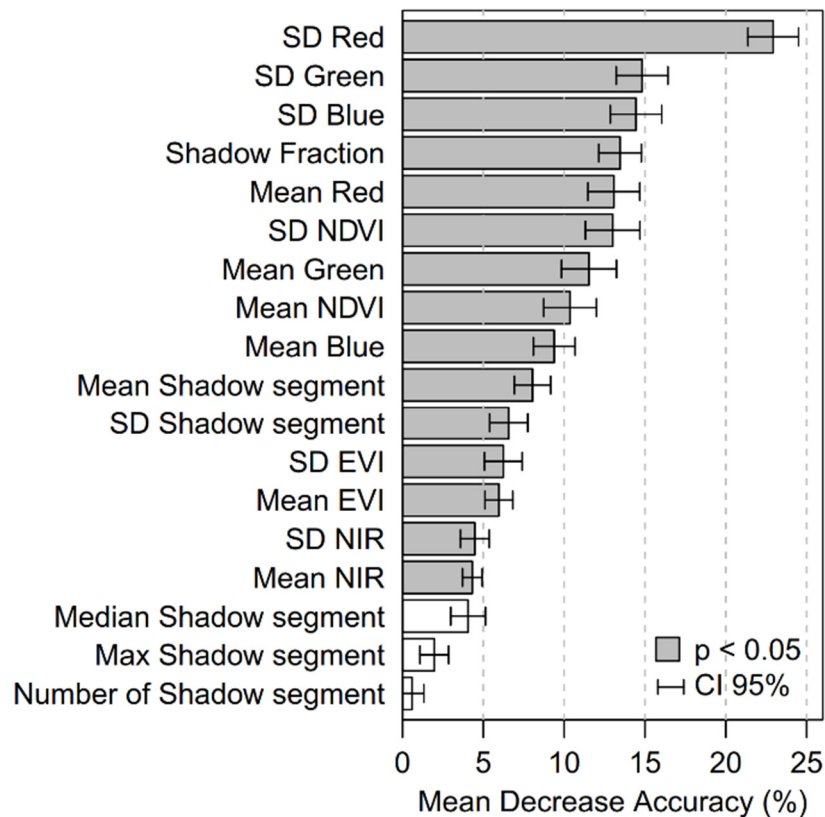
Figure 5.5 - Relative frequency of correct satellite tree loss detections for intervals of (A) LiDAR CHM height differences (Δ CHM), (B) LiDAR CHM pre-logging, and (C) LiDAR CHM post-logging. Mean and error bars (95% confidence interval) were calculated considering the 30 model runs. Numbers inside bars represent the average number of crowns among the 30 model runs.



Source: Produced by the author.

Variables used in the RF modelling were ranked for importance according to their MDA (Figure 5.6). The SD of the red band was ranked highest (23% MDA) among all the variables. In general, the SD metrics were ranked higher than the mean metrics, and the most important variables were the SD of the three visible spectrum bands (Red, Green, Blue), followed by the shadow fraction, mean of visible bands, and SD and mean NDVI. Meanwhile, the NIR band and EVI were the least important of the significant variables ($p < .05$). Only the median, max, and number of shadow segments variables did not significantly contribute to the model ($p > .05$).

Figure 5.6 - Variables' importance derived from the RF model using VHR satellite data to map tree loss events in Jamari National Forest ranked by their MDA. SD corresponds to the standard deviation.

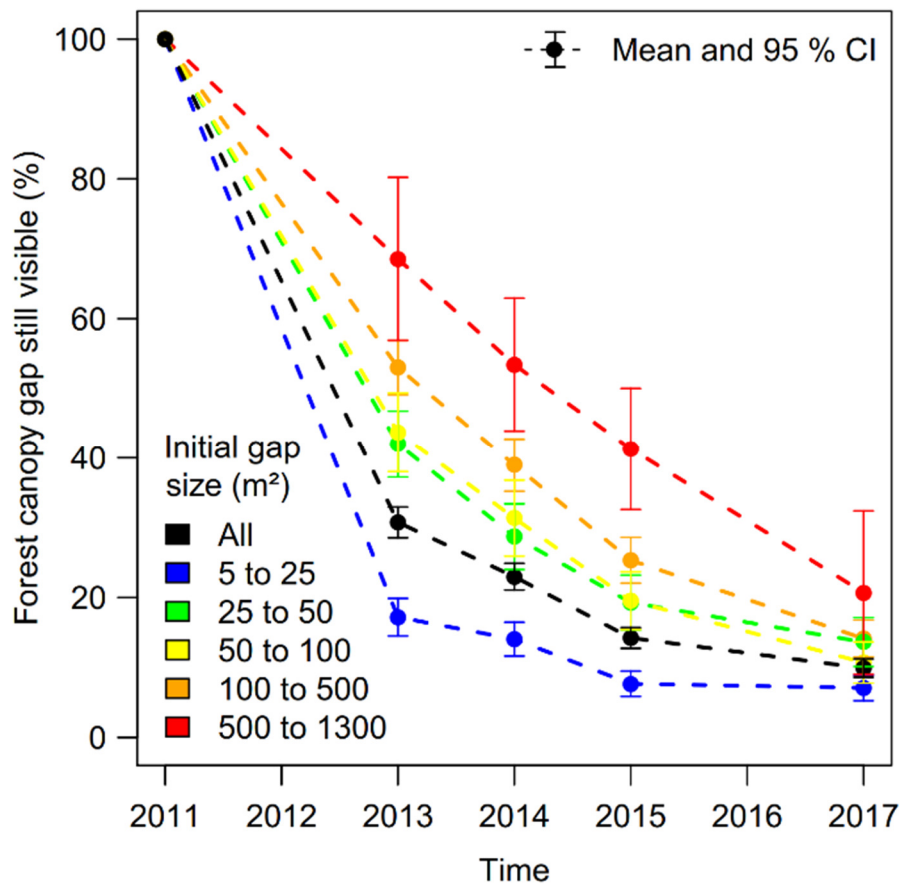


Source: Produced by the author.

5.4.3 Tree-Fall Gap Recovery Assessment Using LiDAR Data

We delineated 724 canopy gaps in the 1.04 km² of forests inside UPA-01 in Jamari National Forest using the LiDAR data of 2011. The detected gaps were predominantly small: 55.3% from 5 to 25 m², 16.4% from 25 to 50 m², 8.8% from 50 to 100 m², 18.5% from 100 to 500 m², and 1% from 500 to 1300 m². From 2011 to 2017, the total gap fraction decreased from 4.61 to 1.96%, whereas 63% of the initial gaps completely closed (Figure 5.7). The average rate of gap filling was 35.4% yr⁻¹ considering all gap sizes and 30% yr⁻¹ when excluding smaller gaps (area < 25 m²). After 1.8 years (2011–2013) and 5.4 years (2011–2017) of recovery, the average gap size consisted of 47% and 13% of their original size, respectively, excluding smaller gaps (area < 25 m²). Therefore, larger gaps were still visible after ~2 years of recovery, but were almost completely closed and invisible after ~5 years.

Figure 5.7 - Filling of forest canopy gaps over time (2011 to 2017) in Jamari National Forest (UPA-01), as a function of the initial gap size class (m²).



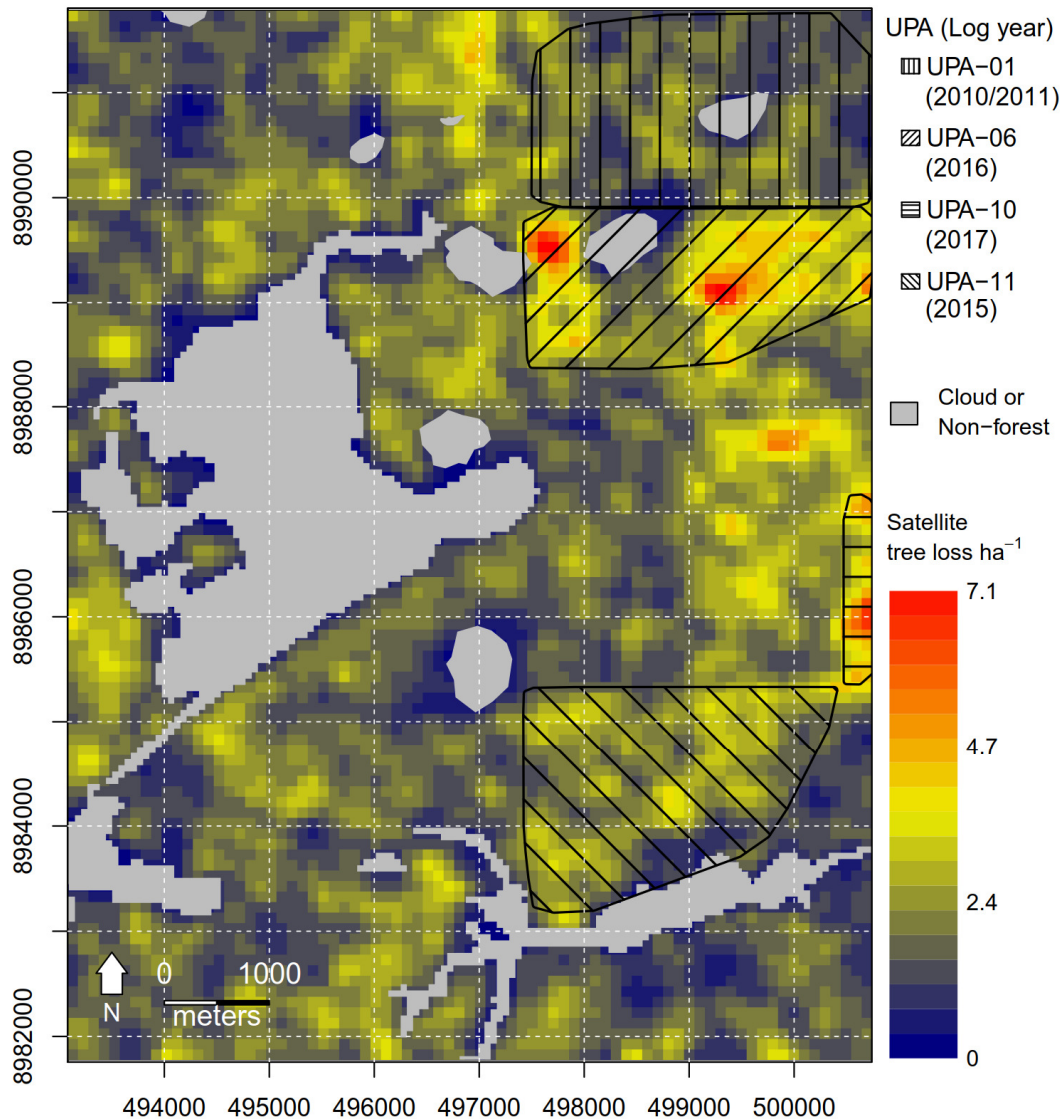
Source: Produced by the author.

We found that 23.3% of pixels inside gap areas experienced further height loss over time. These were probably caused by delayed mortality of remaining vegetation, natural disturbances, or the decomposition of trees that were killed during logging activities. The majority of pixels (76.7%), however, showed height gain. We estimated a maximum vertical growth rate of 3.9 m yr⁻¹ from 2011 to 2013 considering only the gap centers. Using this threshold to separate horizontal from vertical tree growth inside gaps, we estimated that horizontal ingrowth (height change > 3.9 m) corresponded on average to 21.2% of the height gains. The remaining 78.8% of height gains were due to vertical tree growth, with an average growth rate of 1.65 m yr⁻¹ (SD = 0.6).

5.4.4 Landscape Analysis of Satellite-Based Tree Loss Map

Using the VHR satellite data and the RF model, we mapped tree losses over a larger area (76.6 km²) of the Jamari National Forest than covered by LiDAR (Figure 5.8). We found that tree losses were widespread and only a few areas exhibited hotspots of losses up to 7.1 trees ha⁻¹ (red in Figure 5.8): two at UPA-06 and one at UPA-10. Another area outside of the UPAs, located at undisturbed forests near UPA-06 and UPA-10, showed an unexpected higher frequency of tree loss (5.15 trees ha⁻¹).

Figure 5.8 - Satellite-based tree loss map during 2014–2017 for a section of 76.6 km² inside the Jamari National Forest (UTM, datum WGS-84). The background corresponds to the isotropic kernel-smooth density of satellite-based tree losses per hectare. Black lines are the boundaries of the UPAs.



Source: Produced by the author.

We observed a greater frequency of tree loss events (1.63 to 4.39 trees ha⁻¹) inside UPAs compared to the frequency of field logged trees (1.28 to 2.21 logged trees ha⁻¹) (Table 5.3). In addition, tree loss events occurred more frequently (3.08 to 4.39 trees ha⁻¹) in the recently logged areas (UPA-06 and UPA-10) compared to the other UPAs, even though they had the lowest frequency of logged trees in the field (1.28 to 1.38 logged trees ha⁻¹). This was clearly seen in Figure 5.8, where these two UPAs were the only ones with hotspots. Furthermore, the undisturbed forests exhibited a similar but slightly greater frequency of tree loss (1.8 trees ha⁻¹) as UPA-01 (1.63 trees ha⁻¹), but less than the rest of the UPAs. The most likely explanations for the lower frequency of detections in UPA-01 were that the forest in this area had a long time to recover since logging occurred in 2010/2011, and that the logging process removed the tallest trees at the canopy level. Meanwhile, these trees are those that open the largest gaps when they fall. Based on the tree losses over undisturbed forests during the interval between VHR images (2.72 years), and the average number of ITCs (85 trees ha⁻¹), we inferred a canopy turnover time of 129 years. The global forest cover loss product from Landsat data (30 m resolution) did not show any forest loss over the study area.

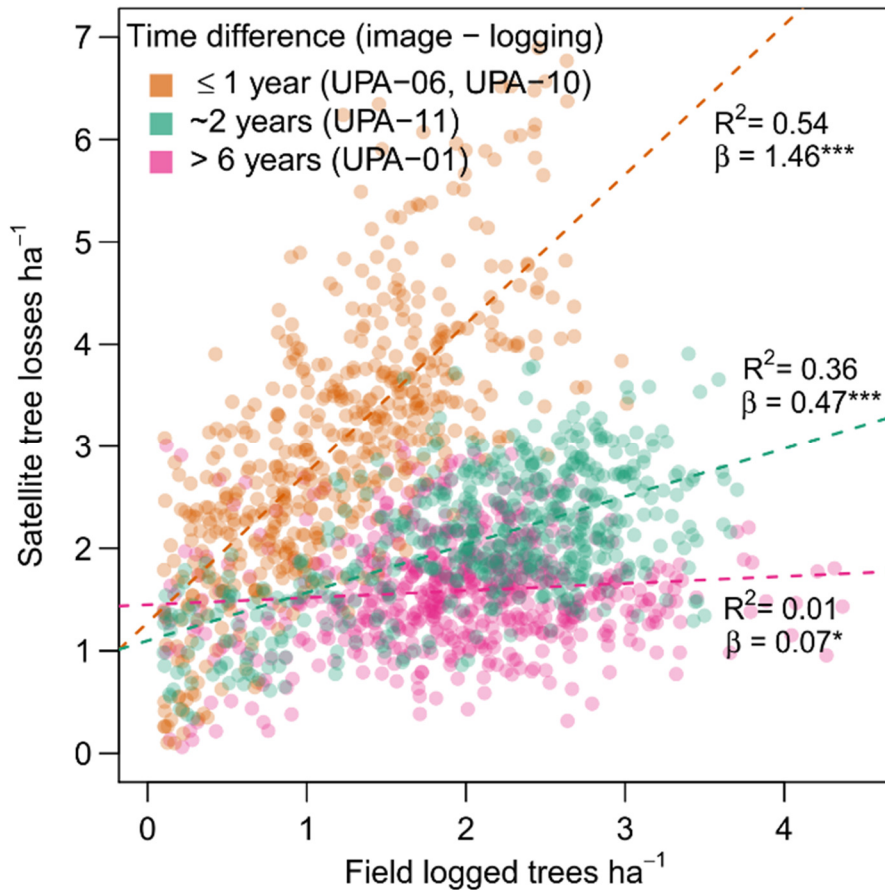
Table 5.3 - Frequency of satellite-based tree loss events and field logged trees per hectare for the UPAs and undisturbed forests.

Region	Area (ha)	Satellite – 2017 (Tree Losses ha ⁻¹)	Field – Multiple Years (Logged Trees ha ⁻¹)
UPA-01 - Logged in 2010/2011	554	1.63	2.08
UPA-11 - Logged in 2015	495	2.15	2.21
UPA-06 - Logged in 2016	426	3.08	1.28
UPA-10 - Logged in 2017	47	4.39	1.38
Undisturbed Forest	5052	1.80	-

Source: Produced by the author.

When we overlaid the kernel density estimates of satellite tree losses and field logged trees of the UPAs, we found that the field logged trees explained part of the satellite tree loss variability for areas that were logged less than one year ($R^2 = 0.54$) and two years ($R^2 = 0.36$) before image acquisition. The same was not verified for areas logged six years before image acquisition (Figure 5.9). The areas that had been logged up to two years before image acquisition also showed very significant regression slopes ($p < .001$).

Figure 5.9 - Relationship between satellite-based tree loss and field logged trees per hectare in the UPAs labeled by the time difference (years) between the logging and last image acquisition (2017). Each point represents a pixel of 100 × 100 m (1 ha) from which the estimates are extracted. Lines represent linear regression models between the two variables. Significance levels for regression slopes (β) are represented by asterisks: * $\leq .05$, ** $\leq .01$, and *** $\leq .001$.



Source: Produced by the author.

5.5 Discussion

Using a unique dataset of multi-date airborne LiDAR and VHR satellite data (pre- and post-logging), and a tree-by-tree field dataset of georeferenced logged trees, we showed that it is possible to use VHR satellite data to detect canopy tree loss associated with logging. Nonetheless, we advise caution regarding the image acquisition frequency. It can severely affect how well tree loss can be detected and, thus, the suitability of using these data for disturbance monitoring. We discuss each of the scientific questions in the paragraphs below.

Besides these general insights, our findings showed that logging drove pervasive changes in the canopy vertical structure. The estimated height difference threshold (-10 m) that we used to define tree loss using LiDAR data should represent a general approximation of the minimal logging impacts to the forest structure. It could be applied in other studies for rough estimates of canopy tree loss. However, we recommend additional tests in other study sites for more precise detection. In a study of forest dynamics in Tapajós National Forest, located in central-east of the Brazilian Amazon, Leitold et al. (2018) found a mean height difference of -11.7 m corresponding to natural tree-fall events from single or multiple trees. While this value was similar to our height difference threshold, it was only half of the mean height difference that we found. This could indicate that even though logging conducted at Jamari Forest is considered “low-impact”, these human-disturbances cause more drastic changes to the forest structure than small-scale natural disturbances. This corroborates the findings from Johns et al. (1996), who observed high impacts over non-targeted trees even when planned logging activities have been performed. During the logging of a single tree, up to five neighbor trees have been smashed or severely damaged. Because part of this ancillary mortality and damage is caused by felling, this mortality will be associated with the same gap as the target tree. This may increase the detectability of the targeted-tree mortality.

Our results show that tree losses associated with logging and other disturbances, most probably natural, can be automatically mapped using VHR satellite imagery and the RF model with an average precision of 64%, while capturing 60% of the events detected by the LiDAR dataset. Even though the accuracy is not optimal, the detected tree losses show a strong spatial correlation with LiDAR detections and logged trees coordinates. Since the model accuracy varied with the model probability cutoff, this parameter must be chosen carefully. It is important to note, however, that our imagery had distinct sun-sensor geometry properties, with a big difference in sun elevation angles between images (~ 20 degrees), which affected the accuracy. The effects of such differences include the obfuscation of smaller trees by taller trees and potential attribution as a tree loss event. In a scenario where both images have a similar acquisition geometry, we expect an improved detection accuracy. Our specific pair of images has a specific set of

view and illumination angles that are unlikely to be replicated when another user attempts to apply your approach. This points to a future paper idea that could investigate the contribution of all these factors to the success of gap detection.

Nevertheless, this result, based on an automatic detection algorithm, advances the visual analysis and manual delineation of tree mortality of Read et al. (2003) and Clark et al. (2004a, 2004b), and opens up new venues for monitoring small-scale disturbances.

The sensitivity of our VHR satellite tree loss detection methodology increased with the presence of more pervasive changes to the canopy, such as bigger gap openings and loss of the tallest trees. Because large trees store most of the aboveground biomass in tropical forests (BASTIN et al., 2018), these disturbances are likely the most impactful to carbon loss. The accurate detection of these bigger events enables the identification of disturbance hotspots, where multiple small-scale events may be occurring locally and simultaneously. Furthermore, our results confirmed the possibility of detecting some of the tree-falls that do not create gaps following Brokaw's definition of ≤ 2 m height above ground (BROKAW, 1982).

Seasonality effects on plant phenology can reduce our ability to extract biophysical information from remote sensing observations in the Amazon (MOURA et al., 2017). Without tree-by-tree phenology field data to support a proper analysis, we are unable to determine the exact impact of seasonality on our detection, but we expect that it may have a minor to moderate impact. Trees that are leafless in one of the two images, or have completely different colors, due to flowering, could indeed be erroneously attributed as a tree loss event. However, if these effects occur roughly at random across the forest, because of the high tree species diversity in tropical forests, they would not prevent the detection of hotspots associated with disturbance. This is because these occur more clustered in space and time. A way to reduce seasonal effects on detection is to fix the multi-year imagery analysis within a fixed period, e.g. dry season.

The most important VHR satellite metrics for tree loss detection were the SD of the reflectance of the visible bands and the shadow fraction and amongst those, especially the red band. The fact that these SD metrics were more important than the mean metrics suggests that there were marked increases in spectral

variability in tree loss areas due to logging. This variability is associated with shadows cast by nearby trees, and the signal mixture from non-photosynthetically active responses of leaves, branches, and trunks, and possibly exposed soil. For the same reason, the shadow fraction turned out to be one of the most important variables. Other studies have also shown that shadow was related to tree mortality (ANDERSON et al., 2010). However, although shadow metrics were important in our study, their performance can vary in other study areas and across sensors, depending on the view-illumination geometry during image acquisition. In our case, we had large differences in solar elevation and azimuth between the two images, which could induce the creation of false new gaps (new shadow patches in the later image). This effect can increase the commission error.

Findings of this study also showed that tree loss detection depends on the time difference between disturbance occurrence and image acquisition, ideally of less than two years. This is explained by the slower in-filling and longer persistence of bigger gaps in the forest, up to five years or more, in comparison to smaller gaps (< 25 m²), which close up very rapidly. In either case, the lateral ingrowth was an important process for gap filling, especially for the smaller gaps. These results are corroborated by the findings of Hunter et al. (2015), which also show a strong influence of gap size on closure rates; as well as similar, or slightly higher, gap persistence estimates in two Amazonian forests sites: Ducke (8.1 years) and Tapajós (9.1 years). Our estimates of annual tree height gains inside gaps (mean = 1.65 m yr⁻¹, max. = 3.9 m yr⁻¹) were slightly higher than field observations of pioneer species commonly found in tropical forest gaps, e.g. *Cecropia* spp., mean = 1.2-1.5 m yr⁻¹, max 2-3 m yr⁻¹) (CLARK; CLARK, 2001). Nevertheless, hotspots were evident in our map in areas with time differences, between disturbance and image acquisition, up to one year. The implication of these findings for small-scale disturbances' monitoring is that disturbances associated with small gaps will most probably be underestimated unless annual imagery is being used.

Our satellite-based map of tree loss disturbances was spatially coherent. It showed a greater density of events in selective logging disturbed forests than in undisturbed forests. However, the rate of tree losses was up to three times greater than the on-the-ground determined logging rate and depended on the

time between disturbance and image acquisition. This is probably related to additional damage caused by logging onto the adjacent trees and natural mortality events. This agrees with findings by Johns et al. (1996). They found that at least half of the ancillary mortality caused by logging occurred at the felling site, i.e. near the targeted tree. Therefore, these rates may indeed cover the damage caused by logging and not only the number of felled and extracted trees. In addition, potential explanations for the observed hotspot of tree loss estimates outside the UPAs include: (i) the presence of a road that crosses that exact location – visible in the pre-logging image – which was likely used for timber transportation; (ii) preparation activities, e.g. opening of trails, for exploration of this area in the near future; and (iii) enhanced and/or delayed natural mortality associated with human-disturbances during the opening of the roads. Our estimate of canopy turnover time (129 years) was lower than the estimate of Hunter et al. (2015) for canopy trees at two central-east Amazon sites (300–370 years). This was probably because of our relatively high rate of omission errors (~40%). Nevertheless, we expect that the presented mapping approach using VHR satellite data can also be useful for the detection of hotspots of natural disturbance.

As a comparison exercise, we acquired and visualized the global forest cover loss product from Hansen et al. (2013) obtained from Landsat data (30 m resolution), and it did not show any forest loss over the study area, even over the managed forests. We believe that this indicates the potential advantages of using VHR imagery for small-scale disturbance detection and monitoring.

A caveat regarding the current mapping approach is the requirement of LiDAR data to calibrate the model before extending the VHR satellite estimates into larger areas. However, as shown in this study, LiDAR data acquisition in small areas can be used for this purpose. For example, in our experiment, the LiDAR calibration area covered 1.4 km² (1 by 1.4 km), while the VHR satellite imagery covered 76.6 km² of forests. Hence, the satellite imagery area was 55 times bigger than the LiDAR area, and has the potential to cover much larger areas, such as >5,000 km², with a single-pass of either WorldView-2 or GeoEye-1 satellites. In addition, further studies can take advantage of the recent technological advances associated with unmanned aerial vehicles to cover larger

areas at reduced costs, with caution to current constraints, e.g. space for taking off, landing, and piloting in dense forest environments. On the other hand, the current mapping approach using an RF model was primarily used as a benchmark to test the VHR imagery potential; other machine learning or statistical approaches, or, perhaps, simpler methods that bypass the calibration step, e.g. thresholding, are possible and should be tested for a more general application over different areas. In the absence of LiDAR data to be used as a reference for model training, other sources of publicly available training data should be considered. For instance, tree loss data at an individual level from forest inventories obtained by the Brazilian Forest Service and/or forest management concessionaires can be useful.

Although the study used WorldView-2 and GeoEye-1 satellite imagery for the experiment, the current method is not, by any means, restricted to these spectral data. The SWIR wavelength was not explored in this study due to the lack of this band in both satellite sensors. However, it could be useful for detecting potential increases in non-photosynthetically active vegetation after the tree loss. The mapping approach could be applied to other available VHR satellite data, e.g. Ikonos, QuickBird, WorldView-3, WorldView-4, and Planet satellites, or, indeed, to satellites to be launched in the near future. Moreover, the combined use of multi-sensors should be required to adapt the current method for detecting canopy tree loss and recovery at broader scales. In this context, the advent of the nanosatellite constellations is an alternative to obtain low-cost data at a very high spatial and temporal resolution. Band positioning and bandwidth should be considered in instrument selection for analysis. Using satellite constellations such as the PlanetScope (3-m resolution), one can obtain nadir-view observations. While contributing to reduce view-illumination effects on the mortality detection, the evaluation of the other factors associated with data intercalibration and spatial resolution requires further studies.

5.6 Conclusions

Logging activities disturb large areas in Amazon forests every year, affecting flora and fauna diversity, impacting forest structure and carbon balance, and enhancing fire probability. To address the remote sensing challenges of detecting

canopy tree loss associated with logging, we explored the use of multi-date VHR satellite imagery (≤ 1 m resolution) and airborne LiDAR to detect these events. Logging caused pervasive changes in the canopy vertical structure, with a mean of -23.5 m, but applying a simple LiDAR height difference threshold of -10 m was sufficient to map almost all the logged trees. We show that canopy tree losses associated with logging can be detected using VHR satellite imagery and an automated machine-learning method with an average precision of 64%. Events associated with large gap openings or tall trees were most successfully detected. The standard deviation metrics were the most important for the mapping, because they indicate change in spectral variability with the tree losses. The detection was also dependent on the time difference between the disturbance occurrence and the image acquisition, thus annual imagery acquisition is highly recommended. Our study showed the potential of VHR satellite imagery for monitoring the logging in tropical forests and detecting hotspots of natural forest disturbance with a low cost at the regional scale. Future research can build upon our work and improve the accuracy of detection using pairs of images with similar sun-sensor geometry properties, and testing additional satellite-based metrics, e.g. texture, and alternative modelling approaches.

6 MODELLING AMAZON TREE MORTALITY FROM LIDAR-BASED GAP DYNAMICS AND ENVIRONMENTAL-CLIMATE DRIVERS ⁶

Abstract: Large uncertainties in tree mortality estimates hamper our success in accurately quantifying climate change effects on the carbon balance. This concern is especially important over the Amazon, where tree mortality modelling is difficult due to the scarcity of ground data across different climatic domains. Airborne LiDAR surpasses the capacity of inventory plots in providing canopy gaps measurements over large areas, while potentially allowing estimates of tree mortality. Here, we generated a model accounting for the drivers controlling gap dynamics, combined with a gap-mortality relationship to quantify tree mortality rates across the Amazon. Specifically, we aimed to: (i) establish a relationship between LiDAR-derived gaps and mortality; (ii) provide a systematic assessment of gap dynamics and tree mortality rates based on their relationships with environmental-climate drivers; and (iii) scale-up tree mortality rates for the entire Amazon. To detect canopy gaps, we used 5 multi-temporal LiDAR datasets and 610 single-date flight lines covering an area >2,300 km². Two gap definitions were tested considering fixed and relative height cutoffs. To quantify the relationship between gaps and landscape- and regional-scale predictors, we employed generalized linear models (GLM). Finally, using the best model and the gap-mortality relationship, we spatialized tree mortality over the entire Amazon region and validated the map using long-term field observations. The results showed that LiDAR-based canopy tree mortality measurements became stable for landscape-scale analysis at a minimum plot area of 5 ha. Gaps delineated by the relative height method represented at least 50% of the tree mortality, being superior to the fixed height cutoff. We found that gaps detected the mortality of shorter trees at canopy level (< 25 m) with increased accuracy (>80%) than that of taller emergent trees (> 25 m; between 17 and 56%). Gap dynamics described a clear spatial pattern from the northwest (lower gap fraction) to the southeast (higher gap fraction) of the Brazilian Amazon. At the landscape scale, none of the drivers tested explained gap occurrence and size distribution. However, at the regional scale, higher gap fractions were associated with increased water deficit, soil fertility, as well as degraded and flooded forests. The predicted tree mortality showed a well-defined spatial pattern, which was consistent with field-based observations. Our results showed higher mean mortality rates at the southeast (0.89%) and west (0.8%) Amazon regions than at the central-east (0.66%) and north (0.65%). These findings highlight the importance of LiDAR observations and gap analysis to study tree mortality at regional scales.

Keywords: tree mortality, gap dynamics, LiDAR, tropical forests, Amazon.

⁶ DALAGNOL, R. *et al.* Modelling amazon tree mortality from LiDAR-based gap dynamics and environmental-climate drivers. To be submitted.

6.1 Introduction

The need for a consistent and comprehensive quantification of small-scale tree mortality and its effect on tropical forests' carbon cycling is pressing. The Amazon biome is an essential component of the global climate system, holding about 40% of the world's tropical forests (EVA; HUBER, 2005) and storing 150-200 Pg of carbon in biomass and soils (FELDPAUSCH et al., 2012). These forests constantly exchange carbon with the atmosphere through the natural processes of productivity, mortality and decomposition. However, these processes can be disrupted by human-induced deforestation, logging and fires (ARAGÃO et al., 2014).

In the Amazon, the majority of mortality and consequent carbon turnover are related to small-scale disturbances from treefalls (ESPÍRITO-SANTO et al., 2014). Tree mortality has been increasing since the past decade due to climate variability (BRIENEN et al., 2015). However, huge uncertainties related to tree mortality mechanisms constrain our ability to accurately quantify tropical forest carbon budget and assess environmental and climate change effects (BUGMANN et al., 2019). This was highlighted in a recent study from Bugmann et al. (2019), who simulated forest dynamics from stand- to global-level using 15 ecosystem models of tree mortality. These models showed markedly different results under the current climate scenario (10-40% deviations) and, especially, under simulated scenarios of climate change (20-170% deviations). Therefore, to accurately predict environmental and climate effects over forest functioning, we must reduce these uncertainties related to tree mortality.

Data related to tropical forest mortality are available from long-term field plots with repeated measurements, such as those acquired by the Amazon Forest Inventory Network (RAINFOR at <http://rainfor.org>; MALHI et al., 2002). This network represents the best available source of tree mortality data for the Amazon forests. However, some studies have claimed that tree mortality estimated from such data are biased by plot positioning and plot size (typically 1 ha), affecting the representation of large-scale mortality events at the landscape level of observation (FISHER et al., 2008; CHAMBERS et al., 2013). For instance, while the growth of tree's diameter at breast height (DBH) has low variability considering typical plot areas of 1 ha (coefficient of variation, CV = 15-20%), tree

mortality estimates have twice that variability at the same scale (CV = 40%) (WAGNER et al., 2010). Therefore, a minimum plot area of 4 ha should be used to attain under 20% CV (WAGNER et al., 2010). Moreover, when studying mortality variability with Landsat satellite imagery and intermediate-scale wind disturbances at Central Amazon, Chambers et al. (2013) recommended a minimum plot size of 10 ha to correct the bias (underestimate) of mortality associated with the mortality spatially and temporally clustered nature. Further studies are necessary to confirm these results, which can benefit from high-resolution remote sensing data.

Remote sensing data and methods can be an alternative to observe large areas and complement field-plot information. For instance, multi-temporal airborne Light Detection And Ranging (LiDAR) data allow the estimates of canopy tree mortality rates based on the differences in Canopy Height Models (CHM) between two dates (LEITOLD et al., 2018). In addition, the analysis of gap-phase dynamics from LiDAR can be used as a proxy for tree mortality (HUNTER et al., 2015). However, since not all mortality events generate gaps (ESPÍRITO-SANTO et al., 2013), we still lack the understanding of how much mortality variability can be measured by gap dynamics. Thus, the sensitivity of the LiDAR-based tree mortality estimates to the measurement scale needs to be better understood.

Gaps consist of holes in the canopy caused by the loss of one or more trees, from either natural mortality or fire/logging. Measurements of gaps are challenging even using remote sensing. For instance, different gap definitions based on height cutoffs in neotropical forests can provide different measurements of gaps from single-date airborne LiDAR data (ASNER et al., 2013; LOBO; DALLING, 2014; HUNTER et al., 2015). Alternatively, the gap delineation can be calibrated to a forest site based on the statistical analysis of its height distribution using mixed models (GOULAMOUSSENE et al., 2017). However, this approach does not account for factors such as the presence of large open areas that are not necessarily treefall gaps; low height vegetation; and degraded or deforested areas. A dynamic definition has also been proposed based on the use of a relative height cutoff and a local moving window (GAULTON; MALTHUS, 2010), but this approach has not yet been tested over tropical forests.

If the gap delineation does not accurately reflect tree mortality, it may cause erroneous interpretations of forest functioning, such as forest turnover estimates. Validation of LiDAR-gap measurements with ground sampling has been attempted in the past and proven very difficult to achieve (GAULTON; MALTHUS, 2010). This is likely because the high precision of LiDAR-gap delineation potentially surpasses that of the ground measurements, which tend to under-sample gaps (LOBO; DALLING, 2014). Nevertheless, an alternative and novel way to assess the gap-mortality relationship consists of using multi-temporal LiDAR data to sample the mortality that occurred in the corresponding time interval (CHM_{date2} minus CHM_{date1}). We can then quantify how much tree mortality is detected by the LiDAR-delineated gaps based on the posterior date (CHM_{date2}).

A few studies using single LiDAR data have analyzed the gap dynamics of neotropical forests and its drivers at the landscape scale (ASNER et al., 2013; HUNTER et al., 2015; GOULAMOUSSENE et al., 2017). Such studies found a significant relationship between topography and gap occurrence likely linked to wind-exposure, light and water availability, and soil fertility. Specifically, forests with fast dynamics showed gaps more frequently at valleys (low values of Height Above the Nearest Drainage - *HAND*) rather than plateaus (high *HAND* values), while large gaps occurred more frequently at hilly areas (high *slope*) (TOLEDO et al., 2012; HUNTER et al., 2015; GOULAMOUSSENE et al., 2017). On the other hand, a study based on plot data showed that there was no observed relationship between mortality and topography over forests with slower dynamics (CHAO et al., 2009).

The relationship of gap variability with environmental and climate variables is still largely unknown at regional scales up to today because of the lack of datasets encompassing different bioclimatic regions. For instance, the aforementioned studies at the landscape scale have sampled a limited area within a specific environment and climate condition. Thus, the regional controls often associated with tree mortality in the Amazon forests have not yet been assessed. At local scales, prior studies were mostly based on long-term field data or medium-scale remote sensing data. Their findings showed that tree mortality was enhanced by water stress (PHILLIPS et al., 2009); increased soil fertility associated to faster forest dynamics (QUESADA et al., 2010); wind disturbance (RIFAI et al., 2016;

NEGRÓN-JUÁREZ et al., 2018); forest degradation and fragmentation (LAURANCE et al., 1998; BROADBENT et al., 2008); and by flooded or seasonally flooded forests (FERRY et al., 2010; GOULAMOUSSENE et al., 2017). Although there are some known patterns of large scale forest dynamics across the Amazon such as the faster dynamics at west than east (FELDPAUSCH et al., 2011; QUESADA et al., 2012), the small-scale gap dynamics extracted from LiDAR data can eventually improve the representation of the Amazonian ecosystem in dynamic vegetation models (FROLKING et al., 2009).

In this study, the objectives were to improve our understanding of canopy gap-mortality relationships and provide a systematic assessment of canopy gaps and tree mortality considering their relationship with environmental and climate drivers in the Amazon forests. Specifically, we aimed to answer the following research questions: (Q1) What is the minimum plot area necessary to obtain stable landscape-scale estimates of canopy tree mortality? (Q2) How do canopy gaps relate to mortality rates of tropical forests and which gap definition best represents this relationship? (Q3) How does canopy gap dynamics derived from airborne LiDAR data vary across the Brazilian Amazon forests? (Q4) What landscape- and/or regional-scale factors drive gap variability in the Brazilian Amazon? (Q5) Does tree mortality modeled from gaps and environmental-climate proxies reproduce spatial patterns derived from plot-based estimates across the Amazon?

6.2 Data and Methods

The study consisted of three parts (Figure 6.1). In the first part, to answer Q1 and Q2, we assessed the relationship between canopy tree mortality and gaps using multi-temporal airborne LiDAR data acquired over five test sites with distinct forest structure and biomass. In the second part (Q3 and Q4), we evaluated the spatial variability of canopy gaps and their drivers across the Brazilian Amazon, using single-date airborne LiDAR data acquired over 610 non-overlapping LiDAR flight lines (single dates), representing a total sampled area of ~2,300 km² of Brazilian Amazon forests. The third and last part (Q5) combined outputs from the

previous analyses to estimate Amazon-wide tree mortality, validating the results with long-term field inventory data.

Figure 6.1 - Overview of the main methodological steps used to answer the research questions (Q1 to Q5). CHM_{date1} and CHM_{date2} correspond to canopy height models derived from LiDAR data acquired on two different dates with a time interval of ~5 years.



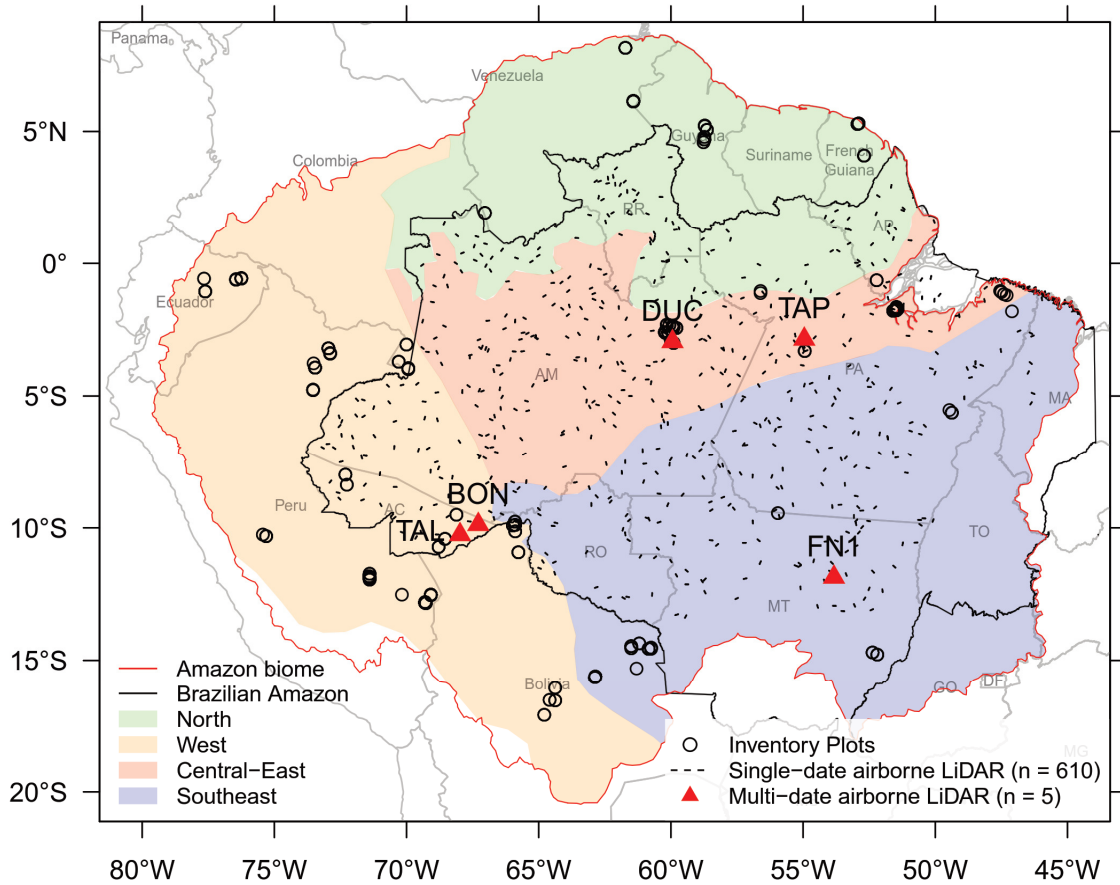
Source: Produced by the author.

6.2.1 Study Area

The study area is the Amazon biome (Figure 6.2), here defined as areas comprehending the Amazon *sensu stricto* (EVA; HUBER, 2005). For the purpose of analysis, we followed the work of Feldpausch et al. (2011) and divided the Amazon into four regions according to geography and substrate origin: (1) the

western Amazon encompassing most of Colombia, Ecuador, Peru and Bolivia, with more fertile soils originated from recently weathered Andean deposits; (2) southeast Amazon encompassing Brazil and part of Bolivia; (3) Central-east Amazon covering Brazil, mostly comprising old sedimentary soils; and (4) northern Amazon, encompassing Guyana, French Guiana and Venezuela.

Figure 6.2 – The Amazon biome in South America with colored regions indicating faster (west and southeast) and slower dynamics (central-east and north). The regions were adapted from Feldpausch et al. (2011). Small black lines represent single-date airborne LiDAR data acquisitions from the EBA project ($n = 610$ flight lines). Red triangles illustrate multi-temporal LiDAR data acquisition over five sites (BON, DUC, FN1, TAL and TAP). Circles indicate the location of field inventory plots.



Source: Produced by the author.

The natural vegetation of the Amazon broadly corresponds to forested areas (broadleaf moist forests and tropical seasonal forests) and other vegetation physiognomies, e.g. campinarana, savannah, bamboo-dominated forests, etc.; amongst which there are *terra firme* and flooded forests (IBGE, 2006). The Amazon shows a wide range of average monthly rainfall (100 to 300 mm) and

dry season length (DSL) (0 to 8 months). The predominant soil types are Ferralsols, Acrisols, Plinthosols, and Gleysols (QUESADA et al., 2011).

Part of the study was conducted over the Brazilian Amazon, an area which covers most (~62%) of the Amazon forest and the different types of climate of the region. Another part of the study was focused on five sites selected for the multi-temporal assessment of tree mortality and canopy gap-mortality relationship (red triangles in Figure 6.2): Adolpho Ducke forest (DUC), Tapajós National Forest (TAP), Feliz Natal (FN1), Bonal (BON) and Talismã (TAL) sites. They were selected to sample distinct forest types, structure and biomass stocks. Repeated airborne LiDAR data was acquired over these sites with relatively long time intervals (5 years). This time interval is sufficient to measure the long-term aggregated estimate of mortality and to match gaps from single-date LiDAR with mortality between the two LiDAR dates.

The selected sites present, in average, a gradient of aboveground biomass (AGB) stocks that increase from TAL (185 Mg.ha⁻¹), FN1 (235 Mg.ha⁻¹), BON (251 Mg.ha⁻¹), and DUC (327 Mg.ha⁻¹) to TAP (364 Mg.ha⁻¹), as illustrated in the AGB map reported by Avitabile et al. (2016). The DUC and TAP consist of dense rain forests, while the FN1 site is composed of seasonal forests. TAL and BON have open rain forests. Local occurrences of bamboo are also observed in the upper canopies of TAL. DUC and FN1 are mostly undisturbed forests. The TAP site underwent fire and/or selective logging in the past, while TAL and BON were affected by a known fire occurrence in 2010 (SATO, 2017).

6.2.2 Data Acquisition and Pre-Processing

6.2.2.1 Airborne LiDAR data

Multi-date airborne LiDAR data were acquired by an airplane over the five sites (Figure 6.2) with time intervals close to 5 years between the years 2012 and 2018 (datasets from the Sustainable Landscapes Brazil freely available at <https://www.paisagenslidar.cnptia.embrapa.br/webgis/>). Multiple LiDAR returns were recorded and a minimum point density of 4 points.m⁻² was obtained (detailed data acquisition information in Table C.1). Also, a total of 610 single-date airborne discrete-return LiDAR data strips (approx. 300 m wide by 12.5 km

long; ~3.75 km² or 375 ha each) were acquired during 2016 using the Trimble HARRIER 68i system at an airplane with average flight height of 600 m above ground and a scan angle of 45° (dataset from the EBA project - Improving Biomass Estimation Methods for the Amazon; TEJADA et al., 2019). The data showed a minimum point density of 4 points.m⁻². Horizontal and vertical accuracy ranged from 0.035 m to 0.185 m and from 0.07 m to 0.33 m, respectively.

LiDAR point clouds (x, y, z coordinates) were processed into canopy height models (CHM) of 1-m spatial resolution. First, we filtered outlier points from the cloud using the *lasnoise* function from LAStools 3.1.1 (ISENBURG, 2018), considering the default parameters of 4 m step and 5 isolated points. This method looks for a minimum number of isolated points on the cloud data over each defined step cell area. Then, we classified the points into ground or vegetation classes using the *lasground*, *lasheight*, and *lasclassify* functions from LAStools. Afterward, we used the ground points to generate a DTM with 1-m spatial resolution using the *TINSurfaceCreate* function from FUSION/LDV 3.6 (MCGAUGHEY, 2016). For the multi-temporal datasets, to ensure that potential acquisition effects between datasets did not interfere with the analysis, we merged their ground points and generated a combined DTM (DALAGNOL et al., 2019). The cloud points' height was then normalized to height above ground by subtracting the DTM height from their values. Finally, we extracted the CHMs considering the highest height of vegetation on each 1x1 m pixel using the *CanopyModel* function from FUSION/LDV.

6.2.2.2 Environmental and climate data

For the analysis of the environmental and climatic drivers of gap dynamics, we considered a spatialized set of variables for the whole Amazon biome. The details of the data acquisition and pre-processing are described below:

- HAND is a digital surface model normalized in relation to the nearest river level (NOBRE et al., 2011). It shows a strong relationship with plant species distribution and may affect the forest gap dynamics (GOULAMOUSSENE et al., 2017). The HAND product (30 x 30 m) (DONCHYTS et al., 2016) was based on the Shuttle Radar Topography Mission (SRTM) with 1 arc-sec, around 30 x 30 m,

spatial resolution (NASA, 2013). The product was developed considering a sparse river drainage delineation level (parameter = 1000).

- Terrain slope (degrees; 30 x 30 m) was extracted from the SRTM data.
- The Soil Cation Concentration (*SCC*) product (11 x 11 km) was derived from the integration of direct soil samples and species-environmental modelling. The product is a proxy for soil nutrients and fertility, representing the sum of exchangeable cations of Potassium (K), Magnesium (Mg) and Calcium (Ca) (ZUQUIM et al., 2019).
- The floodplain cover map (30 x 30 m) was derived from vegetation analyses using the Japanese Earth Resource Satellite 1 (JERS-1) radar data acquired during 1995 and 1996 (HESS et al., 2015). The product presents different flooded or seasonally flooded vegetation classes. For simplicity, they were reclassified into either flooded (1) or non-flooded (0) pixels. All classes of the mask were re-mapped as flooded, except for the ones with the values 0, 1, 44, 66, 88, 200, 255, which represent non-flooded classes.
- The non-forest distance map was created by quantifying the distance (in km) from each pixel to any nearest non-forest area. Because of the inexistence of an Amazon-wide forest degradation product, this approach was used as a proxy for forest degradation, as forests nearby deforestation, human settlements and rivers should be more prone to human-disturbance. Non-forest areas were mapped using the 30-m global forest change dataset v1.4 (2000-2016) (HANSEN et al., 2013), selecting pixels with tree cover below 95%, forest gains (regrowth), forest losses (deforestation between 2000 and 2016), and lakes/rivers using the provided mask.
- Rainfall (mm), climate water deficit (mm) and wind speed ($\text{m}\cdot\text{s}^{-1}$) were acquired from the high-resolution TerraClimate dataset (5 x 5 km) (1958-2015) (ABATZOGLOU et al., 2018). While rainfall and wind speed measurements were derived from data-model reanalysis procedures, the climate water deficit was retrieved using a one-dimensional soil/water balance model. The raw data corresponded to monthly values, which, for simplicity, were aggregated into monthly mean and standard deviation (SD) metrics.

- DSL (0.25 x 0.25 deg.) was estimated for each pixel as the average number of months with rainfall inferior to 100 mm of evapotranspiration (SOMBROEK, 1966). The 100 mm of monthly evapotranspiration demand by evergreen forest is an average for the Amazon basin widely used in the literature (ARAGÃO et al., 2007).

All variables were resampled to 5 x 5 km to match the climate datasets. To resample, average values were calculated for datasets with spatial resolution finer than 5 km, and the nearest neighbor method was used for datasets with spatial resolution coarser than 5 km.

6.2.2.3 Long-term field inventory data

We used long-term field inventory data from plots located across the Amazon biome (Figure 6.2) from the RAINFOR network published by Brien et al. (2015). Tree mortality rates (m ; $\%.\text{yr}^{-1}$) were calculated as the coefficient of exponential mortality (Eq. 6.1, SWAINE et al., 1987) for each census interval and each plot; and then averaged by plot, weighted by the censuses interval length in years (JOHNSON et al., 2016).

$$m = [\ln(N_0) - \ln(N_t)] / t \quad (6.1)$$

where N_0 and N_t are the initial and final number of trees, and t is the censuses interval.

6.2.3 Data Analysis

6.2.3.1 Sensitivity of tree mortality rates to the sampled area (Q1)

We employed a multi-temporal LiDAR analysis to explore the variability of canopy tree mortality and determine the minimum spatial scale that allows stable estimates of tree mortality at the landscape scale. For this purpose, we assessed the coefficient of variation (CV) of tree mortality amongst simulated sub-plots of increasing size. First, we detected events of canopy tree mortality using multi-date LiDAR data on the five study sites: DUC, TAP, FN1, BON, and TAL. The mortality detection was based on a delta height cutoff of 10 m between the two acquisitions (~5 years apart). This cutoff was chosen based on two previous

studies that showed that a canopy height change of 10 m was strongly correlated with individual tree loss due to mortality and/or selective logging in tropical forests (LEITOLD et al. 2018; DALAGNOL et al., 2019). We sub-divided the sites into plot areas ranging from 0.25 to 25 ha; calculated the mortality cover for each plot area; and assessed the tree mortality CV. We hypothesized that the mortality CV would decrease with the increase in the plot area, and stabilize at some point. This point would correspond to the minimum plot area allowing reliable evaluation of canopy tree mortality at the landscape scale.

6.2.3.2 Gap-mortality relationship and gap definition (Q2)

After defining the minimum plot area necessary to obtain stable estimates of tree mortality at the landscape scale, we determined which gap definition would be more suitable to support the optimal gap-mortality relationship. We compared the detection of mortality between LiDAR data, acquired in two different dates (CHM_{date2} and CHM_{date1}) within a 5-year time interval, with the delineation of gaps based only on the posterior date (CHM_{date2}). We compared two types of gap definition methods: one more traditional based on a fixed height cutoff and another alternative based on a relative height cutoff. For both methods, we tested a variety of parameters in the search of an optimal calibration amongst the sites. We followed the assumption that gaps are related to mortality events, allowing us to observe all canopy mortality within a time interval. However, as delineated gaps may also represent mortality that occurred previously to the first LiDAR acquisition, we expect to obtain an underestimate of the true delineation.

The first gap definition was based on the classical concept of Brokaw et al. (1982), who has defined a gap as a 'hole' in the forest canopy extending through all levels down to an average height (H) of 2 m above the ground. Since studies in the literature have been using different H values to describe canopy gaps, in order to assess the association between gaps and mortality, we tested H cutoff parameters (H = 2, 5, 10 m) covering values commonly used in studies of Neotropical forests (ASNER et al., 2013; ESPÍRITO-SANTO et al., 2014; LOBO; DALLING, 2014; HUNTER et al., 2015). Therefore, all pixels with a height below the H cutoff were considered as a gap. The gap delineation was conducted using the *ForestGapR* R-package (SILVA et al., 2019).

The second gap definition was based on the canopy relative height (RH) in comparison to the maximum height within a neighborhood of size W (GAULTON; MALTHUS, 2010). The assumption behind this method was that a mortality event does not necessarily create a gap that extends down to the ground. It can create a hole in the canopy with a relative height below neighboring trees. Therefore, we tested this method by varying window size parameter ($W = 5, 9, 15, 25, 35, 45$) and relative heights ($RH = 0.33, 0.50$ and 0.66). The W parameters range was defined to reach up to very large tree crowns (45 m). The range of RH parameters was empirically chosen to represent heights below a threshold that would consist in a gap, i.e. less than $1/3, 1/2$ or $2/3$ of neighboring trees height. To better delineate gap centers, where this method may underestimate gaps due to potential large distances to neighboring trees, we also included a fixed H cutoff of 2 m.

For both methods, we filtered gaps for a minimum area of 10 m^2 , which corresponded to an approximation of the mean canopy area of trees greater than 5-cm DBH in tropical forests (HUNTER et al., 2015). We filtered the gaps for a maximum area of 1 ha ($1 \text{ ha} = 10,000 \text{ m}^2$) in order to automatically exclude open areas that likely did not correspond to the small-scale disturbance from treefall gaps.

The performance of both methods was assessed by intersecting the gap delineation with the mortality detection and calculating metrics of precision (p), recall (r) and F1-score (F) (Eq. 6.2 to 6.4):

$$\textit{Precision } (p) = \textit{true positives} / \textit{number of gap polygons} \quad (6.2)$$

$$\textit{Recall } (r) = \textit{true positives} / \textit{number of mortality polygons} \quad (6.3)$$

$$\textit{F1-score } (F) = (2 * p * r) / (p + r) \quad (6.4)$$

True positives were defined as individual gap delineations that successfully intersected mortality detections, while covering at least 25% of the detected area of mortality. This criterion was established to ensure confidence in results because simply considering an intersection as success would have overestimated the overall performance. The performance between the five study sites was averaged (“sites-average”) and assessed to verify the transferability of the method and calibrated parameters over them. The methods were ranked

considering their $F_{\text{sites-average}}$. The gap detection was further analyzed as a function of tree height classes.

Finally, we assessed the relationship between gap and mortality at the landscape scale by extracting both variables at the scale defined in section 6.2.3.1, and fitting a statistical model to relate the two variables. To assess model results, we calculated the coefficient of determination (R^2), absolute Root Mean Square Error (RMSE) and relative RMSE (%). A 95% prediction interval was also calculated to describe the variability of tree mortality estimates from the gap fraction.

6.2.3.3 Spatial variability of gaps across the Brazilian Amazon (Q3)

We delineated the gaps on the single-date airborne LiDAR datasets ($n = 610$ flight lines, each covering $12,500 \times 300$ m) using the optimal method and parameters previously assessed in section 6.2.3.2. To characterize the canopy gap variability, we calculated the gap fraction (i.e., the area occupied by gaps in relation to the total area of the strip), mean gap size, mean gap shape complexity index (GSCI). The GSCI is calculated using Eq 6.5:

$$GSCI = \frac{\text{gap perimeter}}{2 * \sqrt{\text{gap area} * \pi}} \quad (6.5)$$

We also assessed the gap size-frequency distribution (SFD) by fitting a discrete power-law probability (Zeta distribution) to each dataset and obtaining the λ -scale parameter that characterized the distribution (ESPÍRITO-SANTO et al., 2014). These procedures mentioned above were conducted using the *ForestGapR* R-package (SILVA et al., 2019).

6.2.3.4 Assessment of landscape- and regional-scale drivers of canopy gaps (Q4)

To quantify the relationship between gaps and landscape- and regional-scale predictors, we employed generalized linear models (GLM) using the R-packages *stats* (R CORE TEAM, 2018) and *lme4* (BATES et al., 2015). We defined here the landscape-scale drivers as those related to topography, showing great heterogeneity intra-site such as the *Slope* and *HAND*. The regional-scale drivers

were assumed here as those having greater variability across sites (inter-site), such as the rainfall (*Mean_pr* and *SD_pr*), wind speed (*Mean_vs* and *SD_vs*), climate water deficit (*Mean_def* and *SD_def*), *DSL*, soil cation concentration (*SCC*), *floodplains cover*, and *Non-forest distance*.

For landscape-scale drivers, we tested whether the environmental variables could predict individual gap occurrence (presence or absence) and gap size distribution. For this purpose, we extracted environmental variables from gap presence and absence. For the gap absence, we randomly distributed samples at non-gap covered areas (same number of gap presence). We fitted a logistic regression to predict the probability of gap occurrence given HAND and slope as predictors (Eq. 6.6):

$$\text{logit}(\text{GapProb}_{ij}) = \ln\left(\frac{p}{1-p}\right) = \beta_0 + \beta_j X_{ij} + u_{ij} X_{ij} + \varepsilon_{ij} \quad (6.6)$$

where *GapProb_{ij}* is the gap probability for pixel *i*, β_0 is the intercept term, β_j is the slope of predictor *j*, *u_{ij}* is the random factor of site, ε_{ij} is the residual error assumed to follow a normal distribution.

We also fitted a linear model to assess whether HAND and slope could predict gap size distribution (Eq. 6.7):

$$\text{GapSize}_{ij} = \beta_0 + \beta_j X_{ij} + u_{ij} X_{ij} + \varepsilon_{ij} \quad (6.7)$$

where *GapSize_{ij}* is the gap size for pixel *i*, and the remaining terms are the same as Eq. 6.6.

We have tested fitting the models considering the site (1 to 610) as a random factor, and testing predictors either individually or combined.

For regional-scale drivers, we employed a Gaussian GLM (similar to Eq. 6.7) to quantify how much of the variability of gap fraction (dependent variable) was explained by the environmental and climate variables (independent variables). We evaluated only the gap fraction because, during our analyses, we learned that the gap size-frequency distribution parameter (λ) showed a very narrow range of values, which were dependent on the gap definition. On the other hand, the gap fraction showed clear spatial patterns and a much more intuitive interpretation. Before fitting the model, to better understand the relationship of predictors and gap fraction, and avoid multicollinearity, we have conducted an

exploratory analysis by a correlation matrix. We selected at least one proxy for each type of variable having stronger correlation to gap fraction, and less correlation ($r < 0.7$) amongst other variables. We conducted variable log-transformation to those which distribution differed from normal.

Models were compared by their explanatory power considering the R^2 and Bayesian Information Criterion (BIC) (SCHWARZ et al., 1978). We investigated the influence of predictors onto the model's response by analyzing the regression coefficients (B), standardized beta coefficients (β), and predictors individual explanatory power considering their ΔR^2 (change in R^2 by adding the variable last on the model). Predictors' multicollinearity within the model was assessed by the variance-inflation factors (VIC), which indicates the degree of interaction/correlation between independent variables (high values = high intercorrelation).

6.2.3.5 Amazon-wide tree mortality prediction and validation (Q5)

To spatialize tree mortality over the Amazon biome, we first applied the model built with environmental and climate drivers that best explained gap variability to predict Amazon-wide gap fraction. Then, we applied the gap-mortality relationship to translate gap fraction into tree mortality. To validate the map, we compared the tree mortality predictions with estimates from long-term field inventory data, fitting a linear model and calculating the R^2 , absolute and relative RMSE. The resultant spatial patterns of tree mortality detected by LiDAR were compared with large-scale forest dynamics reported in the literature. The values of mean modelled mortality per Amazonian region (Figure 6.2) were extracted and compared using one-way ANOVA and post-hoc Tukey-Kramer tests.

6.3 Results

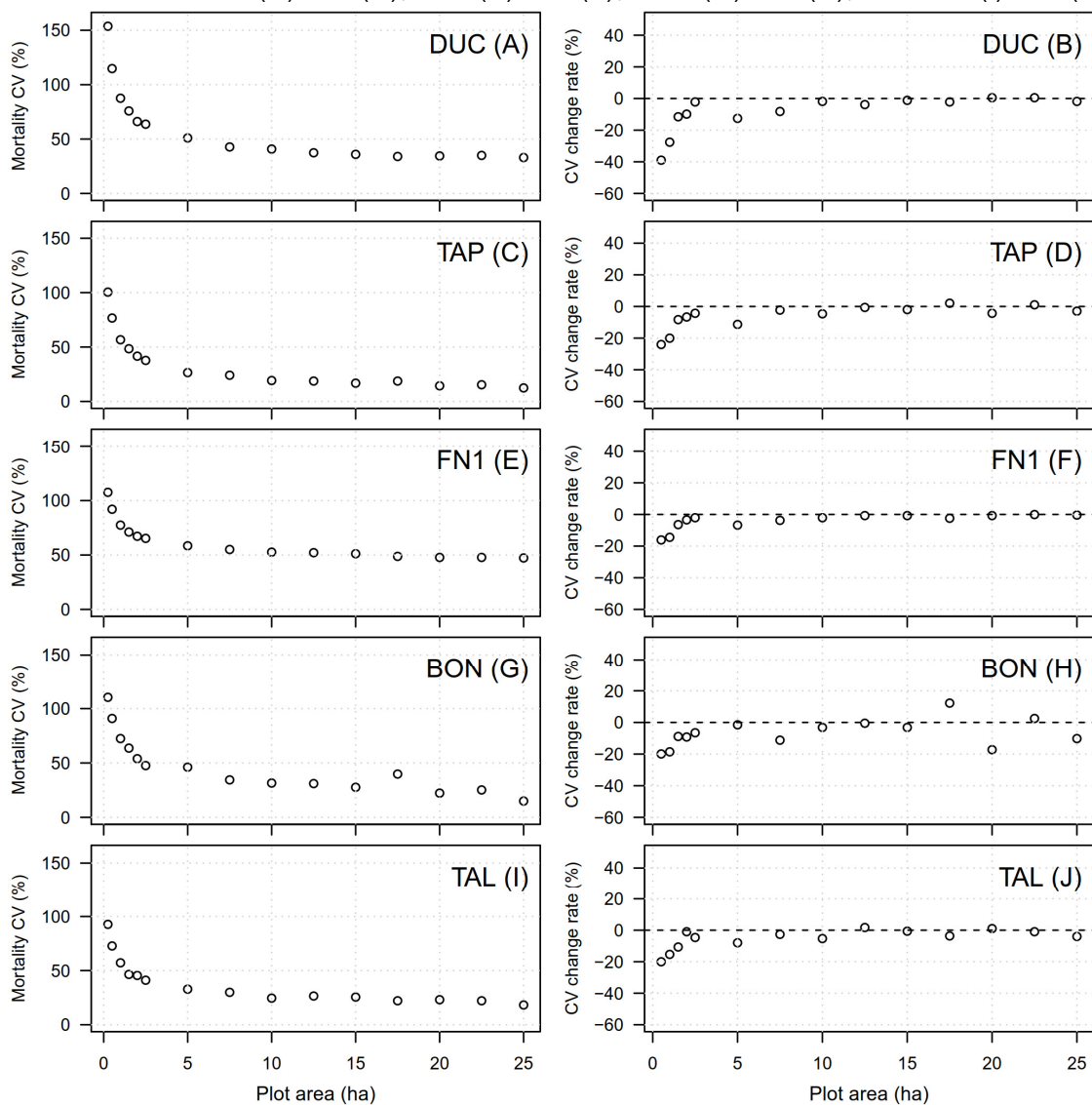
6.3.1 Multi-Temporal Analysis of Gap-Mortality Relationship

6.3.1.1 Tree mortality estimates and plot area sensitivity

Mortality variability (CV%) decreased with plot area and converged close to the 5-ha area, showing mean CV values between 40% and 50% for all sites (Figures

6.3A, C, E, G and I). For the 5-ha plot area, the change rate stabilized to values close to zero (Figures 6.3B, D, F, H and J). Thus, lower mortality variability was observed for plot areas larger than 5 ha. From the selected sites, TAP showed the lowest mortality CV, reaching stable values close to 20% with increasing plot areas from 5 ha to 25 ha (Figure 6.3C). For the same range of plot area, the highest mortality CV was observed at the FN1 site (Figure 6.3E) with values around 50%.

Figure 6.3 - LiDAR-based canopy tree mortality variability with plot area for five Amazonian sites with multi-temporal data. The mortality coefficient of variation (CV) and the CV change rate are shown for DUC (A) and (B); TAP (C) and (D); FN1 (E) and (F); BON (G) and (H); and TAL (I) and (J).



Source: Produced by the author.

Based on the results of Figure 6.3 and using a delta height cutoff of 10 m between the pairs of repeated LiDAR data, we estimated tree mortality rates at the 5-ha plot area. The sites with least to most average annual mortality rates at 5-ha (Mean % yr⁻¹ ± SD, *n* = number of samples) were: DUC (0.38 ± 0.19, *n* = 234), FN1 (0.56 ± 0.33, *n* = 199), BON (1.09 ± 0.50, *n* = 95), TAP (1.23 ± 0.33, *n* = 183) and TAL (1.66 ± 0.54, *n* = 69).

6.3.1.2 Gap-mortality relationship and gap definition

The representation of tree mortality by canopy gaps showed variable performance ($F_{sites-average}$ from 0.01 to 0.51) amongst different combinations of methods and parameters (Table 6.1). The best result amongst all sites ($F_{sites-average} = 0.51$) was obtained by the relative height method using a window size of 5 meters and a relative height cutoff of 50th percentile ($W = 5$, $RH = 50$). Considering individual-site performance, this method achieved the best results for all sites, except for BON and TAL. Over these two sites, the relative height method, considering a larger window of 15 meters and a relative height cutoff of 33rd percentile, yielded a slightly better result (increment of 0.01 in F). The best result amongst sites for the fixed-height method was based on a 10-m height cutoff, achieving a lower performance (Sites-average: $F = 0.48$, $p = 0.47$, $r = 0.55$) when compared to the best result based on relative height.

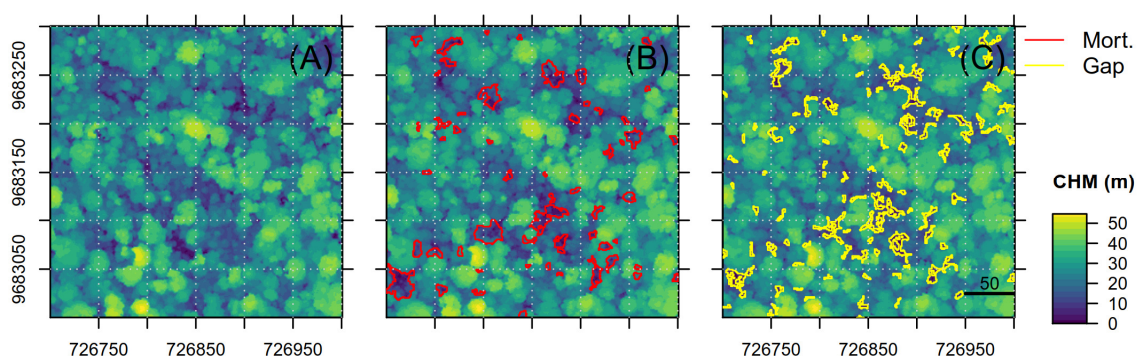
The correspondence between detected mortality and delineated gaps for the best method ($W = 5$, $RH = 50$) is illustrated in Figure 6.4. In this figure, the mortality between 2012 and 2017 is shown in red (Figure 6.4B) and the delineated gaps based on the 2017 data are represented in yellow (Figure 6.4C) for the TAP site. The method was able to map 68% of the mortality areas ($r_{TAP} = 0.68$), but with 58% of commission errors ($p_{TAP} = 0.42$) (Table 6.1). For instance, the top-right area showed some examples of commission errors, i.e. delineated gaps that do not correspond to mortality, while the bottom-middle area showed gaps that successfully matched mortality.

Table 6.1 - Performance of different gap definitions to represent tree mortality for each site and an average between sites (sites-average). Methods and parameters are ranked by the Sites-Average F metric. Method's parameters include: *W* = window size (meters); *RH* = percentile of relative height cutoff; *A* = maximum gap area (ha); and *H* = fixed height cutoff. Performance metrics include: *p* = precision; *r* = recall; and *F* = F1-score. Values of *p*, *r*, and *F* range from 0 to 1, with larger values indicating better performance.

Method and parameters	DUC			TAP			FN1			BON			TAL			Sites-Average		
	<i>p</i>	<i>r</i>	<i>F</i>	<i>p</i>	<i>r</i>	<i>F</i>	<i>p</i>	<i>r</i>	<i>F</i>	<i>p</i>	<i>r</i>	<i>F</i>	<i>p</i>	<i>r</i>	<i>F</i>	<i>p</i>	<i>r</i>	<i>F</i>
Variable: W=5, RH=50	0.48	0.51	0.49	0.42	0.68	0.52	0.49	0.71	0.58	0.35	0.69	0.46	0.37	0.74	0.5	0.42	0.66	0.51
Variable: W=15, RH =33	0.56	0.37	0.45	0.45	0.58	0.51	0.59	0.54	0.57	0.38	0.61	0.47	0.41	0.66	0.51	0.48	0.55	0.5
Variable: W=25, RH =33	0.51	0.43	0.47	0.42	0.65	0.51	0.53	0.57	0.55	0.35	0.67	0.46	0.39	0.66	0.49	0.44	0.6	0.5
Variable: W=35, RH =33	0.48	0.47	0.47	0.4	0.68	0.51	0.5	0.58	0.53	0.33	0.69	0.44	0.37	0.63	0.47	0.42	0.61	0.49
Fixed: H=10	0.59	0.34	0.43	0.53	0.44	0.48	0.43	0.75	0.54	0.37	0.62	0.46	0.41	0.62	0.5	0.47	0.55	0.48
Variable: W=45, RH =33	0.45	0.49	0.47	0.39	0.69	0.5	0.48	0.56	0.52	0.32	0.7	0.44	0.36	0.6	0.45	0.4	0.61	0.48
Variable: W=9, RH =33	0.65	0.29	0.4	0.5	0.48	0.49	0.66	0.46	0.54	0.42	0.52	0.46	0.41	0.59	0.48	0.53	0.47	0.47
Variable: W=9, RH =50	0.34	0.73	0.46	0.33	0.84	0.47	0.36	0.87	0.51	0.26	0.83	0.4	0.3	0.72	0.43	0.32	0.8	0.45
Variable: W=15, RH =50	0.27	0.81	0.41	0.29	0.81	0.43	0.3	0.89	0.44	0.22	0.81	0.35	0.26	0.55	0.35	0.27	0.78	0.4
Variable: W=5, RH =66	0.22	0.88	0.35	0.26	0.92	0.41	0.23	0.96	0.37	0.2	0.84	0.32	0.22	0.57	0.32	0.23	0.83	0.35
Variable: W=25, RH =50	0.23	0.85	0.36	0.26	0.65	0.37	0.24	0.85	0.38	0.18	0.68	0.29	0.23	0.43	0.3	0.23	0.69	0.34
Variable: W=5, RH =33	0.79	0.12	0.21	0.6	0.24	0.35	0.75	0.23	0.35	0.46	0.29	0.35	0.42	0.31	0.36	0.6	0.24	0.32
Variable: W=35, RH =50	0.2	0.87	0.33	0.25	0.55	0.34	0.21	0.81	0.34	0.17	0.54	0.26	0.21	0.34	0.26	0.21	0.62	0.3
Variable: W=45, RH =50	0.18	0.88	0.31	0.24	0.48	0.32	0.19	0.76	0.31	0.16	0.4	0.22	0.2	0.27	0.23	0.19	0.56	0.28
Variable: W=9, RH =66	0.13	0.97	0.23	0.2	0.66	0.31	0.13	0.96	0.23	0.12	0.57	0.2	0.14	0.33	0.2	0.15	0.7	0.23
Fixed: H=5	0.89	0.03	0.06	0.68	0.11	0.19	0.74	0.18	0.29	0.46	0.21	0.28	0.4	0.22	0.29	0.63	0.15	0.22
Variable: W=15, RH =66	0.09	0.98	0.17	0.16	0.35	0.22	0.08	0.86	0.15	0.1	0.14	0.12	0.12	0.13	0.12	0.11	0.49	0.15
Variable: W=25, RH =66	0.06	0.89	0.12	0.15	0.16	0.15	0.06	0.55	0.11	0.1	0.04	0.05	0.09	0.05	0.06	0.09	0.34	0.1
Variable: W=35, RH =66	0.05	0.7	0.1	0.15	0.09	0.11	0.06	0.27	0.09	0.11	0.02	0.04	0.09	0.03	0.04	0.09	0.22	0.08
Variable: W=45, RH =66	0.05	0.51	0.09	0.14	0.05	0.07	0.05	0.16	0.08	0.12	0.02	0.03	0.09	0.02	0.03	0.09	0.15	0.06
Fixed: H=2	0.98	0.01	0.01	0.69	0.01	0.02	0.67	0.01	0.01	0.56	0.01	0.02	0.35	0.01	0.02	0.65	0.01	0.01

Source: Produced by the author.

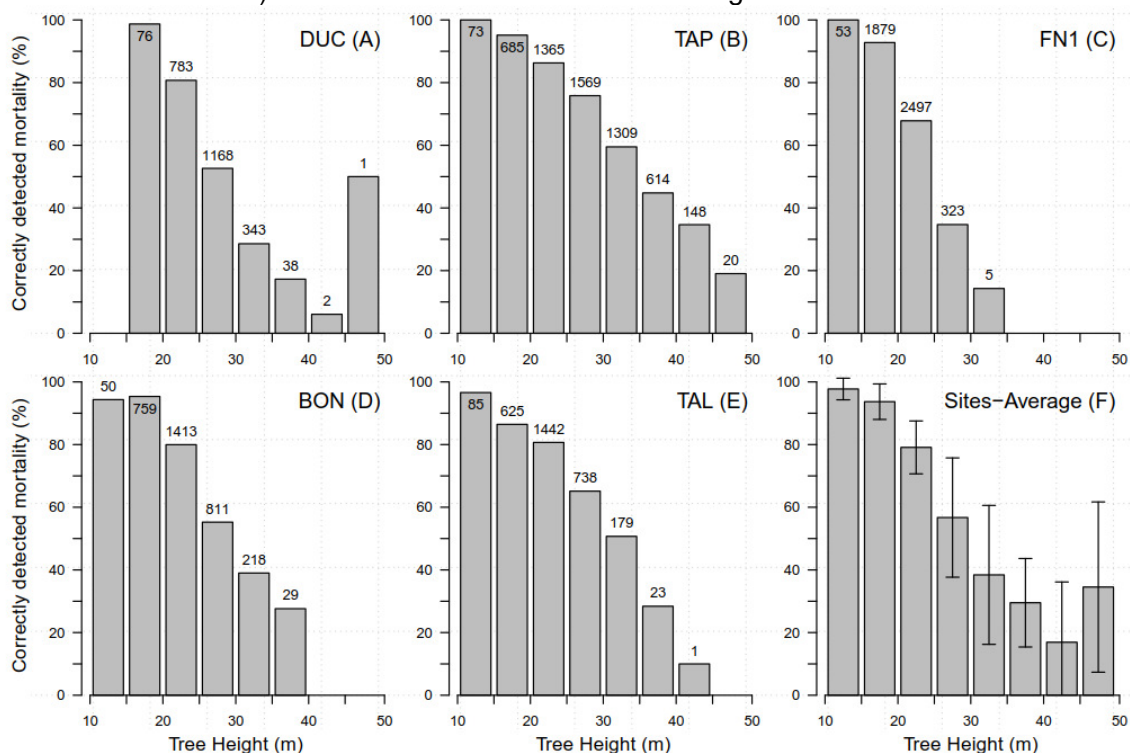
Figure 6.4 - Example of detected canopy tree mortality (red) and gap delineation (yellow) based on relative height ($W=5$, $RH=50$) at the TAP site. The background is a Canopy Height Model (CHM) for 2012 in (A), and 2017 in (B) and (C).



Source: Produced by the author.

In a more detailed inspection, we observed that gaps detected the mortality of shorter trees (< 25 m) with greater accuracy than that of taller trees (> 25 m) (Figure 6.5). The mortality of trees having a height between 10 and 20 m was detected with very high confidence ($>90\%$ mean accuracy), showing significantly higher accuracy than trees taller than 20 m ($p < 0.05$). The mortality for 20-to-25 m tree height was also detected with high accuracy (close to 80%). After this height range, the detection accuracy decreased to values varying between 17 and 56%. The only exception here was the TAP site, which showed high mortality detection accuracy (76%) for the 25-30 m height range. Nevertheless, most events of canopy tree mortality, correctly detected across the sites, were derived from the 10-to-25 m height range (85%; 16,394 out of 19,324 events).

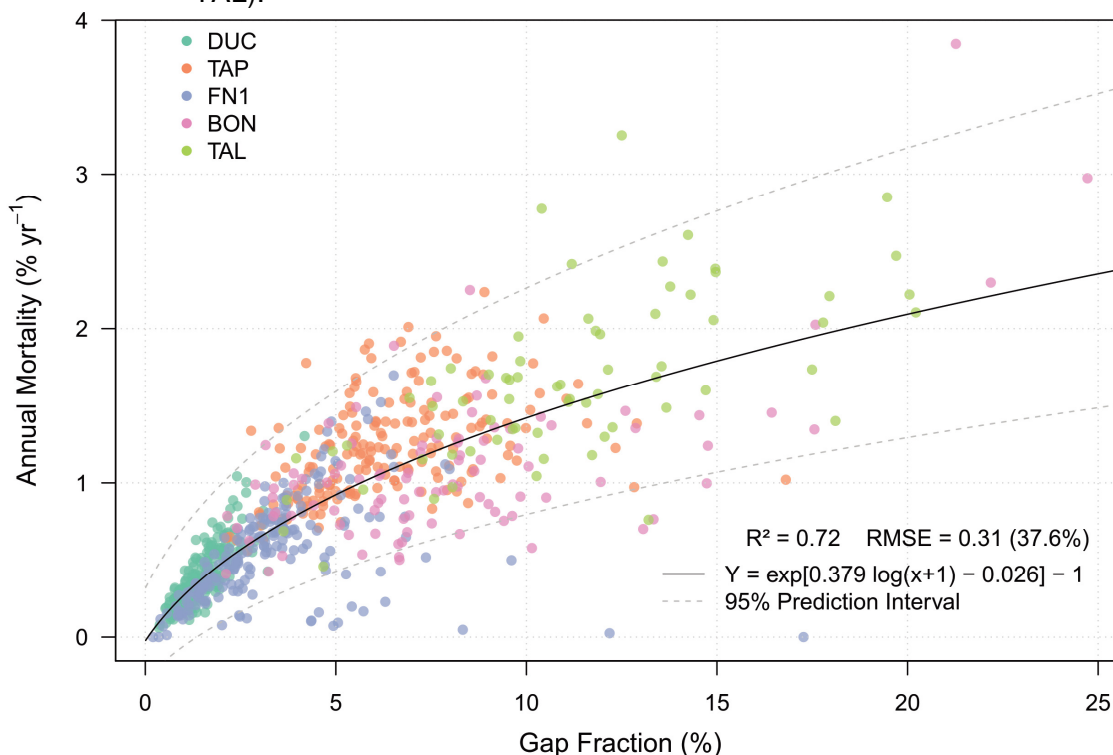
Figure 6.5 - Percentage of correctly detected mortality by delineated gaps (Relative height method, $W=5$, $RH=50$) as a function of tree height classes for the sites: (A) DUC, (B) TAP, (C) FN1, (D) BON, (E) TAL, and (F) sites-average. The numbers close to the bars represent the absolute number of detections for that tree height class. The 95% CI (based on t-value score) is also indicated for the sites-average.



Source: Produced by the author.

The relationship between gap fraction and annual mortality at the 5 ha scale was positive with a logarithmic shape (Figure 6.6). Therefore, we fitted a linear model on the log-transformed variables and observed a significant and strong relationship ($R^2 = 0.72$, $RMSE = 37.6\%$). The uncertainty on estimating mortality from gap fraction increased multiplicatively from small to higher gap fraction values, highlighted by the increasing prediction interval band. The residuals of the model were randomly distributed. The sites with the largest mean gap fraction (Mean Gap Fraction % \pm SD, n = number of samples) estimates at 5-ha scale, in decreasing order, corresponded to TAL (11.18 ± 3.97 , $n = 69$), BON (8.07 ± 4.28 , $n = 95$), TAP (6.4 ± 2.25 , $n = 183$), FN1 (3.3 ± 2.06 , $n = 199$), and DUC (1.47 ± 0.60 , $n = 234$). This gap-fraction ranking was similar to the mortality ranking, except for TAP and BON sites, that is, BON showed higher gap fraction than TAP, while TAP showed higher annual mortality than BON.

Figure 6.6 - Relationship between gap fraction (%) and annual tree mortality (% yr⁻¹) for 5-ha plot areas over the five studied sites (DUC, TAP, FN1, BON, and TAL).



Source: Produced by the author.

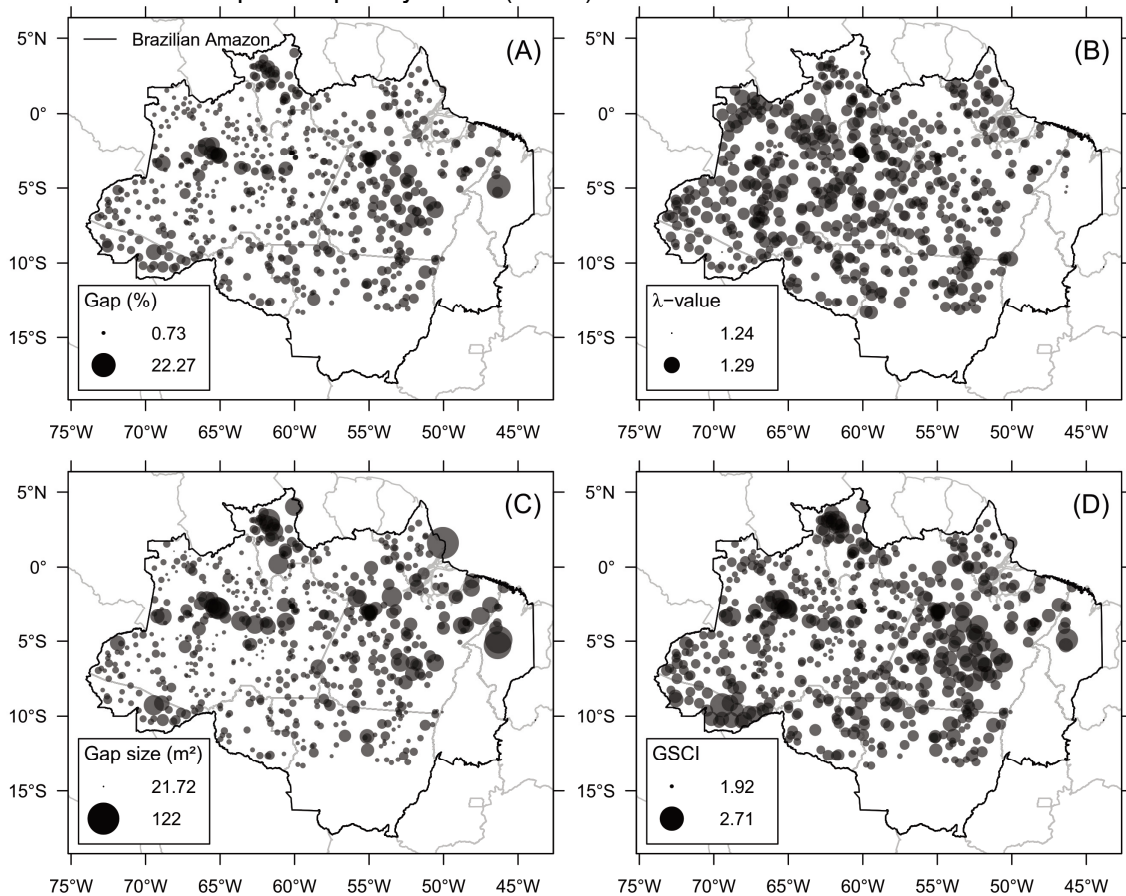
6.3.2 Canopy-Gap Spatial Variability and Landscape and Regional- Drivers Across the Brazilian Amazon

6.3.2.1 Spatial variability of gaps

Using the best parameters for the five tested sites (relative height, RH = 0.5, W = 5 m), we delineated the gaps of the 610 single-date LiDAR strips and found an overall lower gap fraction (Figure 6.7A) over central-east (Mean \pm SD: 3.57 % \pm 3.05) and north (3.68% \pm 2) than at west (4.18% \pm 2.13) and southeast (4.89% \pm 2.47) Amazon regions (as delimited in Figure 6.2). High gap fraction values (>5%) were found over the central portion of the Pará state (~52°W; 5°S) at the southeast region. The spatial variability of gap fraction (Figure 6.7A) was consistent with canopy height variability (Figure C.1). For instance, areas with high gap fraction showed the largest variation in canopy heights (CHM_{SD} from 8 to 14 m) and the lowest “minimum” height (CHM_{P05} < 10 m). We also found a few

areas with very high gap fraction (>10%) close to the center of the Amazonas state (~65°W; 4°S), which were located close to major rivers and floodplains. The λ showed a very narrow variability (λ from 1.24 to 1.29) with smaller values occurring at the same locations where the largest gap fractions were generally located at the center of Pará state (Figure 6.7B). The mean gap size (Figure 6.7C) followed a similar spatial pattern as the gap fraction (Figure 6.7A), with an average gap size across sites of 40.89 m². The GSCI (Figure 6.7D) showed a similar spatial pattern of gap fraction, indicating an increasing shape complexity with gap fraction.

Figure 6.7 - Canopy gaps based on the relative height ($W=5$, $RH=50$) across the Brazilian Amazon ($n = 610$ flight lines): (A) gap fraction (%); (B) gap size-frequency distribution (λ); (C) mean gap size (m²); and (D) mean gap shape complexity index (GSCI).



Source: Produced by the author.

6.3.2.2 Landscape- and regional-scale drivers

In the landscape-scale analysis, the predictors HAND and slope were not able to explain gap occurrence (presence or absence) or gap size (m²) variability, as indicated by R² values close to zero. The same result was achieved by either including or not including the site index as a random factor in the models.

For the regional-scale analysis, all tested variables were significantly correlated to gap fraction ($p < 0.01$) with absolute Pearson's r ranging from 0.21 to 0.46 (Table 6.2). It is important to note that both gap fraction and non-forest distance variables were transformed to log-scale due to non-normal distribution. For instance, the original distribution of *Nonforest_dist* ranged from 0 to 20.6 km, with a mean of 4 km, but was skewed towards smaller distances, where most values ranged between 0.11 and 10.67 km (5th and 95th percentile, respectively). Amongst the variables, those related to climate, either to water stress (*Mean_def*, *SD_def*, *DSL*, *Mean_pr*, and *SD_pr*) or wind disturbance (*Mean_vs* and *SD_vs*), showed significant and strong correlation ($r > 0.7$) with at least one of the other variables. To further reduce multicollinearity effects amongst the model predictors, we have chosen only one water stress variable to be used in the modelling: the one with a stronger correlation with gap fraction (*Mean_def* and *SD_def*). Therefore, the variables *DSL*, *Mean_pr* and *SD_pr* were excluded.

Table 6.2 - Pearson's correlation (r) between gap fraction and predictors. All correlations were significant at 1% statistical level, except for cells left blank.

Variables	Gap Frac.	SCC	NF_dist	Mean_def	DSL	SD_vs	Mean_pr	SD_def	Floodpl.	SD_pr	Mean_vs
Gap Frac.	1	0.46	-0.43	0.42	0.41	0.38	-0.38	0.36	0.27	0.24	0.21
SCC	0.46	1	-	0.35	0.46	0.28	-0.46	0.34	-0.23	0.23	0.11
NF_dist	-0.43	-	1	-0.37	-0.26	-0.25	0.24	-0.34	-0.26	-0.23	-0.28
Mean_def	0.42	0.35	-0.37	1	0.87	0.78	-0.78	0.97	-0.27	0.74	0.55
DSL	0.41	0.46	-0.26	0.87	1	0.62	-0.87	0.86	-0.35	0.77	0.45
SD_vs	0.38	0.28	-0.25	0.78	0.62	1	-0.49	0.75	-0.22	0.55	0.74
Mean_pr	-0.38	-0.46	0.24	-0.78	-0.87	-0.49	1	-0.73	0.3	-0.51	-0.3
SD_def	0.36	0.34	-0.34	0.97	0.86	0.75	-0.73	1	-0.28	0.79	0.54
Floodpl.	0.27	-0.23	-0.26	-0.27	-0.35	-0.22	0.3	-0.28	1	-0.32	-0.11
SD_pr	0.24	0.23	-0.23	0.74	0.77	0.55	-0.51	0.79	-0.32	1	0.38
Mean_vs	0.21	0.11	-0.28	0.55	0.45	0.74	-0.3	0.54	-0.11	0.38	1

SCC = soil cation concentration; Floodpl. = floodplains fraction; NF_dist = non-forest distance; def = water deficit; vs = wind speed; DSL = dry season length; pr = precipitation.

Source: Produced by the author.

The full model with all seven predictors (M1) explained up to 55.7% of gap fraction variability ($R^2 = 0.557$) (Table 6.3). This model still showed multicollinearity highlighted by two large VIC values, e.g. > 10 , of *Mean_def* and *SD_def*. Moreover, the inclusion of wind variables produced only small increments to R^2 . Thus, to simplify the model, we designed a simpler model (M2) excluding the wind variables and considering only one water stress variable (*Mean_def*). This simple model (M2) achieved a relatively inferior goodness of fit ($R^2 = 0.523$, BIC = 360.5) and statistically different ($F = 15.395$, $p < 0.01$) than the full model. However, it had the advantage of simplicity as it only used four predictors. Following our hypothesis of different forest dynamics in floodplains in relation to water stress, we designed another model including an interaction term (*Floodplains:Mean_def*) over the simple model (M3 – Final model), achieving a superior gap fraction explanation ($R^2 = 0.573$, BIC = 299.6) than the full model (M1), although not significantly different ($p = 1$). The final model (M3), although not statistically

different from the full model (M1), showed a BIC value much lower (BIC of M1 = 334.6 and M3 = 299.6), which indicated a better fit with more parsimony amongst the input variables. Moreover, the VIC values of the final model were all below two, meaning low intercorrelation between variables. All models were significantly different from a null model considering only the intercept term ($p < 0.001$). They showed randomly distributed residuals.

Table 6.3 - Estimated regression parameters (B), standard errors (SE B), t values (t) and p-values for the Generalized Linear Model (GLM) to estimate gap fraction. Also, Standardized beta coefficients (β), ΔR^2 (change in R^2 by adding the variable last on the model) and variance-inflation factors (VIC) for each predictor.

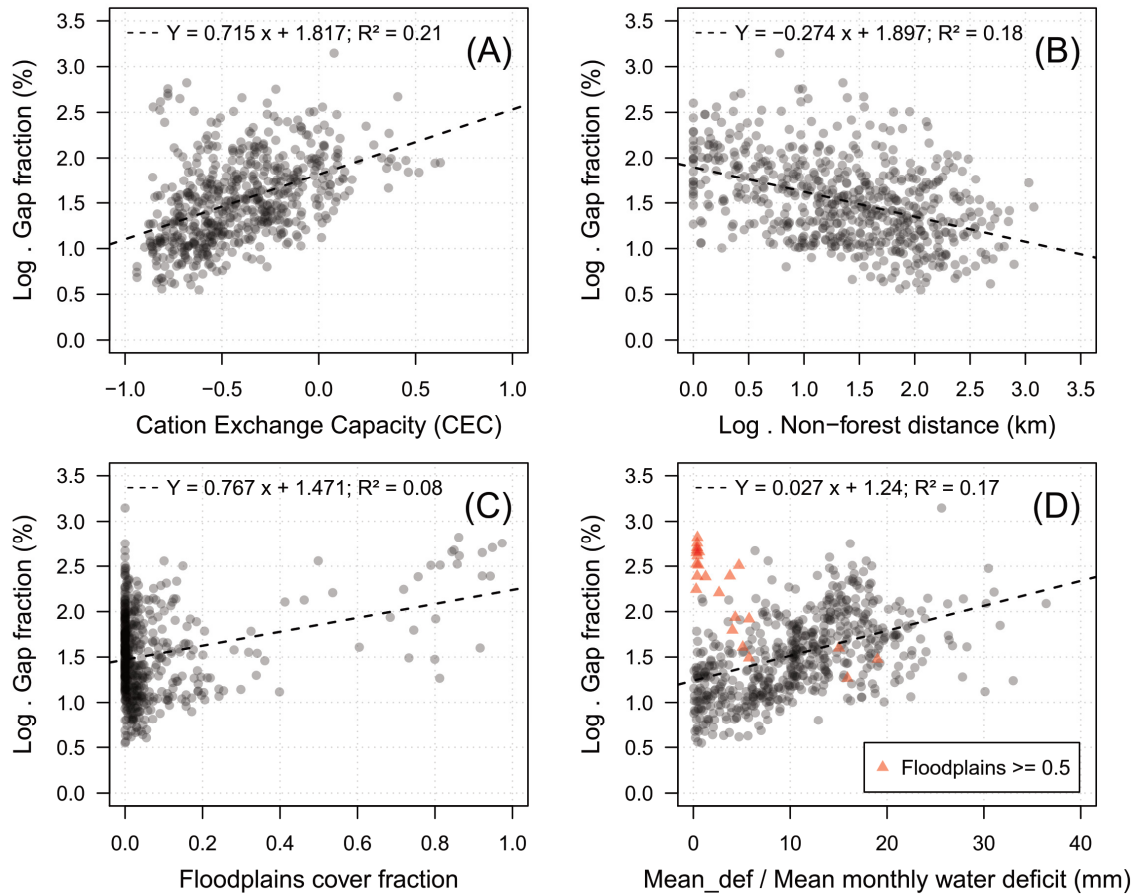
Model	ΔR^2	B	SE B	β	t	p-value	VIC
M1 – Full model	$R^2 = 0.557$; BIC = 334.6; M1 \neq Null model ($p < 0.01$)						
(Intercept)	-	1.9	0.09	-	21.5	< 0.01	-
SCC	0.16	0.68	0.05	0.20	14.6	< 0.01	1.19
Nonforest_dist	0.03	-0.14	0.02	-0.09	-6.53	< 0.01	1.44
Floodplains	0.12	1.12	0.09	0.18	12.86	< 0.01	1.31
Mean_def	0.02	0.04	0.01	0.27	5.2	< 0.01	18.1
SD_def	0.01	-0.02	0.01	-0.21	-4.28	< 0.01	15.3
Mean_vs	0.01	-0.26	0.08	-0.06	-3.4	< 0.01	2.3
SD_vs	0.02	1.81	0.37	0.12	4.83	< 0.01	4.2
M2 – Simple model	$R^2 = 0.523$; BIC = 360.5; M2 \neq M1 ($p < 0.01$)						
(Intercept)	-	1.7	0.06	-	30.13	< 0.01	-
SCC	0.17	0.69	0.05	0.20	14.59	< 0.01	1.17
Nonforest_dist	0.03	-0.13	0.02	-0.09	-5.99	< 0.01	1.39
Floodplains	0.12	1.14	0.09	0.18	12.64	< 0.01	1.31
Mean_def	0.06	0.02	0.002	0.13	8.56	< 0.01	1.53
M3 – Final model	$R^2 = 0.573$; BIC = 299.6; M3 = M1 ($p = 1$)						
(Intercept)	-	1.65	0.05	-	30.6	< 0.01	-
SCC	0.16	0.69	0.05	0.20	15.25	< 0.01	1.17
Nonforest_dist	0.03	-0.13	0.02	-0.09	-6.3	< 0.01	1.39
Floodplains	0.17	1.63	0.10	0.08	15.75	< 0.01	1.94
Mean_def	0.09	0.03	0.002	0.12	11.15	< 0.01	1.68
Floodplains:Mean_def	0.05	-0.11	0.01	-0.12	-8.39	< 0.01	1.61

SCC = soil cation concentration; def = water deficit; vs = wind speed.

Source: Produced by the author.

All predictors showed significant effects on the gap fraction ($p < 0.01$) (Table 6.3). The predictors *SCC*, *Floodplains*, and *Mean_def* presented positive regression coefficients (B), meaning that an increase in these predictors caused an increase in gap fraction. The *Nonforest_dist* and *Floodplains:Mean_def* had a negative B, indicating that decreases in their values caused an increase in gap fraction. These coefficient signs were corroborated by the expected relationship between predictors and gap fraction (Figures 6.8A to 6.8D). *Floodplains* and *SCC* solely explained the most gap fraction variability on the final model (M3) ($\Delta R^2 = 0.17$ and 0.16 , respectively). The order of predictors' importance ranked from the largest to the smallest absolute β values corresponded to: *SCC*, *Mean_def*, *Floodplains:Mean_def*, *Nonforest_dist*, and *Floodplains*. Considering β values, the *Floodplains* variable was not included as the most relevant predictor. However, it is important to note that the explained variability of this metric was shared with the interaction term. Moreover, β values from the simple model (M2), i.e. M3 without the interaction term, showed *Floodplains* as the second important predictor. Therefore, β values from M2 should represent more accurately the individual contribution of each predictor to the model. The interaction term included in M3 (*Floodplains:Mean_def*) caused a significant improvement over M2 likely associated with a better representation of high gap fraction and close to zero water deficit areas, i.e. flooded or seasonally-flooded forests (red triangles in Figure 6.8D).

Figure 6.8 - Relationships between gap fraction (log-scale) and predictors used in the final model: (A) soil cation concentration (SCC); (B) Non-forest distance (km) (log-scale); (C) Floodplains cover fraction; and (D) *Mean_def* / Mean monthly water deficit (mm). The dashed line represents a linear model. Red triangles on panel (D) represent samples with floodplains cover ≥ 0.5 .



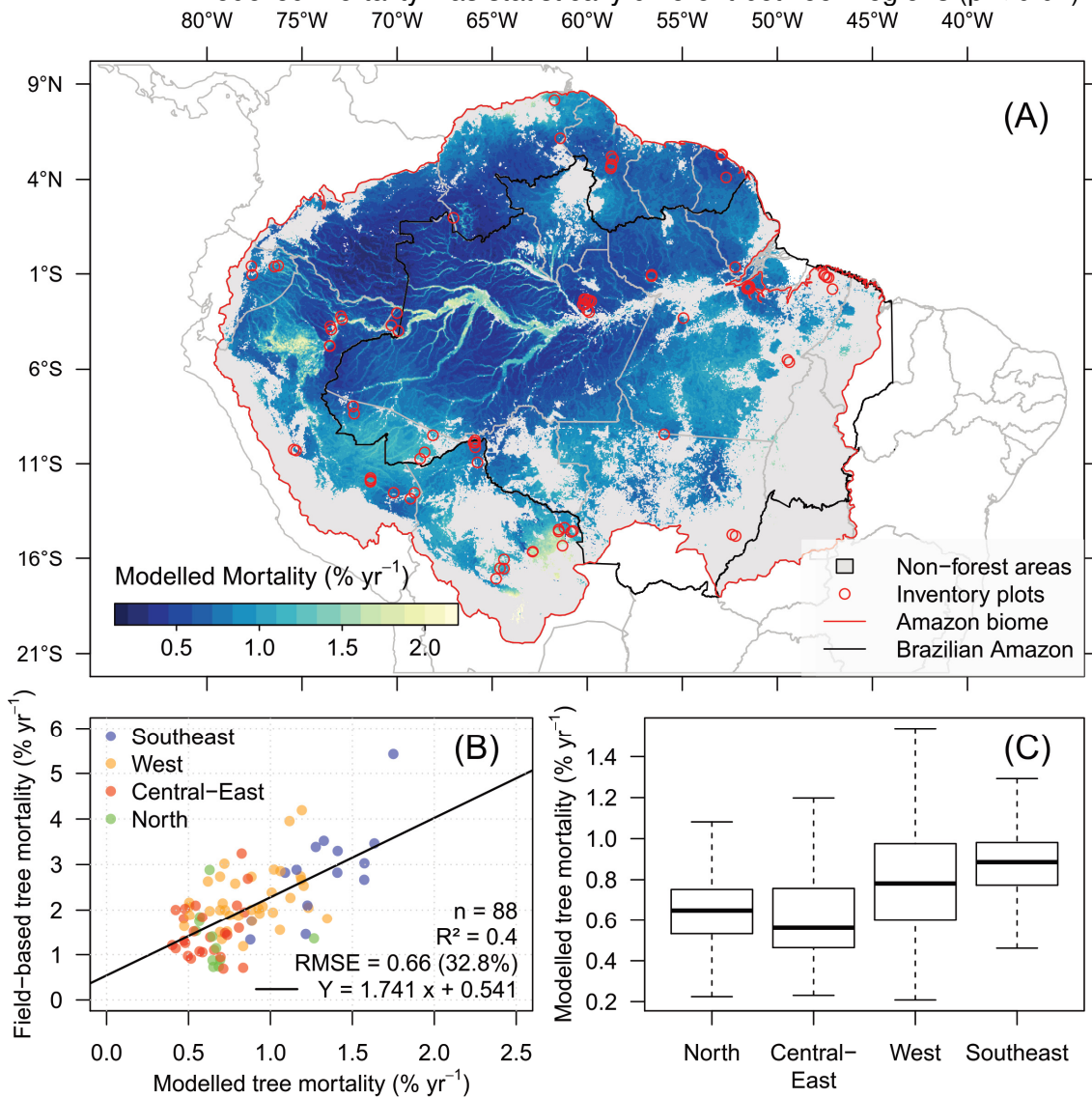
Source: Produced by the author.

6.3.3 Amazon-Wide Tree Mortality Prediction and Validation

We used the gap/environmental-climate model (M3 in Table 6.3) to spatialize gap fraction estimates over the Amazon biome at 5-km spatial resolution (Figure C.2) and then applied the gap-mortality relationship (Figure 6.6) to predict tree mortality (Figure 6.9A). In Figure 6.9A and 6.9C, the predictions showed higher tree mortality over southeast (Mean \pm SD: $0.89\% \pm 0.2$) and west ($0.8\% \pm 0.28$) regions, and lower tree mortality over the central-east ($0.66\% \pm 0.28$) and north ($0.65\% \pm 0.17$) Amazonian regions (see Figure 6.2 for regions). The regions

showed significantly different mean modelled mortality rates considering an ANOVA test ($p < 0.01$) (Figure 6.9C).

Figure 6.9 - Amazon-wide tree mortality prediction and validation. (A) Map of tree mortality (%.yr⁻¹) prediction at 5-km spatial resolution based on gap-mortality relationship (Figure 6.6) and gap/environmental-climate model (Table 6.3); (B) validation of modeled tree mortality using long-term inventory plot data from Brienen et al. (2015). Point colors represent the Amazon regions of Figure 6.2; and (C) modelled mortality (%.yr⁻¹) per Amazonian region. Each boxplot represents $n > 40,000$ 5-km pixels. Mean modelled mortality was statistically different between regions ($p < 0.01$).



Source: Produced by the author.

Floodplain areas at the west and central-east Amazon showed higher tree mortality (>1.5 % yr⁻¹) than other areas. Forests at the southwest, bordering the Andes mountains, and at the southeast, on a vegetation transition from Amazon

rainforest to *Cerrado* savannah, also showed very high mortality ($>1.5\% \text{ yr}^{-1}$). These areas also presented a very high mean water deficit ($> 40 \text{ mm}$). These patterns were consistent with those of individual gap fraction estimates (Figure 6.7A). Moreover, the spatialized SD of gap fraction estimates (Figure C.2B) indicated larger uncertainty for the southeast and west areas with higher gap fraction or tree mortality. The modeled tree mortality was associated with field-based tree mortality ($R^2 = 0.4$, $\text{RMSE} = 32.8\%$, Figure 6.9B), while it systematically underestimated the field-based mortality of 60%.

6.4 Discussion

Using five multi-temporal datasets and a unique single-date dataset ($n = 610$ flight lines) of airborne LiDAR for the Amazon, we explored the relationship between canopy gaps and mortality as well as its variability and drivers over the Amazon forest in an unprecedented way. The main contributions of the work are discussed in the next sub-sections face to the proposed scientific questions.

6.4.1 What is the minimum plot area necessary to obtain stable landscape-scale estimates of canopy tree mortality (Q1)?

Our LiDAR results showed that the variability of canopy tree mortality was greatly reduced over 5-ha plot areas, which would represent the minimum area for stable landscape-scale estimates of tree mortality associated with treefalls. In comparison with measurements at the ground level, this finding was consistent with results obtained by Wagner et al. (2010). They analyzed a tropical forest site in French Guiana (Paracou forest) and detected high variability on estimating forest structure and mortality over 1-ha plot areas, recommending the use of 4 ha for stable measurements in field inventory plots. Moreover, they observed an overall smaller coefficient of variation on their tree mortality estimates at 4-ha ($\text{CV} = 20\%$) when compared to our results at 5-ha ($\text{CV} = 43\%$). One explanation for this difference in variability is likely because the LiDAR sampled more diverse types of vegetation, e.g. forests at bottomlands, slope and plateau, than the ground measurements evaluated by Wagner et al. (2010).

6.4.2 How do canopy gaps relate to mortality rates of tropical forests and which gap definition best represents this relationship (Q2)?

Our findings indicated that 50% of the gaps were associated with canopy tree mortality. Probably, the remaining gaps are mostly mortality derived from past events that are not observed in the time scale of our analysis. This is because gaps are dynamically opened by natural or human-induced disturbances and closed by vegetation regrowth – of either vertical growth or lateral ingrowth. Therefore, the measurement of gaps is limited to the aggregated effect of such processes. When compared to ground observations, a study at Tapajós forest (TAP) found that only 30% of the mortality events were related to gaps measured in the ground (ESPÍRITO-SANTO et al., 2013). However, in that study area, part of the gaps had been probably closed by regeneration when the ground observations of dead fallen-trees (proxy for mortality) were collected, given that the trees' death year was unknown.

In our study, tree height had an unsuspected effect on tree mortality detection by gaps. We observed that LiDAR-gaps more successfully detected the loss of shorter trees at the canopy level (< 25 m) than that of taller emergent trees (> 25 m). This result is important because tree mortality estimated from multi-temporal passive optical multispectral sensors is generally restricted to the tallest trees due to the influence of within-canopy shadows on the detection and the necessity of large changes to offset the variability of view-illumination geometries and trees' phenology between pairs of images (DALAGNOL et al., 2019). In general, by closely inspecting the CHM over mortality locations, we verified that tree loss created holes on the canopy with an approximate size of the tree crowns. It occurred because the crowns were located on the same level of the neighboring canopy, i.e. a unique canopy layer. However, when tall trees died (> 25 m), these events very often did not create 'deep' gaps or exposed the ground. Instead, they revealed an understory within the multi-layered forest structure. Therefore, we expect that LiDAR gaps likely represent the mortality of most trees, but underestimate that of emergent trees (above the mean canopy height). These findings provide quantitative evidence for the field survey results from Leitold et

al. (2018), who found that the loss of large canopy trees did not always generate gaps, because of the tall multi-layered forest structure of the Amazon forests.

The relative height method for gap delineation provided the best relationship with mortality when compared to the fixed height cutoff approach. While the performance of the relative height was comparable with the fixed height cutoff of 10 m, it provides a dynamic adjustment to local height variability, likely providing a more stable and trustworthy gap delineation for large-scale applications over forests of varied structure. In addition, the use of other fixed height cutoffs with lower values (2 and 5 m), which have been traditionally adopted in the literature (BROKAW et al., 1982; LOBO; DALLING, 2014; HUNTER et al., 2015), was not strongly associated with mortality. We expect this finding to contribute to the debate of gap delineation, where the relative height method should be an improvement over the accepted fixed height cutoff approach. This will provide gap delineations more associated with mortality using an easy and adaptable method for multiple-site application.

Although we observed a strong relationship between gaps and mortality at the 5-ha plot areas ($R^2 = 0.72$; Figure 6.6), this relationship was non-linear (logarithmic fitting). This effect was mostly observed over the TAP, BON and TAL sites. BON and TAL had effects of fire disturbance, while TAP was disturbed by fire and logging. Therefore, some of the very high gap fractions were associated with areas that suffered abrupt events of tree mortality in the past caused by fire and high-intensity logging. The increased mortality over large gap fractions was consistent with the expected behavior of burned forests, which have exhibited higher mortality rates, even after many years from the fire event (SILVA et al., 2018). Nevertheless, the observed relationship describes an average annual mortality rate.

6.4.3 How does canopy gap dynamics derived from airborne LiDAR data vary across the Brazilian Amazon forests (Q3)?

Our results showed a consistent differential canopy dynamic across the Brazilian Amazon. We observed slow dynamic canopies at the northwest when compared

to the rest of the region. In our view, these spatial patterns describe the mixed effect between tree mortality and overall forest structure (canopy heterogeneity) and functioning (slower vs. faster dynamics); the presence of flooded or seasonally-flooded forests in some areas especially on the central-east portion; and the potential but limited effect of forest degradation on the gap fractions at the southeast. In the southern flank of the Amazon, there was a prevalence of higher values of gap fraction, driven by larger gaps. This pattern was coincident with very high canopy heterogeneity (high deviations of CHM height). This fact is probably related to different types of vegetation observed in the region, such as those associated with bamboo-dominated forests at the southwest Amazon (DALAGNOL et al., 2018), and the mosaic of vegetation types occurring across the transition zone between Amazon rainforest and savannahs (*Cerrado*) at the southeast region (ROSAN et al., 2019). For instance, LiDAR flight lines between the limits of the Mato Grosso and Pará states (~52°W; 5° to 10° S) sensed an ecotone between dense forests, seasonal forests and savannahs. Liana-infested forests may also contribute to part of the increased gap fractions and mortality over the eastern Amazon since their occurrence over that area was indicated in previous reports (NELSON, 1994), which also described them as having lower heights and heterogeneous canopy. Meanwhile, the productivity of these forests is limited by water (WAGNER et al., 2017) with the region being recently affected by two major droughts in 2010 and 2015/2016. Therefore, we hypothesize that the great vegetation variability and drought effects might have jointly contributed to the observed increased gap fractions and estimated mortality.

The proximity of forests with high gap fractions to the 'deforestation arch', especially in southeast Brazil, also suggests some degree of influence of human disturbance, e.g. logging, fire, fragmentation, on results. However, the systematic observation of higher gap fractions in eastern Amazon from 3° to 12° S (1000 km on a straight line) is an evidence of a stronger influence of this factor, at least locally. Because of the inexistence of a forest degradation product for the Amazon, we attempted to assess this effect by considering the distance to the closest non-forest area. The non-forest distance, although having a significant relationship with gap fraction ($R^2 = 0.18$; Figure 6.8), did not explain much new

gap fraction variability than the other predictors when included last in the model ($\Delta R^2 = 0.03$ at M3; Table 6.3). This suggests that although having an effect on gap fraction, it may not necessarily be causal. Even though, we expect that those regions with higher gap fraction might still show some level of degradation and, thus, mortality estimates can be partly enhanced because of that. In addition, we expect that these effects consist of a long-term process, i.e. recovery from logging or fragmentation (BROADBENT et al., 2008), rather than recent catastrophic events. This is because the observed gap fractions, although higher than other regions, do not correspond to those of forests that undergo catastrophic fire events (BRANDO et al., 2014), as highlighted by very high gap fractions of 10-25% at the BON, TAL and TAP sites (Figure 6.6).

A few sites with large gap fractions were also found nearby major rivers such as the Amazonas, suggesting an association to flooded or seasonally flooded vegetation (floodplains). However, care is necessary for this analysis because: (1) we did not explicitly take into account the date of LiDAR acquisition (spread across the year of 2016), which would have an important effect on the status of the forest (flooded or not flooded); and (2) we did not have available field information *per site* to detail the flooding effect, e.g. height and duration.

6.4.4 What landscape- and/or regional-scale factors drive gap variability in the Brazilian Amazon (Q4)?

Our findings suggest that gap occurrence and size are not linearly related to slope or HAND variables, which are common descriptors of topography. We expected topography to control part of the tree mortality rates at the landscape scale, especially in forests with fast dynamics. On these forests, trees tend to die more frequently at valleys than at plateaus, and large trees die more frequently at sloped areas (TOLEDO et al., 2012). In less dynamic regions, the influence of topography onto the tree mortality is less pronounced or negligible (CHAO et al., 2009). Goulamoussène et al. (2017) showed also that large gaps were more frequent at bottomlands water-logged forests and wind-exposed areas. Since we sampled a broad range of forest types with varying slope and HAND, and, thus

not all forests were expected to have low dynamism, one explanation for the lack of relationship between gaps and topography was the possible occurrence of a non-linear association not captured in our regression analysis.

Water stress has been previously associated with tree mortality and specifically to drought-related mortality, as observed over plots located across the Amazon forests (PHILLIPS et al., 2009). Meanwhile, the variability in forest structure has also been associated with rainfall patterns and specifically the deviation of rainfall (SAATCHI et al., 2007). In our study, the analysis of gap dynamics described a similar pattern as that of water stress in the Amazon, showing a gradient from the northwest (wetter) to the southeast (drier). This relationship has potential implications regarding the long-term reduction of rainfall across Amazon forests associated with climate change. However, more analyses are still needed to assess temporal changes to mortality.

Higher soil fertility in younger alluvial soils of the western Amazon has been associated with faster forest dynamics, which in turn is translated into high tree mortality (QUESADA et al., 2010). The observed spatial pattern of gap fraction matches the patterns of soil fertility represented by the *SCC* product. Therefore, we expect this variable to be an important predictor of gap fraction and tree mortality at the regional scale. Even though *SCC* was an independent source of data that corroborated the gap dynamics and tree mortality at the regional scale, it is important to note a few caveats about the product and its relationship with gap fraction. For instance: (1) the *SCC* product should represent only a portion of soil fertility; (2) the product has uncertainties related to the interpolation method; and (3) the soil sampling used to build the product was rather scarce at the eastern region in the Pará state (ZUQUIM et al., 2019). These facts should not be ignored because of high *SCC* in the eastern region was coincident with the largest gap fraction observations, which might produce bias in the analysis.

Wind should also play an important role in the mortality of tropical forests by uprooting trees, especially over the northwest Amazon (RIFAI et al., 2016; NEGRÓN-JUÁREZ et al., 2018). However, our findings did not support the effect of wind on gap dynamics and mortality. This is most likely because each

individual gap was constrained to a maximum area of 1 ha in order to describe the small-scale disturbances within the forest. Meanwhile, wind-disturbances generally affects areas greater than 25 ha (NEGRÓN-JUÁREZ et al., 2018). Therefore, this effect was not observed in our small-scale canopy gap analysis.

As discussed previously, floodplains and non-forest distance (as a proxy for degradation) were also significant for predicting gap fraction. These findings support the expected effects of increased gaps at water-logged bottomlands (FERRY et al., 2010; GOULAMOUSSENE et al., 2017), potentially increased mortality by flooding (RESENDE et al., 2019), and degradation and fragmentation effects (LAURANCE et al., 1998; BROADBENT et al., 2008).

6.4.5 Does tree mortality modelled from gaps and environmental-climate proxies reproduce spatial patterns from plot-based estimates across the Amazon (Q5)?

Our findings suggest that tree mortality estimates, derived from gap/environmental-climate modelling, match the overall patterns of tree mortality estimated from field inventory data. The regional patterns reported in the literature of increased mortality at the west and southeast Amazon and lower mortality at the central-east Amazon and north (Guiana Shields) were confirmed (QUESADA et al., 2010; JOHNSON et al., 2016). Besides these patterns, other notable areas in our tree mortality map included: (1) lower mortality over large regions of undisturbed forests at northwest Brazil (Amazonas state; 53°W; 12°S) and southeast Brazil (Xingu forests from the Mato Grosso state; 53°W; 12°S); (2) increased mortality in bamboo-dominated forests at the southwest Amazon in the limits from Brazil (state of Acre) and Peru (70°W; 10°S) (DALAGNOL et al., 2018).

The LiDAR-modelled tree mortality was consistent with field-based mortality, even for plots located outside of the initially sampled area. Part of this success was due to the use of the largest dataset of airborne LiDAR data available over the Amazon ($n = 610$ flight lines). This unprecedented mission brought unique data over remote areas of the Amazon forest, where plot data collection is inexistent and extremely hard to be performed. The LiDAR predictions of tree

mortality were systematically lower (about 60%) than those of field measurements. This was because the model was built considering only the mortality of canopy trees, associated with the treefall mode of death, instead of the mortality rate of all trees, i.e. including standing dead and mortality of understory trees. Moreover, the modeled predictions likely showed good agreement with plot data because of an intrinsic relationship between tree mortality and environmental and climate predictors, amongst other drivers, especially water stress (PHILLIPS, et al., 2009) and soil fertility (QUESADA et al., 2010).

Our resultant map of tree mortality for the Amazon biome can be potentially integrated into an ecosystem model, e.g. LPJ-GUESS, as background mortality rates. The expected outputs will be likely more accurate than the current mortality representation, facilitating also the simulations of carbon balance under distinct climate change scenarios. However, additional studies are still needed to further understand gap phase dynamics and relationship with mortality over open forests and floodplain environments. The effect of disturbance can also be further disentangled by the means of ancillary degradation maps, e.g. to be developed using time-series analyses of remote sensing data (LIMA et al., 2019).

6.5 Conclusions

We conclude that tree mortality estimates from repeated airborne LiDAR high-spatial resolution data can provide stable estimates at the landscape scale when sampling an area of at least 5 ha. When only single-date airborne LiDAR data is available, the delineated gaps can be used to represent canopy tree mortality, because they are associated with at least 50% of mortality events. Tree height affected the detection of mortality by gaps. Contrary to the generally observed with passive optical multispectral sensors, LiDAR-gaps detected more successfully the loss of shorter trees at canopy level (< 25 m) than the loss of taller and emergent trees (> 25 m).

This was the first time that gap dynamics were studied using LiDAR data at a regional scale in tropical forests. Our findings showed clear patterns of gap

variability across the Amazon forest, where higher gap fractions occurred in the west and southeast regions. These regions are known by higher tree mortality when compared to the central-east and north areas. These patterns were influenced to some extent by forest degradation. However, water stress (proxied by water deficit) and soil fertility (proxied by SCC) were key predictors of gap dynamics and tree mortality. Considering environmental-climate drivers and tree mortality predictions over the entire Amazon region, the patterns of mortality matched those derived from long-term field inventory data.

7 GENERAL DISCUSSION

Accurate large-scale detection of tropical forest mortality is required to assess environmental and climate change effects. This study addressed new approaches for quantifying and monitoring tropical forest mortality. It contributed to fill knowledge gaps of mortality variability at very diverse and heterogeneous environments across the Amazon forests. Overall, the findings highlighted the feasibility of detecting tropical forest mortality using different sources of passive and active optical remote sensing data. Specifically, three approaches were developed to: (1) study mortality processes of bamboo die-off using MODIS (MAIAC) data at the landscape scale; (2) quantify individual tree loss with multi-temporal VHR passive optical imagery; and (3) relate high-resolution canopy gaps detected from airborne LiDAR data to tree mortality at the local scale, up-scaling gap estimates to produce Amazon-wide mortality maps considering environmental-climate predictors. Since there was no unique strategy to address all scales and processes at once, the best-suited data and methods were assessed for each study.

In Chapter 4, a method was proposed to detect mortality in a specific Amazonian vegetation type: the bamboo-dominated forests. When compared with forest types in the Amazon, increased rates of mortality can be observed over bamboo-dominated forests due to interspecific competition between bamboo and trees. The present findings showed that large-scale bamboo die-off can be automatically detected with very high accuracy (> 80%) using a time series of MODIS (MAIAC) data. Even though the 'bamboo-fire hypothesis' was rejected by our analysis, the fire occurrence was enhanced by bamboo die-off when it occurred nearby human settlements, e.g. agricultural and pasture lands, roads and rivers, and when following severe droughts. This occurs because most of the fire occurrence in the Amazon is dependent on an anthropogenic ignition source since natural fires are rare. Therefore, the generated map portraying the size-age of bamboo structure can be used in further studies to explore tree mortality driven by bamboo dynamics and fire at the southwestern Amazon region. In addition, it can provide strategic information for forest management planning and prevention of major fire events. The map can also constitute a species distribution

layer for Essential Biodiversity Variables (EBV). These EBVs are sets of spatialized variables that report about forest biodiversity. They were first developed around 2015 having increased attention from the scientific community since this year.

In Chapter 5, a method to semi-automatically track canopy tree loss using multi-temporal VHR optical data has been successfully developed and validated. Although the resultant accuracy was not optimal (64%), it consisted of an improvement over the existing methods that either relied on visual assessment of the imagery or only assessed tree species mortality by their flowering events. The accuracy of the current approach can still be improved by utilizing pairs of imagery with more similar view-illumination angles and day of year acquisition. It can also take advantage of more precise tree-crown delineation methods based, for instance, on deep learning techniques. Using better-segmented crowns, one could calculate a more precise spectral difference between the crowns of sequential images. It is important to note that the approach used in Chapter 5 is still limited in terms of area coverage by data availability since there are not many satellites collecting VHR data. The recent advent of satellite constellations could help on this matter. However, new studies should assess whether the spatial resolution of such instruments, such as the 3-m from the PlanetScope satellite constellation, would fit for tree mortality detection.

In Chapter 6, the findings showed that canopy gaps could be used as proxies for small-scale mortality since they represented at least 50% of mortality. In addition, the spatial patterns from the modelled tree mortality matched those of field data. However, if the forest is degraded, the gap-mortality relationship becomes weak, because it is difficult to disentangle the natural disturbance from the human-degradation signal. In this case, multi-temporal LiDAR is still the optimal method to estimate tree mortality. The produced Amazon-wide tree mortality map from LiDAR was the final product of this chapter. The map showed spatial patterns consistent with those observed in field data from the RAINFOR network. It also showed increased tree mortality varying with water deficit and soil fertility gradients; with spatial location alongside floodplains (potential flood mortality) and/or close to rivers; and with disturbance or forest degradation represented by

distances from roads and human settlements. Other potential drivers of tree mortality, proxied by gap dynamics, should be further explored. This is especially true at the landscape scale, where the current analyses have not detected clear drivers of mortality. The resultant map of Amazon tree mortality from Chapter 6 has great potential to be further analyzed. For instance, this tree mortality map should be combined with regional AGB maps in order to calculate average carbon turnover rates for the Amazon forests.

The combined results from Chapters 4, 5 and 6 highlighted the limitations imposed by the nature of the data and the developed methods on tree mortality estimates. For instance, only the mortality associated with treefalls was detected in Chapters 5 and 6, which is the mode-of-death causing larger changes in the canopy structure and opening gaps. This fact should partly explain why the detected gaps do not represent the full extent of tree mortality measured by field plots. Furthermore, studies based on field data have shown that tree mortality is higher at plots with bamboo than without bamboo. However, since their plots have a limited sampling (only a few hectares), the generalization of these patterns to the whole bamboo-dominated forests is a huge leap. Given the availability of VHR imagery over the bamboo-dominated areas, the tree loss detection method developed in Chapter 5 could be applied to detect tree mortality and assess how it varies across different bamboo patches and with bamboo age. Therefore, by confirming patterns observed at the plot scale, such study contributes to precise estimates of carbon turnover in the southwest region. In this region, the bamboo-dominated forests cover a significant area. Nevertheless, the resultant Amazon tree mortality map generated here showed increased tree mortality rates at the southwest Amazon where bamboo dominates. However, this pattern was not directly related to the bamboo occurrence. It was possibly linked to the more fertile soils of the region, which partly drove the mortality estimates.

Additionally, contrasting findings regarding the accuracy of mortality detection with different tree sizes were highlighted in Chapters 5 and 6. While the multi-temporal analysis of multispectral VHR data (Chapter 5) more successfully detected the loss of the tallest and emergent trees, an opposite pattern was observed for LiDAR. The mortality inferred by gaps, delineated using single-date

airborne LiDAR data (Chapter 6), more accurately represented the mortality of the intermediate canopy trees (< 25 m). As an explanation, the VHR approach requires large structural canopy changes for accurate detections in order to offset the different view-illumination geometries and trees' phenology between the pairs of images. On the other hand, in the LiDAR data, as discussed in Chapter 6, the multi-layered canopy might be responsible for rapidly closing the space previously occupied by a large/tall tree, thus not allowing the creation of gaps. Multi-temporal LiDAR data would in fact solve this problem.

It is very important to highlight the LiDAR datasets used in this study. They comprise unique observations over the Amazon forests, in terms of total sampled area (610 flight lines, 2,300 km² total) and sampled locations over remote areas. Most of these sampled areas will be hardly covered by ground surveys over the next decades, especially those located in remote locations of the Amazon. This fact emphasizes the importance of the present broad-scale investigation that has used more than 600 flight lines of LiDAR data in the analysis.

Finally, considering the future LiDAR satellite missions, the assessment of temporal changes of gap dynamics and tree mortality across the Amazon deserves new studies. An alternative and innovative way to tackle both spatial and temporal estimates of tree mortality is the development of a data-model fusion approach. The approach could combine the LiDAR measurements of forest structure to parametrize an ecosystem model, e.g. the LPJ-GUESS model, and use it to model tree mortality. Alternatively, such an approach could leverage the availability of orbital large-footprint LiDAR data from the recent Global Ecosystem Dynamics Investigation (GEDI) mission to help parametrize the model, using the airborne small-footprint LiDAR data for validating the spatial patterns.

8 CONCLUDING REMARKS

This study showed the importance and applicability of passive and active optical remote sensing data, and especially multi-temporal data, for quantifying and monitoring tropical forest mortality considering observations at different scales. From the combined analysis of results, the most relevant findings were:

- (i) Bamboo die-off can be automatically detected with 79% accuracy at coarse MODIS spatial resolution and annual revisit time. The die-off may be associated with increased fire probability during drought years and especially nearby land use areas, suggesting a bamboo-human-fire association. Further studies can use multi-temporal VHR imagery over these areas to quantify individual tree mortality in order to corroborate field estimates at larger scales. This would lead to more consistent estimates of bamboo effects onto southwest Amazon carbon balance.
- (ii) Individual tree losses can be mapped with an average precision of 64% using multi-temporal VHR satellite imagery. The VHR data detected more accurately the loss of the tallest trees that generally opened large canopy gaps. This approach can be further improved by having better tree-crown delineation methods and/or acquiring pairs of images with more similar view-illumination geometries and close dates of collection.
- (iii) Canopy gaps delineated by single-date airborne LiDAR data represented at least 50% of the tree mortality. The mortality of shorter trees at canopy level (< 25 m) was more successfully detected than the mortality of taller emergent trees (> 25 m). The relative height-gap delineation method was superior to the fixed height cutoff approach. Higher gap fractions were associated with increased water deficit, soil fertility, and the occurrence of degraded and flooded forests.
- (iv) Modelled tree mortality, based on the gap dynamics and environmental-climate predictors, reproduced patterns of Amazon forest mortality observed from long-term field inventory data. Increased rates of LiDAR-derived mortality were observed at the western and southeast regions of the Amazon than at the central-east and north regions of this biome.

REFERENCES

- ABATZOGLOU, J. T. *et al.* TerraClimate, a high-resolution global dataset of monthly climate and climatic water balance from 1958-2015. **Scientific Data**, v. 5, p. 1–12, 2018.
- ALLEN, C. D. *et al.* A global overview of drought and heat-induced tree mortality reveals emerging climate change risks for forests. **Forest Ecology and Management**, v. 259, n. 4, p. 660–684, 2010.
- ANDEREGG, W. R. L. *et al.* Meta-analysis reveals that hydraulic traits explain cross-species patterns of drought-induced tree mortality across the globe. **Proceedings of the National Academy of Sciences**, v. 113, n. 18, p. 2–7, 2016.
- ANDERSEN, H. E. *et al.* Monitoring selective logging in western Amazonia with repeat lidar flights. **Remote Sensing of Environment**, v. 151, p. 157–165, 2014.
- ANDERSON, L. O. *et al.* Disentangling the contribution of multiple land covers to fire-mediated carbon emissions in Amazonia during the 2010 drought. **Global Biogeochemical Cycles**, v. 29, n. 10, p. 1739–1753, 2015.
- ANDERSON, L. O. *et al.* Remote sensing detection of droughts in Amazonian forest canopies. **New Phytologist**, v. 187, n. 3, p. 733–750, 2010.
- ARAGÃO, L. E. O. C. *et al.* 21st Century drought-related fires counteract the decline of Amazon deforestation carbon emissions. **Nature Communications**, v. 9, n. 1, p. 1–12, 2018.
- ARAGÃO, L. E. O. C. *et al.* Environmental change and the carbon balance of Amazonian forests. **Biological Reviews**, v. 89, n. 4, p. 913–931, 2014.
- ARAGÃO, L. E. O. C. *et al.* Spatial patterns and fire response of recent Amazonian droughts. **Geophysical Research Letters**, v. 34, n. 7, p. 1–5, 2007.
- ARCHER, E. rfPermute: estimate permutation p-values for random forest importance metrics v.2.1.6. 2018. Available from: <https://github.com/EricArcher/rfPermute>.
- ASNER, G. P. *et al.* Forest canopy gap distributions in the Southern Peruvian Amazon. **PLoS ONE**, v. 8, n. 4, 2013.
- ASNER, G. P. *et al.* High-resolution forest carbon stocks and emissions in the Amazon. **Proceedings of the National Academy of Sciences**, v. 107, n. 38, p. 16738–16742, 2010.
- ASNER, G. P. *et al.* Selective logging in the Brazilian Amazon. **Science**, v. 310, n. 5747, p. 480–482, 2005.
- ASNER, G. P.; KELLER, M.; SILVA, J. N. M. Spatial and temporal dynamics of forest canopy gaps following selective logging in the eastern Amazon. **Global Change Biology**, v. 10, n. 5, p. 765–783, 2004.

- AVITABILE, V. *et al.* An integrated pan-tropical biomass map using multiple reference datasets. **Global Change Biology**, v. 22, n. 4, p. 1406–1420, 2016.
- BADDELEY, A.; RUBAK, E.; TURNER, R. **Spatial point patterns: methodology and applications with R**. London: Chapman and Hall; CRC Press, 2015.
- BAKER, T. R. *et al.* Variation in wood density determines spatial patterns in Amazonian forest biomass. **Global Change Biology**, v. 10, n. 5, p. 545–562, may 2004.
- BALÉE, W. The culture of Amazonian forests. In: POSEY, D. A.; BALÉE, W. (Ed.). **Resource management in Amazonia: indigenous and folk strategies**. New York: New York Botanical Garden, 1989. p. 1–21.
- BARLOW, J. *et al.* Wildfires in bamboo-dominated Amazonian forest: impacts on above-ground biomass and biodiversity. **PLoS ONE**, v. 7, n. 3, 2012.
- BASTIN, J. F. *et al.* Pan-tropical prediction of forest structure from the largest trees. **Global Ecology and Biogeography**, v. 27, n. 11, p. 1366–1383, 2018.
- BATES, D. *et al.* Fitting linear mixed-effects models using lme4. **Journal of Statistical Software**, v. 67, n. 1, p. 1–48, 2015.
- BIRCHER, N.; CAILLERET, M.; BUGMANN, H. The agony of choice: different empirical mortality models lead to sharply different future forest dynamics. **Ecological Applications**, v. 25, n. 5, p. 1303–1318, 2015.
- BOEHM, H. D. V.; LIESENBERG, V.; LIMIN, S. H. Multi-temporal airborne LiDAR-survey and field measurements of tropical peat swamp forest to monitor changes. **IEEE Journal of Selected Topics in Applied Earth Observations and Remote Sensing**, v. 6, n. 3, p. 1524–1530, 2013.
- BRANDO, P. M. *et al.* Abrupt increases in Amazonian tree mortality due to drought-fire interactions. **Proceedings of the National Academy of Sciences of the United States of America**, v. 111, n. 17, p. 6347–52, 2014.
- BREIMAN, L. E. O. Random forests. **Machine Learning**, v. 45, n. 1, p. 5–32, 2001.
- BRIENEN, R. J. W. *et al.* Long-term decline of the Amazon carbon sink. **Nature**, v. 519, n. 7543, p. 344–8, 2015.
- BROADBENT, E. N. *et al.* Forest fragmentation and edge effects from deforestation and selective logging in the Brazilian Amazon. **Biological Conservation**, v. 141, n. 7, p. 1745–1757, 2008.
- BROKAW, N. V. L. Gap-phase regeneration in a tropical forest. **Ecology**, v. 66, n. 3, p. 682–687, 1985.
- BROKAW, N. V. L. The definition of treefall gap and its effect on measures of forest dynamics. **Biotropica**, v. 14, n. 2, p. 158, 1982.
- BUCHANAN, G. M. *et al.* Free satellite data key to conservation. **Science**, v. 361, n. 6398, p. 139–140, 2018.

- BUGMANN, H. *et al.* Tree mortality submodels drive simulated long-term forest dynamics: assessing 15 models from the stand to global scale. **Ecosphere**, v. 10, n. 2, 2019.
- CARVALHO, A. L. *et al.* Bamboo-dominated forests of the southwest Amazon: detection, spatial extent, life cycle length and flowering waves. **PLoS ONE**, v. 8, n. 1, 2013.
- CASTRO, W.; SALIMON, C. I.; MEDEIROS, H. Bamboo abundance, edge effects, and tree mortality in a forest fragment in Southwestern Amazonia. **Plant Ecology**, p. 159–164, 2013.
- CHAMBERS, J. Q. *et al.* Lack of intermediate-scale disturbance data prevents robust extrapolation of plot-level tree mortality rates for old-growth tropical forests. **Ecology Letters**, v. 12, n. 12, p. 22–25, 2009.
- CHAMBERS, J. Q. *et al.* The steady-state mosaic of disturbance and succession across an old-growth Central Amazon forest landscape. **Proceedings of the National Academy of Sciences of the United States of America**, v. 110, n. 10, p. 3949–54, 2013.
- CHAO, K. J. *et al.* How do trees die? mode of death in northern Amazonia. **Journal of Vegetation Science**, v. 20, n. 2, p. 260–268, 2009.
- CHAO, K.-J. *et al.* After trees die: quantities and determinants of necromass across Amazonia. **Biogeosciences Discussions**, v. 6, p. 1979–2006, 2009.
- CLARK, D. A.; CLARK, D. B. Getting to the canopy: tree height growth in a neotropical rain forest. **Ecology**, v. 82, n. 5, p. 1460–1472, 2001.
- CLARK, D. B. *et al.* Application of 1-m and 4-m resolution satellite data to ecological studies of tropical rain forests. **Ecological Applications**, v. 14, n. 1, p. 61–74, jan. 2004a.
- CLARK, D. B. *et al.* Quantifying mortality of tropical rain forest trees using high-spatial-resolution satellite data. **Ecology Letters**, v. 7, n. 1, p. 52–59, 2004b.
- CLEVELAND, R. B. *et al.* STL: a seasonal-trend decomposition procedure based on loess. **Journal of Official Statistics**, v.6, p.3-33, 1990.
- COCHRANE, M. A. Fire science for rainforests. **Nature**, v. 421, n. 6926, p. 913–919, 2003.
- CONDIT, R.; HUBBELL, S. P.; FOSTER, R. B. Mortality rates of 205 neotropical tree and shrub species and the impact of a severe drought. **Ecological Monographs**, v. 65, n. 4, p. 419–439, fev. 1995.
- CONTRERAS-HERMOSILLA, A.; DOORNBOSCH, R.; LODGE, M. The economics of illegal logging and associated trade. **Round Table on Sustainable Development**, v. 33, p. 8–9, 2007.
- COX, P. M. *et al.* Increasing risk of Amazonian drought due to decreasing aerosol pollution. **Nature**, v. 453, n. 7192, p. 212–5, 2008.
- D'OLIVEIRA, M. V. N. *et al.* Estimating forest biomass and identifying low-intensity logging areas using airborne scanning lidar in Antimary State Forest,

- Acre State, western Brazilian Amazon. **Remote Sensing of Environment**, v. 124, p. 479–491, 2012.
- DALAGNOL, R. *et al.* Assessment of climate change impacts on water resources of the Purus Basin in the southwestern Amazon. **Acta Amazonica**, v. 213, n. 2017, p. 213–226, 2017.
- DALAGNOL, R. *et al.* Life cycle of bamboo in the southwestern Amazon and its relation to fire events. **Biogeosciences**, v. 15, n. 20, p. 6087–6104, 18 out. 2018a.
- DALAGNOL, R. *et al.* **Life cycle of bamboo in the southwestern Amazon and its relation to fire events, (Version v2) [Data set]** Zenodo, 2018b.
- DALAGNOL, R. *et al.* Quantifying canopy tree loss and gap recovery in tropical forests under low-intensity logging using VHR satellite imagery and airborne LiDAR. **Remote Sensing**, v. 11, n. 7, p. 817, 4 abr. 2019.
- DANSON, F. M. *et al.* Forest canopy gap fraction from terrestrial laser scanning. **IEEE Geoscience and Remote Sensing Letters**, v. 4, n. 1, p. 157–160, 2007.
- DAUGHTRY, C. Estimating corn leaf chlorophyll concentration from leaf and canopy reflectance. **Remote Sensing of Environment**, v. 74, n. 2, p. 229–239, 2000.
- DENNISON, P. E.; BRUNELLE, A. R.; CARTER, V. A. Assessing canopy mortality during a mountain pine beetle outbreak using GeoEye-1 high spatial resolution satellite data. **Remote Sensing of Environment**, v. 114, n. 11, p. 2431–2435, nov. 2010.
- DENSLOW, J. S.; ELLISON, A. M.; SANFORD, R. E. Treefall gap size effects on above- and below-ground processes in a tropical wet forest. **Journal of Ecology**, v. 86, n. 4, p. 597–609, 1998.
- DIGGLE, P. A Kernel method for smoothing point process data. **Applied Statistics**, v. 34, n. 2, p. 138, 1985.
- DONCHYTS, G. *et al.* Global 30m height above the nearest drainage global 30m height above the nearest drainage new elevation dataset normalized according to the local height found along the drainage network. **EGU European Geosciences Union**, p. 2–3, 2016.
- ESPÍRITO-SANTO, F. D. B. *et al.* Size and frequency of natural forest disturbances and the Amazon forest carbon balance. **Nature Communications**, v. 5, p. 3434, 2014.
- ESPÍRITO-SANTO, F. D. B. *et al.* Gap formation and carbon cycling in the Brazilian Amazon: measurement using high-resolution optical remote sensing and studies in large forest plots. **Plant Ecology & Diversity**, v. 7, n. 1/2, p. 305–318, 3 abr. 2013.
- ESPÍRITO-SANTO, F. D. B. *et al.* Storm intensity and old-growth forest disturbances in the Amazon region. **Geophysical Research Letters**, v. 37, n. 11, p. 1–6, 2010.

- EVA, H.; HUBER, O. **A proposal for defining the geographical boundaries of Amazonia**. [S.l.]: European Commission, 2005.
- FASBENDER, D.; RADOUX, J.; BOGAERT, P. Bayesian data fusion for adaptable image pansharpening. **IEEE Transactions on Geoscience and Remote Sensing**, v. 46, n. 6, p. 1847–1857, 2008.
- FAVA, F.; COLOMBO, R. Remote sensing-based assessment of the 2005-2011 bamboo reproductive event in the Arakan mountain range and its relation with wildfires. **Remote Sensing**, v. 9, n. 1, 2017.
- FEARNSIDE, P. M. Potential impacts of climatic change on natural forests and forestry in Brazilian Amazonia. **Forest Ecology and Management**, v. 78, n. 1–3, p. 51–70, 1995.
- FELDPAUSCH, T. R. *et al.* Height-diameter allometry of tropical forest trees. **Biogeosciences**, v. 8, n. 5, p. 1081–1106, 2011.
- FELDPAUSCH, T. R. *et al.* Tree height integrated into pantropical forest biomass estimates. **Biogeosciences**, v. 9, n. 8, p. 3381–3403, 2012.
- FELDPAUSCH, T. R. *et al.* When big trees fall: damage and carbon export by reduced impact logging in southern Amazonia. **Forest Ecology and Management**, v. 219, n. 2/3, p. 199–215, 2005.
- FERNANDEZ, C.; STEEL, M. F. J. On bayesian modeling of fat tails and skewness. **Journal of the American Statistical Association**, v. 93, n. 441, p. 359–371, 1998.
- FERRY, B. *et al.* Higher treefall rates on slopes and waterlogged soils result in lower stand biomass and productivity in a tropical rain forest. **Journal of Ecology**, v. 98, n. 1, p. 106–116, jan. 2010.
- FISHER, J. I. *et al.* Clustered disturbances lead to bias in large-scale estimates based on forest sample plots. **Ecology Letters**, v. 11, n. 6, p. 554–563, 2008.
- FOSTER, J. R.; TOWNSEND, P. A.; ZGANJAR, C. E. Spatial and temporal patterns of gap dominance by low-canopy lianas detected using EO-1 Hyperion and Landsat Thematic Mapper. **Remote Sensing of Environment**, v. 112, n. 5, p. 2104–2117, 2008.
- FRANKLIN, D. C. *et al.* Bamboo, fire and flood: consequences of disturbance for the vegetative growth of a clumping, clonal plant. **Plant Ecology**, v. 208, n. 2, p. 319–332, 2010.
- FROLKING, S. *et al.* Forest disturbance and recovery: a general review in the context of spaceborne remote sensing of impacts on aboveground biomass and canopy structure. **Journal of Geophysical Research: Biogeosciences**, v. 114, n. G2, jun. 2009.
- GALVÃO, L. S. *et al.* On intra-annual EVI variability in the dry season of tropical forest: a case study with MODIS and hyperspectral data. **Remote Sensing of Environment**, v. 115, n. 9, p. 2350–2359, 2011.

- GAO, B. C. NDWI - A normalized difference water index for remote sensing of vegetation liquid water from space. **Remote Sensing of Environment**, v. 58, n. 3, p. 257–266, 1996.
- GAULTON, R.; MALTHUS, T. J. LiDAR mapping of canopy gaps in continuous cover forests: a comparison of canopy height model and point cloud based techniques. **International Journal of Remote Sensing**, v. 31, n. 5, p. 1193–1211, 2010.
- GLOOR, M. *et al.* Recent Amazon climate as background for possible ongoing special section : **Global Biogeochemical Cycles**, v. 29, n. 9, p. 1384–1399, 2015.
- GOULAMOUSSENE, Y. *et al.* Environmental control of natural gap size distribution in tropical forests. **Biogeosciences**, v. 14, n. 2, p. 353–364, 2017.
- GRISCOM, B. W.; ASHTON, P. M. S. Bamboo control of forest succession: *Guadua sarcocarpa* in Southeastern Peru. **Forest Ecology and Management**, v. 175, n. 1–3, p. 445–454, 2003.
- GRIZONNET, M. *et al.* Orfeo ToolBox: open source processing of remote sensing images. **Open Geospatial Data, Software and Standards**, v. 2, n. 1, p. 15, 2017.
- GUO, Q. *et al.* An object-based classification approach in mapping tree mortality using high spatial resolution imagery. **GIScience & Remote Sensing**, v. 44, n. 1, p. 24–47, 2007.
- HANSEN, M. C. *et al.* High-resolution global maps of 21st-century forest cover change. **Science**, v. 342, n. 6160, p. 850–853, 2013.
- HARRIS, I. *et al.* Updated high-resolution grids of monthly climatic observations - the CRU TS3.10 dataset. **International Journal of Climatology**, v. 34, n. 3, p. 623–642, 2014.
- HESS, L. L. *et al.* **LBA-ECO LC-07 wetland extent, vegetation, and inundation**: lowland Amazon Basin. Oak Ridge, Tennessee, USA: ORNL DAAC, 2015.
- HICKE, J. A.; LOGAN, J. Mapping whitebark pine mortality caused by a mountain pine beetle outbreak with high spatial resolution satellite imagery. **International Journal of Remote Sensing**, v. 30, p. 4427–4441, 2009.
- HILKER, T. *et al.* Vegetation dynamics and rainfall sensitivity of the Amazon. **Proceedings of the National Academy of Sciences**, v. 111, n. 45, p. 16041–16046, 2014.
- HUANG, C. YING; ANDEREGG, W. R. L.; ASNER, G. P. Remote sensing of forest die-off in the Anthropocene: from plant ecophysiology to canopy structure. **Remote Sensing of Environment**, v. 231, p. 111233, 2019.
- HUETE, A. *et al.* Overview of the radiometric and biophysical performance of the MODIS vegetation indices. **Remote Sensing of Environment**, v. 83, n. 1–2, p. 195–213, nov. 2002.

- HUNTER, M. O. *et al.* Structural dynamics of tropical moist forest gaps. **PLoS ONE**, v. 10, n. 7, p. 1–19, 2015.
- INGWELL, L. L. *et al.* The impact of lianas on 10 years of tree growth and mortality on Barro Colorado Island, Panama. **Journal of Ecology**, v. 98, n. 4, p. 879–887, 2010.
- INSTITUTO BRASILEIRO DE GEOGRAFIA E ESTATÍSTICA - IBGE. **Mapa de vegetação do Brasil**. Rio de Janeiro: IBGE, 2006.
- INSTITUTO NACIONAL DE PESQUISAS ESPACIAIS - INPE. **PRODES**: deforestation monitoring program. 2018. Available from: <http://www.obt.inpe.br/OBT/assuntos/programas/amazonia/prodes>.
- ISENBURG, M. **LAStools**: efficient tools for LiDAR processing v.3.1.1. 2018. Available from: <http://lastools.org>.
- JANZEN, D. H. Why bamboos take so long to flower. **Annual Review of Ecology and Systematics**, v. 7, n. 40, p. 347–391, 1976.
- JIMÉNEZ-MUÑOZ, J. C. *et al.* Record-breaking warming and extreme drought in the Amazon rainforest during the course of El Niño 2015–2016. **Scientific Reports**, v. 6, n. May, p. 33130, 2016.
- JOHNS, J. S.; BARRETO, P.; UHL, C. Logging damage during planned and unplanned logging operations in the eastern Amazon. **Forest Ecology and Management**, v. 89, n. 1–3, p. 59–77, 1996.
- JOHNSON, M. O. *et al.* Variation in stem mortality rates determines patterns of above-ground biomass in Amazonian forests: implications for dynamic global vegetation models. **Global Change Biology**, v. 22, n. 12, p. 3996–4013, 2016.
- KEANE, R. E. *et al.* Tree mortality in gap models: applications to climate change. **Climate Change**, v. 51, p. 509–540, 2001.
- KEELEY, J. E.; BOND, W. J. Mast Flowering and Semelparity in Bamboos: the bamboo fire cycle hypothesis. **The American Naturalist**, v. 154, n. 3, p. 383–391, 1999.
- KELLNER, J. R.; CLARK, D. B.; HUBBELL, S. P. Pervasive canopy dynamics produce short-term stability in a tropical rain forest landscape. **Ecology Letters**, v. 12, n. 2, p. 155–164, 2009.
- KELLNER, J. R.; HUBBELL, S. P. Adult mortality in a low-density tree population using high-resolution remote sensing. **Ecology**, v. 98, n. 6, p. 1700–1709, 2017.
- KRATTER, A. W. Bamboo specialization by amazonian birds. **Biotropica**, v. 29, n. 1, p. 100–110, 1997.
- KUMAR, S. S. *et al.* A quantitative study of the proximity of satellite detected active fires to roads and rivers in the Brazilian tropical moist forest biome. **International Journal of Wildland Fire**, v. 23, n. 4, p. 532–543, 2014.
- LAMANNA, J. A.; MARTIN, T. E. Logging impacts on avian species richness and composition differ across latitudes and foraging and breeding habitat preferences. **Biological Reviews**, v. 92, n. 3, p. 1657–1674, 2017.

- LAURANCE, S. G. W. *et al.* Long-term variation in Amazon forest dynamics. **Journal of Vegetation Science**, v. 20, n. 2, p. 323–333, 2009.
- LAURANCE, W. F. *et al.* Effects of a strong drought on Amazonian forest fragments and edges. **Journal of Tropical Ecology**, v. 17, n. 06, p. 771–785, 2001.
- LAURANCE, W. F. *et al.* Rain forest fragmentation and the dynamics of amazonian tree communities. **Ecology**, v. 79, n. 6, p. 2032–2040, 2010.
- LAURANCE, W. F.; BRUCE WILLIAMSON, G. Positive feedbacks among forest fragmentation, drought, and climate change in the Amazon. **Conservation Biology**, v. 15, n. 6, p. 1529–1535, 2001.
- LAWSON, S.; MACFAUL, L. **Illegal logging and related trade**: indicators of the global response. [S.l.]: Chatham House, 2010. 132p.
- LEITOLD, V. *et al.* El Niño drought increased canopy turnover in Amazon forests. **New Phytologist**, v. 219, n. 3, p. 959–971, 2018.
- LEUTNER, B.; HORNING, N.; SCHWALB-WILLMANN, J. RStoolbox: tools for remote sensing data analysis v0.2.1. 2018. Available from: <https://bleutner.github.io/RStoolbox/>.
- LEWIS, S. L. *et al.* The 2010 Amazon drought. **Science**, New York, v. 331, p. 554, 2011.
- LIAW, A.; WIENER, M. Classification and regression by randomForest. **R News**, v. 2, n. 3, p. 18–22, 2002.
- LIMA, T. A. *et al.* Comparing Sentinel-2 MSI and Landsat 8 OLI imagery for monitoring selective logging in the Brazilian Amazon. **Remote Sensing**, v. 11, n. 8, p. 961, 2019.
- LIU, Y. *et al.* Comparison of soil moisture simulated by {HBV96} and estimated from {TRMM} passive microwave observations for a catchment in southern {NSW}, Australia. In: INTERNATIONAL CONGRESS ON MODELLING AND SIMULATION (MODSIM), 2007. **Proceedings...** 2007. p. 1723–1728.
- LOBO, E.; DALLING, J. W. Spatial scale and sampling resolution affect measures of gap disturbance in a lowland tropical forest: implications for understanding forest regeneration and carbon storage. **Proceedings of the Royal Society B: Biological Sciences**, v. 281, e20133218, 2014.
- LOBOVIKOV, M. *et al.* **World bamboo resources**: a thematic study prepared in the framework of the global forest resources, assessment 2005. Rome: FAO, 2007. (FAO Technical Papers).
- LONDOÑO, X.; PETERSON, P. M. Guadua sacocarpa (Poaceae: Bambuseae), a new species of amazonian bamboo with leshy fruits. **Systematic Botany**, v. 16, n. 4, p. 630–638, 1991.
- LUCHT, W.; LEWIS, P. Theoretical noise sensitivity of BRDF and Albedo retrieval from the EOS-MODIS and MISR sensors with respect to angular sampling. **International Journal of Remote Sensing**, v. 21, n. 1, p. 81–98, 2000.

LYAPUSTIN, A. I. *et al.* Remote sensing of environment Multi-Angle Implementation of Atmospheric Correction for MODIS (MAIAC): 3 . atmospheric correction. **Remote Sensing of Environment**, v. 127, p. 385–393, 2012.

LYAPUSTIN, A.; WANG, Y. **MCD19A1 MODIS/Terra+Aqua land surface BRF daily L2G global 500m, 1km and 5km SIN Grid V006 [Data set]**. NASA EOSDIS Land Processes DAAC, 2018. Available from: <https://lpdaac.usgs.gov/products/mcd19a1v006/>.

MALHI, Y. *et al.* An international network to monitor the structure, composition and dynamics of Amazonian forests (RAINFOR). **Journal of Vegetation Science**, v. 13, n. 3, p. 439–450, 2002.

MARRA, D. M. *et al.* Large-scale wind disturbances promote tree diversity in a Central Amazon forest. **PLoS ONE**, v. 9, n. 8, 2014.

MARVIN, D. C.; ASNER, G. P.; SCHNITZER, S. A. Liana canopy cover mapped throughout a tropical forest with high-fidelity imaging spectroscopy. **Remote Sensing of Environment**, v. 176, p. 98–106, 2016.

MCDOWELL, N. *et al.* Mechanisms of plant survival and mortality during drought: why do some plants survive while others succumb to drought? **New Phytologist**, v. 178, n. 4, p. 719–739, jun. 2008.

MCGAUGHEY, R. J. **FUSION/LDV**: Software for LIDAR data analysis and visualization v. 3.6. 2016. Available from: http://forsys.cfr.washington.edu/fusion/fusion_overview.html.

MCMICHAEL, C. H. *et al.* Historical fire and bamboo dynamics in western Amazonia. **Journal of Biogeography**, v. 40, n. 2, p. 299–309, 2013.

MCMICHAEL, C. H.; PALACE, M. W.; GOLIGHTLY, M. Bamboo-dominated forests and pre-Columbian earthwork formations in south-western Amazonia. **Journal of Biogeography**, v. 41, n. 9, p. 1733–1745, 2014.

MEDDENS, A. J. H. *et al.* Evaluating methods to detect bark beetle-caused tree mortality using single-date and multi-date Landsat imagery. **Remote Sensing of Environment**, v. 132, p. 49–58, 2013.

MEDEIROS, H. *et al.* Tree mortality, recruitment and growth in a bamboo dominated forest fragment in southwestern Amazonia, Brazil. **Biota Neotropica**, v. 13, n. 2, p. 29–34, 2013.

MELACK, J. M.; HESS, L. L. Remote sensing of the distribution and extent of wetlands in the Amazon basin. In: JUNK, W. J. *et al.* (Ed.). **Amazonian floodplain forests: ecophysiology, biodiversity and sustainable management**. New York: Springer, 2010. p. 43–60.

MESQUITA, R. C. G.; DELAMÔNICA, P.; LAURANCE, W. F. Effect of surrounding vegetation on edge-related tree mortality in Amazonian forest fragments. **Biological Conservation**, v. 91, n. 2–3, p. 129–134, 1999.

MORISSETTE, J. T. *et al.* Validation of MODIS active fire detection products derived from two algorithms. **Earth Interactions**, v. 9, n. 9, 2005.

MOSER, P. *et al.* Interaction between extreme weather events and mega-dams increases tree mortality and alters functional status of Amazonian forests. **Journal of Applied Ecology**, v. 56, n. 12, p. 2641–2651, 2019.

MOURA, Y. M. *et al.* Seasonality and drought effects of Amazonian forests observed from multi-angle satellite data. **Remote Sensing of Environment**, v. 171, p. 278–290, 2015.

MOURA, Y. M. *et al.* Spectral analysis of amazon canopy phenology during the dry season using a tower hyperspectral camera and MODIS observations. **ISPRS Journal of Photogrammetry and Remote Sensing**, v. 131, p. 52–64, set. 2017.

NATIONAL AERONAUTICAL AND SPACE ADMINISTRATION - NASA. **NASA shuttle radar topography mission global 1 arc second**. Washington: NASA, 2013. (NASA EOSDIS Land Processes DAAC).

NEGRÓN-JUÁREZ, R. I. *et al.* Detection of subpixel treefall gaps with Landsat imagery in Central Amazon forests. **Remote Sensing of Environment**, v. 115, n. 12, p. 3322–3328, 2011.

NEGRÓN-JUÁREZ, R. I. *et al.* Vulnerability of Amazon forests to storm-driven tree mortality. **Environmental Research Letters**, v. 13, n. 5, 2018.

NELSON, B. W. Natural forest disturbance and change in the Brazilian Amazon. **Remote Sensing Reviews**, v. 10, p. 105–125, 1994.

NOBRE, A. D. *et al.* Height above the nearest drainage - a hydrologically relevant new terrain model. **Journal of Hydrology**, v. 404, n. 1/2, p. 13–29, 2011.

OLIVIER, J. *et al.* First macrofossil evidence of a pre-Holocene thorny bamboo cf. *Guadua* (Poaceae: Bambusoideae: Bambuseae: Guaduinæ) in south-western Amazonia (Madre de Dios - Peru). **Review of Palaeobotany and Palynology**, v. 153, n. 1/2, p. 1–7, 2009.

OSAZUWA-PETERS, O. L. *et al.* Selective logging: do rates of forest turnover in stems, species composition and functional traits decrease with time since disturbance? - a 45 year perspective. **Forest Ecology and Management**, v. 357, p. 10–21, 2015.

PADOCH, C. *et al.* Urban forest and rural cities: multi-sited households, consumption patterns, and forest resources in Amazonia. **Ecology and Society**, v. 13, n. 2, 2008.

PHILLIPS, O. L. *et al.* Drought sensitivity of the Amazon Rainforest. **Science**, v. 323, n. 5919, p. 1344–1347, 2009.

PHILLIPS, O. L. *et al.* Pattern and process in Amazon tree turnover, 1976-2001. **Philosophical Transactions of the Royal Society B: Biological Sciences**, v. 359, n. 1443, p. 381–407, 29 mar. 2004.

PLOWRIGHT, A. ForestTools: analyzing remotely sensed forest data v.0.2. 2018. Available from: <https://rdr.io/cran/ForestTools/>.

- QUESADA, C. A. *et al.* Basin-wide variations in Amazon forest structure and function are mediated by both soils and climate. **Biogeosciences**, v. 9, n. 6, p. 2203–2246, 2012.
- QUESADA, C. A. *et al.* Soils of Amazonia with particular reference to the RAINFOR sites. **Biogeosciences**, v. 8, n. 6, p. 1415–1440, 2011.
- QUESADA, C. A. *et al.* Variations in chemical and physical properties of Amazon forest soils in relation to their genesis. **Biogeosciences**, v. 7, n. 5, p. 1515–1541, 2010.
- R CORE TEAM. **R**: a language and environment for statistical computing. Vienna, Austria: R Foundation for Statistical Computing, 2016. Available from: <https://www.r-project.org/>.
- READ, J. M. *et al.* Application of merged 1-m and 4-m resolution satellite data to research and management in tropical forests. **Journal of Applied Ecology**, v. 40, n. 3, p. 592–600, 2003.
- RESENDE, A. F. DE *et al.* Massive tree mortality from flood pulse disturbances in Amazonian floodplain forests: the collateral effects of hydropower production. **Science of the Total Environment**, v. 659, p. 587–598, 2019.
- RIBEIRO, G. H. P. M. *et al.* Mechanical vulnerability and resistance to snapping and uprooting for Central Amazon tree species. **Forest Ecology and Management**, v. 380, p. 1–10, 2016.
- RIFAI, S. W. *et al.* Landscape-scale consequences of differential tree mortality from catastrophic wind disturbance in the Amazon. **Ecological Applications**, v. 26, n. 7, p. 2225–2237, 2016.
- ROCKWELL, C. A. *et al.* Logging in bamboo-dominated forests in southwestern Amazonia: caveats and opportunities for smallholder forest management. **Forest Ecology and Management**, v. 315, p. 202–210, 2014.
- ROSAN, T. M. *et al.* Extensive 21st-Century woody encroachment in South America's Savanna. **Geophysical Research Letters**, v. 46, n. 12, p. 6594–6603, 2019.
- ROUSE, J. W. *et al.* Monitoring vegetation systems in the great plains with ERTS. In: EARTH RESOURCES TECHNOLOGY SATELLITE-1 SYMPOSIUM, 3., 1974. **Proceedings...** 1974. p.301-317.
- ROY, D. P. *et al.* The collection 5 MODIS burned area product - global evaluation by comparison with the MODIS active fire product. **Remote Sensing of Environment**, v. 112, n. 9, p. 3690–3707, 2008.
- SAATCHI, S. *et al.* Distribution of aboveground live biomass in the Amazon basin. **Global Change Biology**, v. 13, n. 4, p. 816–837, 2007.
- SANTOS, H. G. *et al.* **O novo mapa de solos do Brasil**: legenda atualizada. Rio de Janeiro: Embrapa Solos, 2011. 67p.
- SATO, L. Y. Tecnologia Lidar para quantificação dos impactos de incêndios na estrutura. 2016. 128p. Thesis (Doctor in Remote Sensing) – Instituto Nacional de Pesquisas Espaciais, São José dos Campos, 2016.

- SCHWARZ, G. Estimating the dimension of a model. **Annals of Statistics**, v. 6, n. 2, p. 461–464, 1978.
- SHIMABUKURO, Y. E. *et al.* Monitoring deforestation and forest degradation using multi-temporal fraction images derived from Landsat sensor data in the Brazilian Amazon. **International Journal of Remote Sensing**, v. 40, n. 14, p. 5475–5496, 2019.
- SILVA JUNIOR, C. H. L. *et al.* Fire responses to the 2010 and 2015/2016 Amazonian droughts. **Frontiers in Earth Science**, v. 7, p. 1–16, may 2019.
- SILVA, C. A. *et al.* ForestGapR: an r package for forest gap analysis from canopy height models. **Methods in Ecology and Evolution**, v. 2019, p. 1347–1356, 2019.
- SILVA, C. A. *et al.* rLiDAR: LiDAR Data Processing and Visualization v.0.1.1. 2017. Available from: <https://cran.r-project.org/web/packages/rLiDAR/rLiDAR.pdf>.
- SILVA, C. V. J. *et al.* Drought-induced Amazonian wildfires instigate a decadal-scale disruption of forest carbon dynamics. **Philosophical Transactions of the Royal Society B: Biological Sciences**, v. 373, n. 1760, 2018.
- SILVEIRA, M. **A floresta aAberta com bambu no sudoeste da Amazônia: padrões e processos em múltiplas escalas.** 2001. 129p. Thesis (Doctor in Ecology) - Universidade de Brasília, Brasília, 2001.
- SMITH, M.; NELSON, B. W. Fire favours expansion of bamboo-dominated forests in the south-west Amazon. **Journal of Tropical Ecology**, v. 27, n.1, p. 59–64, 2011.
- SOMBROEK, W. G. **A reconnaissance of the soils of the Brazilian Amazon region.** Wageningen: Centre for Agricultural Publication and Documentation, 1966.
- STEFFEN, M. **Comparison of different methods for univariate time series imputation in R.** Köln: Cologne University of Applied Science, 2015. 20p.
- STONE, T. A.; LEFEBVRE, P. Using multi-temporal satellite data to evaluate selective logging in Pará, Brazil. **International Journal of Remote Sensing**, v. 19, n. 13, p. 2517–2526, 1998.
- SWAINE, M. D.; LIEBERMAN, D.; PUTZ, F. E. The dynamics of tree populations in tropical forest: a review. **Journal of Tropical Ecology**, v. 3, n. 4, p. 359–366, 1987.
- TEJADA, G. *et al.* Evaluating spatial coverage of data on the aboveground biomass in undisturbed forests in the Brazilian Amazon. **Carbon Balance and Management**, v. 14, n. 1, p. 1–18, 2019.
- THOMAS, R. Q. *et al.* Low mortality in tall tropical trees. **Ecology**, v. 94, n. 4, p. 920–929, 2013.
- TOLEDO, J. J. DE *et al.* How much variation in tree mortality is predicted by soil and topography in Central Amazonia? **Forest Ecology and Management**, v. 262, n. 3, p. 331–338, 2011.

- TOLEDO, J. J. *et al.* Tree mode of death in Central Amazonia: effects of soil and topography on tree mortality associated with storm disturbances. **Forest Ecology and Management**, v. 263, p. 253–261, jan. 2012.
- TRANCOSO, R. *et al.* Deforestation and conservation in major watersheds of the Brazilian Amazon. **Environmental Conservation**, v. 36, n. 04, p. 277–288, 3 fev. 2010.
- TYMEN, B. *et al.* Evidence for arrested succession in a liana-infested Amazonian forest. **Journal of Ecology**, v. 104, n. 1, p. 149–159, 2016.
- UNITED STATES GEOLOGICAL SURVEY - USGS. **Shuttle Radar Topography Mission, 1 Arc Second, v.2.1**. 2006. Available from: https://www.usgs.gov/centers/eros/science/usgs-eros-archive-digital-elevation-shuttle-radar-topography-mission-srtm-1-arc?qt-science_center_objects=0#qt-science_center_objects.
- VAN GUNST, K. J. *et al.* Do denser forests have greater risk of tree mortality: a remote sensing analysis of density-dependent forest mortality. **Forest Ecology and Management**, v. 359, p. 19–32, 2016.
- VERMOTE, E. *et al.* Second Simulation of the Satellite Signal in the Solar Spectrum (6S). 6S user guide version 2. appendix III: description of the subroutines. **IEEE Transactions on Geoscience and Remote Sensing**, v. 35, n. 3, p. 675–686, 1997.
- WAGNER, F. *et al.* Assessing effects of plot size and census interval on estimates of tropical forest structure and dynamics. **Biotropica**, v. 42, n. 6, p. 664–671, 2010.
- WAGNER, F. H. *et al.* Climate drivers of the Amazon forest greening. **PLoS ONE**, v. 12, n. 7, p. 1–15, 2017.
- WANG, Y. *et al.* Mapping tropical disturbed forests using multi-decadal 30 m optical satellite imagery. **Remote Sensing of Environment**, v. 221, p. 474–488, 2019.
- WATLING, J. *et al.* Impact of pre-Columbian “geoglyph” builders on Amazonian forests. **Proceedings of the National Academy of Sciences**, v. 114, n. 8, p. 1868–1873, 2017.
- WILLIAMSON, G. B. *et al.* Amazonian tree mortality during the 1997 El Niño drought. **Conservation Biology**, v. 14, n. 5, p. 1538–1542, 2000
- WULDER, M. A. *et al.* Multi-temporal analysis of high spatial resolution imagery for disturbance monitoring. **Remote Sensing of Environment**, v. 112, n. 6, p. 2729–2740, 2008.
- YAMAMOTO, I. Forest gap dynamics and tree regeneration. **Journal Of Forest Research**, v. 5, n. 4, p. 223–229, 2000.
- ZUQUIM, G. *et al.* Making the most of scarce data: mapping soil gradients in data-poor areas using species occurrence records. **Methods in Ecology and Evolution**, v. 10, n. 6, p. 788–801, 2019.

APPENDICES A - SUPPLEMENTARY MATERIALS FROM CHAPTER 4

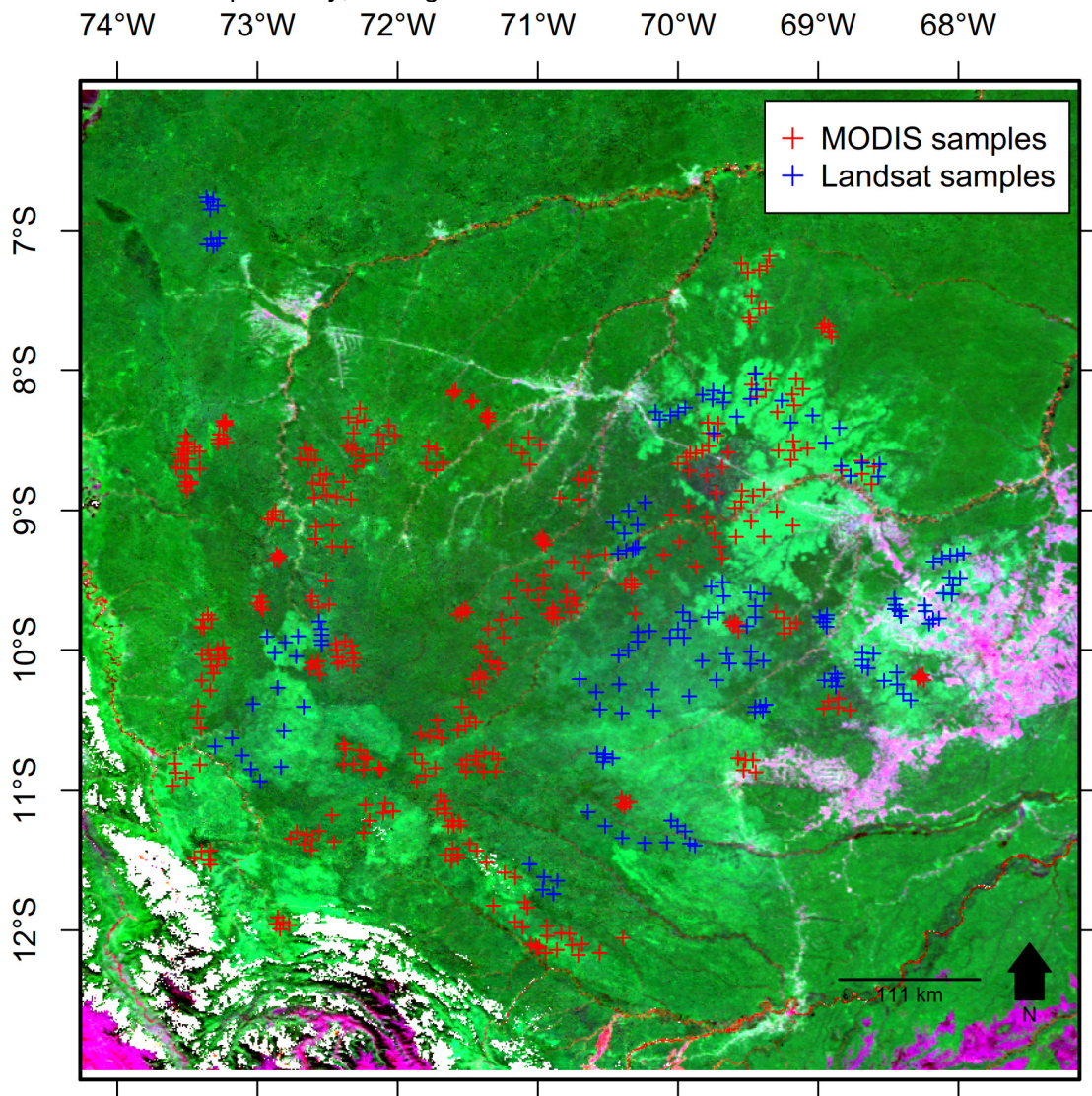
Data availability. The processed MODIS (MAIAC) data and bamboo maps processed in this paper are freely available and published at: <https://doi.org/10.5281/zenodo.1229425>.

Table A.1 - Dates of TM/Landsat-5 images used for validation of bamboo die-off predictions. The date of each image (YYYY-MM-DD) is presented for each path-row (World Reference System 2) in the columns.

Path-Row	006-065	003-066	002-067	003-067	005-067	003-068
Dates	1985-06-28	1985-07-09	1985-09-04	1985-08-26	1985-07-23	1985-07-09
	1986-08-02	1986-07-28	1986-08-06	1986-09-30	1986-07-26	1986-10-16
	1987-08-05	1987-08-16	1987-08-25	1987-08-16	1987-08-14	1987-08-16
	1988-08-07	1988-07-17	1988-08-11	1988-08-18	1988-07-15	1988-06-15
	1989-08-26	1989-07-20	1989-08-14	1989-09-22	1989-09-04	1989-08-21
	1990-04-23	1990-07-07	1990-09-18	1990-07-23	1990-06-19	1990-08-24
	1991-06-13	1991-07-26	1991-07-27	1991-07-26	1991-07-08	1991-07-10
	1992-10-05	1992-08-13	1992-07-21	1992-07-28	1992-08-27	1992-07-28
	1993-08-05	1993-09-01	1993-08-25	1993-06-13	1993-08-14	1993-06-13
	1994-07-23	1994-07-18	1994-07-27	1994-07-18	1994-06-30	1994-07-18
	1995-08-27	1995-08-22	1995-07-30	1995-08-22	1995-06-17	1995-07-05
	1996-07-12	1996-07-23	1996-08-01	1996-07-23	1996-07-05	1996-07-23
	1997-09-01	1997-07-10	1997-07-19	1997-07-10	1997-07-24	1997-08-27
	1998-07-18	1998-07-13	1998-09-24	1998-08-30	1998-09-13	1998-07-13
	1999-08-06	1999-08-01	1999-08-10	1999-08-17	1999-07-30	1999-08-17
	2000-10-11	2000-07-18	2000-07-27	2000-07-18	2000-09-02	2000-09-04

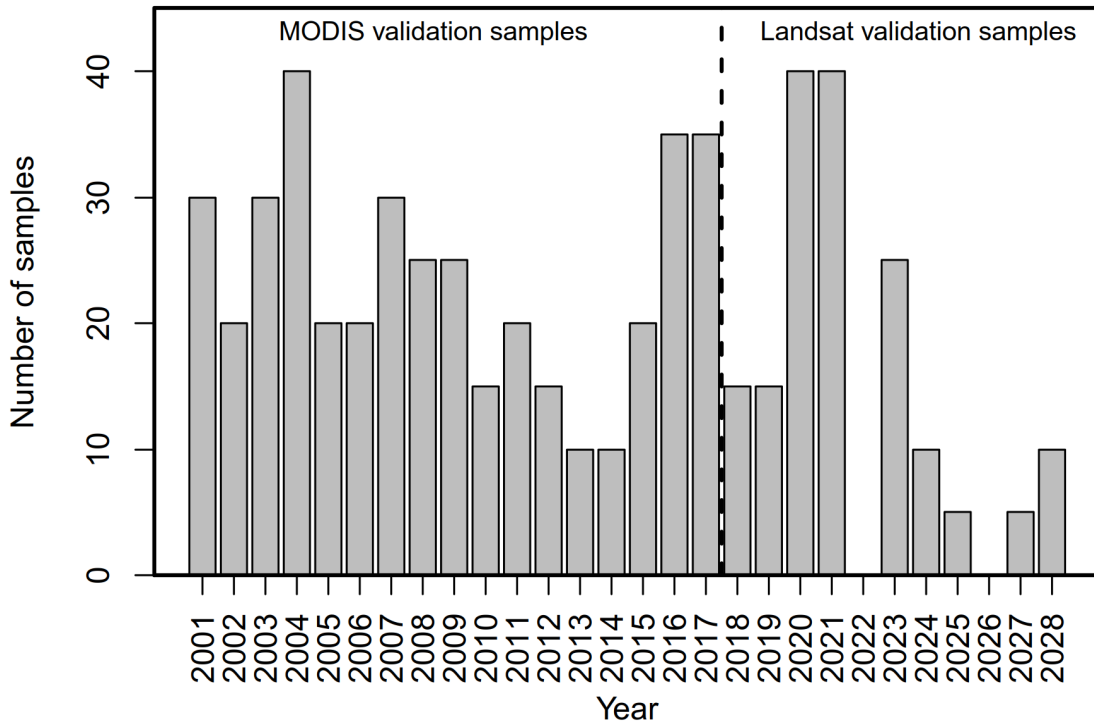
Source: Produced by the author.

Figure A.1 - Spatial distribution of validation samples obtained from MODIS (2001–2017) imagery in red and Landsat (1985–2000) imagery in blue. The image at background is a false-color composite from MODIS (MAIAC) images of bands 1 (Red), 2 (NIR) and 6 (shortwave infrared), in RGB, respectively, in August 2015.



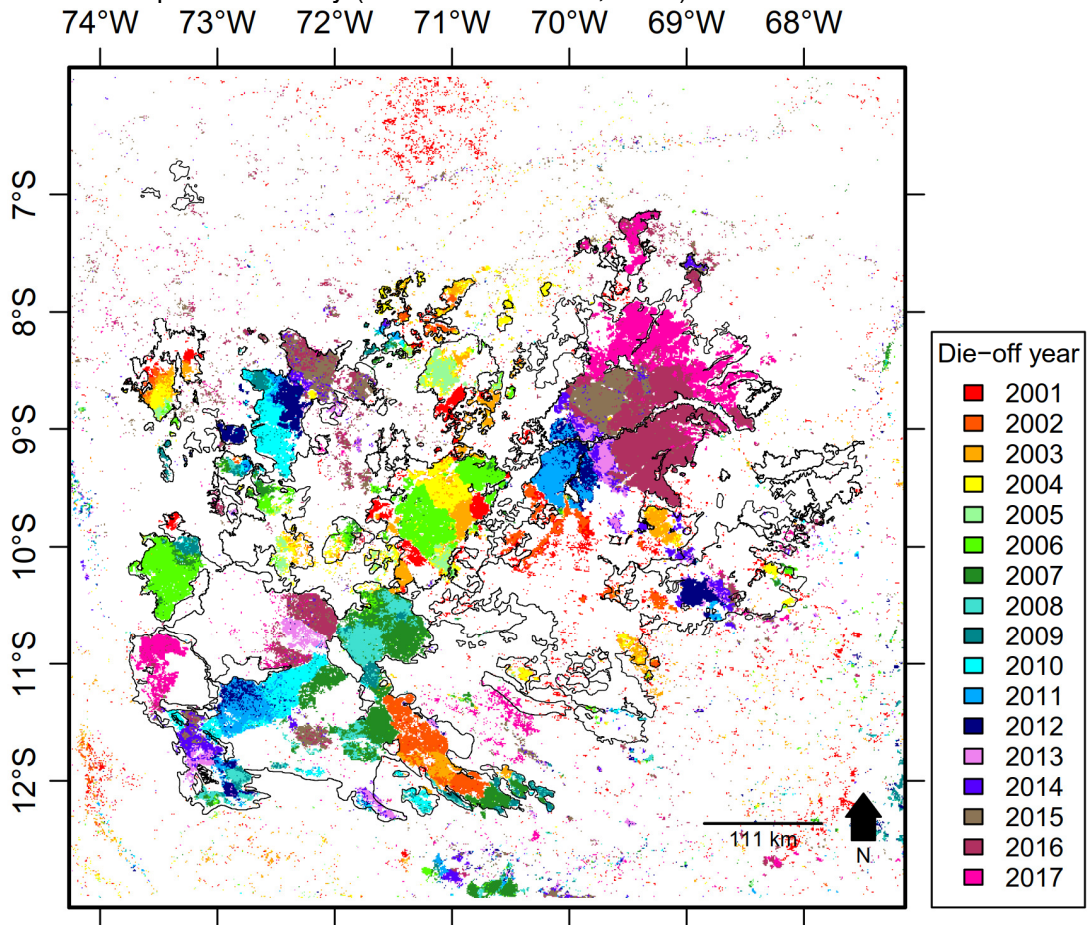
Source: Produced by the author.

Figure A.2 - Temporal distribution of validation samples for bamboo die-off detection (2001–2017) from MODIS imagery; and for bamboo die-off prediction (2018–2028) from Landsat imagery.



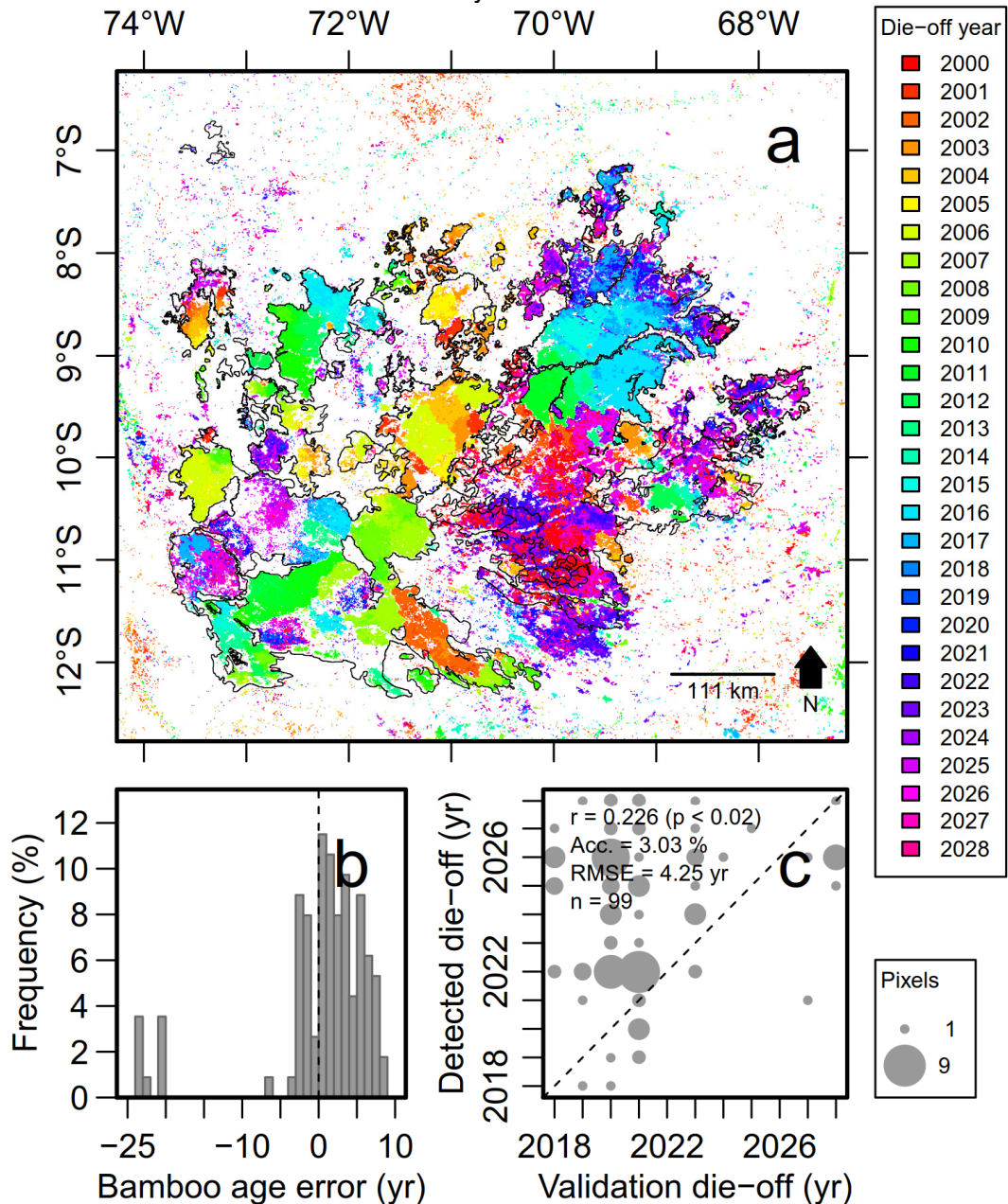
Source: Produced by the author.

Figure A.3 - Bamboo die-off during 2001–2017 from the combined detections using MODIS (MAIAC) NIR-1 and NIR-2 and the bilinear model. The black lines indicate the perimeter of the bamboo-dominated areas delineated in a previous study (CARVALHO et al., 2013).



Source: Produced by the author.

Figure A.4 - MODIS bamboo die-off prediction map from 2000 to 2028 using the empirical reflectance profiles of the near infrared 2 (NIR-2) reflectance as a function of bamboo cohort age (a). Validation between predicted die-off (2017–2028) and visual interpreted die-off from previous life cycle in Landsat false-color composites (1985–2000) (c) and residuals distribution (b). The dashed line represents the 1:1 line in (c) and age residual = 0 in (b). Size of circles is related to the number of pixels that hit the same observed/estimate die-off year.



Source: Produced by the author.

APPENDICES B - SUPPLEMENTARY MATERIALS FROM CHAPTER 5

Two methods were applied for ITC delineation in the study: the voronoi-based method for LiDAR data and the marker-controlled watershed segmentation (MCWS) for very high-resolution (VHR) satellite data. Both methods consisted of detecting the tree tops and then segmenting the tree crowns. The basic assumption for the tree top detection is that tree tops have a higher signal than the rest of the crown, i.e., they reflect more electromagnetic energy or have a higher elevation. Therefore, they can be detected over an image attribute using a moving local maxima filter given a window size. The tree crown segmentation was performed differently for the two methods, as described below.

The voronoi-based method for LiDAR data delineated the tree crowns following a series of steps: (1) defined an initial radius for each tree top based on a fixed maxcrown parameter; (2) segmented the data using the centroidal voronoi tessellation approach; and (3) excluded cells with a height below a percentage of the maximum height inside the tree crown, based on an exclusion percentage parameter. The parameters used for the ITC delineations were: 3x3 m window size, maxcrown of 15 m, exclusion of 0.7, and minimum height threshold of 8 m. The canopy height model (CHM) was used as the input.

The MCWS used with the VHR satellite data delineates the crowns using the watershed concept. The MCWS considers the forest canopy as a topographic surface and segments the tree crowns by virtually flooding the surface with water from the tree tops to the crown lowest values, which are usually shadows. The parameters used were: 5x5 m window size and the reflectance of the near infrared (NIR) band as the input.

For assessment of the automatic ITC delineation parameters, we compared them to a manual delineation by visual assessment. To do that, we randomly selected seven plots of 100 x 100 m (1 ha), equivalent to 5% of the total LiDAR data area, and performed an independent visual assessment where we manually delineated the tree crowns inside the plots based on the visual inspection of natural color composites (Red-Green-Blue) from the satellite data and the CHM from LiDAR

data. Then, we calculated a set of statistical metrics: true positive (TP, correct detection), false positive (FP, commission error), false negative (FN, omission error), precision (p, Eq. B.1), recall (r, Eq. B.2) and F-score (F, Eq. B.3) metrics, over-segmentation (OS), and relative tree density root mean square error (RMSE). OS was calculated as the ratio of tree crowns over-segmented to tree crowns delineated. The tree density RMSE was calculated considering the number of reference trees and detected trees in each plot and then converted to relative RMSE by dividing the RMSE by the average number of reference trees between the plots. The tree crown delineation, i.e., the area mapped by each tree crown, was assessed considering the intersection-over-union (IoU) metric. The IoU is calculated as the ratio between the intersection of areas and the union of areas of each ITC delineated between the manual and automatic methods.

$$p = TP / (TP + FP) \quad (B.1)$$

$$r = TP / (TP + FN) \quad (B.2)$$

$$F = (2 * p * r) / (p + r) \quad (B.3)$$

We found that the mean precision for determining the tree locations was high for both VHR satellite ($p = 0.79$) and LiDAR data ($p = 0.88$) (Table B.1 and B.2). However, the method using LiDAR data more precisely delineated the tree crowns in terms of area (IoU = 0.39) than the VHR satellite data (IoU = 0.27). Regarding the lower IoU of VHR satellite data, this means that the tree crowns automatically delineated using VHR data on average did not represent their true area; however, the ITCs should still show spectral similarity intra-objects, which is the main objective of this application. Overall, the automatic method using VHR satellite data showed a more similar density of trees ($n = 591$) to the reference ($n = 598$), than the automatic method with LiDAR data ($n = 551$) did with its reference ($n = 426$). This probably occurred because neighboring tree crowns, visually, are more easily distinguished by their color difference using VHR satellite data than by their elevation differences using airborne LiDAR data. However, we expect that the automatic method should be able to detect these subtle differences with LiDAR data. This is supported by the high precision, recall, and IoU with LiDAR data.

Table B.1 - ITC delineation assessment per plot for VHR satellite data.

Grid	Nref	Ndet	TP	FP	FN	p	r	F	OS	IoU
1	128	92	69	17	59	0.80	0.54	0.64	0.22	0.22
2	95	86	53	19	42	0.74	0.56	0.63	0.19	0.24
3	84	77	53	12	31	0.82	0.63	0.71	0.17	0.28
4	75	83	48	17	27	0.74	0.64	0.69	0.35	0.29
5	80	90	52	14	28	0.79	0.65	0.71	0.27	0.29
6	73	80	51	7	22	0.88	0.70	0.78	0.24	0.28
7	63	83	44	11	19	0.80	0.70	0.75	0.41	0.32
Total	598	591	370	97	228	0.79	0.62	0.69	0.26	0.27

Nref = Number of reference trees; Ndet = Number of detected trees; TP = true positive; FP = false positive; FN = false negative; p = precision; r = recall; F= F-Score; OS = over-segmentation; IoU = Intersection over Union.

Source: Produced by the author.

Table B.2 - ITC delineation assessment per plot for airborne LiDAR data.

Grid	Nref	Ndet	TP	FP	FN	p	r	F	OS	IoU
1	84	75	62	5	22	0.93	0.74	0.82	0.19	0.35
2	60	81	51	8	9	0.86	0.85	0.86	0.33	0.39
3	58	86	51	11	7	0.82	0.88	0.85	0.31	0.45
4	58	75	46	2	12	0.96	0.79	0.87	0.30	0.34
5	50	81	45	7	5	0.87	0.90	0.88	0.40	0.44
6	57	83	45	11	12	0.80	0.79	0.80	0.44	0.37
7	59	70	43	3	16	0.93	0.73	0.82	0.35	0.37
Total	426	551	343	47	83	0.88	0.80	0.84	0.33	0.39

Nref = Number of reference trees; Ndet = Number of detected trees; TP = true positive; FP = false positive; FN = false negative; p = precision; r = recall; F= F-Score; OS = over-segmentation; IoU = Intersection over Union.

Source: Produced by the author.

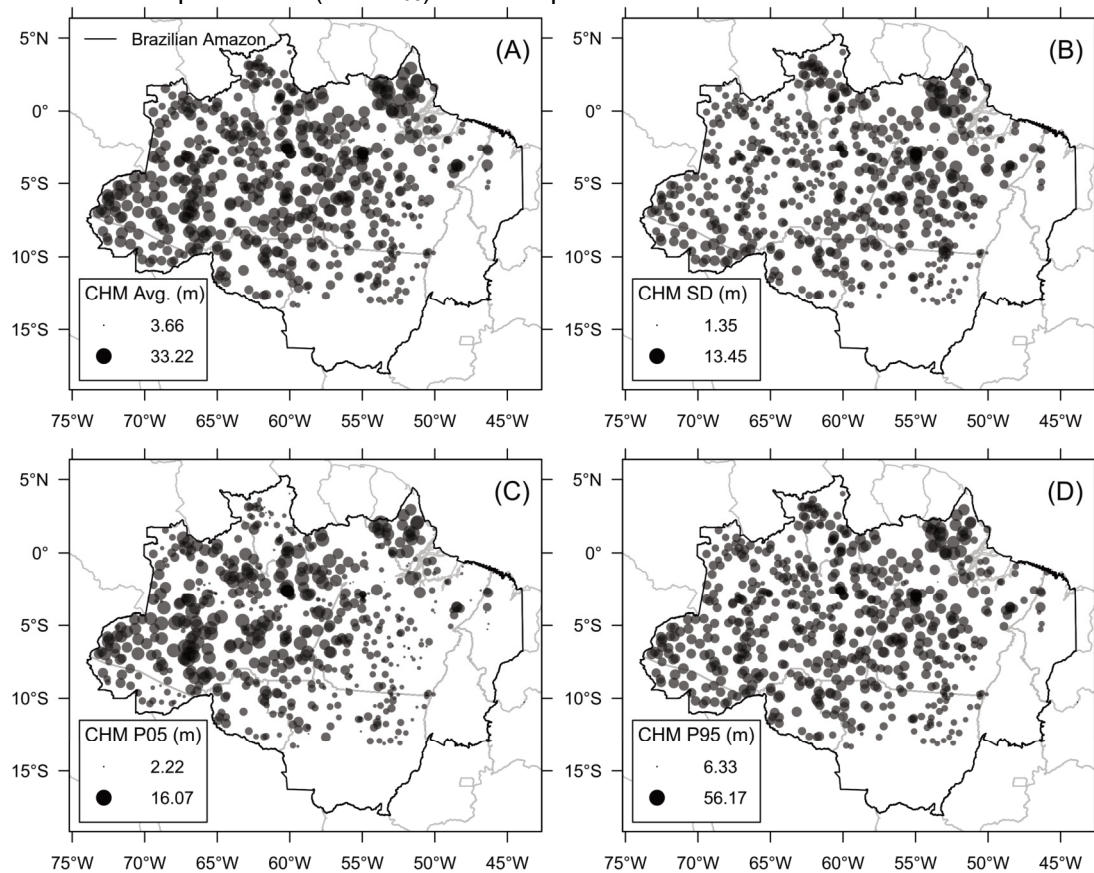
APPENDICES C - SUPPLEMENTARY MATERIALS FROM CHAPTER 6

Table C.1 - Multi-temporal airborne LiDAR data acquisition information.

Site	Acquisition Date	Sensor	Flight altitude (m)	Scan frequency (kHz)	Area (ha)
DUC	17 Feb 2012	Optech ALTM 3100	850	59.8	1200
	09 Apr 2017	Optech ALTM 3100	850	40	
TAP	31 Jul 2012	Optech ALTM 3100	850	59.8	1047
	06 Mar 2017	Optech ALTM 3100	850	40	
FN1	15 Aug 2013	Optech Orion M300	850	67.5	992
	06 Oct 2018	Optech ALTM 3100	750	40	
BON	16 Sep 2013	Optech Orion M300	900	61.4	572
	08 Oct 2018	Optech ALTM 3100	750	40	
TAL	29 May 2014	Optech Orion M300	900	61.4	480
	08 Oct 2018	Optech ALTM 3100	750	40	

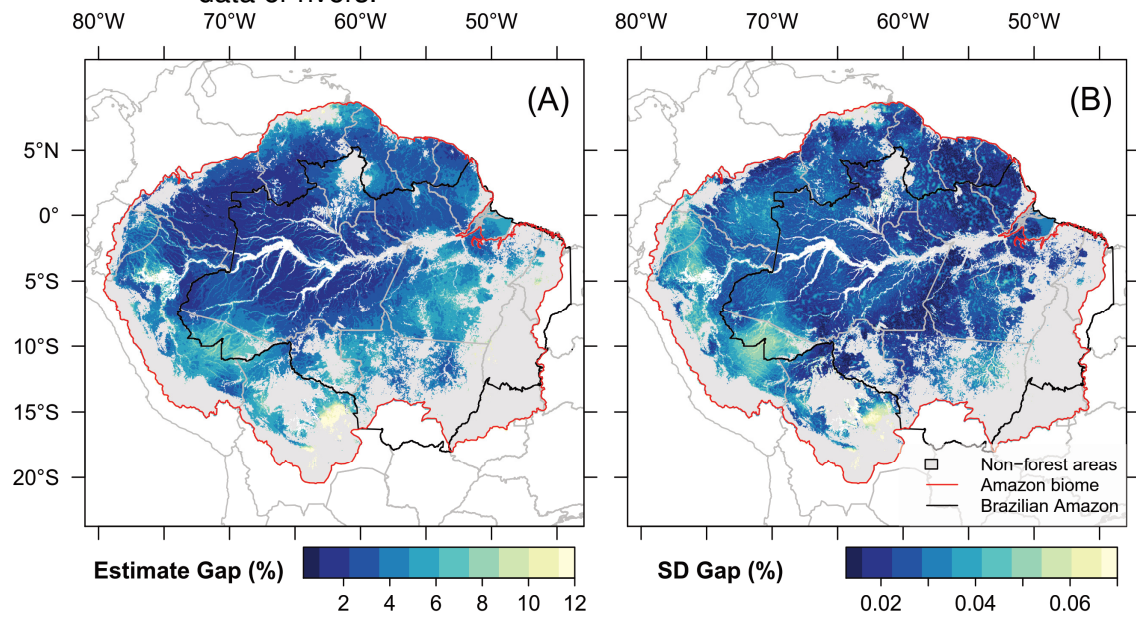
Source: Produced by the author.

Figure C.1 - Spatial variability of canopy height model (CHM) across the Brazilian Amazon ($n = 610$ flight lines): (A) CHM average (CHM_{AVG}), (B) CHM standard deviation (CHM_{SD}), (C) 5th percentile (CHM_{P05}), and (D) 95th percentile (CHM_{P95}). Units represent meters.



Source: Produced by the author.

Figure C.2 - Amazon-wide gap fraction prediction based on environmental and climate drivers. (A) Estimate gap fraction (%), and (B) standard deviation (SD) of gap fraction estimate (%). Areas in white correspond to either missing data or rivers.



Source: Produced by the author.